UNIVERSITY OF BIRMINGHAM

Crystallisation and microstructure in stamp formed fibre reinforced polyamide 66

By

William Hamby

A thesis submitted to the University of Birmingham

for the degree of

Doctor of Philosophy

School of Metallurgy and Materials

College of Engineering and Physical Sciences

University of Birmingham

April 2022

ACKNOWLEDGEMENTS

Firstly, I would like to express my sincere thanks and gratitude to my supervisor Dr. Mike Jenkins for his continual guidance and encouragement throughout the entirety of my PhD.

For their technical support, constructive feedback and invaluable advice, I would like to give my thanks to Frank Biddlestone and Dr. Catherine Kelly.

Further, I would like to pass on my gratitude to Neil Reynolds and Warwick Manufacturing Group for their collaboration and assistance in manufacturing of samples, without whom much of this work would not have been possible.

Finally, I would like to thank my family for their unwavering love and support throughout my time in academia. Their resounding belief in me has provided great encouragement and without them, none of this would have been possible.

ABSTRACT

Thermoplastic fibre reinforced composites have the potential to reduce the CO_2 emissions of automotive vehicles through processes such as vehicle lightweighting. In comparison to the current structural metallic components, composites offer considerable improvements in the strength-to-weight ratio of automotive parts, ultimately enhancing the fuel efficiency of the vehicle. Polyamide 66 (PA66) is an affordable, tough and durable engineering thermoplastic with intrinsically good tribological and chemical resistance properties. Further, the mechanical properties and dimensional stability of polyamides can be improved by the addition of continuous glass fibre reinforcement. This work aims to characterise through-thickness crystallinity and microstructural morphology in stamp formed glass fibre reinforced polyamide 66 (PA66/GF).

As determined by calorimetry, the through-thickness degree of crystallinity of an 11-ply PA66/GF composite was shown to be inversely proportional to the rate of heat loss throughout the stamp forming process. Within the surface layers of the composite, where cooling rates were observed to reach 1400 °C/min, crystallinity was found to be 3.0% lower than that of the central layers which, by comparison, crystallised under quasi-isothermal conditions. The variation in crystallinity owing to the disparity in cooling rates was further confirmed by x-ray diffraction (XRD). Analysis of one-dimensional (1D) wide angle x-ray scattering (WAXS) patterns demonstrated that despite the distinctly non-isothermal crystallisation conditions of the stamp forming process, the matrix polyamide rapidly crystallises into a triclinic unit cell characteristic of the α-phase of PA66. However, despite this, the intensities of the α_1 and α_2 peaks representative of the (100) and (010)/(110) crystallographic planes, respectively, were found to differ through the thickness of the laminate, indicative of a change in crystal structure.

Isothermal crystallisation kinetics of PA66/GF were analysed over a crystallisation temperature (T_c) range of 245 to 249 °C where, owing to both models accounting for the contribution of secondary crystallisation, the parallel Velisaris-Seferis and Hay equations were shown to provide the best fit

to the experimental data ($R^2 > 0.995$). Hay's assumption that both primary and secondary crystallisation occur simultaneously and that total crystallinity at time *t*, is the sum of the two contributions, was confirmed. Further, having not previously been applied to polyamides or thermoplastic reinforced composites, the findings of this study support the use of the Hay model in determining the isothermal crystallisation kinetics of polymeric materials.

Non-isothermal crystallisation kinetics were also evaluated using models developed by Jeziorny, Ozawa and Mo and over a cooling rate range of 10 to 60 °C/min. Mo's theory - a combined Avrami/Ozawa approach, was proven to be more successful than the Jeziorny and Ozawa models in describing the non-isothermal crystallisation of PA66/GF.

Post-stamp forming, low temperature annealing (T_a) of unidirectional and cross-ply PA66/GF laminates over the T_a range 60 to 110 °C was shown to improve the creep performance of the laminates. DSC thermograms obtained post-annealing showed the appearance of a low temperature melting peak (T_m') characteristic of the melting of thin crystalline structures. The value of T_m' was shown to be dependent on T_a with a 46.7 °C difference in T_m' observed between annealing temperatures of 60 and 110 °C (t = 4 hrs). With rising T_a the thickness of the thin lamella structures forming within the interlamella amorphous regions was found to increase which, in accordance with the Thomson-Gibbs equation resulted in T_m' shifting to higher temperatures. Further, by constraining the amorphous chains, the thin lamella structures developed at T_a of 110 °C were shown to improve load transfer between the matrix and fibres, increasing creep modulus and reducing creep strain by up to 25.2 GPa and 450%, respectively.

CONTENTS

CHAPTER 1 – INTRODUCTION 1
1.1 The importance of thermoplastics for automotive applications 1
1.1.1 Engineering Thermoplastics 4
1.1.2 Susceptibility of thermoplastics to creep behaviour 4
1.1.3 Manufacturing of thermoplastic composites for automotive applications 5
1.2 Microstructure of thermoplastics 7
1.2.1 Amorphous 7
1.2.2 Semi-crystalline 7
1.3 The crystallisation process 9
1.3.1 Primary crystallisation: nucleation and growth 9
1.3.1.1 Temperature dependence of crystal growth 12
1.3.2 Secondary crystallisation 15
1.4 Polyamides 16
1.4.1 Polyamide 66 16
1.4.1.1 Fibre reinforcement 19
1.5 Scope of the work 23

CHAPTER 2 - METHODOLOGY 24
2.1 Materials 24
2.1.1 Fibre reinforced thermoplastic tape 24
2.1.2 Tape consolidation - stamp forming 24
2.2 Experimental techniques 25
2.2.1 Differential scanning calorimetry (DSC) 25
2.2.1.1 Calculating the degree of crystallinity from the enthalpy of fusion 26
2.2.2 Thermogravimetric analysis (TGA) 27
2.2.3 Muffle furnace 28
2.2.4 Fourier transform infrared spectroscopy (FTIR) 28
2.2.5 Wide angle x-ray scattering (WAXS) 29
2.2.6 Creep tests 29

CHAPTER 3 - THROUGH THICKNESS CHARACTERISATION OF AN 11-PLY PA66/GF STAMP FORMED COMPOSITE 30
3.1 Introduction 30
3.1.1 Temperature dependence on through-thickness crystallinity as measured by differential scanning calorimetry (DSC) 30
3.1.2 Crystallinity measurements using Fourier transform infrared (FTIR) spectroscopy 33
3.1.3 Aims and objectives 37
3.2 Methodology 38
3.2.1 Materials and sample preparation 38
3.2.2 Differential scanning calorimetry (DSC) 39
3.2.2.1 Preliminary DSC experiments 40
3.2.2.1.1 Influence of heating rate 40
3.2.2.1.2 Effect of localised fibre distribution on heat of fusion measurements 40
3.2.2.2 Calculating the through-thickness degree of crystallinity of a stamp formed PA66/GF composite 41
3.2.2.3 Determining polyamide matrix mass fraction 43
3.2.3 Fourier transform infrared spectroscopy (FTIR) 43
3.2.3.1 Crystallisation on cooling from the melt 43
3.3 Results and discussion 44
3.3.1 Temperature profile of stamp forming process 44
3.3.1.1 Preheating of the thermoplastic composite (0 to 340 seconds) 45
3.3.1.2 Transfer from oven to mould (340 to 358 seconds) 47
3.3.1.3 Closing of the tool and application of the applied load (358 to 370 seconds) 49
3.3.1.4 Conclusion of forming cycle (370 to 500 seconds) 52
3.3.2 Characterisation of a stamp formed PA66/GF composite by differential scanning calorimetry (DSC) 54
3.3.2.1 Determination of matrix mass fraction using thermogravimetric analysis (TGA) and muffle furnace 54
3.3.2.2 Preliminary testing 56

3.3.2.2.1 Influence of heating rate on polymer characterisation – cold crystallisation vs thermal lag 57
3.3.2.2.2 Variation in fibre distribution and its effect of matrix mass 59
3.3.2.3 Temperature dependence of through-thickness crystallinity 62
3.3.3 Fourier transform infrared spectroscopy (FTIR) 71
3.3.3.1 Suitability of FTIR spectroscopy in obtaining reliable measurements of crystallinity 71
3.4 Conclusions 74

CHAPTER 4 - CHARACTERISATION OF A STAMP FORMED 11-PLY PA66/GF COMPOSITE BY X-RAY DIFFRACTION 76
4.1 Introduction 76
4.1.1 Microstructure of polyamide 66 and characterisation using x-ray diffraction (XRD) 76
4.1.1.1 Characterisation of the Brill transition in polyamides 78
4.1.2 Crystallinity variations as measured by wide angle x-ray scattering (WAXS) 80
4.1.3 Influence of fibre reinforcement on the development of a transcrystalline layer 81
4.1.4 Aims and Objectives 82
4.2 Methodology 83
4.2.1 Sample preparation 83
4.2.2 Experimental procedure 84
4.3 Results and discussion 86
4.3.1 Data processing 86
4.3.2 Through-thickness characterisation of a PA66/GF laminate using WAXS 89
4.4 Conclusions 94

CHAPTER 5 - ISOTHERMAL CRYSTALLISATION KINETICS OF PA66/GF 96
5.1 Introduction 96
5.1.1 Quantification of isothermal crystallisation kinetics 97
5.1.1.1 The Avrami model 97

5.1.1.1.1 Limitations associated the use of the Avrami model 98
5.1.1.2 Tobin model 99
5.1.1.3 Malkin model 99
5.1.1.4 Urbanovici-Segal model 100
5.1.2 Models accounting for the contribution of secondary crystallisation 101
5.1.2.1 Velisaris-Seferis model 101
5.1.2.2 Hay model 102
5.1.3 Suitability of the isothermal kinetic models – A review of the literature 104
5.1.4 Aims and objectives 106
5.2 Methodology 108
5.2.1 Materials and sample preparation 108
5.2.2 Isothermal crystallisation kinetics 108
5.3 Results and discussion 113
5.3.1 Qualitative analysis of isothermal crystallisation kinetics using Differential Scanning Calorimetry (DSC) 113
5.3.2 Traditional analysis and quantification of the isothermal crystallisation kinetics of PA66/GF using Differential Scanning Calorimetry (DSC) 119
5.3.2.1 Crystallisation kinetic analysis using the Avrami model 119
5.3.2.2 Crystallisation kinetic analysis using the Tobin model 121
5.3.2.3 Crystallisation kinetic analysis using the Malkin model 123
5.3.2.4 Non-linear regression analysis of the Avrami, Tobin and Malkin kinetic parameters 125
5.3.2.4.1 Conclusions 131
5.3.2.5 Non-linear multi-variable regression analysis of the isothermal crystallisation of PA66/GF 132
5.3.2.5.1 Modelling of the experimental data using the Urbanovici-Segal equation 138
5.3.2.5.2 Modelling of the experimental data using the Velisaris-Seferis equations 141
5.3.2.5.3 Comparison of the standard error of the regression of the models fitted using non-linear regression multi-variable regression analysis 146
5.3.2.5.4 Conclusions 152

5.3.3 A new analytical approach to quantifying isothermal crystallisation kinetics using Differential Scanning Calorimetry (DSC) 153
5.3.3.1 Theory of the Hay approach 153
5.3.3.1.1 Quantifying the secondary crystallisation contribution 155
5.3.3.1.2 Quantifying kinetic parameters from the primary contribution 160
5.3.3.2 Comparison of Hay's theory to traditional methods of analysis 161
5.3.3.2.1 Deriving the kinetics of primary crystallisation 161
5.3.3.2.2 Curve fitting of the predetermined kinetic parameters using SPSS software 162
5.3.3.2.3 Non-linear multi-variable regression analysis using SPSS software 165
5.3.3.2.3.1 Modelling of the Hay equation versus traditional equations 167
5.3.3.2.4 Summary of comparison 171
5.3.3.3 The applicability of Hay's theory to the Avrami, Tobin and Malkin kinetic models 172
5.3.3.3.1 Standard error of the regression analysis 176
5.3.3.4 Non-linear multi-variable regression analysis of the kinetic models using isothermal data modified by the Hay approach 180
5.3.3.5 Conclusions 190

CHAPTER 6 - NON-ISOTHERMAL CRYSTALLISATION KINETICS OF PA66/GF 191
6.1 Introduction 191
6.1.1 Jeziorny model 192
6.1.2 Ozawa model 192
6.1.3 Mo's model 193
6.1.4 A review of the literature 194
6.1.4.1 Influence of fillers on the crystallisation rate of polymer matrix composites (PMC) 194
6.1.4.2 Suitability of non-isothermal crystallisation kinetic models 195
6.1.5 Aims and objectives 197
6.2 Methodology 198
6.2.1 Materials and sample preparation 198

6.2.2 Non-isothermal crystallisation kinetics 198
6.3 Results and discussion 199
6.3.1 Quantitative analysis of non-isothermal crystallisation kinetics using Differential Scanning Calorimetry (DSC) 199
6.3.2 Non-isothermal crystallisation kinetic analysis using the Jeziorny model 205
6.3.3 Non-isothermal crystallisation kinetic analysis using the Ozawa model 207
6.3.4 Non-isothermal crystallisation kinetic analysis using Mo's theory 212
6.4 Conclusions 215

CHAPTER 7 - THE EFFECT OF LOW TEMPERATURE ANNEALING ON MORPHOLOGICAL EVOLUTION AND CREEP RESISTANCE IN PA66/GF COMPOSITES 216
7.1 Introduction 216
7.1.1 Thermoplastics and creep behaviour 216
7.1.2 Annealing of thermoplastics 219
7.1.2.1 Influence of moisture on annealing of polyamides 223
7.1.3 Aims and objectives 224
7.2 Methodology 225
7.2.1 Morphological effects of low temperature annealing as measured by DSC analysis 225
7.2.1.1 Materials and sample preparation 225
7.2.1.1.1 Annealing process 225
7.2.1.2 Differential scanning calorimetry measurements 225
7.2.2 Creep testing 226
7.2.2.1 Materials and sample preparation 226
7.2.2.1.1 Annealing process 226
7.2.2.2 Creep measurements 227
7.3 Results and discussion 228
7.3.1 Morphological refinements of PA66/GF with low temperature annealing 228
7.3.1.1 Characterising the low temperature endothermic peak – Tg or Tm? 229
7.3.2 Effect of annealing temperature and time on the low temperature melting peak 230

7.3.2.1 Temperature dependence of lamella thickness 239
7.3.3 Effect of low temperature annealing on the high temperature melting peak 240
7.3.4 Creep behaviour of a PA66/GF laminate 243
7.3.4.1 Effect of moisture on the creep performance of an annealed PA66/GF composite 246
7.3.4.2 Effect of low temperature annealing on creep performance of PA66/GF laminates 247
7.3.4.3 Influence of annealing temperature and time on creep behaviour 252
7.4 Conclusions 256

CHAPTER 8 - CONCLUSIONS AND FUTURE WORK 258
8.1 Conclusions 258
8.2 Future work 262

APPENDICES 285
Appendix A – Materials datasheet PA66/GF 286

CHAPTER 1 - INTRODUCTION

1.1 The importance of thermoplastics for automotive applications

As legislated by the European Union [1], the reduction in carbon dioxide (CO_2) emissions of automotive vehicles is being achieved through a variety of means. One such process is vehicle lightweighting. Lightweighting reduces the CO_2 emissions of vehicles by enhancing fuel efficiency and can be achieved by the replacement of structural metallic components with parts manufactured from fibre reinforced polymer matrix composites (PMC). Composites offer considerable improvements in the strength-to-weight ratio and corrosion resistance of automotive parts [2,3], with carbon or glass fibre reinforcement ensuring the required mechanical properties are satisfied (Table *1.1*) [2].

The polymer matrix of PMC can be one of two distinct forms: thermosetting or thermoplastic. Though both provide a significant weight saving when compared with metallic alloys, the production time required to process thermoplastic parts is considerably quicker than that of thermosets. This difference originates from the shape-stabilisation mechanisms of the two polymer forms.

Thermosetting polymers undergo a curing process in which shape-stabilisation occurs through cross-linking of the polymer chains. During this process, irreversible covalent bonds are formed between the chains resulting in a component, the geometry of which, once set, cannot be changed. Typically, thermosetting polymers are stronger and better suited to high-temperature (>100 °C) applications than thermoplastics, however, due to the permanent nature of their cross-links they are not re-usable or recyclable [4].

Shape-stabilisation of thermoplastics occurs through crystallisation (section 1.3), a process in which a highly ordered structure is formed from a disordered phase (usually on cooling from

above the melting temperature). The entire crystallisation process is usually complete in a matter of minutes [5], a fraction of the time associated with the curing of thermosets, which can often take several hours. Furthermore, dissimilar to thermosets which set on cooling, crystallisation is a reversible process, meaning that once formed, the thermoplastic can be re-heated and re-shaped into an alternative component geometry [2,3]. In general, thermoplastics offer significant benefits over thermosets for automotive applications. Thermoplastics are inherently more ductile, resulting in products with greater toughness and impact resistance [4,5], and recyclable, ensuring that the end-of-life of the component is economically and environmentally beneficial to the automotive industry [2,3].

Table 1.1: Comparison of the thermal and mechanical properties of polyamide 66 (PA66), polyetheretherketone (PEEK), aluminium (5 series), high strength low alloy steel and single-ply polyamide 66 glass fibre reinforced (40 vol.%) composites (PA66/GF) as listed in CES Edupack [6].

Properties	**PA66**	**PEEK**	**Aluminium**	**Steel**	**PA66/GF**
Young's Modulus (Gpa)	1.5	3.9	66.0	210.5	10.0
Specific Stiffness (MPa/kg/m^3)	1.3	3.0	-	26.8	6.9
Yield Strength (Mpa)	57.5	100.0	276.0	330.0	160.0
Specific Strength (MPa/kg/m^3)	0.05	0.08	0.07	0.04	0.11
Hardness (HV)	17.0	29.5	92.0	138.0	48.0
Fracture Toughness (Mpa.m$^{0.5}$)	3.5	3.5	21.5	44.3	10.3
Flexural Strength (Mpa)	96.5	110.5	184.5	330.0	270.0
Melting Temperature (°C)	260	334	660	1470	-
Glass Transition Temperature (°C)	50	150	-	-	-

1.1.1 Engineering Thermoplastics

Two of the most important engineering thermoplastics used across a variety of industries are polyetheretherketone (PEEK) and polyamides (PA). PEEK displays excellent mechanical properties [7] (Table *1.1*) and is widely used in high performance applications where outstanding thermal resistance and tribological properties are paramount. Polyamides are not as thermally stable at high temperatures (>100 °C) as PEEK, but are tough, durable materials with intrinsically good tribological and chemical resistance properties [8–10]. In comparison to other polyamides and thermoplastics such as polyolefins, poly(hexamethylene adipamide) (PA66) possesses the best combination of thermo-mechanical, heat resistant and fatigue strength properties [9,11]. It is also substantially more cost effective than PEEK and requires drastically lower processing temperatures [10].

The mechanical properties and heat deflection temperature (resistance to distortion under an applied load at an elevated temperature) of PA66 can be further improved by the addition of glass fibre (GF) reinforcement (Table *1.1*). The addition of continuous fibres to the PA66 matrix enhances the dimensional stability, fatigue strength (64 MPa) [6], impact energy and functional service temperature of the thermoplastic [11,12]. It is for these reasons that polyamide 66 glass fibre reinforced (PA66/GF) thermoplastic composites are becoming increasingly more useful for engineering applications with stricter thermo-mechanical requirements [10].

1.1.2 Susceptibility of thermoplastics to creep behaviour

Despite excellent thermal and mechanical properties, thermoplastics are inherently susceptible to creep. Creep is a time-dependent permanent deformation process resulting from prolonged exposure to a constant stress below the elastic limit (yield stress) of a material. Owing to their viscoelastic nature, that is, demonstrating solid- or liquid-like behaviour as a function of time,

thermoplastics are inherently susceptible to creep [13,14]. Creep behaviour is incredibly important in engineering applications, especially for structural components where dimensional stability is a necessity. Thermoplastics demonstrating significant time sensitive properties under the working environmental conditions (~25 °C, 40% r.h.) will be of limited use as such, part design, crystal microstructure and the addition of fillers/fibre reinforcement must be carefully considered [13,15].

1.1.3 Manufacturing of thermoplastic composites for automotive applications - Stamp forming

The manufacturing of automotive parts from thermoplastic polymer matrix composites (PMC) can transpire in many ways including thermoforming techniques such as vacuum forming and stamp forming. Typically, thermoforming techniques utilise pre-impregnated PMC tape, manufactured by casting a thermoplastic film over the reinforcement fibres and passing the materials through heated rollers thereby forcing the polymer to impregnate the fibres.

Stamp forming is a high-speed, streamline thermoforming technique extensively used within the automotive industry for sheet metal forming [5]. A technique suitable for part manufacture in large volumes, stamp forming is highly transferable and suitable for use with thermoplastic composites, resulting in no further capital investment for automotive manufacturers. Forming of thermoplastics involves the heating of a pre-consolidated laminate to above the melting temperature (T_m) of the polymer matrix in an appropriate oven. The sample is then quickly transferred to the press and positioned between two tools (moulds). The press is closed, and a consolidation pressure applied. PMCs deform by a combination of intra-ply shearing and interply slippage [3] taking the shape of the tool geometry. Though a seemingly straight forward

technique, the final morphology of the polymer matrix and resulting mechanical properties of the part are heavily dependent on the numerous forming parameters. These include the initial pre-heat temperature, tool temperature, tool opening/closing velocity, consolidation pressure and hold time [16,17]. Forming of PMC is considered to be highly temperature dependent, with optimum formability achieved when the polymer matrix is maintained above T_m during the initial application of the consolidation pressure [5,16]. Furthermore, in addition to enhancing the forming mechanisms (i.e. intra-ply shearing), maintaining the temperature above T_m is imperative in delaying the onset of crystallisation [3,5]. It was proposed previously in a study of polyamide-6 (PA6) that a critical crystallinity ($\geq$ 1%) exists, beyond which, issues relating to formability rise significantly [3]. Consequently, a 'forming window' between the transfer of the PMC to the heated tool and the time taken to reach critical crystallinity of the polymer matrix was established. Despite restricting forming time, the duration of the window is not set and can be extended by optimising the aforementioned forming parameters.

1.2 Microstructure of thermoplastics

Depending on the degree of microstructural order, thermoplastics can be classified as either amorphous or semi-crystalline materials.

1.2.1 Amorphous

Amorphous polymers are highly disordered and lacking in structural regularity. Above the melting temperature (T_m), in the liquid-state, the polymer chains are chaotic, coiled and in a constant state of long-range motion. The thermal energy of the system is sufficient for chains to freely rotate, allowing for unrestricted conformational change. As the temperature decreases below T_m, chain mobility is significantly reduced, with the polymer now considered to be in the 'rubbery' state. Chain mobility continues to fall with decreasing temperature, until eventually, there is insufficient thermal energy available to overcome the barrier to chain rotation [18]. The temperature at which this occurs is referred to as the glass-to-liquid transition temperature (T_g). Below T_g the polymer is deemed to be in a glass-like state where, it retains the disordered morphology described above T_g, but no longer has the required energy to undergo long-range chain motion or conformational change.

1.2.2 Semi-crystalline

Semi-crystalline polymers consist of a disordered amorphous phase constrained between highly ordered, crystalline lamella. Identical to that of amorphous polymers, in the liquid-state (above T_m), the polymer chains are highly disordered and in a constant state of long-range motion. On cooling below T_m, chain alignment and intermolecular interactions between neighbouring chains result in the formation of crystalline lamella structures with a high degree of long-range

order. The morphology of these structures can be defined by the regularity in the folding of the polymer chains (Figure 1.1).

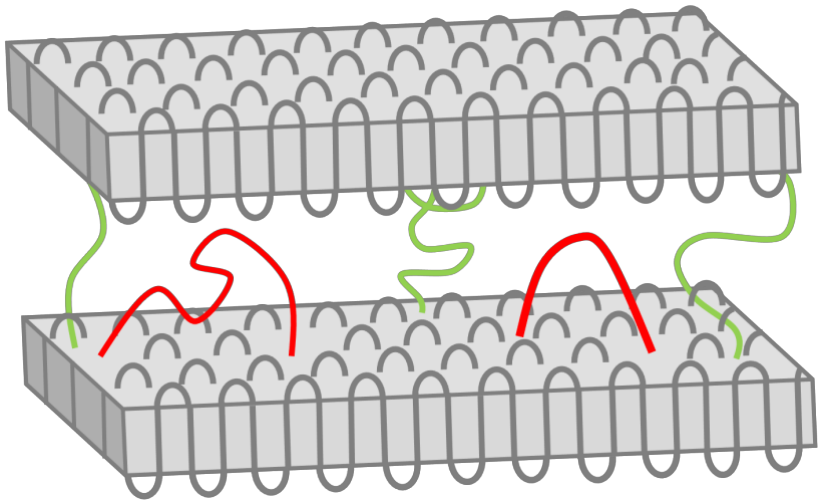

Figure 1.1: Schematic representation of the chain-folded arrays characteristic of the crystalline microstructure within semi-crystalline thermoplastics; regular chain-folding (*grey*), random re-entry (*red*) and tie molecules (*green*).

Regular chain-folded arrays are formed when the re-entry of the aligned polymer chains into the crystalline lamella is adjacent and uniform. This results in a highly regular lamella structure, where the closely packed chains fold back and forth with hairpin-type turns [19] (Figure 1.1). Conversely, some of the chains do not re-enter the lamella structure in such an orderly and sequential way. Instead, the chains meander throughout the disordered amorphous phase (situated between the crystalline lamella) before randomly re-entering the crystalline structure at various locations [18,19]. This random re-entry of the chain-folded segments is defined as the switchboard model (Figure 1.1 (*red*)). Furthermore, similar to the switchboard model described above, tie molecules leave the closely packed arrangement of one crystalline lamella structure and traverse through the amorphous phase before randomly re-entering an adjacent crystalline lamella (Figure 1.1 (*green*)).

1.3 The crystallisation process

Crystallisation can be thought of as the formation of a closely packed, highly ordered array developed on cooling from the disordered melt. The crystallisation of thermoplastics from the liquid melt can be defined by a two-stage process: nucleation and growth.

1.3.1 Primary crystallisation: nucleation and growth

Nucleation signifies the onset of the crystallisation process and can be sub-divided into two key components: primary and secondary nucleation. The primary process is initiated on cooling below T_m, where random rotations about the polymer chains result in the alignment and formation of small-ordered aggregates known as nuclei (or embryos). This form of spontaneous nucleation is defined; homogeneous [20]. The nuclei that form are rarely comprised of an entire polymer chain and are considered to be metastable as they often revert back to the disordered amorphous phase before reforming – this process, however, depends on the free energy of the system [21,22].

The free energy difference (ΔG) between the formation of a solid crystallite and the disordered, viscous melt is a key driving force of the crystallisation process and can be described using the Gibbs free energy equation:

$$\Delta G = \Delta H - T\Delta S$$

Equation 1-1

Where ΔH is the enthalpy change, ΔS the entropy change and T the isothermal crystallisation temperature. On cooling below T_m, the free energy of the system becomes negative ($\Delta G < 0$) and as such, the thermodynamic driving force for crystallisation increases.

Upon nucleation, the overall excess free energy of the system is proportional to the sum of the surface free energy and volume free energy of the nuclei. Surface free energy (ΔG_S) is a positive quantity relative to the square of the nuclei radius (r^2), whereas volume free energy (ΔG_V) is a negative quantity corresponding to the cube of the nuclei radius (r^3). When formed, nuclei possess a positive surface energy and thus, initially increase the ΔG of the system.

As the nuclei grow so does the surface energy and with it, ΔG. However, due to the disproportionate effects of the surface and volume free energies, as the radius of the nuclei increases, the surface-to-volume ratio decreases and with it the overall positive contribution to ΔG. This dependence of ΔG on nuclei radius causes the excess free energy to go through a maximum, past which ΔG continues to fall as the nuclei grows (Figure 1.2). This maximum corresponds to the critical nuclei size beyond which, the nuclei is considered to be stable and will continue to grow spontaneously as the persistent reduction in ΔG is thermodynamically favoured [18].

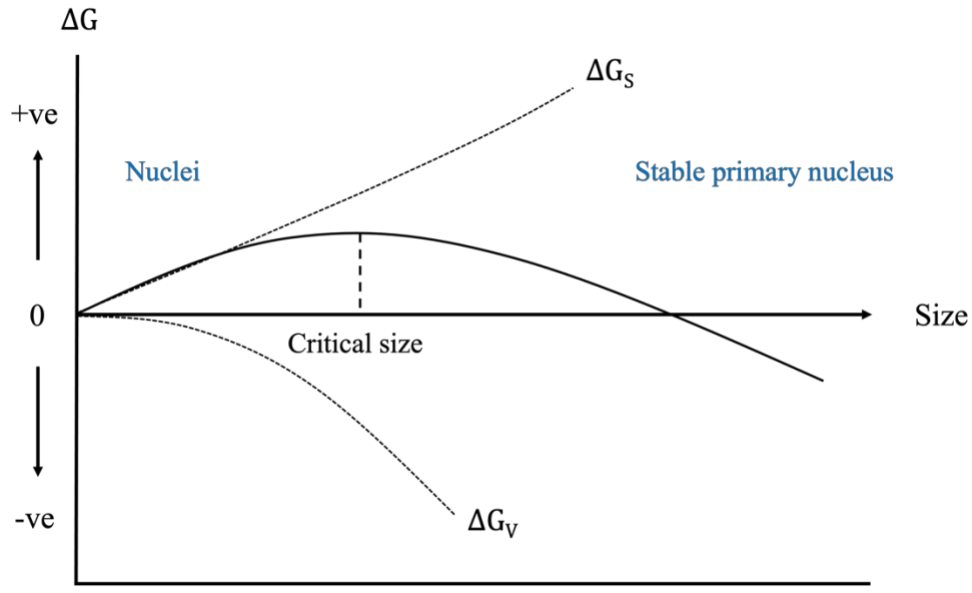

Figure 1.2: Schematic representation of the changes in free energy (ΔG) associated with the nucleation process.

Once a stable primary nucleus has been formed, secondary nucleation is initiated, whereby molecules are added to the growth face of the pre-existing nucleus through a chain-folding process [23]. The energy barrier to secondary nucleation is lower than that associated with primary nucleation due to the continuous reduction in the surface-to-volume ratio of the nucleus as it grows [24]. Secondary nucleation can also be artificially induced by impurities or foreign particles within the polymer melt. This is defined as heterogeneous nucleation and is the most common nucleation mechanism as the absence of primary nucleation is thermodynamically favoured.

Secondary nucleation can be considered the growth process of crystallisation whereby rotational motion about the polymer backbone leads to the alignment and chain-folding of polymer molecules forming fibrils which spread outwards into the surrounding amorphous phase. These fibrils form the crystalline lamellae which grow radially from the nucleus into the melt, branching out and entrapping the disordered amorphous phase between them [18]. The structures formed are known as spherulites. Providing sufficient thermal energy and time are available, these spherulites continue to grow radially until impingement occurs. Upon impingement linear boundaries are formed between the growing spherulites resulting in crystals which are polyhedral in shape (Figure 1.3).

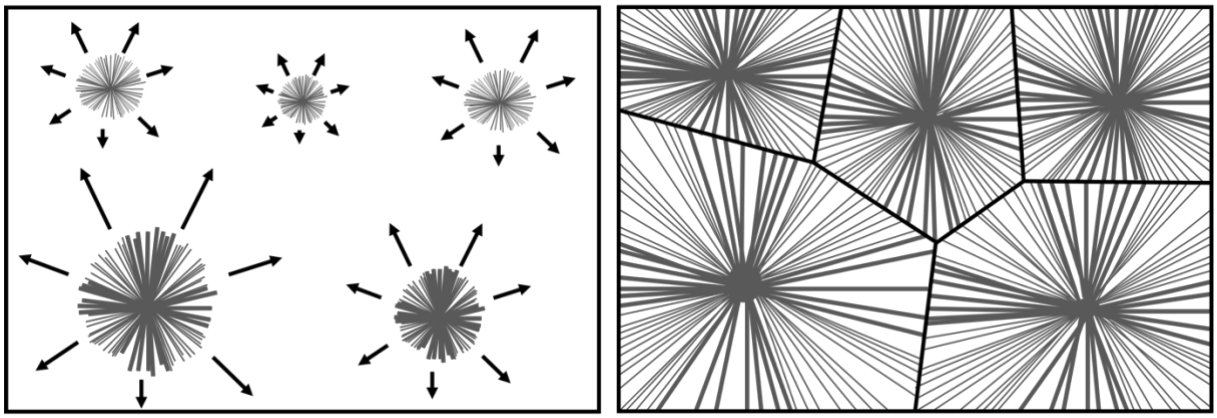

Figure 1.3: Schematic images of spherulitic growth on cooling from the liquid melt, showing radial growth (*left*) and the impingement process resulting in linear boundaries and the formation of polyhedral shaped crystals (*right*).

1.3.1.1 Temperature dependence of crystal growth

Crystallisation from the melt is highly temperature dependent and is only possible between two bounds: T_m and T_g. Above the melting temperature, the polymer is considered to behave as a liquid, chains are in a constant state of motion and disorder, and the formation of a stable growth nucleus is not possible. In contrast, below T_g, chains are essentially immobile, and the thermal energy is insufficient in overcoming the barrier to chain motion and thus, crystal growth.

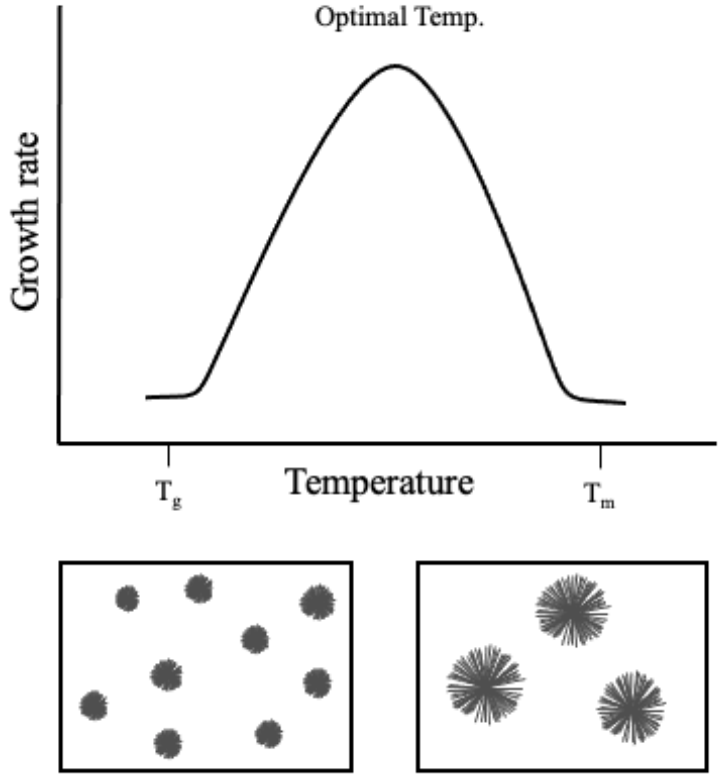

Figure 1.4: Schematic representation of the temperature dependence of crystallisation and the two competing processes; nucleation and growth. At T_c close to T_g a large number of small nuclei are typically formed and at T_c close to T_m a small number of large nuclei are formed.

At crystallisation temperatures (T_c) close to T_g (high degree of super-cooling), nucleation is thermodynamically favoured, resulting in a higher rate of primary nuclei formation. Despite this, growth of the newly formed nuclei is slow. A reduction in the thermal energy of the system at lower crystallisation temperatures, limits the mobility of the polymer chains and as such, the rate at which molecules are transferred to the crystal growth face is significantly reduced. As a result, crystallisation at temperatures close to T_g is said to be growth limited and the resulting morphology consists of a vast number of small spherulites (Figure 1.4).

Conversely, at high crystallisation temperatures, close to T_m (low degree of super-cooling), growth is thermodynamically favoured (Figure 1.4). Chain mobility and segmental motion is

greater at these elevated temperatures and as such, the formation of stable primary nuclei is challenging [18]. Crystallisation at temperatures close to T_m is said to be nucleation limited with the resulting morphology consisting of a small number of larger spherulites [25].

Consequently, the isothermal temperature at which crystallisation occurs can have a radical effect on the morphology and ultimately, the mechanical performance of a polymer. Crystallisation at temperatures close to T_g, leading to the formation of many small spherulites, generally results in a ductile polymer with low modulus, but high toughness and elongation to break. In contrast, a polymer crystallised close to T_m, with a small number of large spherulites, often demonstrates brittle behaviour, exhibiting a greater tensile strength and modulus but with lower toughness and elongation to break. The resulting failure mechanism (ductile or brittle) is greatly dependent on the distribution of fracture energy at spherulite boundaries [26,27]. Large spherulites typically heighten the fracture energy at the boundary surface of the lamellar often promoting microcrack initiation and resulting in brittle fracture [27]. Conversely, by reducing spherulite diameter the failure energy is dissipated across numerous boundary surfaces thereby increasing the toughness and ductility of the material [27,28]. As a result, a compromise between the two crystallisation temperatures (T_g and T_m) is regularly required.

Attributable to the conflicting temperature dependence of nucleation and growth, the greatest rate of crystallisation can be observed at an optimal temperature between T_m and T_g (Figure 1.4). Knowledge of the temperature dependence of crystal growth is imperative to the crystallisation process of polymers and allows the morphology and thus, mechanical properties of the polymer to be somewhat tailored to the desired application.

1.3.2 Secondary crystallisation

Secondary crystallisation can be considered the final stage of the crystallisation process. Unlike primary crystallisation which occurs freely on cooling from the melt, secondary crystallisation takes place within a confined environment between the existing lamellar structures formed during the primary process [29]. Observed as an increase in crystallinity post-spherulite impingement, secondary crystallisation can occur by two discrete mechanisms: lamellar thickening or lamellar infill. Lamellar thickening is the process by which polymer chains are incorporated from within the disordered amorphous phase onto the surface of pre-existing lamellar structures causing them to thicken. Conversely, lamellar infill is the formation and growth of small crystalline regions materialising from within the amorphous phase of the primary crystallite (Figure 1.5).

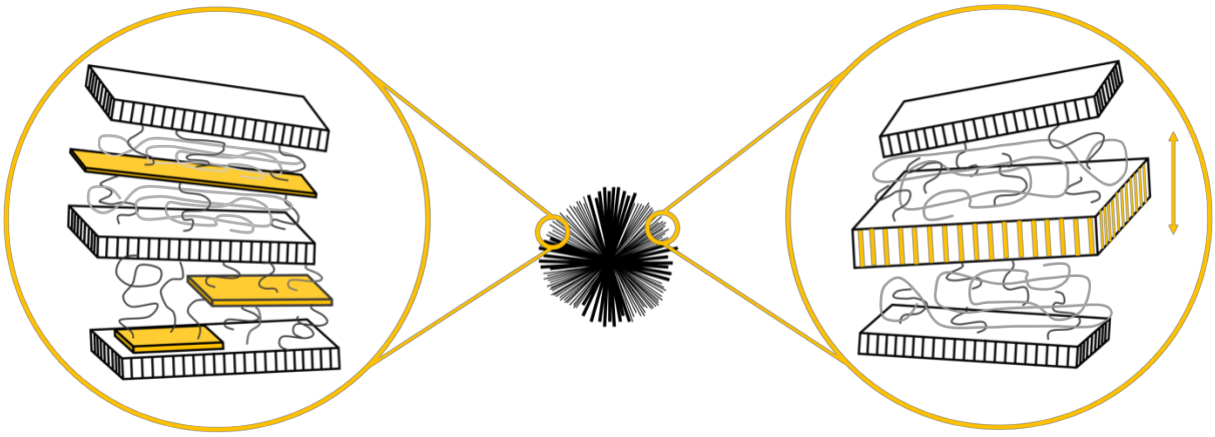

Figure 1.5: Schematic image depicting two secondary crystallisation processes; lamella infill (*left*) and lamella thickening (*right*).

1.4 Polyamides

Polyamides are semi-crystalline aliphatic polymers typically produced via a condensation reaction between a diamine and diacid. They are numerically defined by the length of methylene segments (CH_2) between the characteristic amide functional group (CONH) and their degree of crystallinity fundamentally dependent on the formation of hydrogen bonds and close-packed nature of the polymer chains. Hydrogen bonds are an intermolecular force formed between the induced dipole of the amine (N-H) and highly polar carbonyl group (C=O) of a neighbouring chain. These bonds maintain the highly ordered structure of polyamides and are reportedly so strong, that up to 20% of hydrogen bonds are retained within the liquid melt [30,31].

1.4.1 Polyamide 66

Hexamethylene adipamide (or polyamide 66 / PA66) is one of the most frequently used polyamides for engineering applications. Synthesised from a polycondensation reaction between hexamethylenediamine and adipic acid (Figure 1.6), the molecular weight of polyamide 66 is defined by the extent of step-growth polymerisation, whereby monomer units of the polyamide combine to form oligomers before eventually forming a long chain polymer. Compared to various other polyamides used for engineering applications, PA66 offers superior mechanical properties (Table *1.1*), fatigue strength (26 MPa) [6], toughness and wear resistance, and is one of the most thermally stabile polyamides with a typical glass-to-liquid transition and melting temperature of 50 °C [11] and 260 °C [32] respectively. Readily crystallising on cooling from the melt, polyamide 66 typically adopts one of two crystallographic forms: α-crystals or γ-crystals (Chapter 4).

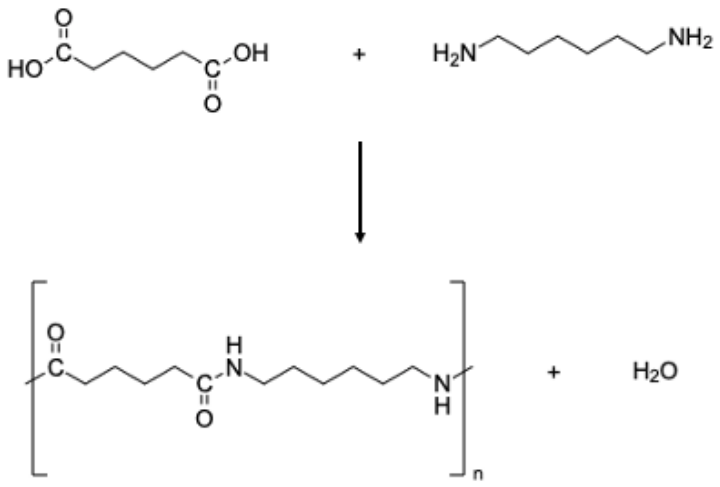

Figure 1.6: Polycondensation reaction between hexamethylenediamine and adipic acid forming Hexamethylene adipamide (polyamide 66) and water.

Characterisation of polyamides is widely reported throughout the literature using a variety of techniques including differential scanning calorimetry (DSC) [33–35], fast scanning chip calorimetry (FSC) [8,33], fourier transform infrared spectroscopy (FTIR) [36,37], x-ray diffraction (XRD) [38–40] and raman spectroscopy [41].

Capable of identifying thermal transitions such as the glass-to-liquid transition temperature (T_g), crystallisation temperature (T_c) and melting temperature (T_m), along with quantifying the kinetics of crystallisation (Chapters 5 and 6) and the degree of crystallinity (Chapter 3), thermal analysis by DSC is undoubtedly one of the most frequently used techniques for characterising polyamides [33–35] and polyamide matrix composites [3,11,42]. Comparable to other semi-crystalline polymers such as polyethylene terephthalate (PET) (Figure 1.7), the melting of polyamide 66 appears as a broad endothermic peak on a DSC trace, with peak melting temperature and the width of the melting peak characteristic of crystal perfection. Generally, the higher the value of T_m and narrower the width of the peak, the more ordered the crystalline

structure and the smaller the deviation between the perfection of the crystals. Conversely, lower values of T_m and broader peaks often symbolise a more disordered crystal arrangement.

Characteristic of the crystalline portion and representative of the energy required during melting of a semi-crystalline polymer, the area of the endothermic melting peak can be used to quantify the degree of crystallinity (X_c) using:

$$X_c = \Delta H_f / \Delta H_{f\infty}$$

Equation 1-2

Where ΔH_f is the heat of fusion (J/g) on melting and $\Delta H_{f\infty}$ the heat of fusion (J/g) of a theoretically perfect polyamide 66 crystal – taken to be 191 J/ g [43]. The degree of crystallinity is largely a function of the thermal history of the polymer, with a typical crystallinity value of ~30% for polyamide 66 [2,33]. Despite this, additives such as mineral fillers and fibre reinforcement can also drastically influence the resulting degree of crystallinity and microstructure of thermoplastic polymers.

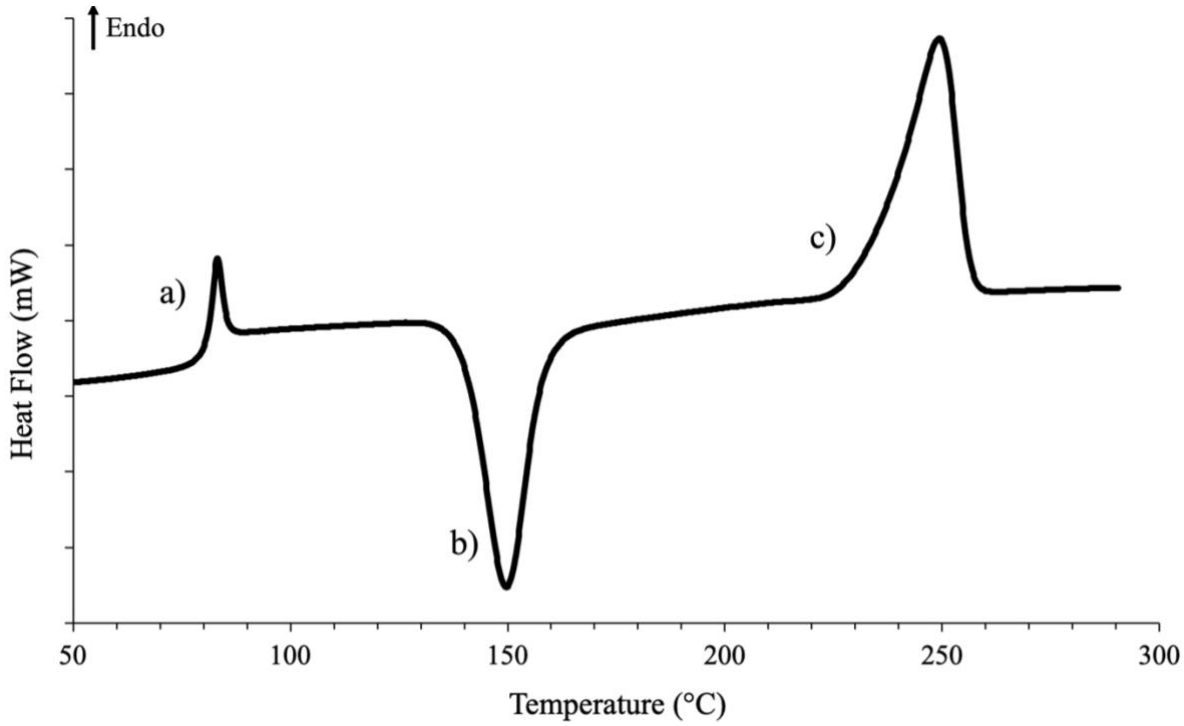

Figure 1.7: Schematic differential scanning calorimetry (DSC) trace of polyethylene terephthalate (PET), typical of semi-crystalline polymers, showing; a) stepped increase in heat capacity characteristic of the glass-to-liquid transition temperature, with a superimposed small endothermic peak associated with an enthalpy relaxation process, b) crystallisation exotherm and c) endothermic melting of the polymer crystals.

1.4.1.1 Fibre reinforcement

Polymer matrix composites (PMC) are becoming increasingly popular in the automotive industry for structural applications such as dashboards, air intake manifolds and engine covers [2,44], in which lightweighting and the specific strength and stiffness of the part are of critical importance [45]. As of 2016 almost 99% of PMC sold on the European composite market relate to glass fibre reinforcement [45], with 63% using thermosets as the matrix polymer compared to the 37% made of thermoplastics [45]. Despite this, resulting from their superior toughness, faster processing times and potential for recyclability, the use of thermoplastics in PMC is gaining momentum in the automotive industry [44,45].

The type of matrix polymer (thermoset or thermoplastic) and class of fibre reinforcement (short or long fibres) determine the possible manufacturing routes, with moulding techniques such as injection and vacuum infusion common with short fibre reinforced thermoplastics, whereas resin transfer moulding is more suited to long fibre reinforced thermosets [44,45].

The addition of fibre reinforcement to thermoplastics not only improves the mechanical properties and thermal stability of the polymer, but also produces a PMC suitable for engineering applications often with a higher specific strength and stiffness than many metal alternatives [3,11]. Compared with unfilled polyamides (Table *1.1*), glass filled polyamides are shown to have improved Young's modulus (10 GPa) and ultimate yield strength (160 MPa) [6,10]. When incorporated into the polyamide matrix, the surface of glass fibres behave as nucleating agents, promoting heterogeneous nucleation by reducing the free energy of the system. In doing so, the thermodynamic driving force for nucleation is increased and with it, the degree of supercooling required to initiate the onset of the nucleation process is reduced.

The crystalline structure arising off the surface of the glass fibres is fundamentally different to that formed in the bulk matrix. This is attributed to the nucleation density associated with each region [46]. The synergistic effect of the fibres results in nuclei forming off the surface of the glass being thermodynamically favoured [9]. As such, nucleation density along the fibre is typically much higher than that of the bulk matrix. During secondary nucleation (crystal growth), early impingement of the nuclei growing from the surface of the glass fibre occurs, preventing radial growth and the formation of spherulites characteristic of crystallisation in the polymer matrix. Instead, post impingement, the crystal interface grows into the matrix, perpendicular to that of the fibre surface (Figure 1.8) resulting in a columnar-like crystal structure regularly referred to as transcrystallisation [11,46].

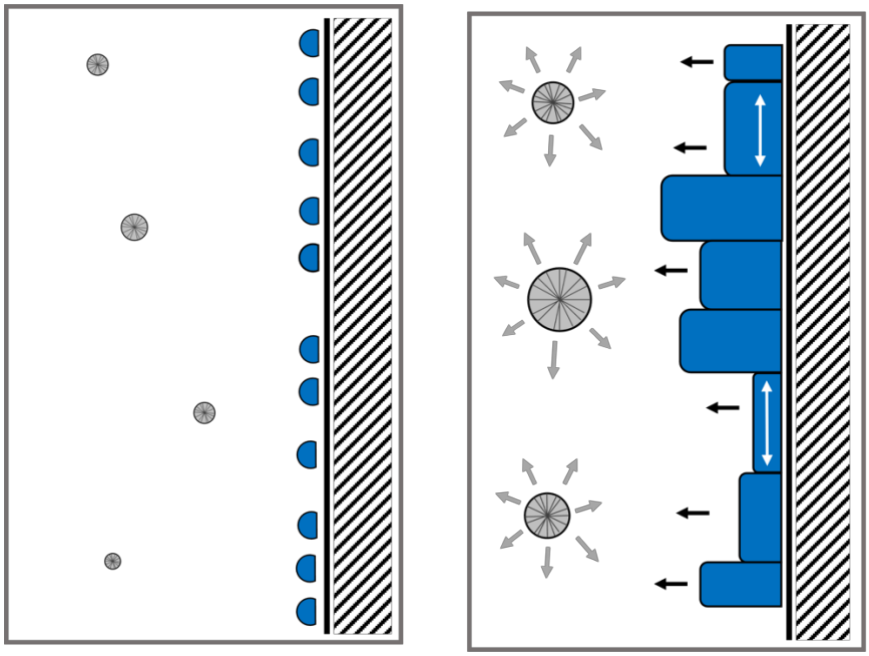

Figure 1.8: Schematic images showing the nucleation and perpendicular growth of the transcrystalline layer (blue) off the surface of a reinforcement fibre (striped) into the matrix and the radially growing spherulites (grey).

A secondary, low temperature shoulder peak is also occasionally observed during the melting of polyamide 66 fibre reinforced composites [2]. The origin of this low-temperature shoulder remains ambiguous, with variations in crystallographic form [2], thickness of the crystalline lamella [47] and simultaneous melt-recrystallisation [48] the most plausible explanations. In addition, the inclusion of glass fibre reinforcement into PMC has been demonstrated to both increase the overall crystallisation kinetics of the composite [49] and reduce crystallisation induction time (time taken for the onset of crystallisation after cooling to an isothermal Tc) [49]. That said, the incorporation of glass fibres into the matrix of polyamide 66 is reported to have a negligible effect on the overall degree of crystallinity of the polymer [9]. Furthermore, the quantity of fibre reinforcement has been observed to have a finite effect on the crystallisation of PMC, with fibre quantities greater than 40 wt.% shown to hinder the crystallisation process [9]. Frihi et al. [9] postulate that excessive fibre fractions impede chain

diffusion to the growth face of crystals, resulting in the impingement of growing spherulites and constrained crystals [9].

Research into the morphological changes and associated degree of crystallinity of polyamide composites as a function of the stamp forming process are limited. The majority of the existing literature focuses on the optimisation of stamp forming parameters for the purpose of formability and production of high quality (defect-free) products [3,50–53]. Processing temperature, matrix viscosity and the mechanisms of composite geometry configuration (interply/intraply slip and shear) have been evaluated [5,16,17,53,54], though there is little consideration of these processing effects on the resulting crystallinity or potential orientation in matrix morphology.

1.5 Scope of the work

This work aims to characterise the through-thickness crystallinity and microstructural morphology of stamp formed, glass fibre reinforced polyamide 66 (PA66/GF) using a variety of characterisation techniques, including thermal analysis and synchrotron x-ray diffraction. Further, owing to the time-temperature dependence of the crystallisation process, it is important to gain an understanding of both the isothermal and non-isothermal crystallisation kinetics of PA66/GF. Finally, it is hoped that the findings of this study will be fundamental in understanding how crystal microstructure effects the creep performance of PA66/GF laminates and ultimately, how modifications in the aforementioned microstructure, resulting from post-processing annealing, can improve the creep behaviour of these viscoelastic materials.

Each individual chapter will contain a review of the relevant literature, where the aims and their rationale will be discussed.

CHAPTER 2 - METHODOLOGY

2.1 Materials

2.1.1 Fibre reinforced thermoplastic tape

This work uses E-glass fibre reinforced polyamide 66 (PA66/GF) supplied by Celanese (Sulzbach, Germany). The PA66/GF tape consists of 60 wt.% and 40.2 vol.% unidirectional continuous E-glass fibre reinforcement and has a tape thickness of 0.3 mm. In accordance with ISO 11357-1, the glass-to-liquid transition and melting temperatures of the polyamide 66 matrix are reported to be 50 and 260 °C, respectively.

2.1.2 Tape consolidation - stamp forming

Multi-ply laminates of various fibre orientation were produced by Warwick Manufacturing Group (Coventry, UK) using an industrial stamp forming press to consolidate pre-laminated sheets of PA66/GF tape. The rapid thermoforming procedure is shown schematically in Figure 2.1 and involved heating the pre-laminated tape to a forming temperature of 270 °C before quickly transferring the laminate to a heated press and clamping force applied. Tool temperature and clamping force were 120 °C and ~800 kN, respectively. The laminate was then allowed to cool for a short period of time, enabling crystallisation to occur within the polyamide matrix before being ejected from the tool.

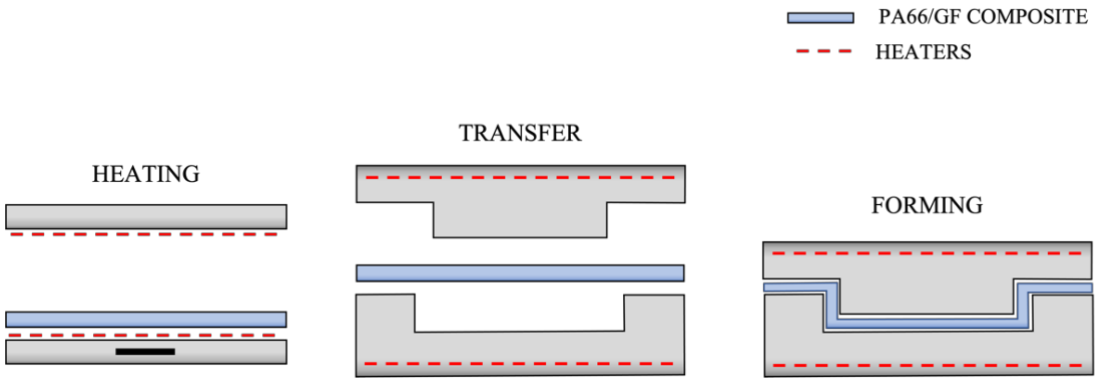

Figure 2.1: Schematic diagram of the stamp forming procedure including; *heating* of the composite, *transfer* of the composite to the heated mould and *forming* of the composite, where the composite conforms to the geometry of the mould.

A variety of tool geometries and ply arrangements were used in the manufacturing of the laminates and will be discussed in greater detail within the relevant results and discussion chapters.

2.2 Experimental techniques

The experimental procedures performed using each of the below techniques will be discussed in the relevant results and discussion chapters.

2.2.1 Differential scanning calorimetry (DSC)

Differential scanning calorimetry is a common analytical technique used to measure thermal transitions in both amorphous and crystalline materials. DSC records heat flow as a function of temperature and time, allowing for thermal and physical changes within a materials structure to be identified. Changes in heat flow, defined as *transitions*, can be positive (endothermic) such as the glass-to-liquid transition and melting of a material, or negative (exothermic) for instance, crystallisation. In addition to relatively simple observations, DSC can also be used for

more complex characterisation such as calculation of the degree of crystallinity (Chapter 3) and crystallisation kinetics (Chapters 5 and 6).

DSC experiments were performed on a Mettler Toledo DSC 1 (Greifensee, Switzerland) operated using STARe software (v.16.00). The heat flux DSC was connected to a Huber TC100 intracooler capable of cooling to -90 °C. The furnace of the DSC was purged with nitrogen at a flow rate of 30 ml/min to prevent oxidative degradation of the polyamide samples. Calibration of the instrument was performed from the onset of melting and heat of fusion of a known mass of 99.999% pure indium and zinc.

2.2.1.1 Calculating the degree of crystallinity from the enthalpy of fusion

The enthalpy of fusion equates to the heat energy required to melt a material and was determined by integrating the area of the melting endotherm and interpolated baseline between the onset and endset of melting (Figure 2.2). Due to localised variations in glass fibre distribution (discussed in Chapter 3), the polyamide 66 mass fractions of individual samples were accounted for in the measuring of the enthalpies of fusion via a matrix burnout procedure (section 2.2.3).

The degree of crystallinity (X_c) was then determined using Equation 1-2 and a theoretical enthalpy of fusion of a perfectly crystalline polyamide 66 crystal, taken as 191 J/g [43]. Melting temperature (T_m) and crystallisation temperature (T_c) were taken as peak temperatures unless otherwise stated.

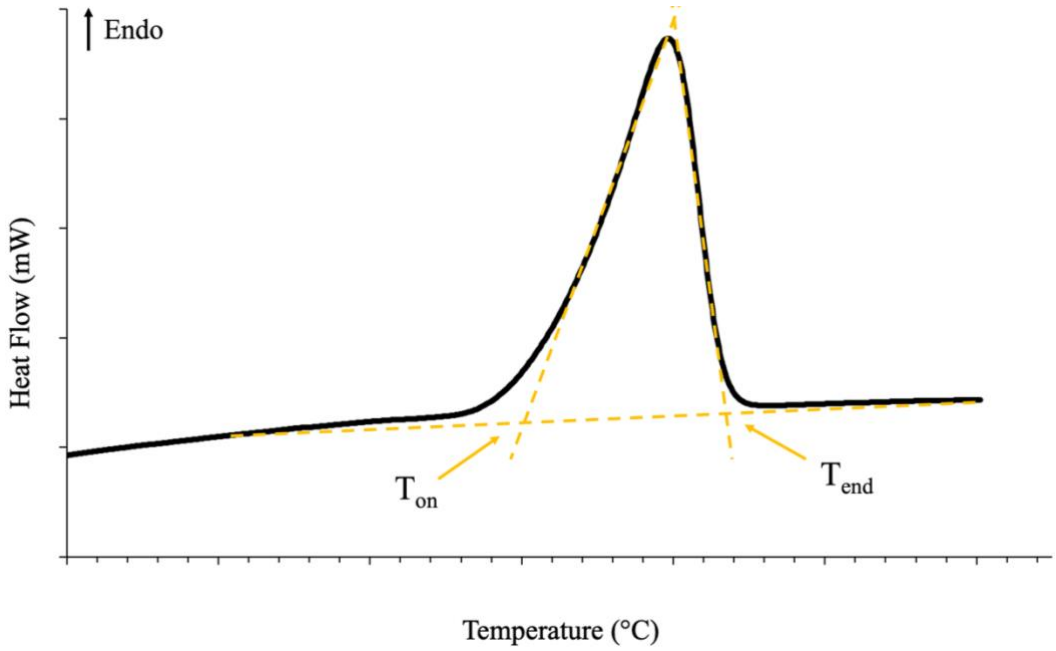

Figure 2.2: Schematic of a DSC thermogram showing the melting endotherm of a polymer; labelled are the onset (T_{on}) and endset (T_{end}) of melting determined by the intersection point of the baseline and inflectional tangents. The heat of fusion (ΔH_f) is typically calculated from the area beneath the melting endotherm.

2.2.2 Thermogravimetric analysis (TGA)

Thermogravimetric analysis is used to determine the thermal stability of a material by monitoring mass loss as a function of temperature. TGA experiments were performed on a Netzsch STA 449 C (Selb, Germany). Experimental procedures were performed in an air atmosphere (flow rate 100 ml/min) from room temperature to 900 °C at a heating rate of 10 °C/min, with buoyancy corrections made prior to each experiment. Samples were weighed in advance and placed into 70 µl alumina crucibles. Mass loss was recorded continuously throughout the experiments and analysis performed upon completion.

2.2.3 Muffle furnace

Recognising both the importance of measuring constituent mass fractions to accurately and reliably characterise polymer matrix composites (PMC), and the impracticality of using TGA for such a large volume of samples - batch matrix burnout procedures were performed using a muffle furnace.

On completion of DSC analysis, samples were removed from the aluminium pans and re-weighed. Samples were then placed into fireclay boats, which had been lightly spray-coated with boron nitride to prevent adhesion between the boat and sample upon heating. The experimental procedure involved heating the samples to 900 °C (determined from TGA results) at approximately 15 °C/min in an air atmosphere, where on reaching maximum temperature, samples were held for 1 hour before the furnace was powered off and samples allowed to air cool over a 24-hour period. The mass of thermally stable glass fibres was then measured, and the polyamide-to-glass fibre mass fractions determined.

2.2.4 Fourier transform infrared spectroscopy (FTIR)

Fourier transform infrared spectroscopy is a material characterisation technique used to obtain spectral data of compounds. FTIR uses an interferometer to generate a frequency spectrum from which, spectral patterns consisting of peaks of various intensity are produced. Each peak is representative of the stretching, bending and/or vibration of a particular chemical bond at a given frequency and appears at a specific wavenumber characteristic of the functional groups present and their environment.

A Nicolet 8700 FTIR spectrophotometer (Waltham, USA) with DTGS detector, attenuated total reflectance (ATR) attachment and OMNIC software were used throughout this work. The wavelength ranged from 700 to 4000 cm^{-1}, with number of scans and resolution set to 100 and

4, respectively. Prior to sample analysis, a background trace was first collected and subtracted from the subsequent sample spectra to remove atmospheric effects such as carbon dioxide and water vapour.

2.2.5 Wide angle x-ray scattering (WAXS)

X-ray diffraction measurements were performed on the I22 beamline at Diamond Light Source synchrotron facility (Oxfordshire, UK) using a monochromatic, microfocus x-ray beam of 30 μm diameter and 14 keV energy. The exact experimental procedures performed will be discussed in the relevant chapter (Chapter 4).

2.2.6 Creep tests

Creep measurements were performed under flexural bending using a three-point bend testing fixture. Test specimens were carefully positioned atop two support fixtures (100 mm apart) and a constant load of 0.5 kg (hooked weight) applied to the centre of the test beams. Measurements of displacement (mm) as a function of time under constant load were recorded for all samples. The exact experimental procedures performed will be discussed in the relevant chapter (Chapter 7).

CHAPTER 3 - THROUGH THICKNESS CHARACTERISATION OF AN 11-PLY PA66/GF STAMP FORMED COMPOSITE

3.1 Introduction

3.1.1 Temperature dependence on through-thickness crystallinity as measured by differential scanning calorimetry (DSC)

Though a seemingly straight forward manufacturing technique, the efficacy of the stamp forming procedure is greatly dependent on various processing parameters (Chapter 1.1.3). Forming of polymer matrix composites (PMC) is a highly temperature dependent process and as such, parameters including the initial pre-heat temperature, transfer time and tool temperature must be carefully considered and controlled. Optimising formability and reducing the likelihood of defects depends on the viscosity and viscoelastic behaviour of the matrix polymer, which is highly sensitive to temperature and the development of crystallinity [3,55]. Consequently, the applied consolidation pressure and subsequent forming of the part should be completed whilst the thermoplastic is above, or close to its melting temperature (T_m) [3].

During pre-heating stage, the initial increase in temperature is reported to be uniform throughout the thickness of the part [55,56]. However, upon approaching T_m, it is thought that residual stresses within the individual layers of the laminate are released [55,56]. This results in delamination of the PMC and a deviation in the heating rate between the central and surface plies due to reduced thermal conduction and through-thickness heat transfer [55]. Once at the target temperature, the PMC is transferred to the mould. Here transfer time is of critical importance, with Lessard et al. [55] showing that a 16 second transfer time considerably hinders consolidation compared to that of a 10 second transfer time, reporting that despite the

temperature of the central plies remaining considerably constant, the rate of surface heat loss is rapid [55]. It is expected that within the automotive industry transfer of the laminate to the mould will be automated to ensure repeatability of the process.

Once transferred, the laminates are generally in contact with a colder tool (~120 °C difference). Tool temperature is of significant importance to the forming process as it not only dictates cycle duration, which is of financial interest to industry as it determines the rate and volume of part production, but also directly influences the morphology and resulting mechanical properties of the part [3,55,57,58]. Although lowering the temperature of the tools is cost effective and reduces cycle duration, the time available for efficient consolidation of the part also decreases. Upon contact with the tool, the surface layers instantaneously start to cool, however, due to poor thermal conductivity and de-consolidation of the thermoplastic from the heating process, non-uniform through-thickness cooling rates are typically observed [3,57–63]. In a study of carbon fibre reinforced polyphenylenesulfide (PPS/CF), Parlevleit et al. [58] found that an approximate 40 and 100 °C difference exists between the surface and central plies of 10 and 20 mm laminates, respectively [58]. This discrepancy in the rate of cooling of surface and central plies leads to through-thickness thermal gradients, which regularly result in thermal and morphological surface-core effects [57,61,64]. Thermal effects generally relate to the parabolic distribution of residual stresses, whereby crystallisation and the associated volume shrinkage of the central plies is constrained by the already solidified surface layers. This subsequently results in the generation of tensile and compressive residual stresses in the core and surface plies, respectively [60,61,64]. Furthermore, McCallum et al. [60] reported that in comparison to a unidirectional laminate, the variance in through-thickness residual stresses of carbon fibre reinforced polyetheretherketone (PEEK/CF) is highest in cross-ply laminates [60].

Morphological surface-core effects relate to the variation in the through-thickness degree of crystallinity and microstructure of the polymer matrix with differing cooling rates [61,64]. Due to the differing temperatures of the pre-consolidated laminate and tool, cooling of the surface layers is typically fast with rates ranging between 400 °C/min [55] and 17,400 °C/min [3] reported depending on the temperature variation of the tool and PMC. Despite the rapid rate of cooling, some semi-crystalline thermoplastics such as polyamides and polyethylene crystallise so readily that a crystal structure is still formed [58]. That said, the relative degree of crystallinity and crystal perfection within these regions is generally quite low [58]. Comparatively, resulting from the poor thermal conductivity of polymer matrices and thus, slower cooling of the central plies, the degree of crystallinity and crystal perfection is higher within the central regions. This is supported by Ijaz et al. [59] and Parlevliet et al. [58] who report through-thickness parabolic crystallinity gradients in glass fibre reinforced polypropylene (PP/GF) and PPS/CF laminates measured using DSC and micro-hardness, respectively, with Lawrence et al. [57] also reporting a 15% disparity in the degree of crystallinity between the surface and core of a 20-ply PEEK/CF composite [57–59]. The variation in through-thickness crystallinity of thermo-formed PMC is regularly analysed by DSC [55–58], resulting in the process simulated laminate (PSL) technique often being employed in order to separate and individually analyse the constituent layers [57,58]. PSL involves incorporating a non-adhesive polymeric sheet between individual plies preventing full consolidation of the laminate upon forming. The PSL technique has proven successful when characterising PEEK/CF, with the authors concluding that the non-adhesive polyimide sheets had no influence on the final morphology of the part or heat transfer throughout the forming process [57].

Despite the recurrent use of DSC in characterising the degree of crystallinity of thermoplastic composites, the experimental error associated with the technique is relatively high. This can lead to overlapping standard deviations, whereby, a parabolic trend in through-thickness crystallinity is observed, however, the results are not significant [58]. Parlevliet et al. showed that in a study on PPS/CF, the combined error in the determination of the heat of fusion and accuracy in measuring the PPS matrix mass fraction was ~4% and fell within the variation of the results and thus, significant conclusions could not be drawn [58].

3.1.2 Crystallinity measurements using Fourier transform infrared (FTIR) spectroscopy

An alternative analytical technique frequently used in the study of polyamides [65–70] and polyamide composites [36,71] is Fourier transform infrared (FTIR) spectroscopy. Infrared spectra typically consist of a series of peaks characteristic of the stretching, bending and/or vibration of a molecular bond, the interaction of which determine the morphological structure of the polymer and regulate the frequency, height and width of the peaks observed. Band assignment of the peaks of interest are shown in Table 3.1. Supplementary to DSC, numerous authors have employed FTIR spectroscopy to characterise morphological changes and the degree of crystallinity in thermoplastics [65,67,70,71]. Despite this, a lack of correlation in the determination of crystallinity is believed to exist between frequently used analytical techniques such as density measurements, heat of fusion, spectroscopy and x-ray diffraction [66,72].

Assuming polyamides satisfy a two-phase structure (amorphous and crystalline), Vasanthan and Salem [66,67] report that the crystalline fraction can be determined from the normalised absorbance ratio between two truly amorphous and crystalline peaks [66,67]. Their study of PA66 showed crystallinity to increase with heat treatment temperature, with peaks located at

936 and 1200 cm^{-1} (associated with the crystalline fraction) becoming narrower and stronger with increasing temperature (Figure 3.1), whereas the amorphous band at 1180 cm^{-1} was observed to become weaker as crystallinity increased [67].

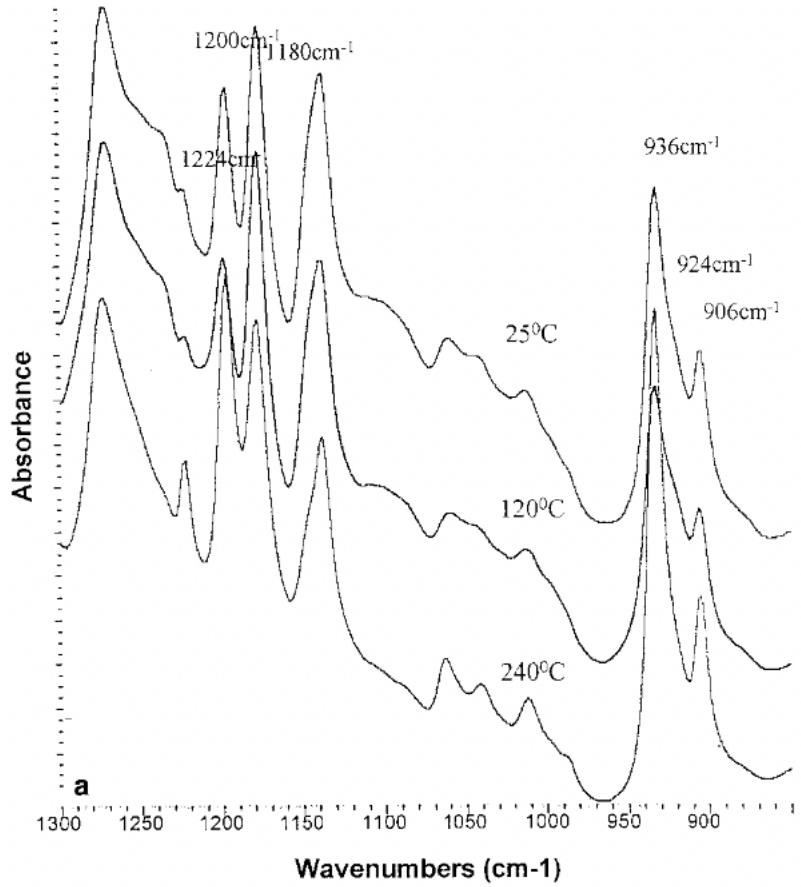

Figure 3.1: Infrared spectra of PA66 heat treated at 25, 120 and 240 °C, showing the variation in peak width and intensity of key crystalline (936 and 1200 cm^{-1}) and amorphous (1180 cm^{-1}) peaks over a wavenumber range of 850 – 1300 cm^{-1} [67].

Normalisation of the peaks requires that the absorbance of the amorphous and crystalline bands be divided by that of a reference peak deemed to be independent of crystallinity. Multiple studies report the absorbance of the amide 1 band (~1630 cm^{-1}) characteristic of the carbonyl functional group (C=O), to be impartial to changes in crystallinity and thus, use this band as an

internal reference [65–68,71]. However, despite the integrated area of the band remaining appreciably (~7%) unchanged when heated from room temperature to the onset of melting [70], Skrovanek et al. [70] and Lu et al. [36] report that the amide I band is highly sensitive to local order and characteristic of hydrogen bonding throughout the polyamide microstructure [36,70]. This was also confirmed by Galimberti et al. [69] who show that both frequency and intensity of the carbonyl peak are drastically influenced by the perfection and ordering of hydrogen bonds, thus, conclude that the amide I band cannot be considered independent of crystallinity [69].

Table 3.1: Reported infrared band classifications of polyamides

Frequency (cm^{-1})	Classification
906	Crystalline [66–69]
924	Amorphous [66,67]
936	Crystalline [65–67]
1144	Amorphous [65] Crystalline [69]
1180	Reference Peak [36,66,67]
1200	Crystalline [36,66,67]
1630	Reference Peak [65–67] Crystalline [36,69,70]

The geometry and frequency at which the amide I band occurs is strongly dependent on the perfection of hydrogen bonding and has been observed to fluctuate with varying crystallinity

[36,69,70]. The band consists of contributions from both ordered and disordered hydrogen-bonded C=O stretching, with deconvolution of the band revealing that the contribution of the ordered component (~1632 cm^{-1}) appears at a lower frequency to that of the disordered state (~1643 cm^{-1}) [36,70]. This results from the greater strength of the hydrogen bonded C=O groups within the crystalline phase [36]. Furthermore, the band width of the disordered state is reported to be approximately double that of the ordered one, reflecting the poorer distribution of hydrogen bonding within the amorphous phase [36]. The contributions of the two states to the overall geometry and frequency of the amide I band can be influenced by rate of cooling or subsequent annealing [36,70]. In a study of PA66, Lu et al. [36] demonstrate how by annealing a quench cooled sample close to T_m, the rearrangement of hydrogen bonds within the disordered state results in an increase in hydrogen bonding within the ordered state, resulting in an amide I band with greater peak height and narrower band width [36]. Skrovanek et al. [70] conclude that whilst FTIR spectroscopy cannot readily be used to measure an absolute value of crystallinity in polyamides, the ratio of the ordered C=O band to that of the total integrated area of the peak often correlates well with crystallinity [70]. This has been demonstrated previously in various thermoplastics including poly(ethylene terephthalate) [73] and poly(ε-caprolactone) [74].

3.1.3 Aims and objectives

Using the process simulated laminate (PSL) technique and strategically placed thermocouples, this chapter aims to measure the rate of heat transfer observed throughout the stamp forming process of an 11-ply PA66/GF composite. Further, for completeness, the ensuing through-thickness degree of crystallinity of the polyamide matrix will be quantitatively measured using DSC (heat of fusion) and FTIR (peak fitting) to determine to what extent variations in the temperature profile of the forming cycle affects the crystal morphology of the laminate.

Crystallinity is a highly temperature dependent process and influential in determining the thermo-mechanical properties of a PMC. Therefore, an understanding of the impact that processing conditions have on the resulting degree of crystallinity is of critical importance and should enable the future optimisation of stamp forming procedures.

3.2 Methodology

3.2.1 Materials and sample preparation

Pre-impregnated sheets of glass fibre reinforced polyamide 66 (PA66/GF) tape were stacked into an 11-ply laminate of sequence 0/90/90/0/0/90/0/0/90/90/0°. Thermocouples were inserted into the laminate to record the variation of temperature with time throughout the forming process (Figure 3.2). To facilitate the measurement of heat of fusion in the individual plies of the stamp formed part, squares (25 mm^2) of polytetrafluoroethylene (PTFE) film (thickness 0.01 mm) were placed in a vertical stack between each of the 11-plies to prevent localised consolidation of the layers (Figure 3.2). Despite a minor difference in the thermal conductivity of PA66 (0.24 W/K.m) [6] and PTFE (0.26 W/K.m) [75] it is not expected that heat transfer and thus, the crystallinity measurements will be affected. The process simulated laminate (PSL) approach enabled the recovery of samples that were suitable for thermal and spectroscopic analysis.

The 11-ply laminate was heated to 270 °C in a contact heating oven before being rapidly transferred to the heated stamping-press for forming. Forming time was ~140s, with tool temperature and applied clamping force approximately 120 °C and 800 kN, respectively. The geometry of the tool was comparable to that shown schematically in Figure 2.1 (Chapter 2.1.2) and resulted in a ‘U-shaped’ composite part of thickness 3.1 mm.

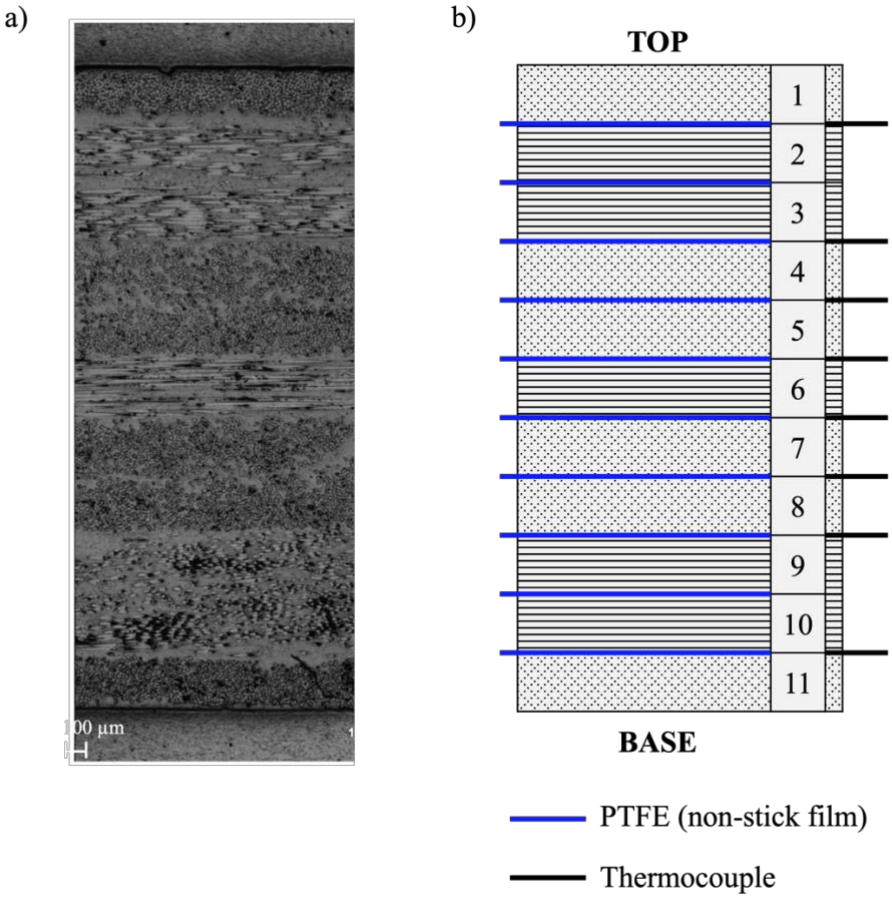

Figure 3.2: a) Optical microscopy image showing fibre orientation and lay-up of the 11-ply consolidated stamp formed composite and b) schematic of the 11-ply laminate arrangement showing fibre orientation, the arrangement of PTFE film and the distribution of the 8 thermocouples.

3.2.2 Differential scanning calorimetry (DSC)

A Mettler Toledo DSC1 (Greifensee, Switzerland), calibrated with indium and zinc standards was used for all DSC analysis (Chapter 2.2.1). The use of tape or consolidated laminate samples varied across experiments; however, all samples were prepared using a circular hole-punch (4.8 mm diameter) and hermetically sealed in 40 µl aluminium crucibles.

3.2.2.1 Preliminary DSC experiments

3.2.2.1.1 Influence of heating rate

To determine the effect of heating rate on cold crystallisation and thermal lag, samples were taken from the pre-impregnated PA66/GF tape (sample mass 11.65 mg ± 0.5 mg) and heated to 290 °C at 40 °C/min. The samples were then held isothermally at 290 °C for 1 minute to erase the effects of thermal history, before being cooled (10 °C/min) to room temperature. Finally, samples were re-heated from room temperature to 290 °C at various heating rates ranging from 10 to 100 °C/min to determine the influence of heating rate on the recorded DSC traces.

3.2.2.1.2 Effect of localised fibre distribution on heat of fusion measurements

Inspection of the PA66/GF tape indicated that fibre volume fraction was non-uniform across the width of the material. Therefore, to investigate the effect of fibre distribution on the measurements of heat of fusion, 10 samples were taken from transverse and longitudinal locations across the pre-impregnated tape (Figure 3.3).

The thermal history of the samples was erased on heating to 290 °C and holding isothermally for 1 minute. Samples were then cooled to room temperature (10 °C/min) before being re-heated to 290 °C at 40 °C/min. A heating rate of 40 °C/min was adopted to reduce the possibility of reorganisation of the polyamide matrix on heating. Post analysis, samples underwent a matrix burnout procedure to determine the polyamide mass fraction of each of the samples. Sample mass was then adjusted on the STARe software, with heat of fusion measured by integration of the area of the melting peak and the degree of crystallinity calculated using Equation 2-1 (Chapter 2.2.1.1).

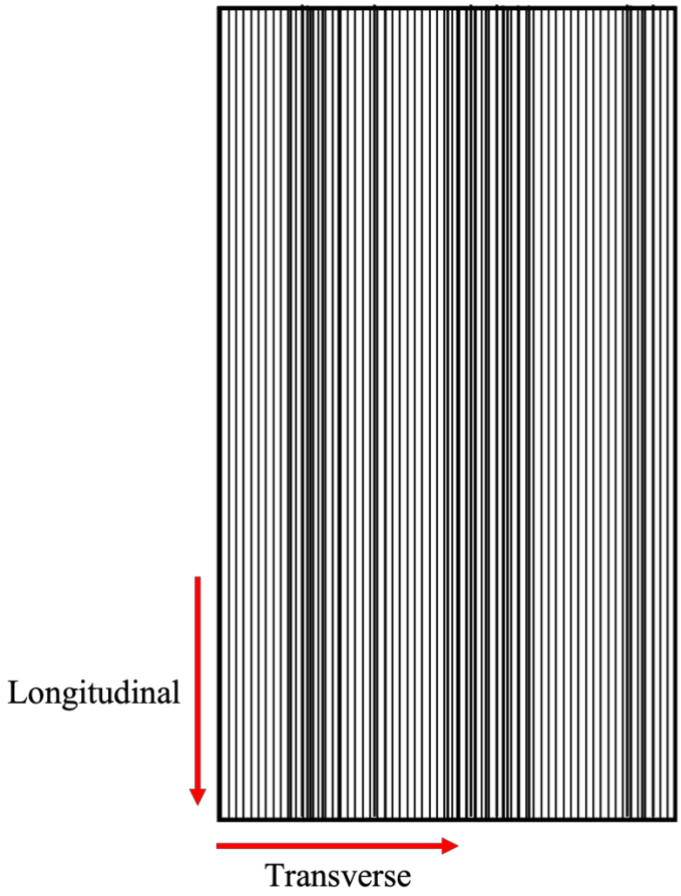

Figure 3.3: Schematic representation of the PA66 continuous glass fibre tape, showing the non-uniformity of fibre distribution.

3.2.2.2 Calculating the through-thickness degree of crystallinity of a stamp formed PA66/GF composite

Post-stamp forming, the 'U-shaped' composite part was divided into 5 sections (A-E) (Figure 3.4). DSC analysis was performed on section C, whereby the 25 mm^2 segment containing the PTFE film was extracted using a bandsaw. Resulting from the non-adhesive film preventing consolidation of the 11-ply laminate within this region, each of the plies could be easily separated. Four samples were tested per ply, with the locations in which the samples were extracted maintained through the thickness of the laminate (Figure 3.4).

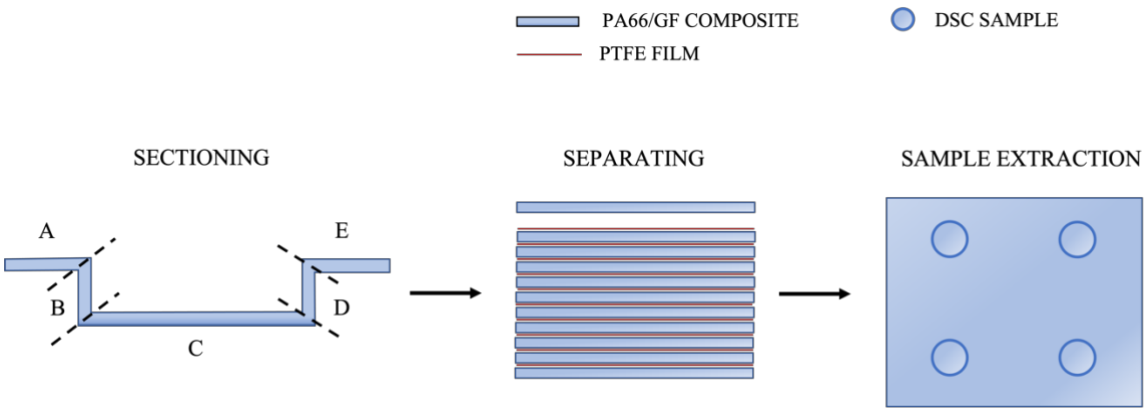

Figure 3.4: Schematic diagram of the through-thickness characterisation sample preparation procedure including *sectioning* of the stamp formed composite, *separating* of the unconsolidated layers into 11 individual plies and *sample extraction* from each of the plies in 4 through-thickness locations.

To measure the heat of fusion, samples were heated from 25 to 290 °C at 40 °C/min. The heat of fusion was then calculated by integrating the area of the melting peak and interpolated baseline between the onset of melting and last trace of crystallinity (Chapter 2.2.1.1). The degree of crystallinity was determined using Equation 1-2 (Chapter 1.4.1), where a literature value of 191 J/g [43] was used for the heat of fusion of a perfectly crystalline PA66 sample ($\Delta H_{f\infty}$). The standard deviation of the results across each of the individual plies was determined using Equation *3-1*;

$$\sqrt{\frac{\sum(X_c - \bar{X}_c)^2}{n-1}}$$

Equation 3-1

Where X_c is the degree of crystallinity of a sample, $\overline{X}_c$ the mean degree of crystallinity determined from a total of four samples per layer and n, the sample size.

Further, values were statistically evaluated using analysis of variance (ANOVA) tests to determine the significance ($p < 0.05$) of the results through the thickness of the composite. A

Tukey post-hoc test was applied with a 95% level of confidence via SPSS software (IBM, Portsmouth, UK).

3.2.2.3 Determining polyamide matrix mass fraction

Given that the measurement of the heat of fusion requires an accurate value for the polyamide mass fraction, each of the thermal analysis samples was subjected to a matrix burnout procedure outlined in Chapter 2.2.3.

3.2.3 Fourier transform infrared spectroscopy (FTIR)

A Nicolet 8700 FTIR spectrophotometer with DTGS detector, attenuated total reflectance (ATR) attachment and OMNIC software were used throughout this work (Chapter 2.2.4).

3.2.3.1 Crystallisation on cooling from the melt

To monitor changes within the infrared spectra of PA66/GF through the crystallisation process, a circular sample (diameter 4.8 mm) was extracted from the PA66/GF tape, positioned, and melted (290 °C) onto the diamond crystal of the ATR attachment. The heating source was then powered off and the sample allowed to air cool to room temperature over a 30-minute period. Throughout the cooling process an IR trace was recorded every 30 seconds to collect a series of spectra from which the peak alterations throughout non-isothermal crystallisation could be monitored.

3.3 Results and discussion

3.3.1 Temperature profile of stamp forming process

The temperature profiles of each of the 8 thermocouples (A-H) recorded throughout the duration of the stamp forming cycle are shown in Figure 3.5. Furthermore, tool (platen) position and clamping force were overlaid to emphasise the forming stage and consolidation process.

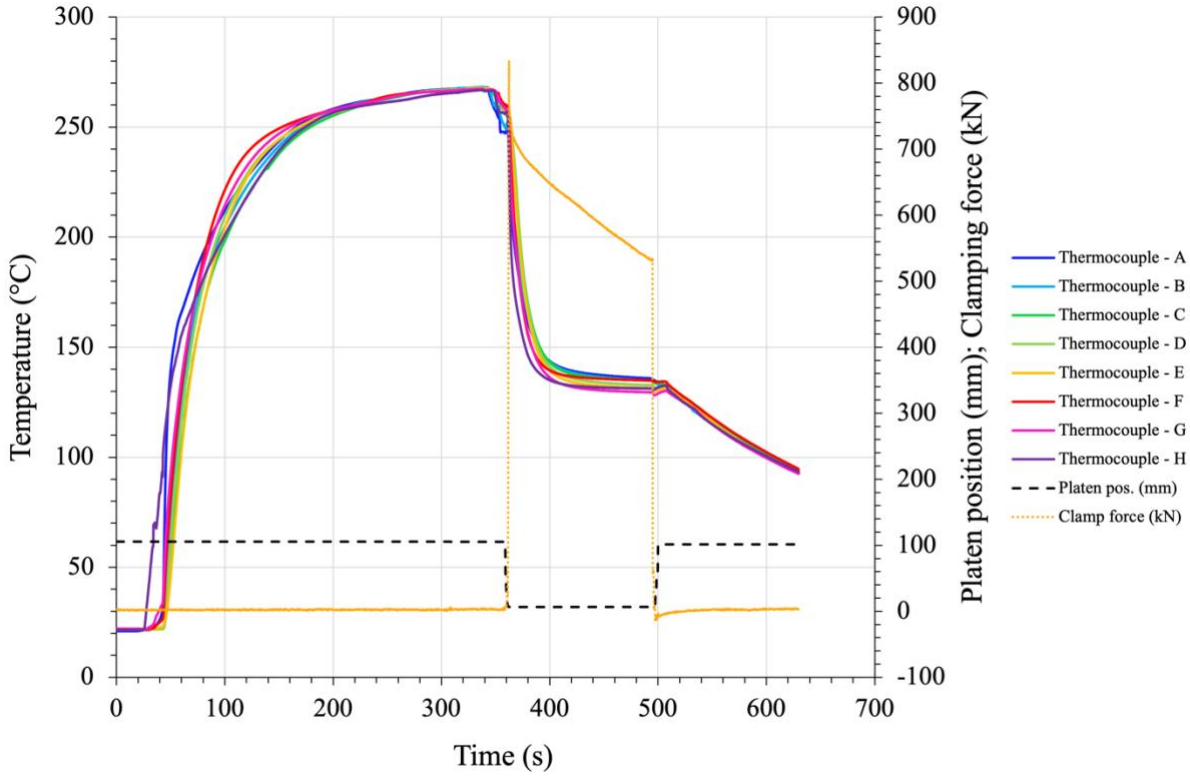

Figure 3.5: Temperature profiles recorded by each of the 8 thermocouples positioned within the 11-ply composite during the stamp forming cycle (0-630 s), with tool (platen) position and clamping force overlaid to emphasise the consolidation stage.

The stamp forming cycle can be divided into four important areas: preheating of the composite (~20 – 340 s), transfer to the mould (~340 – 358 s), closing of the tool and application of clamping force (~358 – 370 s), and the conclusion of the forming cycle (~370 – 490 s). To facilitate comparisons of the through-thickness temperature variations observed throughout the

aforementioned stages of the forming cycle, the 11-ply composite was sub-divided into 3 regions (Figure 3.6) contingent on the positioning of the 8 thermocouples: Top (thermocouples A and B), Central (thermocouples C to F) and Base (thermocouples G and H).

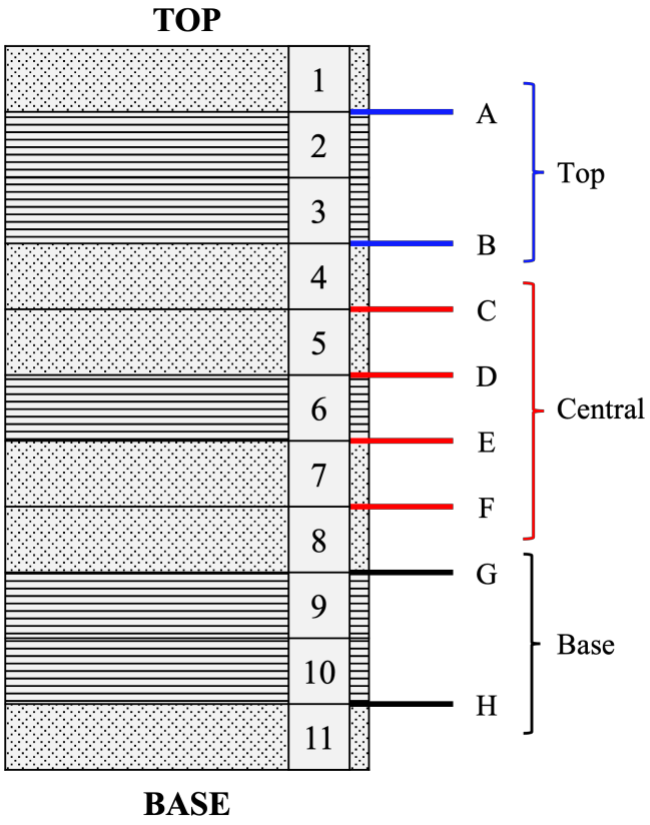

Figure 3.6: Schematic showing the positioning of the 8 thermocouples within the 11-ply composite (labelled A to H) and the 3 locational regions (top, central, base) into which the thermocouples were divided for comparative analysis.

3.3.1.1 Preheating of the thermoplastic composite (0 to 340 seconds)

Preheating of the composite is the first and longest stage of the stamp forming cycle, whereby the polyamide matrix was heated to 270 °C (10 °C above T_m) over a 5-minute period. The temperature profile of the individual thermocouples is shown in Figure 3.7.

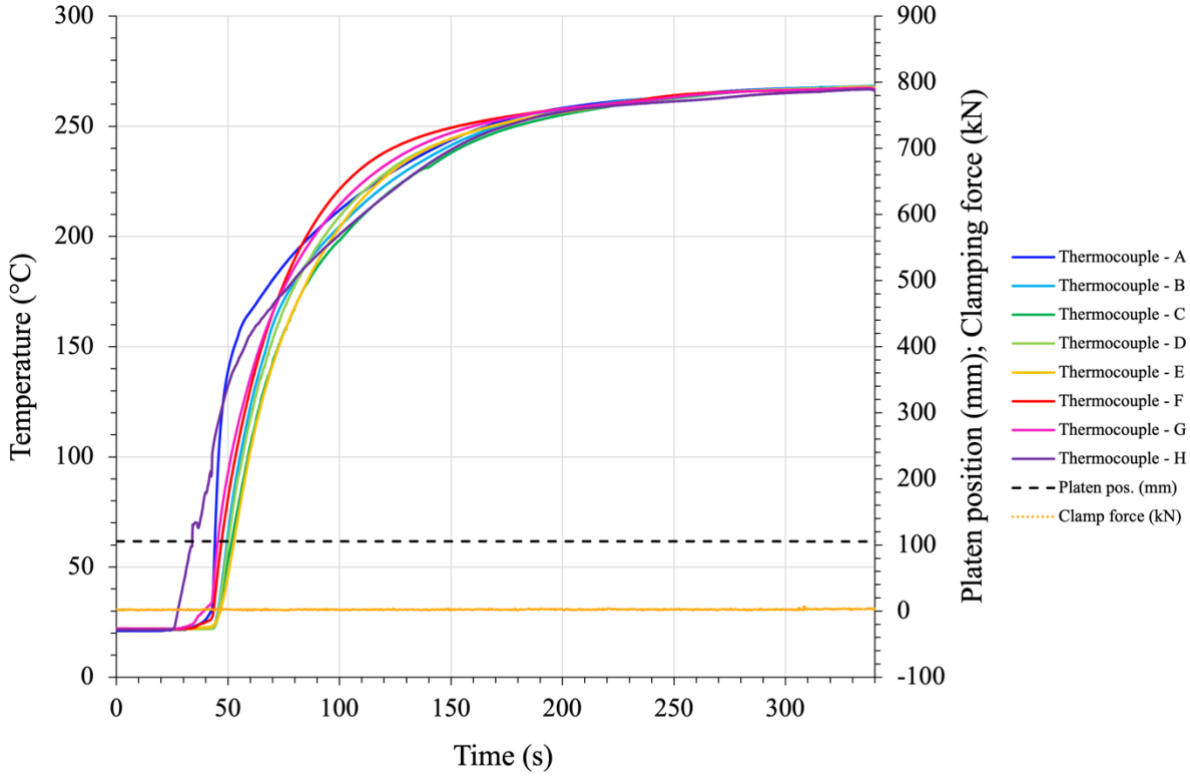

Figure 3.7: Temperature profiles recorded by each the 8 thermocouples during the preheat stage of the stamp forming cycle (0-340 s).

As illustrated in Figure 3.7, after a relatively linear preliminary surge in temperature at the start of the preheat process, the heating rate over this stage of the forming cycle is non-linear, whereby heating rate decreases as a function of increasing temperature.

The initial rise in temperature observed in the base layer of the pre-preg composite after 25 s, coincides with its placement onto the oven drawer. Temperature increases quickly in this region, with the base of the composite (thermocouple H) shown to rise from room temperature to 59 °C at a rate of 260 °C/min. On closing the oven drawer and immerging the composite under the heaters (~ 40 s), the temperature within the top region rapidly rises. The top outer layer (thermocouple A) instantaneously increasing from room temperature to 100 °C at a rate of 2000 °C/min. Conversely, despite still showing a relatively rapid rate of heating, the temperature of the central plies remains lower than that of the two outer regions over the initial

60 s of oven exposure. This results from the time dependent heat transfer (thermal conductivity) from the outer layers through the thickness of the composite. That said, above ~200 °C, the temperature within the central layers of the composite is observed to be greater than that of the two outer surfaces and remains elevated until reaching T_m (260 °C) where the temperature throughout all regions is observed to be uniform. This contradicts the findings of Lessard et al. [55], who although showing differences in temperature between the outer and central regions of the composite, reports that due to delamination of the pre-consolidated laminate, heat transfer through the composite is reduced and thus, the centre plies appear cooler than that of the outer plies [55]. Despite fluctuations in temperature and heating rate throughout preheating, the through-thickness temperature difference is within 1.7 °C at the end of this stage of the forming cycle.

3.3.1.2 Transfer from oven to mould (340 to 358 seconds)

Post preheating, the pre-preg composite must be transferred to the mould for forming. Upon opening the oven drawer (~343 s) the top layers of the composite immediately start to cool at approximately 55 °C/min as heat is lost to the environment. Here, the convective heat loss in the top few plies results in the temperature within this region falling to below T_m over the initial 6 seconds of the transfer process (Figure 3.8). However, despite the immediate heat loss within the top layers, the temperature of the base and central plies remains relatively stable over this period (342 to 348 s). This coincides with the findings of Lessard et al. [55], who report that whilst the temperature within the central plies stays considerably constant, the rate of heat loss within surface layers open to the environment is rapid [55]. Due to the base of the composite remaining in contact with the oven drawer for an extended period prior to being quickly shifted

to the mould, the time in which heat energy dissipation can occur within this region is significantly reduced.

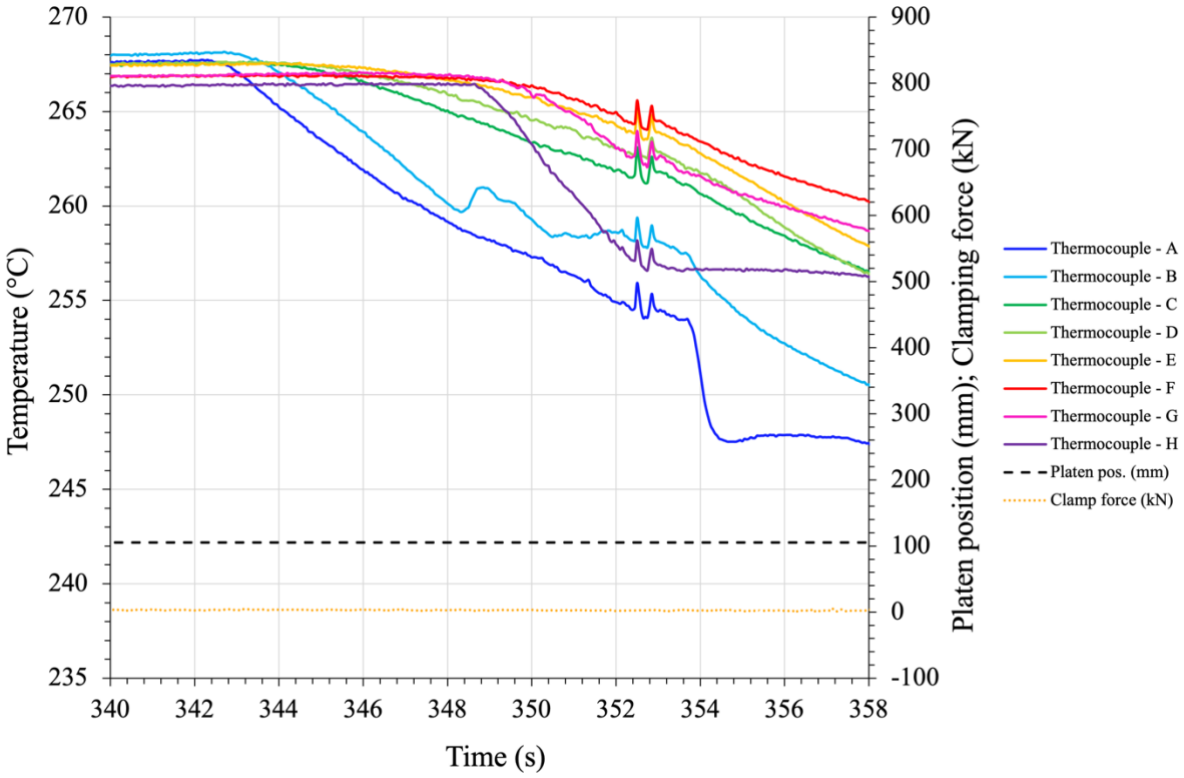

Figure 3.8: Temperature profiles recorded by each the 8 thermocouples during the transfer stage of the stamp forming cycle (340-358 s).

Following the opening of the oven drawer and quick transfer to the mould, the composite is carefully placed between the two heated tools (Figure 2.1, Chapter 2.1.2). Upon contact with the mould (~348 s) and resulting from the approximate 140 °C temperature difference between composite and tool, a reduction in temperature is observed across all three regions of the composite (Figure 3.8). Initial heat loss is shown to be greatest in the base layer, where a 10 °C drop in temperature is seen over a 5 s period. The temperature of the base is then observed to plateau at 258 °C likely due to the geometry of the mould, where full contact between the tool and base is not achieved until the tool is closed (Figure 2.1, Chapter 2.1.2). Conversely, heat

loss within the top and central plies is initially slower than that of the base and occurs at a comparable rate. However, after 354 s an instantaneous 7 °C drop in temperature is seen in the top ply (Figure 3.8), possibly resulting from contact with the upper tool on positioning of the composite into the centre of the mould.

By the end of the transfer process, prior to closing of the tool (358 s) and application of the stamping force, the temperature of the composite is below T_m at almost every through-thickness thermocouple location. Averages of the base and central regions were shown to be comparable in temperature at ~257 °C (3 °C below T_m), whereas the average of the top region was approximately 11 °C below T_m at 249 °C. This correlates to a 19 °C reduction in temperature from the end of the preheat stage to the conclusion of the transfer cycle within the top region, 8 °C more than that observed in the centre and base of the composite.

3.3.1.3 Closing of the tool and application of the applied load (358 to 370 seconds)

On the closing of the platen and application of the stamping force, the base of the composite comes into contact with the colder tool and the base layer rapidly cools at a rate of 1783 °C/min. Despite both outer surfaces being in contact with the tool and instantaneously reducing in temperature, the rate of cooling within the base is ~1060 °C/min faster than that of the top as demonstrated in Figure 3.9 and by the differing gradients of the two temperature profiles shown in Figure 3.10. This difference likely originates from the temperature variance between the two regions prior to the closing of the platen, where the base of the composite was shown to be hotter than the top and as such a larger temperature difference exists between the base region and temperature of the tool (120 °C) resulting in a faster rate of cooling. The observed cooling rates fall within the range reported in the literature, where typically surface layers are shown to

cool at rates between 400 and 17,000 °C/min dependent on the temperature difference between mould and sample [3,55].

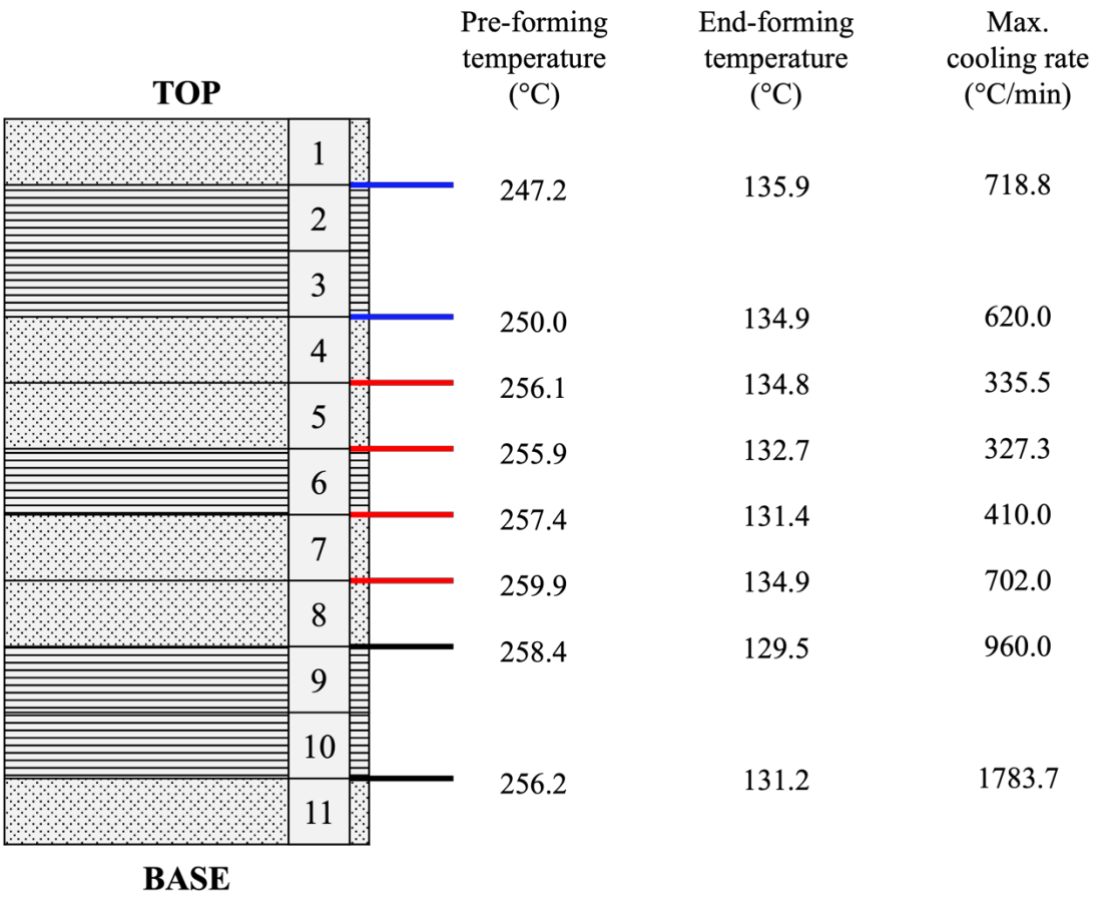

Figure 3.9: Showing a schematic of the 11-ply composite along with the pre- and end- forming temperatures (°C) and maximum cooling rates (°C/min) observed throughout each of the plies during the forming process.

Conversely, within the central region of the composite, the average temperature remains consistent throughout the closing of the platen and initial application of the loading force. This results from the relatively poor thermal conductivity of polymers (polyamide 66; 0.24 W/K.m) consequentially leading to a delay in heat dissipation from within the central region. Furthermore, as the clamping force reaches a maximum (834 kN; 362 s) and the composite

conforms to the shape of the mould, the temperature of the central region remains unchanged, whereas the surface layers continue to rapidly cool. This leads to an extensive temperature difference between the three regions at maximum stamping force, with the central plies averaging 256 °C (only 4 °C below T_m) whilst the outer surfaces are shown to be approximately 15 °C cooler.

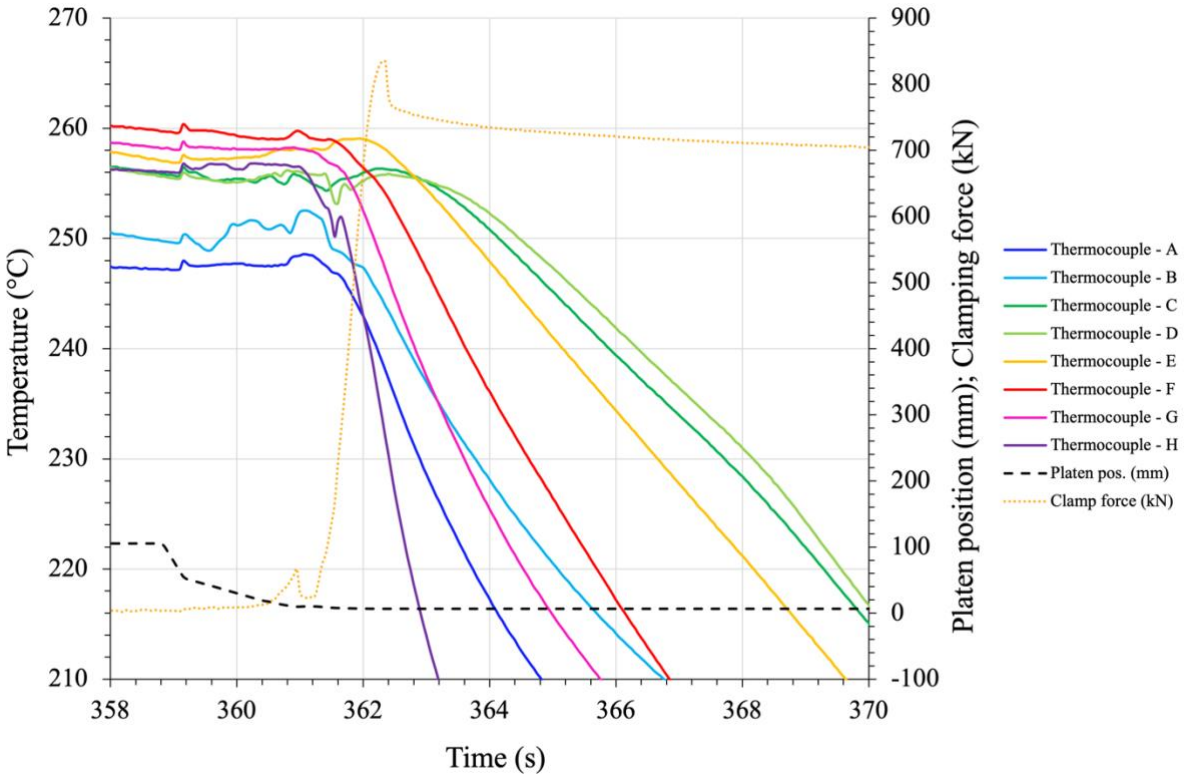

Figure 3.10: Temperature profiles recorded by each the 8 thermocouples during the closing of the tool (358-370 s).

Post maximum stamping force, plies within the central region are observed to cool at an initially linear rate as heat energy dissipates through the composite towards the surface layers and is lost via conduction to the colder tooling. Throughout this initial quasi-linear cooling period, the temperature variance between the central and outer regions continues to grow due to the differing through-thickness cooling rates (Figure 3.9). Despite temperature of the central plies

remaining above that of the outer layers, it was observed that the rate of heat loss differed within the central region, with plies closest to the base of the composite (thermocouple E and F) initially cooling at a faster rate than those nearest the top surface (thermocouples C and D). However, comparable to previous studies on thermoplastic composites, approximately 7 s after the initiation of tool closure, average temperature within the central region is 25 °C and 38 °C greater than that of the top and base surface regions, respectively [58,60]. These thermal gradients resulting from the rate of heat loss can produce skin-core residual stresses and through-thickness variations in morphology and degree of crystallinity [58,60].

3.3.1.4 Conclusion of forming cycle (370 to 500 seconds)

As the forming stage progresses, the temperature continues to fall throughout the thickness of the composite as shown in Figure 3.11. Despite an initially large temperature difference between the top and central regions of the composite on application of the clamping force, the degree of heat loss within most central layers equilibrates with that of the top surface region at a temperature of 157 °C after 383 s of the forming cycle (Figure 3.11). Furthermore, beyond 390 s and despite seemingly comparable cooling rates, the top region of the composite remains at a higher temperature than that of the central plies. Conversely, after initially, instantaneously cooling upon contact with the mould, the temperature of the base layers are consistently below that of the top and central regions throughout the duration of the forming cycle.

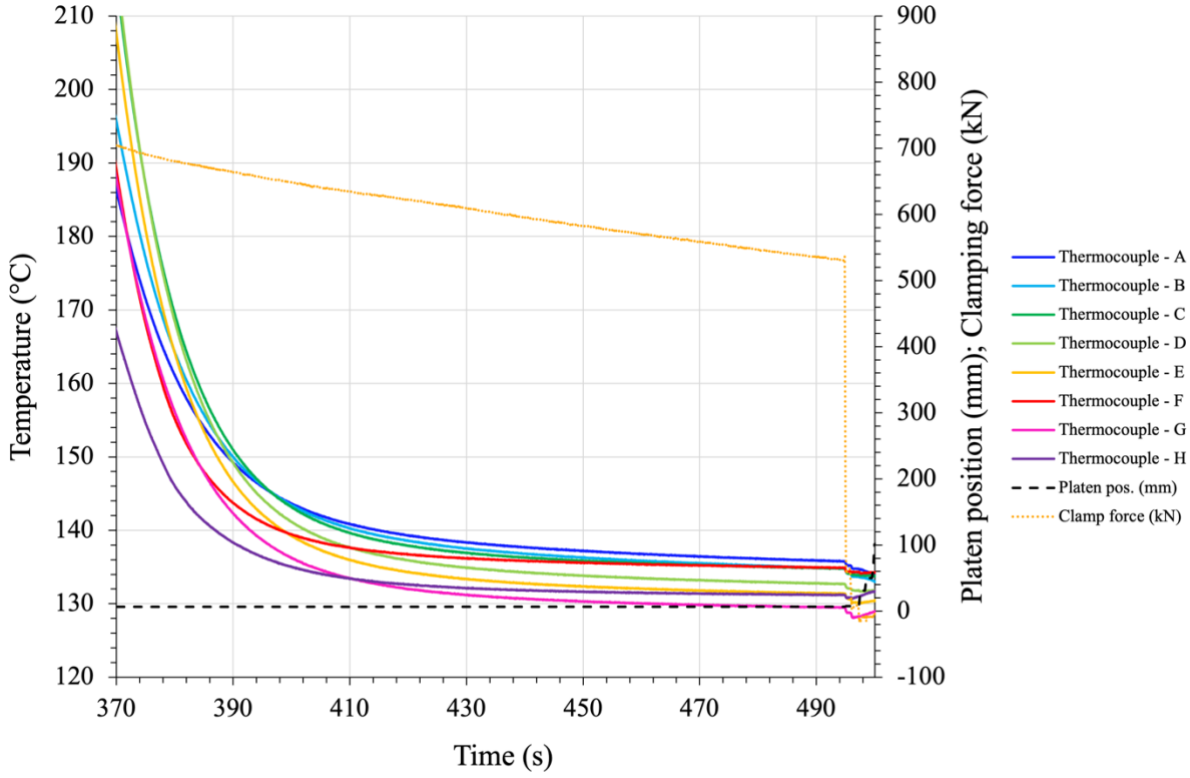

Figure 3.11: Temperature profiles recorded by each the 8 thermocouples during the conclusion of the forming cycle (365-500 s).

As the clamping force gradually reduces from 834 to 530 kN over the 133 s forming phase, the rate of through-thickness cooling becomes non-linear and continuously decreases with forming time (Figure 3.11). This results in a plateau in temperature across each of the through-thickness locations. However, despite the rate of heat loss being comparable throughout the 3 regions, as emphasised by the similarity in the shape of the temperature profiles (Figure 3.11), the plateau temperature varies from region to region. By the end of the forming cycle (495 s), all plies remain above the temperature of the mould (120 °C) yet, the average temperature of the top region is observed to be 135 °C, 1.9 and 4.9 °C greater than that of the central and base regions, respectively (Figure 3.11).

3.3.2 Characterisation of a stamp formed PA66/GF composite by differential scanning calorimetry (DSC)

3.3.2.1 Determination of matrix mass fraction using thermogravimetric analysis (TGA) and muffle furnace

As emphasised in Chapter 2, to determine the enthalpy of fusion and degree of crystallinity of a PMC sample accurately and reliably, it is imperative to know the mass of the matrix polymer. This can be achieved using thermogravimetric analysis (TGA). In addition to measuring mass loss as a function of temperature and thus, determining the constituent masses of a composite system, TGA provides supplementary information such as loss of volatiles, matrix degradation temperature, combustion temperature and the maximum rate of mass loss. Figure 3.12 shows the TGA trace of a PA66/GF sample measured in an air atmosphere over the temperature range 100 to 900 °C.

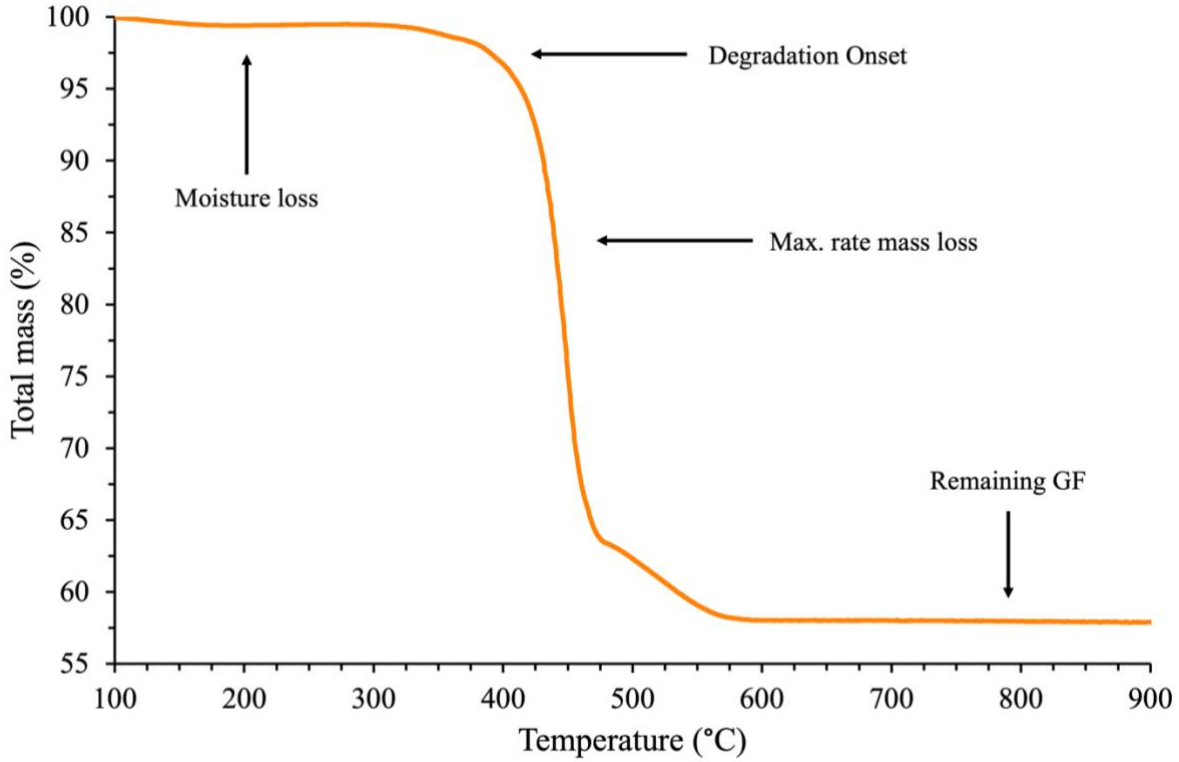

Figure 3.12: Thermogravimetric analysis of a pre-impregnated PA66 glass fibre reinforced sample, showing degradation onset temperature (~325 °C) and remaining thermally stable glass fibres post-polyamide degradation.

TGA analysis (Figure 3.12) shows the polyamide 66 matrix to be stable on heating to temperatures below 300 °C, with the only recognised mass loss (0.65 wt.%) attributed to the loss of volatiles such as water vapor. Upon heating to temperatures above 325 °C a change in the total mass of the sample is observed as the polyamide starts to degrade. The rate of degradation is initially slow between 325 and 400 °C, before rapidly increasing to a maximum at 440 °C. Furthermore, a ~37% mass loss was observed over a 145 °C temperature range between the onset of degradation (325 °C) and 470 °C, beyond which, sample mass continued to fall; however, the rate of degradation was significantly reduced. Resulting from the oxidative atmosphere, the ~6% mass loss measured over the 125 °C temperature range between 475 and 600 °C was attributed to the combustion of the carbon residue formed on degradation of the

polyamide. Above 600 °C the rate of mass loss became negligible as the degradation of the polyamide matrix was considered to be complete, with the total mass of the sample remaining unchanged at 57.9% over the 300 °C temperature increase to 900 °C. This remaining 57.9% total mass constitutes the wt.% of glass fibres within the composite sample, which are thermally stable to temperatures above 1000 °C [6].

TGA analysis shows the mass fractions of the polyamide 66 matrix and glass fibre reinforcement to be 42.1 and 57.9%, respectively. The values differ to those stated in the material datasheet (Appendix A) by ±2.1%, emphasising the importance in determining the constituent mass fractions of each individual sample to avoid local mass variations and ultimately inaccuracies in the determination of the enthalpy of fusion and degree of crystallinity.

Due to the sheer volume of DSC samples tested, measuring of the polyamide and glass fibre mass fractions by TGA was impractical and thus, measurements were performed using a muffle furnace (Chapter 2.2.3) and matrix burnout procedure.

3.3.2.2 Preliminary testing

Prior to through-thickness characterisation of the stamp formed composite, the influence of heating rate on the resulting polymer morphology and thus, enthalpy of fusion need to be better understood in order to optimise the characterisation process. Furthermore, due to poor uniformity in the distribution of glass fibres throughout the polyamide matrix (Figure 3.3 and 4.5), undoubtedly leading to variations in fibre mass fraction across samples, the effect of these localised changes in the polyamide to glass fibre ratio must be determined.

3.3.2.2.1 Influence of heating rate on polymer characterisation – cold crystallisation vs thermal lag

Previous studies on the temperature dependence of through-thickness crystallinity in polymer matrix composites (PMC) characterised by differential scanning calorimetry (DSC) have typically used heating rates within the range of 5 to 20 °C/min [55–58]. However, few acknowledge how the chosen heating rate can influence polymer morphology and thus, the melting temperature and degree of crystallinity they set out to measure. Figure 3.13 shows the effect of heating rate (10 to 100 °C/min) on the resulting melting endotherms of PA66/GF characterised using DSC analysis.

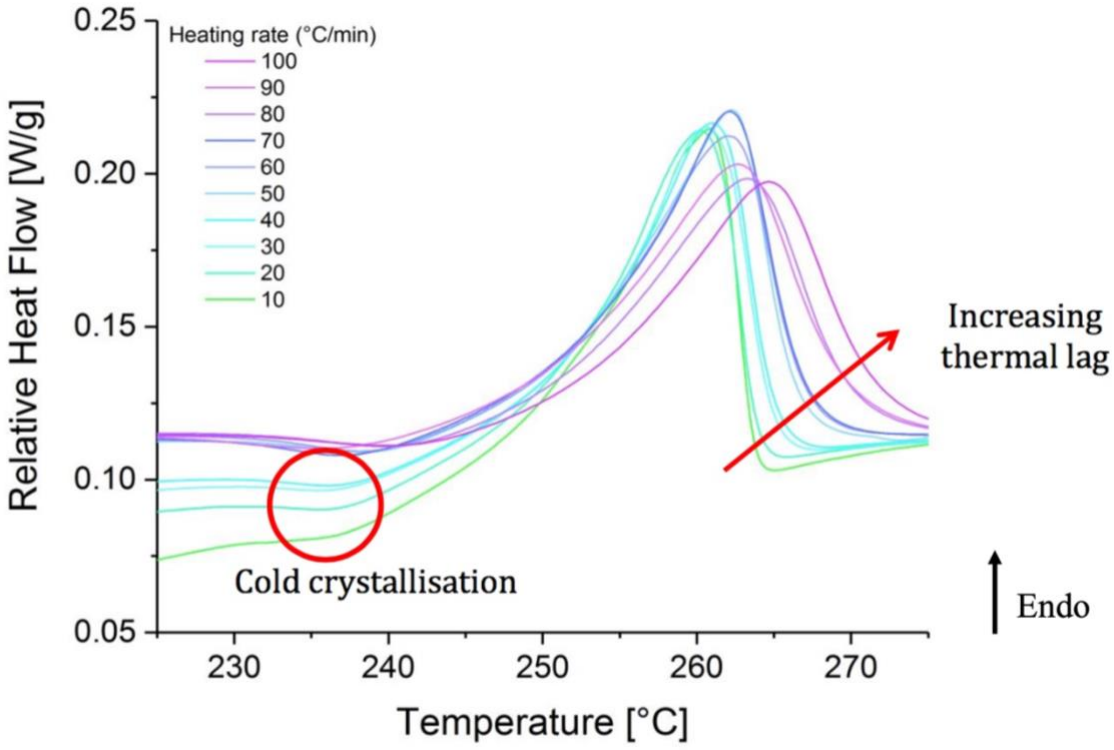

Figure 3.13: DSC thermograms showing the influence of heating rate (°C/min) on the resulting melting endotherm of PA66/GF, highlighting the small exothermic peak prior to the onset of melting (cold crystallisation) and peak shift associated with thermal lag.

As shown in Figure 3.13, at low heating rates (10 to 40 °C/min) a small exothermic peak can be observed within the DSC trace prior to the onset of melting. This peak, characteristic of cold crystallisation is typically observed when sufficient time is available for the reordering and perfecting of pre-existing polymer crystals and the growth of new crystalline structures upon heating above T_g. Despite some thermoplastics readily crystallising on cooling from the melt [58], the high cooling rates associated with the stamp forming process (Figure 3.9) limits the time available for crystallisation on cooling and can result in metastability of the polymer matrix. Upon re-heating of the quench cooled thermoplastic composites during thermal analysis, providing sufficient time is available (i.e. at low heating rates), the matrix polymer will further crystallise and/or conformational change will occur, whereby polymer chains rotate about their axes into a preferred energy state. This cold crystallisation can result in an increase in the degree of crystallinity as observed by Vasanthan and Salem during the characterisation of PA66 [67], and if not accounted for, will lead to inaccuracies in the measuring of enthalpy of fusion developed during the stamp forming process. Conversely, if the chosen heating rate is too high, a lag between the instrument and sample temperature exists. This results in the appearance that the melting endotherm shifts to a higher temperature as can be seen in Figure 3.13 at heating rates between 50 and 100 °C/min.

To quantify the effect of stamp forming parameters on the degree of through-thickness crystallinity, the enthalpy of fusion and melting temperature must be accurately determined. Therefore, the chosen heating rate must be optimised to reduce the effect of both cold crystallisation and thermal lag. Analysing the traces presented in Figure 3.13, a heating rate of 40 °C/min was considered an ideal compromise between cold crystallisation and thermal lag, and thus, was used throughout the ensuing through-thickness characterisation studies.

3.3.2.2.2 Variation in fibre distribution and its effect of matrix mass

Comparable to dismissing the effects of heating rate, several studies within the literature fail to acknowledge localised variances in the fibre mass fraction between PMC samples [55–57]. Instead, fibre mass and volume fractions are taken from the material datasheet or theoretically calculated using said datasheet value and density measurements [56,57]. However, as shown schematically in Figure 3.3 and 4.5, fibre distribution was found to vary significantly across the pre-impregnated composite tape. Thus, fibre mass fractions provided within the material datasheet can only be considered accurate and representative over a large sample volume, with error in the value increasing as sample mass is reduced.

To test the reliability of using the fibre mass fraction given in the material datasheet, circular DSC samples (4.8 mm diameter) were taken from the pre-preg tape in transverse and longitudinal locations (Figure 3.3). If it is assumed that the composite satisfies a two-phase system (polyamide matrix and glass fibre reinforcement) free of voids, where the ratio of each phase remains consistent across the tape, the mass of each DSC sample should, in theory, be the same (i.e. contain 60 wt.% GF). Furthermore, assuming manufacturing conditions were also kept consistent, if the total mass is comparable across all samples, the measured enthalpy of fusion and degree of crystallinity of each sample should be proportional.

The results of the transverse and longitudinal study are presented in Table 3.2, where in addition to the total mass of the samples, the polyamide mass fraction (determined via a matrix burnout procedure), enthalpies of fusion (ΔH_f) and degree of crystallinity (X_c) are also reported. As shown in the transverse samples (1-5), total mass varied considerably across all five samples (11.33 mg ±0.93 mg) emphasising the non-uniform distribution of glass fibres throughout the polyamide matrix. This was further accentuated by considering the polyamide mass fraction, whereby PA66 wt.% was shown to fluctuate either side of the 40 wt.% stated in the material

datasheet, with a 4.8% difference in mass observed between the two extremes. Moreover, as shown in Table 3.2, polyamide mass fraction directly influences the enthalpy of fusion and degree of crystallinity, as highlighted by the variations in crystallinity values calculated using the experimentally determined polyamide mass (X_c) and that taken from the material datasheet (X_c^*).

Conversely, due to samples being extracted from along the same fibre axes, the total mass difference between longitudinal samples (I-V) was much smaller (11.14 mg ±0.14 mg). However, resulting from the chosen axis having a low fibre density, the PA66 mass fraction was consistently greater than the 40 wt.% value stated in the material datasheet. Thus, comparable to the transverse results, crystallinity measured using the experimentally determined mass fraction differs from that of the crystallinity calculated using the datasheet wt.% values.

The results of the transverse and longitudinal study emphasise the requirement to experimentally determine the polyamide to glass fibre ratio in each sample, only then can the enthalpy of fusion and resulting degree of crystallisation be accurately and reliably determined. As shown in Table 3.2, when crystallinity is determined using the true polyamide mass fraction (as determined from matrix burnout), X_c values were found to be consistent in both the transverse and longitudinal directions, demonstrating that the presence of glass fibres does not affect the overall degree of crystallinity. This implies that differences in crystallinity are a result of the crystallisation conditions rather than the volume of glass fibres within samples. Throughout the subsequent through-thickness crystallisation analysis, post-testing, each sample was subjected to a matrix burnout procedure to determine the exact ratio of PA66:GF before the ensuing evaluation of the DSC data.

Table 3.2: The effect of localised fibre volume fraction on polyamide 66 (PA66) matrix mass and the resulting enthalpy of fusion (ΔH_f) and degree of crystallinity (X_c) of samples taken in transverse (1-5) and longitudinal (I-V) directions across the tape. The theoretical degree of crystallinity (X_c^*) by assuming a PA66 matrix mass fraction of 40% is also listed for comparison.

Sample	Total (mg)	PA66 (wt.%)	PA66 (mg)	ΔH_f (J/g)	X_c (%)	X_c^* (%)
1	11.4	41.5	4.7	70.7	37.0	38.4
2	12.3	39.2	4.8	68.3	35.7	35.0
3	12.0	38.5	4.6	71.0	37.2	35.8
4	11.4	39.2	4.5	70.7	37.0	36.3
5	10.4	43.3	4.5	69.1	36.2	39.1
I	11.3	44.3	5.0	70.2	36.8	40.7
II	11.1	44.3	4.9	70.5	36.9	40.9
III	11.0	46.0	5.1	72.5	37.9	43.6
IV	11.1	44.7	5.0	70.9	37.1	41.5
V	11.2	45.3	5.0	70.0	36.7	41.5

3.3.2.3 Temperature dependence of through-thickness crystallinity

To analyse the morphological effects of the parabolic temperature gradients observed through the thickness of the composite throughout the stamp forming process, the degree of crystallinity was measured by differential scanning calorimetry. Due to a modest amount of non-adhesive polytetrafluoroethylene (PTFE) film strategically placed within the composite prior to forming, most of the individual plies could be separated ready for DSC analysis. That said, resulting from unanticipated movement of the PTFE film within the base region of the composite during transfer to the mould, the base layers (9 to 11) were fully consolidated during the stamping process. This meant only the top 8 plies could be separated, with the base layers adhered together and unable to be divided for DSC analysis.

To more accurately determine the enthalpy of fusion and degree of crystallinity through the thickness of the composite, DSC samples were subjected to a post-analysis matrix burnout procedure. Mass fractions of the polyamide matrix and glass fibre reinforcement for each of the DSC samples used in characterising the individual layers of the stamp formed composite are reported in Table 3.3.

Table 3.3: Sample mass (mg) and constituent mass fractions (%) of PA66/GF samples used in the characterisation of the through-thickness crystallinity of stamp formed composites as determined via matrix burnout using a muffle furnace.

Composite layer	Sample	Mass (mg)			% Mass	
		Total	GF	PA66	GF	PA66
1	1	11.65	6.75	4.86	58.14	41.86
	2	11.72	6.95	4.71	59.61	40.39
	3	12.37	7.56	4.81	61.12	38.88
	4	12.08	7.04	5.03	58.33	41.67
2	1	11.33	6.89	4.49	60.54	39.46
	2	10.70	6.35	4.35	59.35	40.65
	3	11.55	6.69	4.84	58.02	41.98
	4	11.95	6.92	4.99	58.10	41.90
3	1	10.41	6.31	4.12	60.50	39.50
	2	9.95	6.05	3.87	60.99	39.01
	3*	10.52	6.09	4.43	57.89	42.11
	4	10.85	6.33	4.46	58.67	41.33
4	1	12.42	7.29	5.12	58.74	41.26
	2	13.90	8.21	5.68	59.11	40.89
	3	13.01	7.82	5.06	60.71	39.29
	4	12.76	7.59	5.14	59.62	40.38
5	1	11.73	6.78	4.92	57.95	42.05
	2	13.70	8.14	5.52	59.59	40.41
	3	12.99	7.92	5.10	60.83	39.17
	4	11.64	6.75	4.83	58.29	41.71
6	1	11.12	6.39	4.75	57.36	42.64
	2	11.38	6.70	4.68	58.88	41.12
	3	9.98	6.08	3.88	61.04	38.96
	4	10.46	5.86	4.59	56.08	43.92
7	1	12.87	7.52	5.30	58.66	41.34
	2	10.51	6.28	4.17	60.10	39.90
	3	12.21	7.25	4.94	59.47	40.53
	4	12.30	7.13	5.19	57.87	42.13
8	1	12.02	6.79	5.21	56.58	43.42
	2	10.66	6.27	4.35	59.04	40.96
	3	12.45	7.38	5.11	59.09	40.91
	4	12.49	7.09	5.34	57.04	42.96

*Measured via TGA

Aiming to quantify the effects of the stamp forming process and attribute changes in the through-thickness degree of crystallinity to the temperature profiles observed throughout the forming cycle, DSC analysis was performed on the results of the first heating run. Melting endotherms of the 8 plies in four through-thickness sample locations using DSC analysis are shown in Figure 3.14.

As observed in Figure 3.14, the peak melting temperature (T_m) is approximately 260 °C, which agrees with T_m values of polyamide 66 reported in the literature [32]. Average peak melting temperature across each of the 8 plies is listed in Table 3.4, where slight, but significant ($p < 0.05$) differences in T_m (±1.5 °C) can be noticed through the thickness of the composite. Typically, T_m gives an indication as to the crystal perfection and lamella thickness of a polymeric material, whereby the more perfectly arranged a crystal microstructure, the higher the melting temperature. Therefore, it could be assumed that the degree of crystal perfection and thickness of the crystalline lamellar are generally higher within the central region (layers 4-8) than the top of the composite (layers 1-3).

In addition to peak melting temperature, the enthalpies of fusion (ΔH_f) were also measured, with average values across each of the layers listed in Table 3.4. Enthalpies were measured by integrating the area of the melting endotherm and interpolated baseline between the onset and endset of melting. Due to the release of residual stresses established during the forming process, artifacts can often appear within the first heating run of DSC traces (Figure 3.14) making the analysis process slightly more complex. The polyamide mass fractions determined by a matrix burnout procedure outlined in Chapter 2.2.3 were also accounted for and reported in Table 3.4, alleviating the effects of non-uniform fibre distribution on sample mass and thus, ΔH_f.

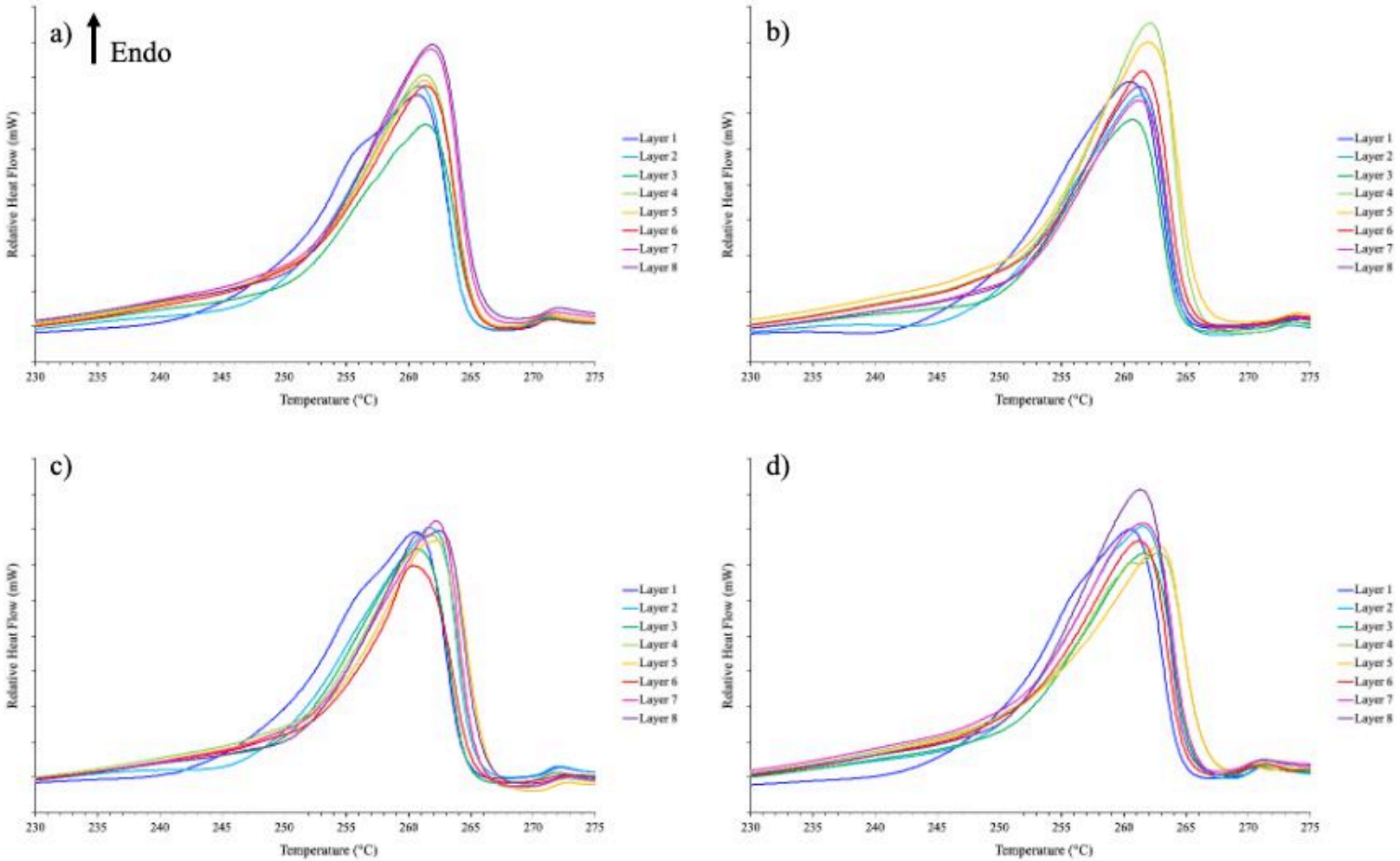

Figure 3.14: Comparison of the melting endotherms recorded in four though-thickness locations (a-d) of an 11-ply stamp formed PA66/GF composite by differential scanning calorimetry.

Table 3.4: Average values of the polyamide matrix mass fraction, peak melting temperature (T_m), heat of fusion (ΔH_f) and degree of crystallinity (X_c) as a function of composite layer; averages and standard deviations determined from a total of four samples per ply, with samples taken from identical through thickness locations. Average values ± standard deviations are reported, values with repeated letters in the same columns are not significantly different ($p < 0.05$) by Tukeys post-hoc test.

Layer	Mass			DSC analysis		
	Total (mg)	PA66 (mg)	PA66 (wt.%)	T_m (°C)	ΔH_f (Jg^{-1})	X_c (%)
1	11.9	4.9	40.7	260.5 ± 0.1^{a}	63.5 ± 1.5	33.2 ± 0.8^{x}
2	11.4	4.7	41.0	261.3 ± 0.3^{ab}	65.3 ± 2.5	34.2 ± 1.3^{xy}
3	10.4	4.2	39.9	261.2 ± 0.5^{ab}	66.4 ± 0.6	34.8 ± 0.3^{xyz}
4	13.0	5.3	40.5	261.9 ± 0.6^{b}	67.3 ± 1.0	35.2 ± 0.5^{xyz}
5	12.5	5.1	40.8	262.1 ± 0.7^{b}	67.1 ± 1.5	35.2 ± 0.8^{xyz}
6	10.7	4.5	41.7	261.1 ± 0.5^{ab}	69.2 ± 2.6	36.2 ± 1.4^{z}
7	11.9	4.9	41.0	261.6 ± 0.4^{ab}	67.8 ± 1.0	35.5 ± 0.5^{yz}
8	11.9	5.0	42.1	261.7 ± 0.5^{ab}	65.8 ± 0.7	34.4 ± 0.3^{xyz}

Typically, as the area of melting endotherm is representative of the heat energy required to melt the crystalline portion of a material, assuming heating rate remains unchanged and sample mass is correctly accounted for, the larger the area of the endotherm, the greater the crystalline fraction. As shown in Table 3.4, the enthalpy of fusion is observed to increase by 5.7 Jg^{-1} from the top of the composite (Layer 1) to the central ply (Layer 6). This difference implies that the central region of the composite contains a higher crystalline portion than that of the top. To confirm this assumption, the degree of crystallinity was determined using Equation 2-1, with average values and standard deviations across each of the 8 layers presented in Table 3.4.

Comparable to that of T_m, the degree of through-thickness crystallinity was observed to follow a parabolic profile, significantly ($p < 0.05$) increasing in value from the outer plies towards the centre of the composite. This finding is in good agreement with that of Lawrence et al. [57] and Ijaz et al. [59], both of whom reported through-thickness crystallinity gradients in PEEK/CF and PP/GF composites respectively [57,59]. A visual representation of the degree of crystallinity as a function of through-thickness location is shown in Figure 3.15, where a 3.0% difference between the top and central ply can be observed.

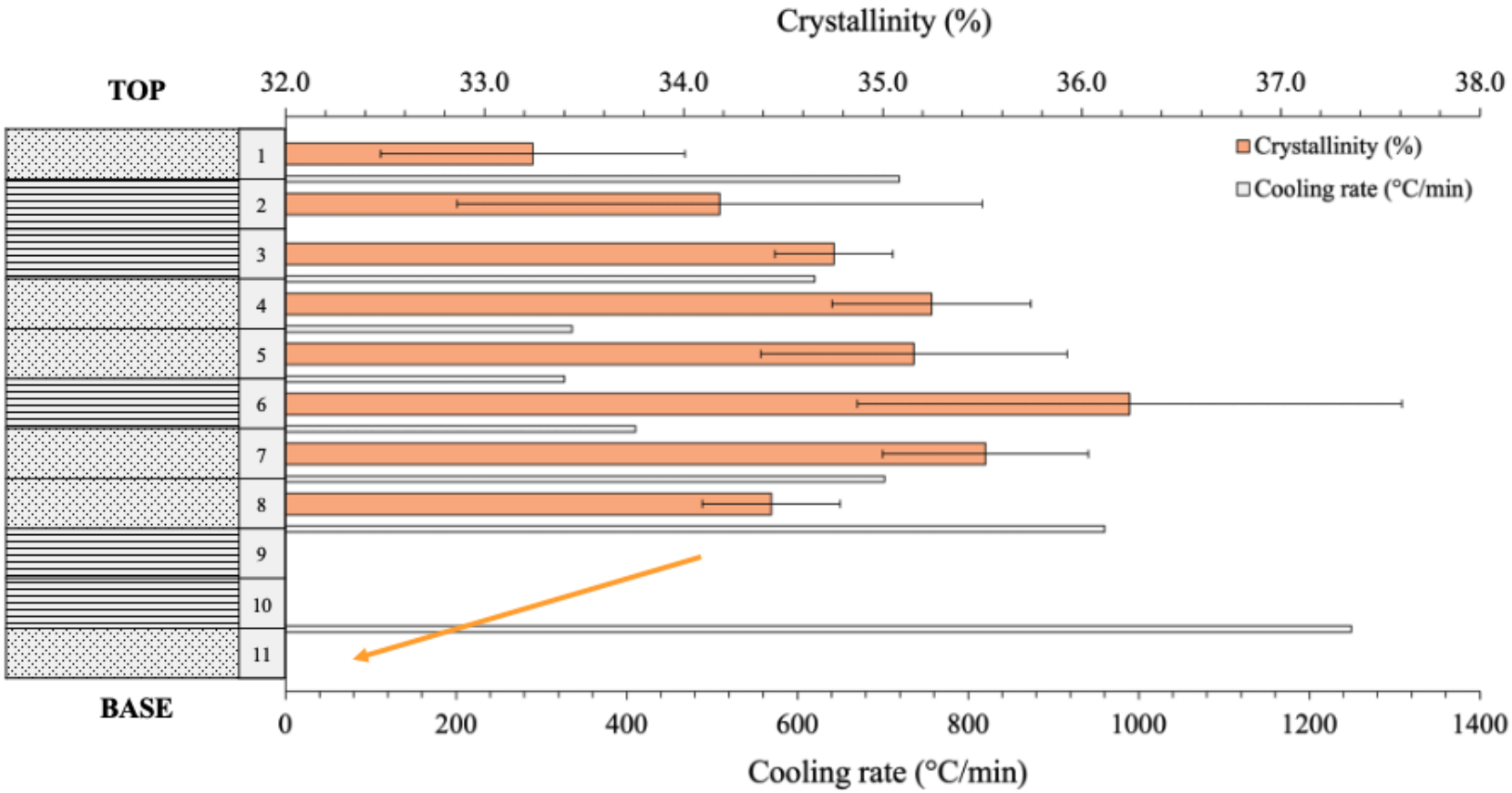

Figure 3.15: Comparison of maximum cooling rate (°C/min) throughout the stamp forming process and resulting degree of crystallinity as a function of through-thickness location in an 11-ply PA66/GF composite. Degree of crystallinity is presented as an average value determined from a total of four measurements per ply with error bars depicting the standard deviation of the results across the individual layers. The orange arrow represents the expected fall in the degree of crystallinity resulting from the increased cooling rates observed towards the base of the composite on forming.

This difference was attributed to variations in temperature loss between the preheating and forming stages, and to the differing maximum cooling rates observed at the onset of forming. As discussed in greater detail in Chapters 5 and 6, PA66/GF readily crystallises upon cooling from the melt irrespective of the cooling rates achievable in the stamp forming process. That said, at slower cooling rates, crystallisation time is extended and thus, a crystalline microstructure with superior lamella thickness and perfection can be achieved.

After preheating to ~268 °C, the temperature within the top surface layers was observed to decrease by ~19 °C during the transfer of the composite to the mould. Furthermore, due to being in direct contact with the colder tool, the top surface of the composite rapidly cooled on closing of the platen and application of the clamping force. Conversely, resulting from poor thermal conductivity of the polyamide matrix and thus, a reduction in the rate of heat dissipation from the core of the composite, the central region was maintained at a higher temperature for an extended period. Subsequently, this resulted in a 25 °C temperature difference between the central and top surface of the composite only a few seconds after closure of the tool. The maximum cooling rates that were observed at the onset of forming are listed in Figure 3.9 and shown graphically alongside the measured through-thickness crystallinity in Figure 3.15. Here an inversely proportional relationship between cooling rate and through-thickness crystallinity is generally observed. That is, at relatively high cooling rates, such as those observed within the top region of the composite (718.8 °C/min), the degree of crystallinity is comparatively low, whereas within the central region, where the cooling rate was found to be much slower (410.0 °C/min) the degree of crystallinity is at its highest. This disparity in the degree of crystallinity between the surface and core is comparable to that reported in previous studies of PP/GF [59], PPS/CF [58] and PEEK/CF [57]. Despite evidence that the outer surface readily crystallises on cooling (Table 3.4 and Figure 3.15), the reduction in the rate of heat loss within

the central plies increases the time available for crystal formation and the thickening of lamella structures, subsequently resulting in a higher degree of crystallinity and greater crystalline perfection of the microstructure.

Furthermore, owing to the extremely high cooling rate (1783.7 °C/min) observed at the base of the composite, it is expected that had it been possible to separate the base layers (9 to 11), the degree of crystallinity within these plies would have continued to obey the parabolic trend outlined above. It is anticipated that crystallinity would have continued to fall below that of layer 8 and ultimately, due to a ~1060 °C/min difference in cooling rate between the top and bottom ply, layer 11 is expected to possess the lowest value of crystallinity and crystal perfection.

Despite the study of Parlevliet et al. [58] on PPS/CF, where it was shown that the combined error in the determination of the heat of fusion and accuracy in measuring the polymer matrix mass fraction fell within the variation of the results [58], this study showed somewhat conclusive evidence of the temperature dependence of crystallinity, with the parabolic trends in through-thickness T_m and X_c found to be significant ($p < 0.05$).

3.3.3 Fourier transform infrared spectroscopy (FTIR)

The infrared spectra of PA66/GF tape is shown in Figure 3.16, with peaks of interest including the amide I peak (~1630 cm^{-1}) and amide III (~936 cm^{-1}) peak labelled.

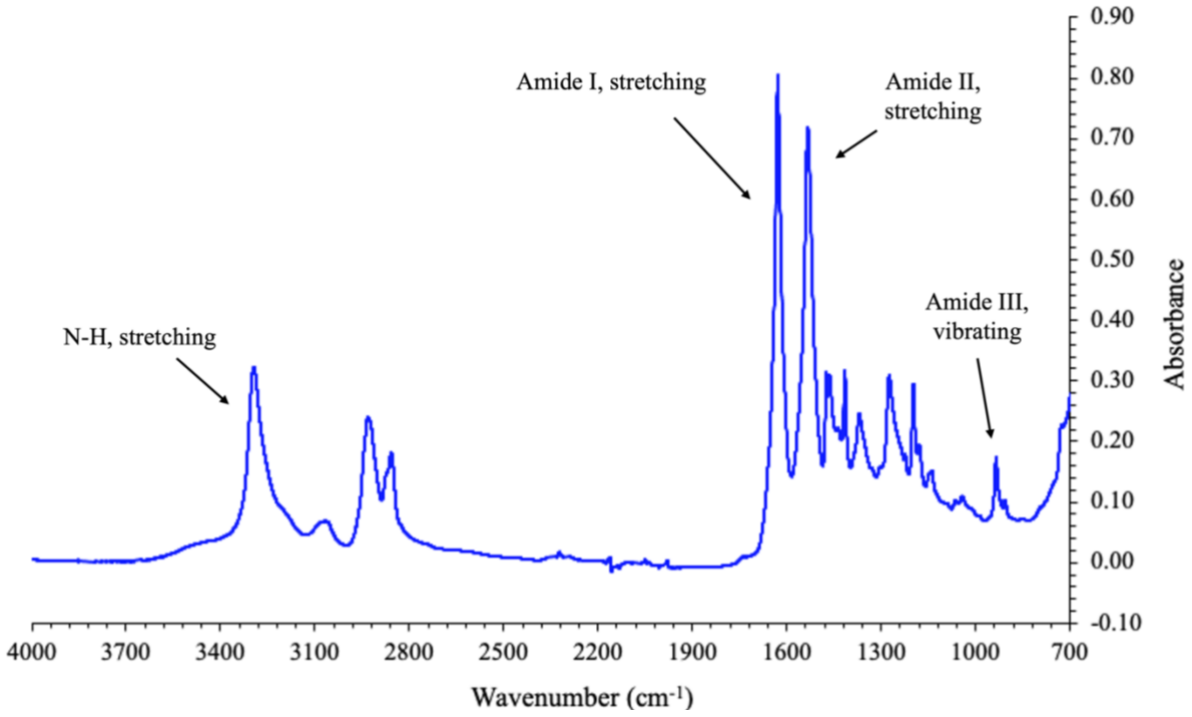

Figure 3.16: FTIR spectra of PA66/GF recorded within the frequency range 4000-700 cm^{-1}.

3.3.3.1 Suitability of FTIR spectroscopy in obtaining reliable measurements of crystallinity

As previously reported [36,70] and illustrated in Figure 3.17 a), the amide I band is sensitive to local order. Representative of the degree of perfection of hydrogen bonded C=O groups, the amide I peak is observed to shift to lower frequencies, whilst simultaneously increasing in peak intensity and reducing in band width as crystallisation develops on cooling from the melt (Figure 3.17 a)). This is in good agreement with the findings of Skrovanek et al. [70] and Lu et

al. [36] who show that despite total peak area remaining reasonably constant (~7% change), variations in peak intensity, frequency and band width are all observed to change as the ordered fraction of hydrogen bonds consumes that of the disordered fraction throughout the crystallisation process [36,70].

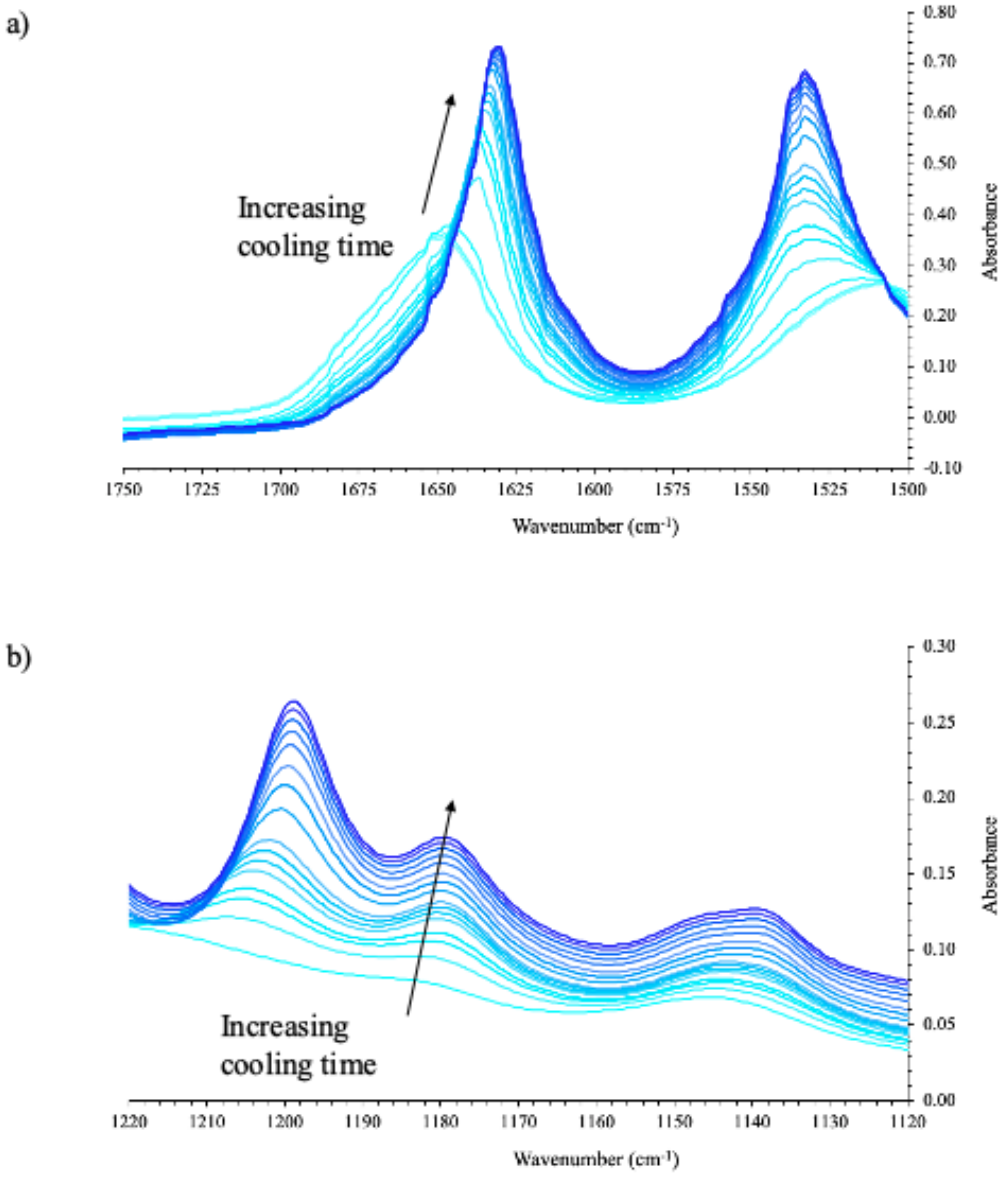

Figure 3.17: FTIR spectra of PA66/GF recorded during crystallisation on cooling from the melt among the regions: a) 1750 - 1500 cm^{-1}, b) 1220 - 1120 cm^{-1}.

As discussed in section 3.1.2, obtaining accurate and reliable measurements of the degree of crystallinity from IR spectra is challenging. The characteristic bands that appear within the IR spectra of a material rarely constitute an individual peak, but rather consist of multiple peaks, the frequency and intensity of which, is dependent on molecular interactions. Typically, deconvolution of the bands into the individual peaks is necessary for crystallinity measurements and requires complex curve fitting and the use of a multitude of parameters. Many studies utilise peak resolve functions to deconvolute IR bands, however, few disclose how accurately and reliably the resulting peak fitting compares to that of the experimental trace. Therefore, as previously stated by Skrovanek et al. [70], raises questions about the validity of the peak fitting process if one can attain any desired solution [70].

Multiple authors have previously attempted to obtain a measurement of the degree of crystallinity by assuming a two-phase model and comparing the normalised absorbance of bands representative of the amorphous and crystalline phases [65–67]. Normalisation of the bands is achieved via an internal reference peak, the absorbance of which should be independent of crystallinity. Typically, the amide I band, characteristic of stretching of the carbonyl functional group (C=O) and believed to be independent of crystallinity, has been used as an internal reference [65–68]. However, the findings within this study confirm that the amide I band is sensitive to changes in crystallinity and thus, cannot be considered a suitable internal reference band (Figure 3.17 a)). Furthermore, in studies conducted by Vasanthan and Salem [67] and Lu et al. [36] it is assumed that the band located at 1180 cm^{-1} is independent of crystallinity and is therefore an appropriate internal reference band [36,67]. However, as shown in Figure 3.17 b), similar to that of the amide 1 band, the 1180 cm^{-1} band is shown to be sensitive to local order, albeit to a lesser extent.

Ascertaining crystallinity measurements from the ratio of the ordered (crystalline) portion to that of the total area of the carbonyl (C=O) band has proven successful in thermoplastics such as poly(ethylene terephthalate) [73] and poly(ε-caprolactone) [74]. However, due to the overlapping amide II band, the amide I band never returns to a baseline value, this, and the aforementioned difficulties associated with peak fitting of IR spectra meant that peak resolve analysis of the amide I band and thus, crystallinity measurements could not accurately and reliably be performed.

3.4 Conclusions

As determined by calorimetry, the degree of crystallinity of a stamp formed 11-ply PA66/GF composite was shown to be inversely proportional to the cooling rates experienced throughout the forming process. The use of the process simulated laminate (PSL) technique and the insertion of thermocouples through the thickness of the laminate allowed for individual layers to be characterised and the morphological differences resulting from the thermal gradients associated with the stamp forming process analysed. Data acquired from the 8 thermocouples showed the maximum rate of heat loss to be observed upon closing of the tool, with an approximately 1400 °C/min disparity in cooling rate between the base of the composite and that of the central regions. Further, in good agreement with previous studies, it was observed that PA66 crystallises rapidly on cooling from the melt [58]. However, despite this, the degree of crystallinity as determined via DSC analysis, was shown to be cooling rate dependent with crystallinity found to increase by 3.0% on moving from the surface regions to the central plies of the composite.

The use of FTIR spectroscopy to accurately and reliably quantify the degree of crystallinity in stamp formed PA66/GF composites was not possible. Typically, the determination of X_c from an FTIR spectra has required complex deconvolution of spectral peaks into their crystalline and amorphous contributions before normalising the peaks using an internal reference band. However, previously thought to be independent of crystallinity and used as an internal reference band, it was shown that the Amide I peak (1630 cm^{-1}), characteristic of the carbonyl functional group, shifts to lower frequencies and increases in intensity with developing crystallinity. Further, despite attempting to calculate X_c by resolving the Amide I peak, the deconvolution process proved somewhat challenging owing to the overlapping Amide II peak.

In summary, throughout the stamp forming process, thermal gradients were observed to exist through the thickness of the composite, ultimately resulting in disparities in crystal morphology between the surface and central layers of the laminate. However, despite values of crystallinity being readily accomplished by traditional characterisation techniques such as calorimetry, issues such as the meta-stability of the crystalline phase, re-organisation that occurs on heating and sample-to-sample variation in polymer matrix mass must be carefully considered. Therefore, it could be beneficial to analysis the through-thickness microstructure of PA66/GF laminates using a more advanced characterisation technique such as x-ray diffraction.

CHAPTER 4 - CHARACTERISATION OF A STAMP FORMED 11-PLY PA66/GF COMPOSITE BY X-RAY DIFFRACTION

4.1 Introduction

4.1.1 Microstructure of polyamide 66 and characterisation using x-ray diffraction (XRD)

Upon cooling from the liquid melt, polyamide 66 (PA66) crystallises into one of two crystallographic forms: α-crystals or γ-crystals. When the rate of cooling is slow and at high crystallisation temperatures, the more stable α-crystals are formed. Here the molecular chains are fully extended and arranged into a triclinic crystal structure (Figure 4.1) forming uniform lamella within highly ordered spherulitic 'super-structures' [8]. The chains adopt a planar zigzag conformation, whereby the formation of hydrogen bonds between neighbouring chains results in a planar sheet-like arrangement [8,76–78]. On heating from room temperature towards the melt, the triclinic α-phase transforms into its high temperature α'-modification over a temperature range (80 – 200 °C) [30] commonly referred to as the Brill transition (section 4.1.1.1). The conversion of the α-crystals into the pseudohexagonal crystal structure of the α'-phase, is thought to be caused by the thermal expansion of the polymer and thus, increased distance between the hydrogen bonds of neighbouring chains at higher temperatures [8]. Upon cooling from these higher temperatures, the α to α' transformation is fully reversible.

Quenching from the melt or crystallisation at temperatures close to the glass-to-liquid transition temperature (T_g), results in the formation of the less stable γ-crystals. Unlike the triclinic unit cell of the α-phase, the γ-phase crystallises into a pseudohexagonal cell arrangement. Despite a comparable unit cell arrangement to the α'-crystals, the γ-phase is believed to be highly

irregular and lacking a highly ordered spherulitic crystal structure [8]. The exact morphology of the γ-form of polyamide 66 is still relatively unknown, though a non-planar arrangement of hydrogen bonds between pleated sheets of methylene units, rather than within the crystallographic sheets as is the case with the α-form, is suggested [8,76–78]. On heating, the γ-mesophase transforms into the more stable α'/α-crystals in an irreversible process. Despite recognising the existence of the γ-form, as a result of the elevated rate of crystallisation of polyamide 66 compared to shorter chain polyamides such as polyamide 6, the γ-form rarely appears in PA66 at room temperature [8,30,76].

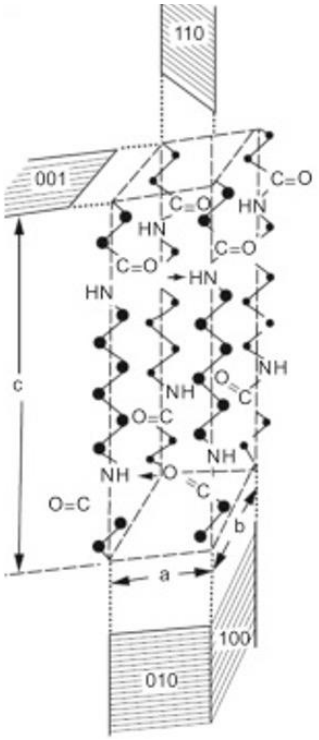

Figure 4.1: Triclinic unit cell of polyamide 66 [79].

4.1.1.1 Characterisation of the Brill transition in polyamides

First reported in 1942 using x-ray diffraction (XRD) [80], the Brill transition represents a polymorphic phase transformation from a triclinic to a pseudohexagonal crystal structure over a seemingly wide temperature range between the T_g and the melting temperature (T_m). Unique to polyamides, the Brill transition is considered a first order process (similar to melting), however, evidence of the transition is seldom seen in characterisation techniques such as differential scanning calorimetry (DSC), but rather observed more clearly through x-ray crystallography such as wide-angle x-ray scattering (WAXS).

Unless sufficiently quenched, at room temperature the polymorphic structure of polyamide 66 consists of highly ordered α-crystals arranged into a triclinic crystallographic structure (Figure 4.1). The resulting two-dimensional (2D) WAXS patterns typically feature two diffraction rings characteristic of the (100) and (010/110) crystal planes and indicative of the triclinic crystal structure generally observed below the Brill transition temperature (T_B) [39]. In one-dimensional (1D) diffraction patterns (Figure *4.2*) the α-form appears as two crystalline peaks, with reported 2θ values of approximately 20° and 24° [8,38,76–78,81] representative of the α_1 and α_2 peaks, respectively. The α_1 peak arises from the distance between the hydrogen bonded chains, whereas the α_2 peak is characteristic of the separation of the hydrogen bonded sheets [38,76–78]. On heating, as the temperature exceeds T_g, the mobility of the polyamide chains increases. This is reflected in the x-ray diffraction patterns. Over a relatively wide temperature range of ~80 to 200 °C, the (100) diffraction ring of the 2D diffraction pattern is observed to shift towards that of the (010/110) plane, with the distance between the α_1 and α_2 peaks gradually diminishing, until only a solitary peak (2θ = ~22°) remains in the 1D pattern [8,30,38,39,76,81]. This represents the triclinic to pseudohexagonal phase transformation characteristic of the Brill transition. The temperature of the Brill transition can be determined

by monitoring the distance between the (100) and (010/110) peaks, with T_B taken as the temperature at which the two peaks merge [8,39]. The exact crystal structure of the pseudohexagonal phase is disputed, with some authors referring to the transition as an α to γ transformation [76–78], whilst others claim that the structure retains its spherulitic nature and merely reverts into its high temperature α'-modification [8,38]. Despite this, there is universal agreement that a polymorphic transformation is observed and that on cooling the crystal structure reverts to its original state.

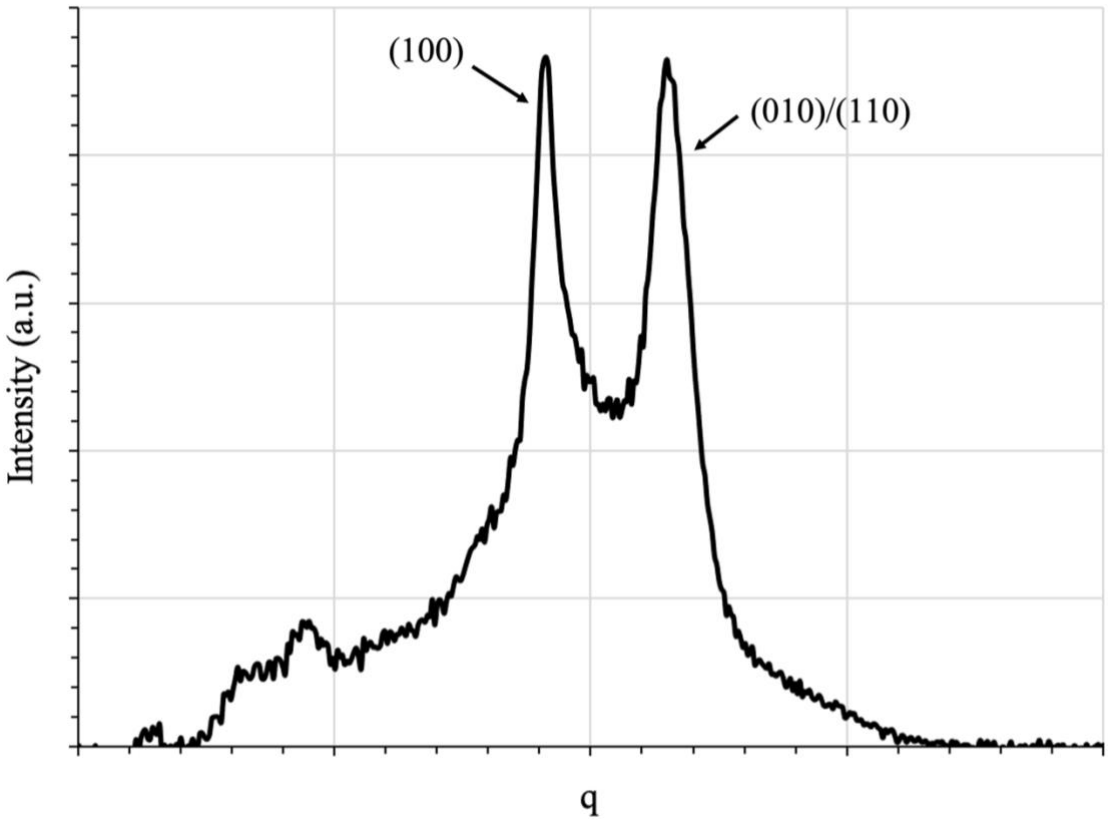

Figure 4.2: Schematic 1D WAXS pattern showing two crystalline peaks associated with the (100) and (010)/(110) crystallographic planes and characteristic of the α-crystals of PA66.

4.1.2 Crystallinity variations as measured by wide angle x-ray scattering (WAXS)

As previously highlighted in Chapter 3, the processing of thermoplastics and PMC can often lead to the generation of skin-core effects, particularly in polymers with poor thermal conductivity or where a significant temperature difference exists between the thermoplastic and the mould [56–58]. X-ray crystallography including WAXS [8,82–84] can be used to characterise the morphological gradients associated with high temperature processing and the subsequently rapid cooling rates. Unlike DSC, which is specifically used to characterise the through-thickness degree of crystallinity, x-ray diffraction can be employed to provide additional information on the microstructural differences between the surface and core, including variations in crystal form and orientation. Spoerer et al. [83] report that as a result of the cooling rates associated with the injection moulding of PA66, a non-lamella mesophase of imperfect α-crystals exists at the surface of the part, with the first detection of a spherulitic microstructure found 50 μm from the surface and increasing in size towards the core [83]. This corresponds to the findings of Parlevliet et al. [58] who also showed that despite imperfections in the microstructure, certain thermoplastics readily crystallise on cooling from the melt independent of the cooling rate of the process. Furthermore, even in the non-spherulitic regions, Spoerer et al. [83] confirm the existence of the triclinic α-phase as detected by WAXS. The 1D diffraction patterns feature the two characteristic peaks resulting from scattering of the (100) and (010/110) crystallographic planes and indicative of the triclinic α-phase [83]. The distance between the two peak maxima was shown to incrementally increase as a function of distance from the surface, which in accordance to the findings of Bunn and Garner [85] indicates an improvement in the crystal perfection of the polyamide microstructure [83,85]. Variations in through-thickness crystallinity have also been quantified using WAXS, where a 12 and 20%

difference in the degree of crystallinity of surface regions and the core was reported for PA66 [83] and poly(butylene terephthalate) [84], respectively.

4.1.3 Influence of fibre reinforcement on the development of a transcrystalline layer

Generally, due to the low interfacial free energy between the fibre and matrix, heterogeneous nucleation off the surface of fibre reinforcement is thermodynamically favoured during the crystallisation of thermoplastic composites [86]. Subsequently, resulting from the high nucleation density within these regions, the formation of spherulites is rare and a columnar-like crystal structure is more regularly observed. This densely packed, orientated microstructure is commonly referred to as a transcrystalline layer.

Due to the typically submillimetre diameter of an x-ray beam, WAXS is capable of characterising the crystallographic microstructure within the interface regions between fibre and matrix, including crystal form and orientation [86–89]. Klein et al. [89] report that the two-dimensional (2D) diffraction pattern of the bulk polyamide 66 matrix lacks crystal alignment and consists of two rings of uniform intensity, characteristic of α_1 ((100) plane) and α_2 ((010/110) planes) crystals [89]. Conversely, within the interfacial regions, two broad arcs appear in the 2D diffraction pattern [87,89]. These arcs, located on the equator and meridian of the WAXS patterns, are representative of an orientated crystal structure and reportedly result from the diffraction of the *bc* planes of a triclinic unit cell and H-bonded *ac* planes within the (010/110) doublet [87,89].

Feldman et al. [87] and Klein et al. [89] account that the orientation and preferential alignment of crystals formed in the interfacial regions is a consequence of secondary nucleation (crystal growth) and the thickness of the transcrystalline layer dependent on crystallisation temperature and distance from the bulk crystallinity forming in the matrix [87,89]. Furthermore, in a

separate study on PA66 fibre reinforced composites, Feldman et al. [88] report the effects of various carbon and aramid fibres on the crystal packing and thickness of the interfacial transcrystalline layer. It was concluded that the transcrystalline layer grows perpendicular to the fibre axis, with carbon fibres (27 – 40 μm) inducing a larger transcrystalline layer than aramid fibres (15 – 20 μm) [88]. This can be of significant importance to the mechanical properties of fibre reinforced thermoplastics, with studies showing an improvement in the longitudinal stiffness of the part with increasing orientation and thickness of the transcrystalline layer [87,89].

4.1.4 Aims and Objectives

The objectives of this chapter are to use synchrotron x-ray diffraction to expand on the conclusions of Chapter 3 by elucidating local crystalline morphology and mapping variations in crystal structure (α- or γ-crystals) through the thickness of an 11-ply stamp formed PA66/GF composite. Further, owing to the limitations of the thermal analysis techniques discussed in Chapter 3, this chapter aims to quantitatively measure the degree of crystallinity of the 11-ply stamp formed PA66/GF composite so a direct comparison to that of the DSC and FTIR results can be drawn.

4.2 Methodology

4.2.1 Sample preparation

Prior to forming, pre-impregnated sheets of PA66/GF tape were stacked into an 11-ply laminate of the following sequence: 0/90/90/0/0/90/0/0/90/90/0°. In an almost identical procedure to that outlined in Chapter 3, the 11-ply laminate was placed into a contact heating oven set to 270 °C before being quickly transferred to the stamping-press for forming once at the desired temperature. Forming time was ~140 s, with tool temperature and applied clamping force approximately 150 °C and 800 kN, respectively. The geometry of the tool was comparable to that shown schematically in Figure 2.1 (Chapter 2.1.2).

Once formed, an approximate 20 x 20 x 3 mm section was cut from the base of the laminate using an abrasive wheel cutter and cold moulded vertically in Buehler EpoxiCure resin and hardener (Figure 4.3 a)). The samples were then ground flat and polished, with the final polishing stage using a 0.05 μm alumina suspension and micro-cloth to achieve the desired finish. A precision cutting saw was then used to slice a thin (~200 μm) section from the surface of the polished part, before being bonded into an aluminium holding slide to support the section during XRD analysis (Figure 4.3 b)).

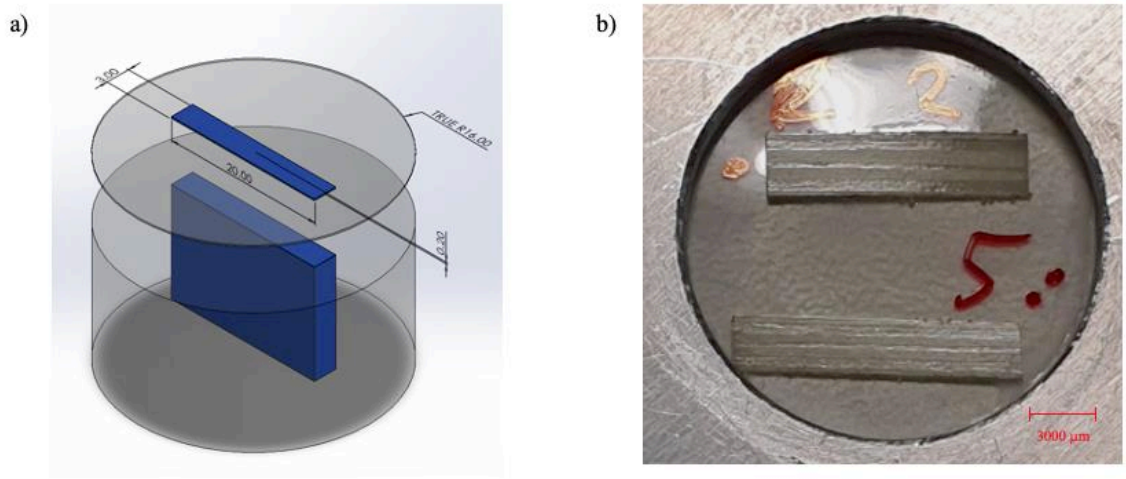

Figure 4.3: a) Schematic of the sections and cold moulded laminate, showing the thin (~200 µm) slice removed from the top surface and b) bonded in the aluminium holding slide.

4.2.2 Experimental procedure

X-ray diffraction measurements were performed using the I22 beamline at Diamond Light Source synchrotron facility (Oxfordshire, UK). The XRD samples, as prepared according to section 4.2.1, were mounted vertically onto a motorised X-Y stage attached to the I22 beamline (Figure 4.4). An optical microscope was used to locate and correctly position the sample within the beamline, with a monochromatic, microfocus x-ray beam of 30 µm diameter and 14 keV energy used to scan the sample. The sample was translated vertically and horizontally using the fly mapping function, with 2D WAXS patterns obtained at 50 µm intervals and a data acquisition rate of 1 s.

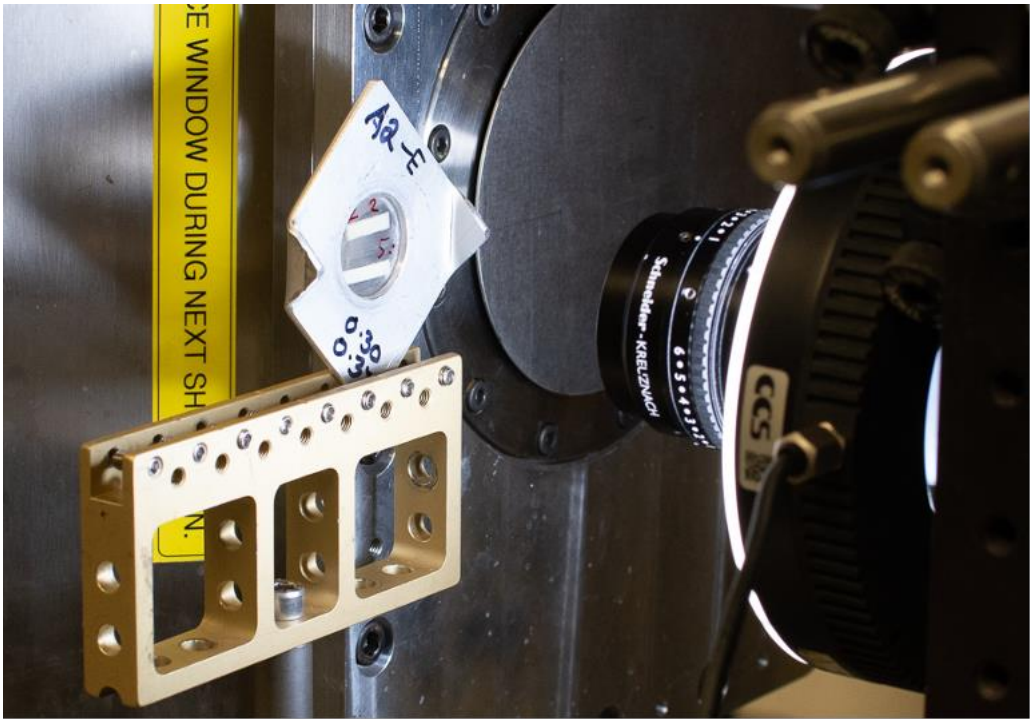

Figure 4.4: Photographic image showing the XRD sample fixed within the aluminium slide and mounted onto the X-Y stage of the I22 beamline (Diamond Light Source, Oxfordshire). The image illustrates optical analysis in which, both sample and camera are off-axis of the beamline. (Image courtesy of Neil Reynolds, Warwick Manufacturing Group).

4.3 Results and discussion

4.3.1 Data processing

Owing to the cross-ply sequencing of the laminate and the adverse effect of glass fibres on the signal-to-noise (S/N) ratio of diffraction patterns, scanning of the cross-sectional area was limited to the 0° segments of the laminate (Figure 4.5). Furthermore, in attempting to identify any microstructural differences resulting from the variable cooling rates observed throughout the stamp forming process (Chapter 3.3), spatial mapping of crystalline morphology was performed in four through-thickness locations (Figure 4.5).

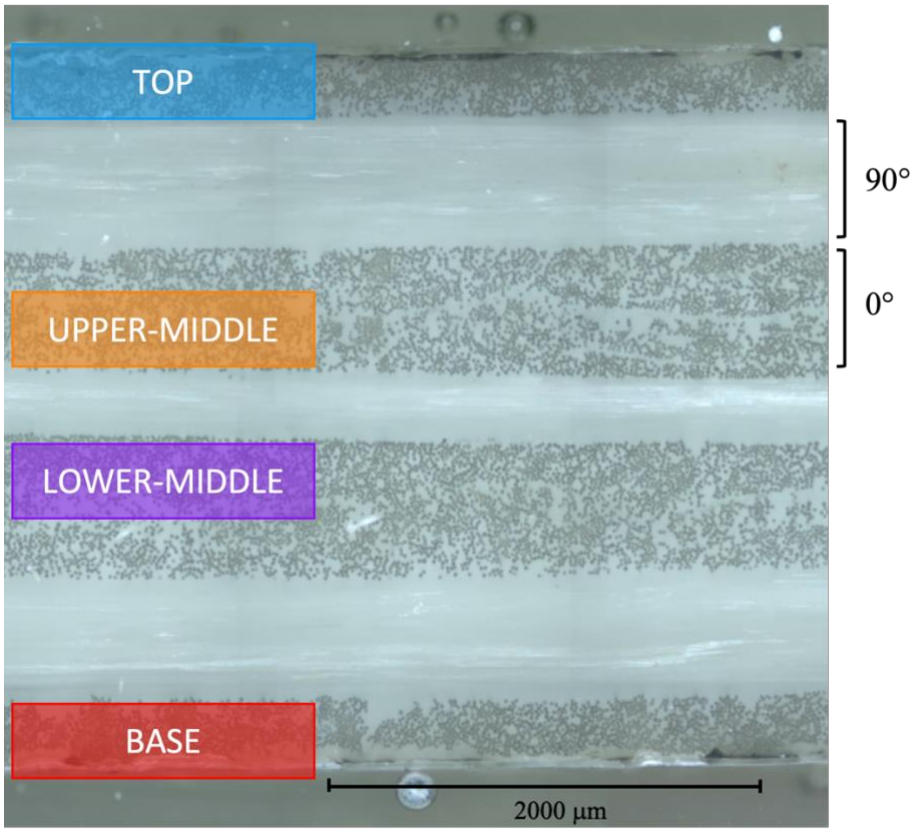

Figure 4.5: Optical microscopy image, showing the cross-sectional microstructure of an 11-ply PA66/GF laminate, with fibre orientation (0 or 90 °) and the four through-thickness locations in which WAXS analysis was performed labelled.

Total fibre volume fraction within each of the four regions was determined using Fiji image analysis software [90] and calculated to be ~40% (Figure 4.6). This is in keeping with values stated on the material datasheet (Appendix A). However, several spot measurements (sampling area: 100 x 100 µm) taken over the four regions showed local fibre density to be highly irregular, with fibre volume fractions ranging from 4.7 to 96.9%.

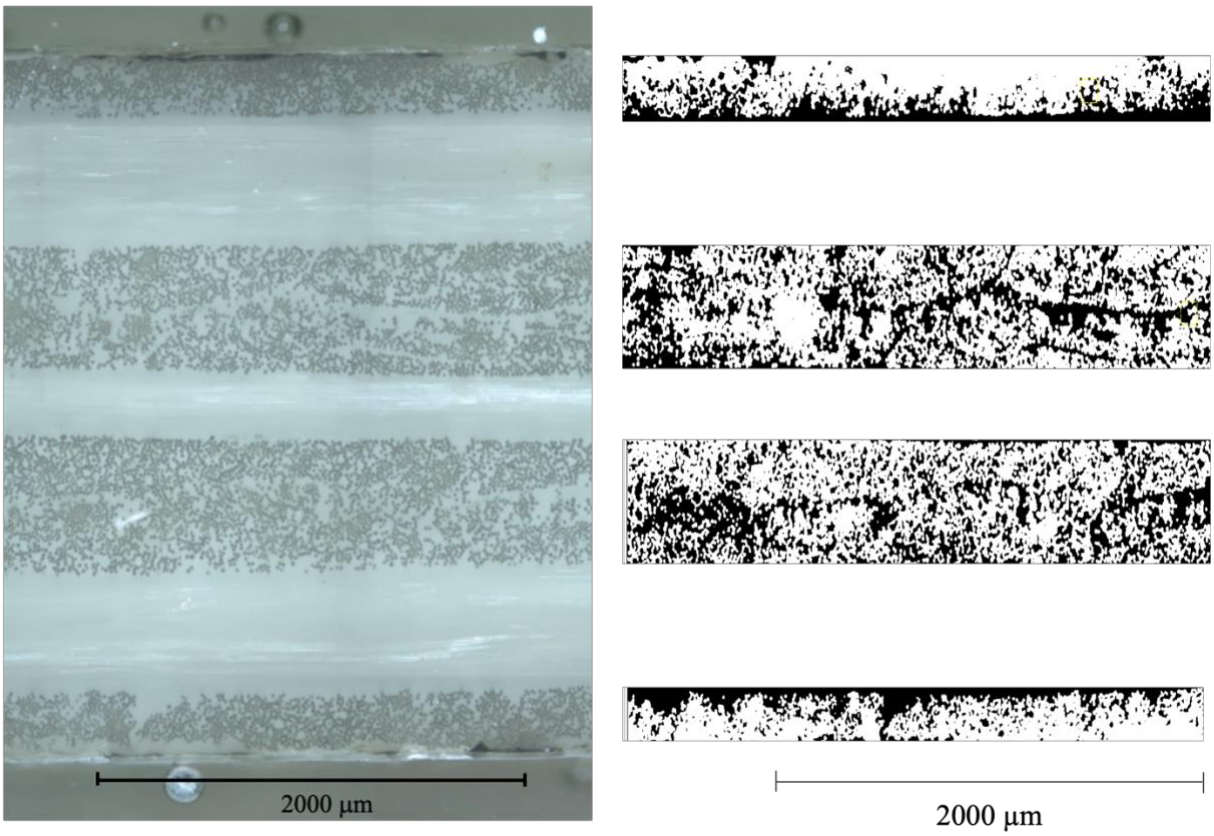

Figure 4.6: Optical microscopy image of an 11-ply PA66/GF laminate, with fibre orientation (0 or 90 °) (*left*), and image analysis of the four 0° regions taken using Fiji image analysis software [90] used to calculate total and local fibre volume fractions (*right*).

By limiting data acquisition to within these four regions, it was anticipated that spot-measurements could be made within the resin-rich pockets that exist between glass fibres.

Nevertheless, resulting from the inadequate resolution of the camera attached to the optical microscope and beam size (30 μm), it was evident that targeting of the resin-only regions for spot-microfocus WAXS would not be possible. Instead, a fly scanning approach was adopted (section 4.2.2). However, resulting from the short integration time of the fly scanning technique and the detrimental effect of the glass fibres on the majority of WAXS measurements, the S/N of the subsequent patterns was limited. As illustrated in Figure 4.7, scanning of regions containing the presence of glass fibres resulted in considerable noise within the diffraction patterns (*blue*). That said, where polymer-rich regions were encountered (*red*), clear evidence of the (100) and (010)/(110) peaks, characteristic of a triclinic unit cell and the existence of α-crystals, was observed (Figure 4.7).

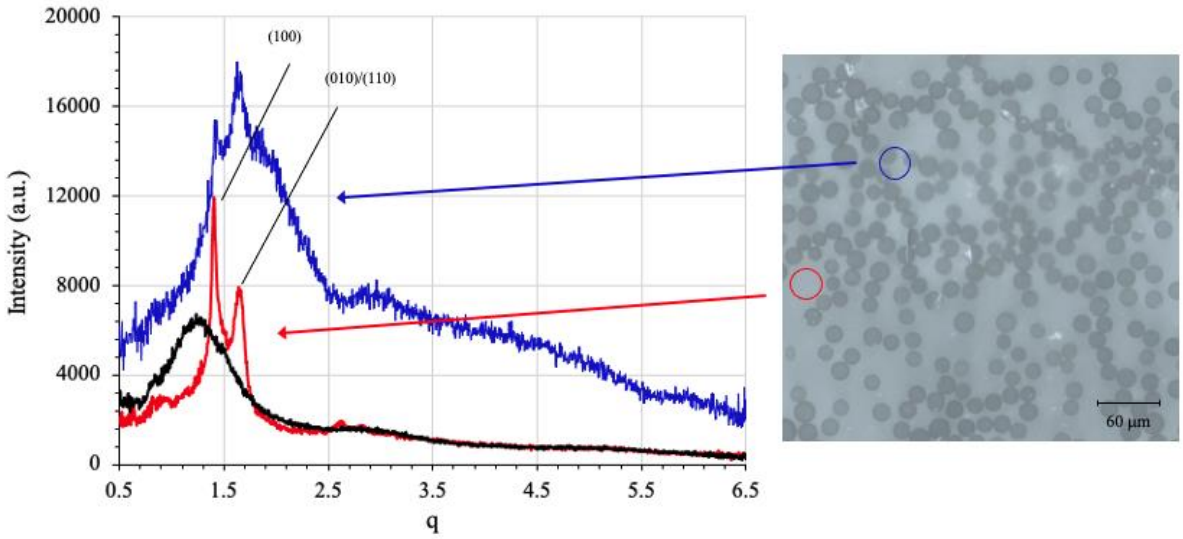

Figure 4.7: Optical image of a 0° ply section of the laminate and corresponding 1D WAXS patterns recorded using a fly scanning approach - showing the variation in the S/N of patterns recorded within polymer-rich regions (*red*) and those adversely effected by the presence of glass fibres (*blue*). The diffraction pattern of the epoxy resin (*black*) is overlaid for comparison and diffraction peaks characteristic of the (100) and (010)/(110) crystallographic planes of PA66 clearly labelled.

Measurements were taken horizontally at 50 μm intervals across the four aforementioned regions of the sample (Figure 4.5), before being translated vertically (50 μm) and the process repeated over eleven consecutive rows. Owing to the results of the DSC analysis (Chapter 3.3.2) and aiming to correlate morphological differences throughout the thickness of the part to disparities in the rate of cooling on forming, it was assumed that the greatest difference in microstructure would exist between the rapidly cooled outer surfaces and central plies that crystallised in comparatively quasi-isothermal environment. Therefore, after eliminating diffraction patterns resulting from the epoxy layers (Figure 4.7), the first three rows of the outer surfaces (top and base) were analysed along with three consecutive rows from the upper- and lower-middle regions closest to the centre of the laminate.

Data processing involved extraction of the 1D patterns and integration of the peak area of each of the measurements across the chosen three rows. The results were then assorted and co-ordinates of the data points with the lowest integrals identified – in accordance with Figure 4.7, it was perceived that traces corresponding to the smallest integrals signified resin-only regions (*red*), with that of the largest integrals characteristic of glass fibre interference (*blue*). The five WAXS patterns with the smallest integrals per row were then averaged and an auto-baseline function applied between scattering vectors (q) 0.5 and 3. This process was then repeated over each of the three rows within a region and across all four regions.

4.3.2 Through-thickness characterisation of a PA66/GF laminate using WAXS

The 1D WAXS patterns obtained over four distinct regions throughout the thickness of laminate are illustrated in Figure 4.8. The two peaks located at q values of 1.40 and 1.64 are indicative of a triclinic unit cell and characteristic of the α_1 (100) and α_2 (010)/(110) crystallographic

planes. Moreover, there is evidence to suggest that the γ-phase, which generally develops on faster cooling, coexists with that of the more stable α-phase (Figure 4.8).

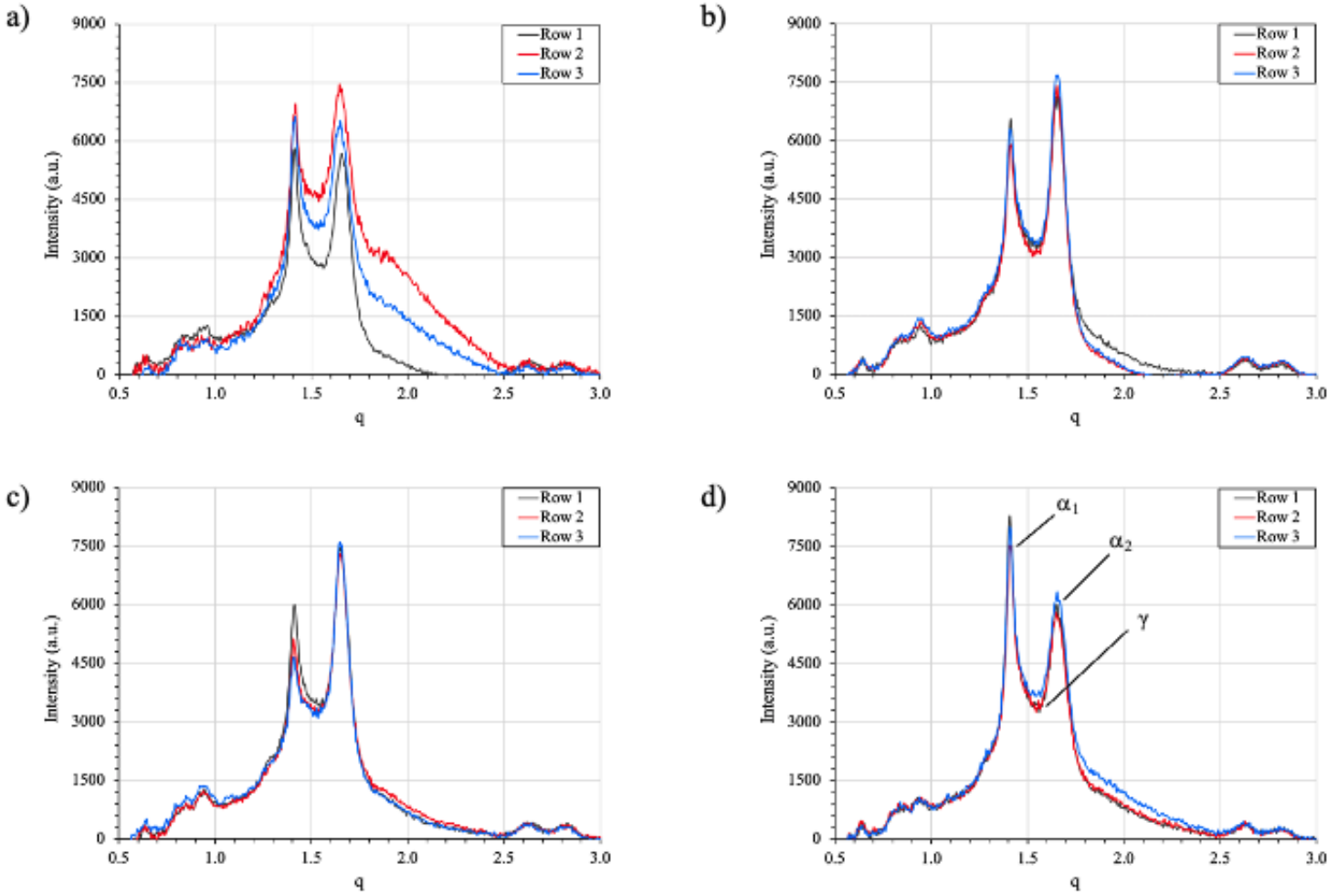

Figure 4.8: Illustrating the row averaged 1D WAXS diffraction patterns recorded from four through-thickness locations throughout the laminate; a) top surface, b) upper-middle, c) lower-middle and d) base surface. Diffraction peaks characteristic of the α_1, α_2 and γ-phase are labelled.

A variation in intensities of the (100) and (010)/(110) peaks was observed through the thickness of the laminate (Figure 4.8), with the peak ratio of the α_1 to α_2 peaks considered to be cooling rate dependent. This corresponds with the findings of Chapter 3.3, where it was highlighted that the individual layers of multi-ply laminates experience significantly different cooling rates throughout the stamp forming process. As demonstrated in Figure 4.8 (d), at the base of the laminate, where the rate of heat loss upon closing of the tool was found to be at its greatest (Chapter 3.3), the intensity of the α_1 peak was shown to be greater than that of the α_2 peak. However, within the top surface of the laminate, where the cooling rate was reported to be less than that of the base region, the ratio in intensity of the two peaks was observed to be far more even (Figure 4.9). Furthermore, with increasing distance from surface of the laminate, cooling rate was shown to continuously reduce towards the centre of the part (Chapter 3.3). This coincided with a shift in the intensity of the α_1 and α_2 peaks, whereby in contrary to the rapidly cooling base region, the intensity of the α_2 peak was found to be superior to that of the α_1 peak within the slower cooling central regions of the laminate (Figure 4.8 and Figure 4.9). A similar observation was made by Meng et al. [11] in their study of long-GF/PA66. They report that at higher annealing temperatures, crystallisation of the α_2 crystals is favoured and thus, results in the intensity of the (010)/(110) peak being greater than that of the alpha1 (100) peak [11]. A change in intensity of two peaks representative of the same crystal phase (e.g. α-phase) is often seen where there is some preferential orientation of the crystallographic planes. Typically, this difference originates due to the processing conditions in which the polymer chains crystallise, whereby one crystal plane crystallises preferentially to another. Thus, as illustrated in Figure 4.9 by the differing ratios of the (100) and (010)/(110) planes, it could be assumed that orientation within the crystal structure differs slightly between the surface and central regions of the laminate. These observations are indicative of a change in crystal structure and in good

agreement with the work of Spoerer et al. [83] on injection moulded PA66 and with earlier results obtained by DSC analysis (Chapter 3.3.2), where a parabolic trend in through-thickness crystallinity and inverse relationship between X_c and cooling rate were observed. Despite the differing intensities of the α_1 and α_2 peaks, the distance between the two peak maxima was not observed to noticeably change through the thickness of the laminate. This contradicts previous reports on rapidly cooled, injection moulded PA66 components [83] where it was found that with increasing distance from the surface of the part, the distance between the α_1 and α_2 peak maxima incrementally broadens characteristic of improvements in the crystal structure [83,85]. Further, with increasing crystallinity and improved perfection of a crystalline structure a narrowing of the diffraction peaks is generally observed. Typically, this is quantitatively described by the Scherrer equation, whereby the crystalline domain size can be determined from both the diffraction angle and full width at half maximum (FWHM) of the peak amongst other parameters. That said, determination of FWHM values requires deconvolution of the diffraction peaks into their constituent bands via a complex peak resolve process. However, resulting from the combined detrimental effect of the fly scanning approach and beam diameter on the S/N ratio, it was not possible to accurately resolve the peaks into their respective α_1, α_2 and γ-phase contributions and thus, quantitative analysis including the determination of crystallinity and variations in the γ/α ratio through the thickness of the composite were limited.

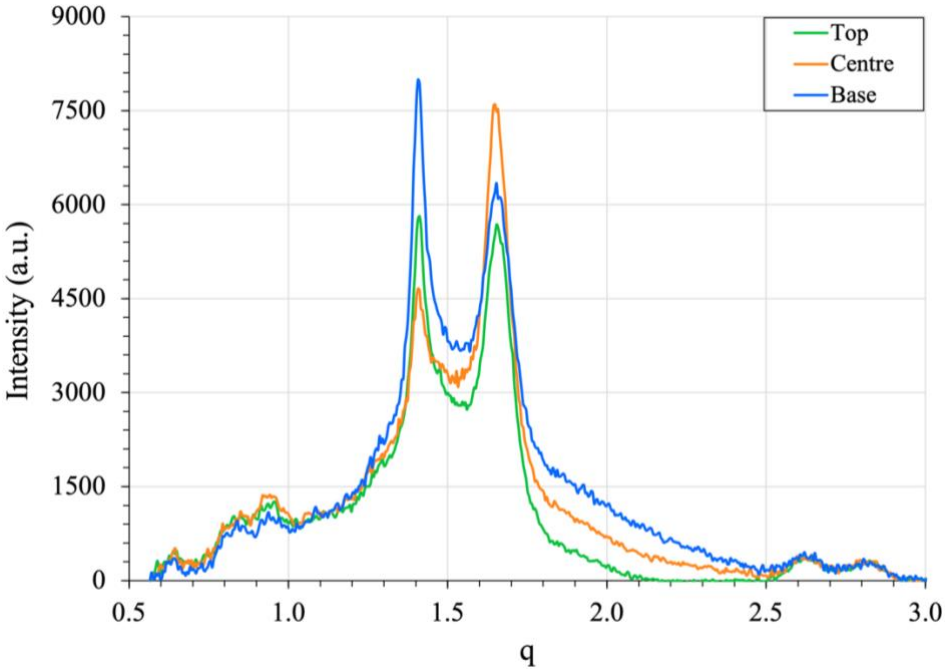

Figure 4.9: Illustrating the shift in intensity of the α_1 and α_2 peaks moving through the thickness of the composite.

4.4 Conclusions

In summary, the assessment of bulk crystallinity is readily accomplished by calorimetry, however, issues such as the meta-stability of the crystalline phase and re-organisation that occurs on heating from T_g to T_m must be carefully considered. Therefore, mapping of the crystal morphology through the thickness of a PA66/GF laminate was performed using XRD analysis. As shown in the 1D WAXS patterns, the results demonstrate that despite the distinctly non-isothermal crystallisation conditions associated with that of the stamp forming process, the polyamide matrix rapidly crystallises into the more stable triclinic unit cell characteristic of the α-phase of PA66. However, despite this, the intensities of the α_1 and α_2 peaks were found to differ through the thickness of the laminate, indicative of a change in crystal structure resulting from the disparity in cooling rates observed on forming. These findings were in good agreement

with that of Chapter 3, where it was found that a significant difference in melting temperature (characteristic of thicker, more perfect crystals) and degree of crystallinity were observed between the rapidly cooling surface layers of the composite and that of the slower cooling central plies. That said, owing to poor S/N of the diffraction patterns, resulting from several factors including: the resolution of the optical camera, the fly scanning approach (necessitating the averaging of data over rows rather than obtaining discrete mapping measurements), and beam diameter, quantitative analysis including crystallinity calculations were limited.

CHAPTER 5 - ISOTHERMAL CRYSTALLISATION KINETICS OF PA66/GF

5.1 Introduction

As described in Chapter 1, the onset and subsequent rate of crystallisation of the polymer matrix profoundly affects the forming mechanisms and the ease at which the composite laminate conforms to the geometry of the mould. Consequently, the optimisation of formability and reduction in the likelihood of forming related defects requires a fundamental understanding of the crystallisation kinetics of the matrix material.

In addition to the improvements in formability, knowledge of the crystallisation kinetics allows precise control of the polymer morphology throughout the forming process. Understanding and controlling the rate of crystallisation allows the thermal and mechanical properties of the composite to be somewhat tailored to the application.

Isothermal crystallisation kinetics have been extensively studied in a multitude of polymers using numerous characterisation techniques including: fourier transform infrared spectroscopy [91,92], laser flash analysis [93] and wide angle x-ray scattering (WAXS) [94], however, the most widely used characterisation technique is differential scanning calorimetry (DSC).

Determining the kinetics of isothermal crystallisation requires the thermoplastic to first be heated to above its melting temperature and sufficient time allowed to ensure complete melting of the pre-existing polymer crystals. Once in the liquid state, the sample is quickly cooled to the chosen crystallisation temperature and held at this temperature for a predetermined amount of time. Throughout this period the DSC monitors any fluctuations in heat flow and a subsequent trace of heat flow versus time is recorded. The observation of an exothermic peak

is characteristic of isothermal crystallisation, the area of which is representative of phase change as a function of time. As described in section 5.2.2, once integrated, the exotherm can be used to define the isothermal crystallisation kinetics of the polymer system.

5.1.1 Quantification of isothermal crystallisation kinetics

5.1.1.1 The Avrami model

Multiple models profess to best describe the kinetics of crystallisation in polymeric materials, however, the most extensively used is that proposed by Avrami. In addition to quantifying the rate of crystallisation, the Avrami model [95–97] endeavours to describe the mechanism of nucleation and geometry of crystal growth (Equation 5-1).

$$1 - X_t = exp(-k_a t^{n_a})$$

Equation 5-1

Where X_t is fractional crystallinity at time, t; k_a is the Avrami crystallisation rate constant and n_a is the Avrami exponent. The Avrami exponent is a numerical value used to describe the mechanism and geometry of nucleation. It is the combined sum of the two values assigned to the constituent components and should be an integer between 1 and 4. The mechanism of nucleation can take one of two forms; instantaneous nucleation (heterogeneous nucleation) or sporadic nucleation (homogeneous nucleation). Instantaneous nucleation is considered a zeroth-order process and as such is assigned a value of 0, conversely, sporadic nucleation, assumed to be a first-order process, is ascribed a value 1. The geometry aspect relates to the dimensionality of the subsequent crystal growth. Values of 1, 2 or 3 are assigned indicative of the formation of one-dimensional rods, two dimensional discs or three-dimensional spheres,

respectively. Table 5.1 details the Avrami exponent values according to the nucleation mechanism and geometry of crystal growth.

Table 5.1: Interpretation of the Avrami exponent values according to the nucleation mechanism and geometry of crystal growth.

Nucleation Mechanism	Avrami Exponent, *n*	Dimensionality of Crystal Growth	Resulting Morphology
Instantaneous	1	1	Rods
Sporadic	2	1	
Instantaneous	2	2	Discs
Sporadic	3	2	
Instantaneous	3	3	Spheres
Sporadic	4	3	

5.1.1.1.1 Limitations associated the use of the Avrami model

Despite being extensively used, the Avrami model has been severely criticised [98–100], and a comprehensive list of limitations revealed. In practise the model is only applicable to primary crystallisation and inadequately describes the latter stages of crystallisation once spherulite impingement has occurred [101,102]. In addition, the mechanism of nucleation and growth described by the Avrami exponent often returns non-integer *n* values [100–102]. This gives limited meaning to the assumptions proposed by Avrami and thus, does not fully describe the mechanisms of nucleation. Further experimental limitations include failure to consider the induction time and the frequent use of incomplete exotherms, leading to errors associated with integration of the traces [98]. The theoretical assumptions of the model are also not without

their limitations. These include the presumption of constant radial growth, complete transformation of the polymer sample, no volume change throughout the transformation process and the involvement of only one nucleation mechanism [99,103]. Numerous authors have proposed alternative models, many of which merely modify and adapt the existing Avrami equation in an attempt to resolve the limitations and account for the presence of secondary crystallisation. The most notable of which being Tobin [104–106], Malkin [107], Urbanovici-Segal [108,109], Velisaris-Seferis [110] and Hay [48,91,92,111], these will be discussed in the following sections.

5.1.1.2 Tobin model

Attempting to account for spherulite impingement, Tobin adapted the Avrami equation to better define the latter stages of crystallisation. In keeping with that of Avrami, the Tobin equation (Equation 5-2) contains both a rate constant (k_t) and exponent (n_t). The Tobin exponent shares a similar physical meaning to that of Avrami with the exception that n_t need not be an integer [104–106].

$$X_t = \frac{k_t t^{n_t}}{1 + (k_t t^{n_t})}$$

Equation 5-2

Where X_t is fractional crystallinity at time, t.

5.1.1.3 Malkin model

With an obvious disparity from the models proposed by Avrami and Tobin, Malkins theory is derived from the assumption that the overall rate of crystallisation equates to the summation of

the rate of primary nuclei formation and the rate of subsequent crystal growth [107]. The Malkin equation is given by:

$$X_t = 1 - \frac{C_0 + 1}{C_0 + e^{C_1 t}}$$

Equation 5-3

Where C_0 denotes the Malkin exponent and is proportional to the ratio of crystal growth rate to nucleation rate; C_1 is the Malkin crystallisation rate constant and relates to the overall rate of crystallisation. Dissimilar to the models of Avrami and Tobin, the Malkin parameters (C_0 and C_1) may only be determined through curve fitting procedures, however, the kinetic parameters can be derived from those obtained from the Avrami analysis [112].

5.1.1.4 Urbanovici-Segal model

Urbanovici and Segal have since derived a new kinetic model to describe the crystallisation process, which is essentially a generalisation of the Avrami model [108];

$$X_t = 1 - [1 + (r-1)(k_{us}t)^{n_{us}}]^{1/(1-r)}$$

Equation 5-4

Where n_{us} and k_{us} are the Urbanovici-Segal exponent and rate constant parameter respectively, both of which, share a similar physical meaning to that of the Avrami kinetic parameters. r is a parameter that satisfies the condition $r > 0$, where when r tends to 1, the Urbanovici-Segal equation becomes identical to that of the Avrami equation. It has been suggested previously by Supaphol [113] that r is merely a parameter used to assess the deviation between the Urbanovici-Segal and Avrami models [113].

5.1.2 Models accounting for the contribution of secondary crystallisation

Besides the proposed models outlined above, which attempt to account for the recognised limitations associated with the Avrami equation, a few authors have also endeavoured to derive models that specifically acknowledge and account for the secondary crystallisation process.

5.1.2.1 Velisaris-Seferis model

Velisaris and Seferis devised a kinetic model based on the observation of two competing processes in a standard double-log Avrami plot of PEEK [110]. They attributed these distinct regions to the primary and secondary crystallisation processes. The model proposes that the two crystallisation processes (primary and secondary) can occur either in series (Equation 5-5); whereby secondary crystallisation commences only after the completion of the primary process, or in parallel (Equation 5-6), where the two processes are considered to occur simultaneously. [Note: the secondary process can only occur after the onset of primary crystallisation].

$$\frac{X_\infty}{X_t} = \frac{w_p}{1 - e^{-k_p t^{n_{vs}}}} + \frac{w_s}{1 - e^{-k_s t^{m_{vs}}}}$$

Equation 5-5

$$\frac{X_t}{X_\infty} = w_p\left(1 - e^{-k_p t^{n_{vs}}}\right) + w_s\left(1 - e^{-k_s t^{m_{vs}}}\right)$$

Equation 5-6

Where X_t and X_∞ are the fractional crystallinities at time, *t* and at infinite time, respectively; w_p and w_s are weight fractions of the primary and secondary processes, the summation of which is

equal to 1; k_p and k_s are the rate constants of the primary and secondary processes and n_{vs} and m_{vs} are the exponents for both processes.

5.1.2.2 Hay model

In recent studies of the crystallisation kinetics of PET [91] and PCL [92] using infrared spectroscopy, Hay et al. detected a square root time dependence on the growth of crystalline lamellar following completion of the primary crystallisation process [91,92]. Representative of secondary crystallisation and indicative of a diffusion-controlled process, this post-primary crystallisation thickening of the existing lamellar was shown to be greatest at the centre of the spherulites [91]. This implies that secondary crystallisation proceeds almost immediately upon formation of the growing spherulites and verifies the assumption of Velisaris-Seferis' parallel model, where it was predicted that the primary and secondary processes occur simultaneously and that total crystallinity at any given time is the sum of the two contributions. Mindful of these findings, Hay derived a new kinetic model which has been validated using infrared spectroscopy [91,92], laser flash analysis [93] and most recently DSC [111]. The applicability of the Hay model to the isothermal crystallisation of both polyamides and fibre reinforced thermoplastics is yet to be determined.

It remains that fractional crystallinity at time, *t* is equal to the summation of the two individual constituents:

$$X_t = X_{p,t} + X_{s,t}$$

Equation 5-7

Where X_t, $X_{p,t}$ and $X_{s,t}$ are the total, primary and secondary fractional crystallinities at time, *t*.

Primary crystallisation continues to follow the Avrami equation:

$$X_{p,t} = X_{p,\infty}\left(1 - e^{-k_p t^n}\right)$$

Equation 5-8

Whilst the secondary process follows a root time dependence and is reliant on some degree of prior primary crystallisation:

$$X_{s,t} = X_{p,t} k_s t^{1/2}$$

Equation 5-9

The combination of Equation 5-7 – Equation 5-9 gives:

$$X_t = X_{p,\infty}\left(1 - e^{-k_p t^n}\right)\left(1 + k_s t^{1/2}\right)$$

Equation 5-10

Where $X_{p,\infty}$ is fractional crystallinity on completion of the primary process, k_p and k_s are the Avrami rate constants of the primary and secondary processes respectively, and n is the Avrami exponent.

On completion of primary crystallisation, the value of $e^{-k_p t^n}$ becomes negligibly small and so it is deduced that the rate of crystallisation will become solely dependent on the square root of time:

$$X_{p,t} = X_{p,\infty}\left(1 + k_s t^{1/2}\right)$$

Equation 5-11

Previous work on the crystallisation kinetics of PET and PCL using DSC and infrared spectroscopy have shown that despite the traditional assumption that crystallisation is complete on return of the DSC trace to the baseline value, secondary crystallisation can continue for extended periods of time [114,115]. More recently in a study by Kelly et al. on PHB-co-HV, it was observed that the isothermal DSC trace never returned to a baseline value [111]. This was attributed to the significant contribution of the secondary crystallisation process. The trace was seen to plateau and despite changes in the recorded heat flow slowly diminishing, crystallisation rate was shown to continue at the rate of secondary crystallisation [111].

The traditional methods of quantifying the isothermal crystallisation kinetics of polymers from DSC analysis assume that crystallisation ends upon the approximate return of the recorded heat flow to the baseline value. This time point is typically obtained by the drawing of a tangent from t_i across the exothermic crystallisation peak, with t_{end} taken as the time point at which the trace re-meets the tangent (section 5.2.2). This is not without its limitations. As later discussed in section 5.3.3, t_{end} is often determined by eye, resulting in increased human error of the analysis, additionally, the sensitivity of the DSC can make detecting small changes in heat flow over the secondary process difficult to identify.

Dissimilar to the traditional methods of analysis which only assume the completion of the crystallisation process, Hays approach models the data and calculates where secondary crystallisation tends to zero, thus, more accurately estimates the end of the crystallisation process.

5.1.3 Suitability of the isothermal kinetic models – A review of the literature

Despite its limitations (section 5.1.1.1.1), the Avrami equation is undoubtably, still the most frequently used of the isothermal crystallisation kinetic models. Often applied in isolation, the

model has repeatedly been used to quantify the crystallisation kinetics of numerous polyamides including, PA6 [116,117], PA66 [118,119], PA9,11 [120], PA10,12 [121] and PA12 [122]. The Avrami exponent *n*, of pure polyamides is regularly reported to be a non-integer value of approximately 3, with most authors inferring three-dimensional crystal growth [117,120,123]. Derived through modifications of the Avrami equation and predicting a more suitable fit to the isothermal crystallisation kinetics of polymer systems, the Tobin, Malkin, and Urbanovici-Segal models are commonly applied alongside the Avrami model for comparison. Authors generally apply a combination of the models, assessing their suitability in describing the crystallisation kinetics of pure polymers [124–126], polymer blends [127,128] and polymer matrix composites [129], however, only a selection of papers critically evaluate the applicability of all four models [113,129,130].

Comparing the fit of all four models to the experimental data of polyethylene terephthalate (PET) and PET/nanocomposites, Nikam and Deshpande [130] conclude that the Avrami, Malkin and Urbanovici-Segal equations adequately describe the kinetics of isothermal crystallisation, with the Tobin equation performing less satisfactorily when describing nanocomposites [130]. This is in agreement with studies on poly(ethylene oxide) monomethacrylate (PEGMA) [129] and syndiotactic polypropylene (s-PP) [113], where the Urbanovici-Segal model was shown to best describe the crystallisation process, followed by the Avrami and Malkin models, respectively [113,129]. Nevertheless, despite being considered unsuitable in describing the crystallisation kinetics of PET/nanocomposites, PEGMA and s-PP, it was reported that the Tobin model provides a satisfactory fit when modelling the crystallisation of pure PET [130]. Thus, the applicability of the four kinetic models is profoundly dependent on the polymer system and hence, no kinetic model is shown to be consistently inferior across all polymers.

In contrast to the aforementioned models, which are limited in their ability to describe secondary crystallisation, the Velisaris-Seferis model endeavours to account for the secondary process. Despite this, use of the model in describing the isothermal crystallisation kinetics of polymers is rare. This is somewhat surprising considering the model has proven to be more effective in the modelling of the isothermal crystallisation kinetics of poly(3-hydroxybutyrate-co-3-valerate) (PHB-co-HV) [131], PP and PP/talc composites [132] than both the Avrami and Malkin models.

More recently, Kelly and Jenkins critically evaluated the applicability of the Avrami, Tobin, Malkin, Urbanovici-Segal, Velisaris-Seferis and Hay models to describe the isothermal crystallisation of PHB-co-HV [131]. It was found that the Hay model was most successful in modelling the entire crystallisation process, with the Avrami, Tobin and Malkin models providing a good fit to the experimental data over the primary crystallisation process. As of today, the recently published Hay model is yet to be applied to both polyamides and thermoplastic composites.

5.1.4 Aims and objectives

The following chapter aims to critically evaluate the applicability of the six kinetics models outlined above, providing a quantitative comparison using regression analysis and coefficients of determination (R2), as to which of the models most adequately describes the isothermal crystallisation kinetics of PA66 glass fibre reinforced composites. In addition to statistical modelling, the chapter aims to provide a qualitative discussion on the validity of each of the models in describing the crystallisation kinetics of PA66/GF over an isothermal crystallisation temperature range of 245 to 249 °C. Furthermore, the applicability of the Hay model, never

previously used in describing the kinetics of isothermal crystallisation of thermoplastic composites will be determined.

5.2 Methodology

5.2.1 Materials and sample preparation

Samples were obtained from the pre-impregnated glass fibre reinforced polyamide 66 (PA66/GF) tape and consist of three hole-punched discs (4.8 mm diameter); ensuring that the combined mass of the polyamide matrix was comfortably above the level of sensitivity of the instrument (sample mass = 27.6 ± 1.2 mg).

5.2.2 Isothermal crystallisation kinetics

All isothermal crystallisation kinetic data was obtained using a Mettler Toledo DSC 1 (Greifensee, Switzerland) with Huber TC100 intracooler attachment and nitrogen purge (30 ml/min). Samples were initially heated to above the equilibrium melting temperature (T_m^0) of 300 °C and held for 3 minutes to erase the thermal history of the polyamide and remove any residual stresses from the tape forming process. Furthermore, this enabled the three discs to consolidate into a single sample. The samples were then cooled at a predetermined rate of 70 °C/min to one of five selected crystallisation temperatures: 245 to 249 °C. The chosen cooling rate was assumed to be an optimal compromise between preventing crystallisation on cooling and avoiding a temperature overshoot when approaching the desired crystallisation temperature. Once at T_c samples were held for 240 minutes and heat flow recorded as a function of time.

Generally, in the case of polymers, the geometry of crystal growth is observed to be either two- or three-dimensional [98] and thus, even if nucleation is sporadic (a zeroth order process), the Avrami exponent *n*, should be ≥ 2 [98]. It was shown previously via modelling, that for an Avrami exponent ≥ 2 the longest time period before crystallisation rate returns to zero and the primary crystallisation process perceived to be complete, is three times the half-life of the

primary process [131]. The half-life was determined in a preliminary experiment by subtracting the induction period prior to the onset of crystallisation from the time taken to reach peak minima of the exotherm. In this study it was ensured that the selected isothermal hold time was greater than six times the half-life of the primary crystallisation process. By increasing the time to six half-lives, this effectively guarantees full completion of the primary process and still allows sufficient time for secondary crystallisation to proceed in isolation.

A schematic representation of a crystallisation exotherm is shown in Figure 5.1. Application of kinetic models require that the elapsed time between arriving at the desired crystallisation temperature and the initial deviation from the baseline be disregarded. This so-called induction period is characteristic of instrument settling and the time prior to the onset of nucleation. Kinetic models do not generally account well for this time period and as such, a revised zero-time point from which the model is to be applied must be determined. This time point is commonly referred to as the induction time, t_i. Following the induction period and onset of nucleation, an exothermic peak characteristic of isothermal crystallisation is typically observed. The width and depth of the peaks generally provide a good indication of the rate of crystallisation and the temperature dependence of crystal growth.

The time point at which the exotherm first returns to baseline is traditionally deemed to be the end of the crystallisation process, t_{end} and the final point to which a kinetic model is applied. This approach was applied throughout the analysis, excluding section 5.3.3 when using the Hay model, where an alternative method to defining t_{end} was employed.

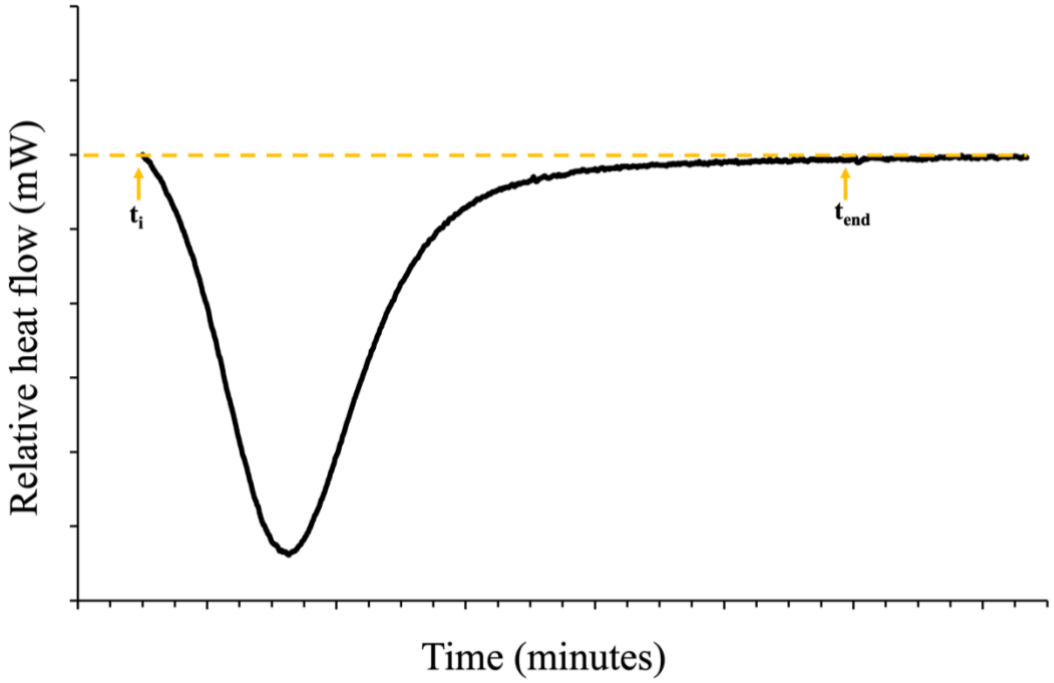

Figure 5.1: Schematic illustration of a crystallisation exotherm showing change in heat flow as a function of time. Labelled are the experimental times representative of the onset of crystallisation (t_i) and end of the crystallisation process (t_{end}) as defined using the traditional methods of analysis.

Crystallisation kinetics describe phase transformation as a function of time. The extent of this transformation is directly proportional to the area beneath both the baseline and the two aforementioned limits (t_i and t_{end}) of a crystallisation exotherm. Calculation of this area is achieved through integration via application of the trapezium rule. The cumulative area at each sequential time point denotes the extent of phase change and if divided by the cumulative area at t_{end} gives a sigmoidal curve indicative of the fractional crystallinity as a function of time (Figure 5.2). From this curve the crystallisation half-life can be more accurately measured and is denoted in Figure 5.2 as $t_{1/2}$.

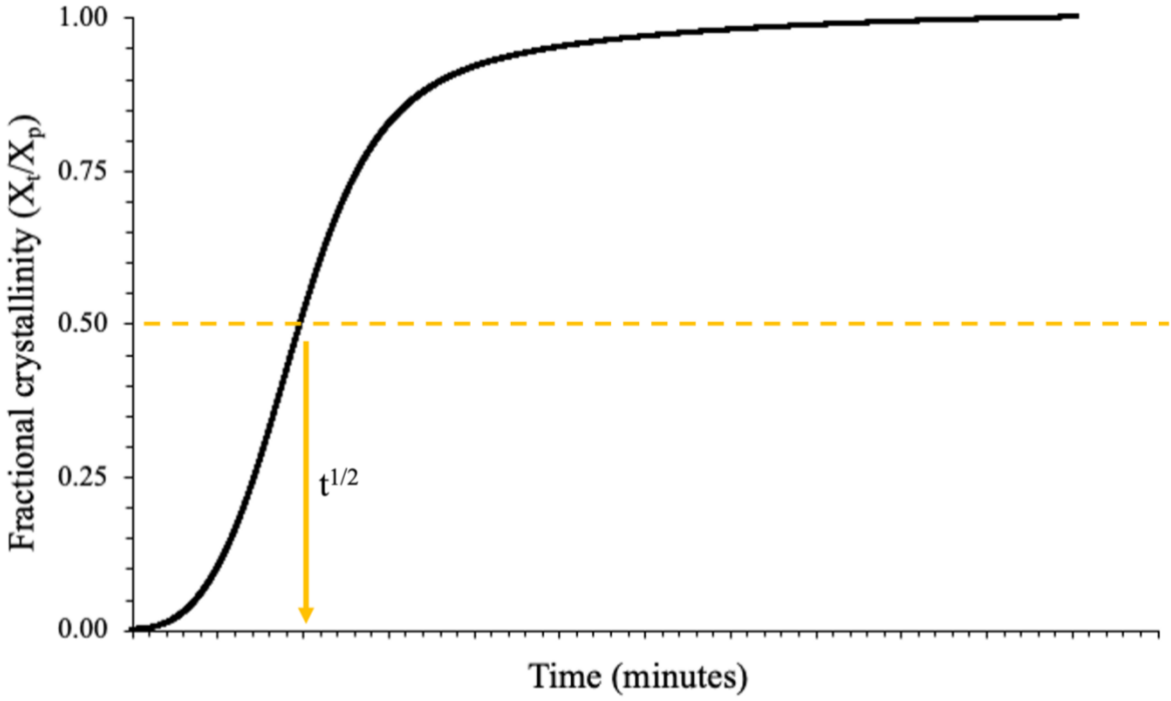

Figure 5.2: Schematic representation of a sigmoidal curve, indicative of the development of fractional crystallinity as a function of time, obtained from integration of the crystallisation exotherm and the subsequent division of the cumulative area at sequential time points by the cumulative area at t_{end}.

After restricting the raw data to time periods between t_i and t_{end}, the isothermal crystallisation kinetics of PA66/GF were quantified using each of the kinetic models outlined in section 5.1.1 (excluding Hay's model). The kinetic parameters of the Avrami and Tobin models were determined using traditional double log plots, from which, the crystallisation kinetic parameters can be determined from the gradient and intercept of the plots, respectively. Additionally, the Malkin kinetic parameters were determined directly from the Avrami parameters. The fit of the models to the experimental data was also determined by the coefficients of determination (R^2) generated. Once defined, the kinetic parameters were then applied as fitting parameters to the models and the resulting traces compared to the experimental data using SPSS software (IBM, Portsmouth, UK) to measure the R^2 values.

Unlike the aforementioned models, where the kinetic parameters are determined through the generation of double log plots, the Urbanovici-Segal and Velisaris-Seferis parameters were defined using the SPSS software (IBM, Portsmouth, UK) and non-linear multi-variable regression analysis. The suitability of each of the Avrami, Tobin and Malkin models was also analysed using this approach to provide a direct comparison.

Kinetic analysis using the Hay model was performed separately and discussed in more detail in section 5.3.3.

5.3 Results and discussion

5.3.1 Qualitative analysis of isothermal crystallisation kinetics using Differential Scanning Calorimetry (DSC)

Crystallisation exotherms recorded using differential scanning calorimetry over an isothermal crystallisation temperature range of 245 to 249 °C are shown in Figure 5.3. All traces were overlaid to enable easier qualitative comparisons and for clarity. Exotherms were limited to the time period between t_i and t_{end} - traditionally believed to be the start and end of the crystallisation process in polymers. As highlighted in section 5.2.2, the width and depth of the exothermic peaks provide a good indication of the rate of crystallisation and the temperature dependence of crystal growth. At crystallisation temperatures close to T_m, where the rate of crystallisation is typically slow, broad, shallow exotherms are frequently observed. Conversely, with decreasing T_c, peaks become profounder and narrower, distinctive of an increasing rate of crystallisation.

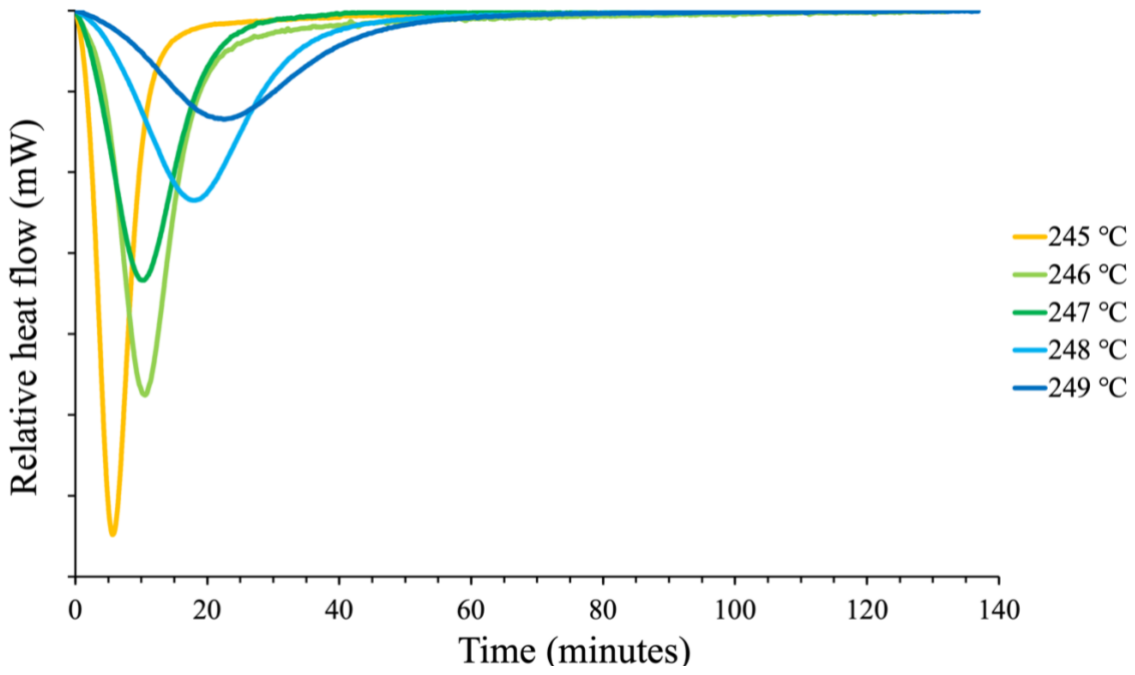

Figure 5.3: Relative heat flow (mW) as a function of time (minutes) recorded using DSC over an isothermal temperature range 245 to 249 °C.

Despite only recording the isothermal crystallisation process over a narrow temperature range, preliminary DSC experiments showed that it would not be possible to increase the T_c range and maintain accuracy in quantifying the crystallisation kinetics of PA66/GF. In broadening the T_c range to isothermal crystallisation temperatures below 245 °C incomplete crystallisation exotherms were recorded. This was a result of missing the onset of crystallisation and was attributed to the rapid crystallisation of PA66. Li et al. [133] showed previously that on cooling from the melt, polyamides with a high amide density, such as PA46 and PA66 crystallise more rapidly and at higher temperatures than polyamides with longer methylene chain segments and lower amide densities [133]. In an attempt to reach the desired T_c prior to the onset of crystallisation, cooling rate was increased. This was unsuccessful and led to an overshoot of the crystallisation temperature and fluctuations in heat flow, which ultimately masked the induction time as the instrument settled.

Additionally, broadening the crystallisation temperature range by increasing T_c to above 249 °C was also impractical. The upper bound of the crystallisation temperature range is close to the onset of melting, and as such, increasing T_c reduces the likelihood of the formation of critically sized nuclei. The rate of crystallisation also reduces significantly with increasing T_c and any slight changes in heat flow can often go undetected by DSC.

Despite the speed at which PA66 crystallises, the isothermal crystallisation temperature range is predominantly limited by the rate of cooling and sensitivity of the instrument. This resulted in a narrow temperature range where a degree of overlap between sequential crystallisation temperatures is observed. It is apparent in Figure 5.4 that despite being closer to the optimum crystallisation rate temperature, the time taken for complete transformation is greater at a crystallisation temperature of 246 °C than at 247 °C.

Crystallisation kinetic models such as the Avrami, Tobin and Malkin models are traditionally applied to isothermal data recorded using DSC over a time period of t_i to t_{end}. However, it has been reported previously that conventional DSC can be insensitive to small changes in crystallinity such as those observed during secondary crystallisation [73,74]. It follows that if such slight transformations can go undetected throughout the secondary process, does DSC possess the sensitivity to register the minuscule changes in heat flow associated with primary nucleation. This raises questions about the validity of the induction period and whether primary nucleation does in fact start at t_i or whether this initial deviation from the baseline comes sometime after the onset of nucleation and is merely the first detection of crystallinity.

Despite the low sensitivity of the instrument and thus, the disputed validity of the induction period, t_i is typically assumed to be the point at which a DSC trace first deviates from the baseline value. Additionally, traditional methods of analysis assume that the crystallisation process ends upon the approximate return of the recorded heat flow to the baseline value. This is open to interpretation and is often determined by the drawing of a tangent from t_i across the isothermal trace, with t_{end} taken as the time point at which the trace first re-meets the tangent (section 5.2.2, Figure 5.1). This method is open to human error as the individual must determine the end of the crystallisation process by eye and as previously discussed, small changes in heat flow over the secondary crystallisation process can be difficult to identify.

Fractional crystallinity (X_t) as a function of time at each isothermal crystallisation temperature was quantified by dividing the cumulative area at sequential time points by the total area of the exotherm at t_{end}. The resulting traces, indicative of the rate of isothermal crystallisation at various temperatures, follow a characteristic sigmoidal shaped curve, typical of phase transformation in polymers (Figure 5.4).

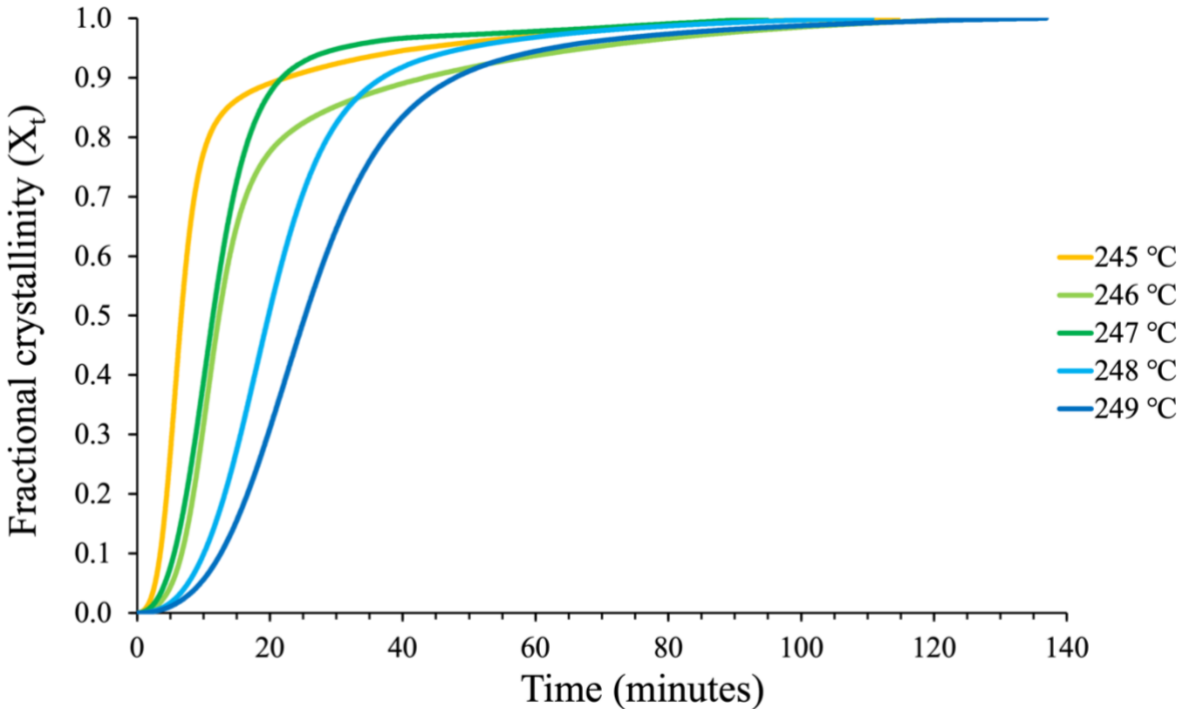

Figure 5.4: Fractional crystallinity (X_t) as a function of time (minutes) calculated from the integration of the isothermal DSC traces over the crystallisation temperature range 245 to 249 °C.

It is evident in Figure 5.3 from the width and depth of the exothermic peaks that crystallisation temperature has a considerable impact on the kinetics of isothermal crystallisation. This is emphasised in Figure 5.4, where the rate of phase transformation is generally observed to increase with decreasing crystallisation temperatures. It is additionally apparent from the plot of fractional crystallinity versus time that the rate of phase transformation differs throughout the stages of the crystallisation process.

The initial rate of crystallisation ($X_t < 0.1$) occurs fastest at lower isothermal crystallisation temperatures. This can be explained by the thermodynamics of nucleation and growth described in Chapter 1.3.1.1. Confined by an upper and lower bound (T_g and T_m), the rate of crystallisation follows a parabolic temperature dependence. At temperatures approaching T_m, the rate of crystallisation is hindered by a reduction in the formation of stable nuclei. As the crystallisation

temperatures used in these experiments cover a narrow range, close to T_m, it is expected that the observed differences in the initial rate of crystallisation is unlikely due to variations in melt viscosity (as expected if T_c was close to T_g), but rather the ease at which nuclei of critical size and stability can be formed with decreasing T_c.

As nuclei of suitable size and stability are formed and crystal growth proceeds, a sharp increase in fractional crystallinity ($0.1 < X_t < 0.7$) over a relatively short time period is observed (Figure 5.4). This sudden rise in crystallinity occurs universally across all crystallisation temperatures; however, crystallisation rate is visibly higher at lower T_c. This is also shown in Figure 5.3 where the width and depth of the exothermic peaks become narrower and more profound, respectively, with decreasing T_c. This increase in crystallisation rate is a result of the T_c being closer to the optimum crystallisation rate temperature between T_g and T_m. A similar trend has also been reported by Zhang et al. [116] and Won et al. [119] in comparable kinetic studies on PA6 and PA66, respectively.

Radial crystal growth persists at a constant rate until the impingement of the growing spherulites. Throughout the impingement process crystallisation rate continuously decreases and a transition period between the primary and secondary crystallisation processes is observed ($0.7 < X_t < 0.9$). The point at which linear boundaries are formed between neighbouring spherulites and crystal growth ceases, is commonly assumed to be the end of the primary crystallisation process with secondary crystallisation then proceeding in isolation. Secondary crystallisation persists despite the observed decrease in crystallisation rate and continues as fractional crystallinity approaches 1. Mechanisms of the secondary process include thickening

of existing lamella and the sporadic formation of miniature crystals in the trapped amorphous regions of spherulites formed during the primary process [73,74].

Half-life of crystallisation is an alternative approach commonly used to quickly compare crystallisation rates across a range of isothermal crystallisation temperatures. Defined as the time taken for crystallisation to reach 50% completion, half-life was observed to decrease with T_c by almost 20 minutes over the 5 °C temperature range (Figure 5.5), emphasising the effect of T_c on the rate of the crystallisation process. It also confirms the earlier observation that the rate of primary crystallisation is highest as T_c decreases and tends towards the optimum crystallisation rate temperature.

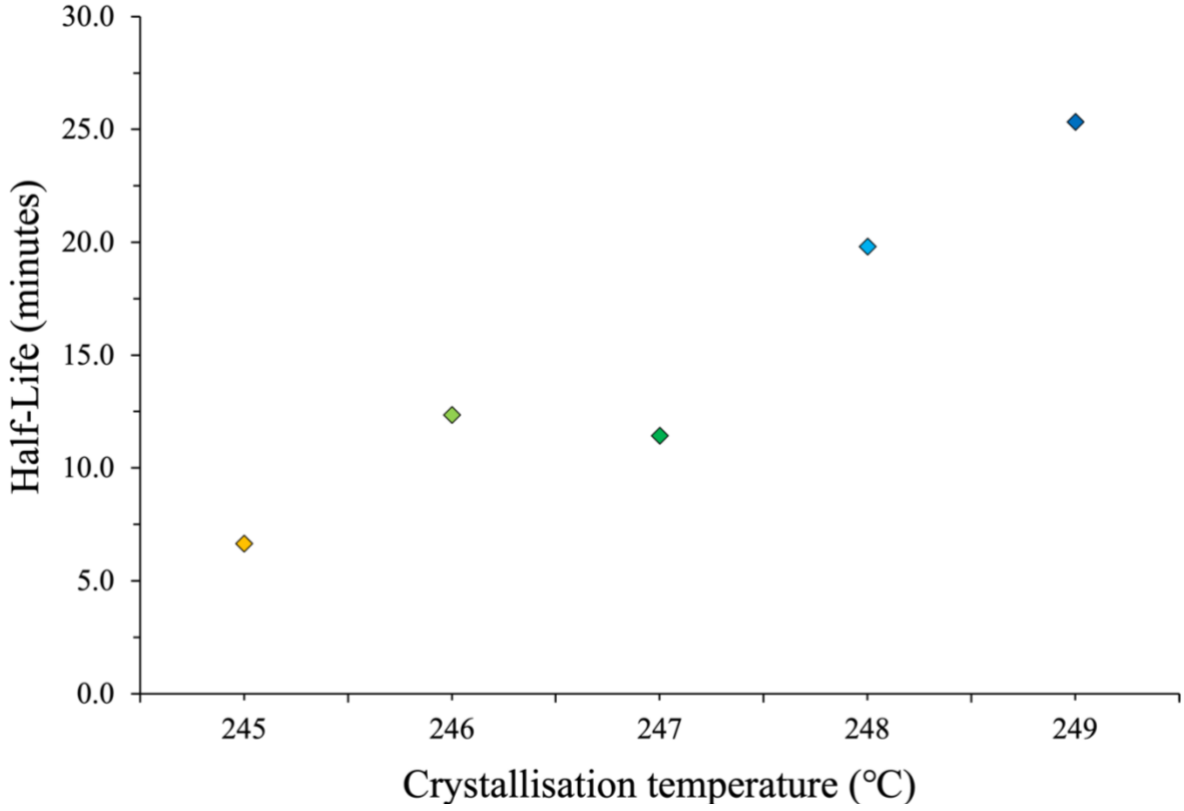

Figure 5.5: Crystallisation half-life (minutes) as a function of temperature, calculated as time taken to reach 50% fractional crystallinity.

5.3.2 Traditional analysis and quantification of the isothermal crystallisation kinetics of PA66/GF using Differential Scanning Calorimetry (DSC)

5.3.2.1 Crystallisation kinetic analysis using the Avrami model

Crystallisation kinetics, including the mechanisms of nucleation and crystal growth, can be described by applying the Avrami equation (Equation 5-1) and by the creation of the standard Avrami double log plots (Figure 5.6) using,

$$\ln(-\ln(1 - X_t)) = \ln k_a + n_a \ln(t)$$

Equation 5-12

Where X_t is fractional crystallinity at time t, n_a is the Avrami exponent and k_a is the Avrami crystallisation rate constant. As the Avrami model inadequately describes the latter stages of crystallisation and is only truly applicable to the primary process (section 5.1.1.1.1), where the crystallisation rate is constant, the experimental data must be limited. Data presented in Figure 5.6 was restricted to the fractional crystallinity range 0.1 to 0.5. This ensured the outer limits of the crystallisation process, namely nucleation and secondary crystallisation, where the rate of transformation is inconsistent, were removed. Equation 5-12 is shown to provide good linearity in the fit of the model to the experimental data over the restricted X_t range, emphasised by coefficient of determination (R^2) values greater than 0.9994.

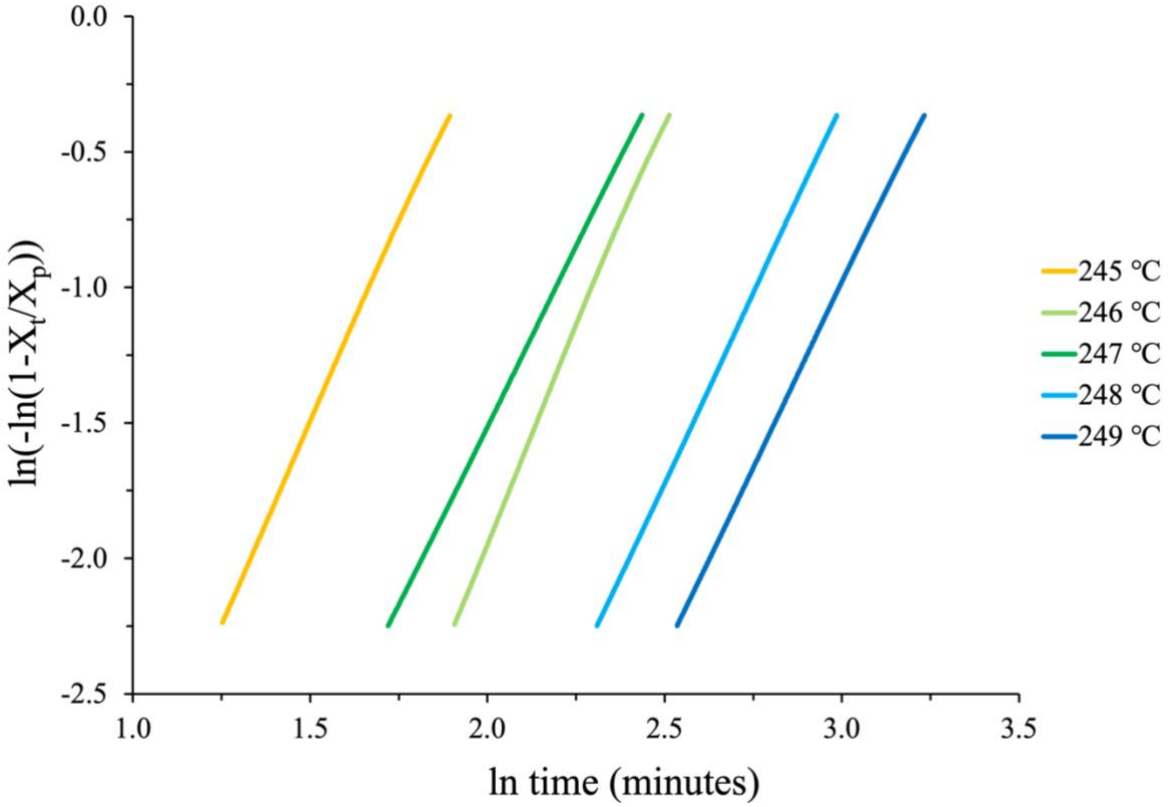

Figure 5.6: Avrami plot of fractional crystallinity ($0.1 < X_t < 0.5$) over the isothermal crystallisation temperature range of 245 to 249 °C.

Avrami exponents, n_a and crystallisation rate constants, k_a can be determined from the gradient and intercept of the traces, respectively. As shown in Table 5.2 and discussed in section 5.1.1.1.1, Avrami exponents often return non-integer *n* values. This can make the prediction of the mechanisms of nucleation difficult. Despite this, all values of n_a recorded over the chosen crystallisation temperature range tended to 3.0. This is consistent with observations made by Neugebauer et al. [123] and Cui et al. [120] on studies using polyamide samples and implies that nucleation is instantaneous with three-dimensional crystal growth. Conversely, it could be disputed that the non-integer n_a values signify a combination of both instantaneous and sporadic nucleation [102]. This would not be beyond reasoning in thermoplastic composites where

sporadic nucleation transpires in the matrix and the reduced surface energy of the reinforcement fibres promote instantaneous nucleation.

Table 5.2: Avrami crystallisation kinetic parameters and coefficients of determination (R^2) derived from double log plots over the isothermal crystallisation temperature range of 245 to 249 °C.

T_c (°C)	$t^{1/2}$ (min)	n_a	k_a x10^{-3} (min^{-n})	R^2
245	6.7	2.94	2.72	0.9996
246	12.4	3.14	0.27	0.9994
247	11.4	2.65	1.10	1.0000
248	19.8	2.80	0.16	1.0000
249	25.3	2.72	0.11	0.9999

With exception to the Avrami crystallisation rate constant at T_c = 246 °C, k_a decreases with increasing isothermal crystallisation temperature (Table 5.2). This follows the general trend observed with crystallisation half-life, whereby the rate of crystallisation is shown to continuously reduce with increasing T_c towards T_m.

5.3.2.2 Crystallisation kinetic analysis using the Tobin model

Tobin modified the Avrami equation in an attempt to better define the latter stages of crystallisation and account for spherulite impingement (section 5.1.1.2). Comparable to the Avrami model, the Tobin exponent, n_t and crystallisation rate constant, k_t are determined from the gradient and intercept of a double log plot (Figure 5.7). Experimental data was again limited to a period in which the rate of phase transformation was consistent ($0.2 < X_t < 0.55$). The

values of n_t and k_t are reported in Table 5.3 along with the coefficients of determination, which show the Tobin model to provide a good fit to the experimental data over this fractional crystallinity range.

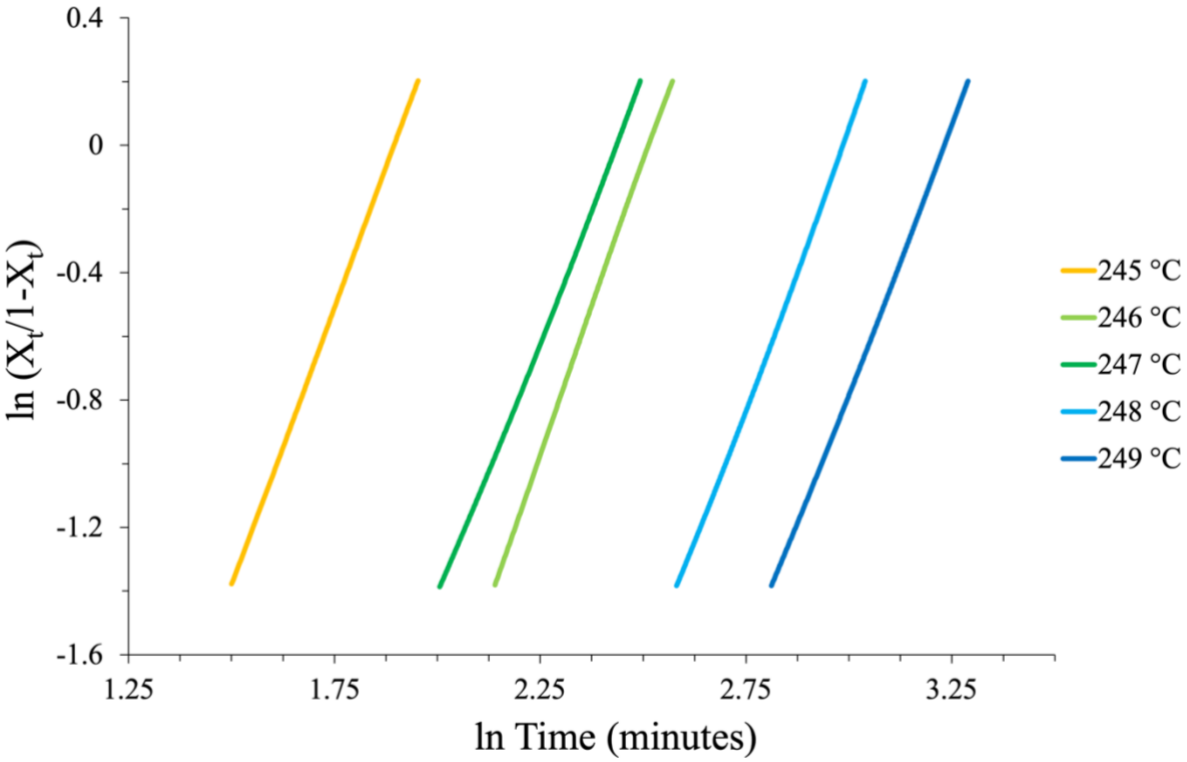

Figure 5.7: Tobin plot of fractional crystallinity ($0.2 < X_t < 0.55$) over the isothermal crystallisation temperature range of 245 to 249 °C.

Table 5.3: Tobin crystallisation kinetic parameters and coefficients of determination (R^2) derived from double log plots over the isothermal crystallisation temperature range of 245 to 249 °C.

T_c (°C)	$t^{1/2}$ (min)	n_t	$k_t \times 10^{-3}$ (min^{-n})	R^2
245	6.7	3.51	1.29	1.0000
246	12.4	3.70	0.09	0.9999
247	11.4	3.27	0.34	0.9994
248	19.8	3.47	0.03	0.9994
249	25.3	3.33	0.02	0.9997

Despite a similar physical meaning to the Avrami exponent, the value of n_t need not be an integer and was calculated to be between 3.27 and 3.70 for the crystallisation temperature range studied. By comparison, n_t was consistently greater than n_a over the T_c range, where on average $n_t \approx n_a + 0.6$. This observation is in agreement with previously published results on the comparison of the Avrami and Tobin models [102,113].

The values of the recorded Tobin crystallisation rate constants follow the same tendency to decrease with decreasing crystallisation temperature as k_a. Additionally, the goodness of fit of the Tobin model to the experimental data over the restricted fractional crystallinity range is very similar to that observed using the Avrami model, with R^2 greater than 0.9994 recorded across all crystallisation temperatures.

5.3.2.3 Crystallisation kinetic analysis using the Malkin model

Malkin's theory assumes that the overall rate of crystallisation equates to the summation of the rate of primary nuclei formation and subsequent crystal growth (section 5.1.1.3). Unlike the

models proposed by Avrami and Tobin, the Malkin exponent, C_0 and crystallisation rate constant, C_1 cannot be determined directly from double log plots, and without the use of curve fitting, can be derived from the previously obtained Avrami parameters. Equation 5-13 and Equation 5-14 were used to calculate the values of C_0 and C_1 from the Avrami exponents and rate constants, respectively (Table 5.4).

$$C_0 = 4^{n_a} - 4$$

Equation 5-13

$$C_1 = \ln(4^{n_a} - 2) \left(\frac{k_a}{\ln(2)}\right)^{1/n_a}$$

Equation 5-14

As C_0 and C_1 are derived directly from the prior Avrami analysis, it follows that both parameters should observe a similar temperature dependence and physical meaning to that of the Avrami parameters, n_a and k_a.

Table 5.4: Malkin crystallisation kinetic parameters derived from Avrami exponents and rate constants over the isothermal crystallisation temperature range of 245 to 249 °C.

T_c (°C)	C_0	C_1
245	55.0	0.61
246	74.2	0.36
247	35.3	0.32
248	44.6	0.19
249	39.4	0.15

5.3.2.4 Non-linear regression analysis of the Avrami, Tobin and Malkin kinetic parameters

Non-linear regression analysis using IBM SPSS software was used to determine which of the Avrami, Tobin and Malkin models best describes the crystallisation kinetics of PA66/GF over the full fractional crystallinity range at isothermal crystallisation temperatures of 245 to 249 °C. The SPSS software uses the pre-determined kinetic parameters specified by each of the models (Table 5.2 – Table 5.4) as 'fitting parameters' to measure the coefficient of determination (R^2) and verify the fit of the models to the experimental data. To enable a direct comparison to later models described in this chapter, the experimental data was first converted from *relative* fractional crystallinity, where X_t is a comparative value between 0 and 1, to *actual* fractional crystallinity, where X_t now corresponds to the real crystalline volume fraction of the sample - prior to performing the SPSS analysis. The goodness of the fit using these parameters is shown in Figure 5.8 for an isothermal crystallisation temperature of 248 °C and quantitatively in Table 5.5 for the entire T_c range.

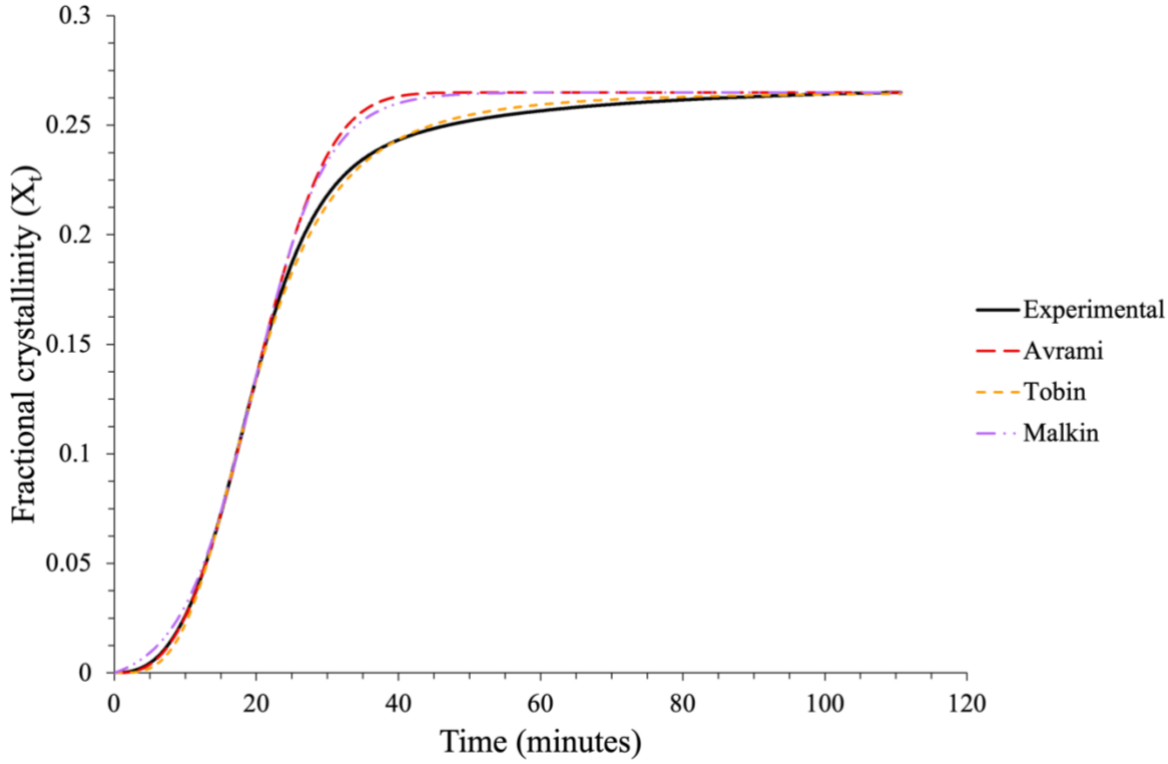

Figure 5.8: Comparison of the curve fitting of the Avrami, Tobin and Malkin models to the experimental data using fitting parameters predetermined from double log plots at an isothermal crystallisation temperature of 248 °C.

Table 5.5: Comparison of the coefficients of determination (R^2) of the Avrami, Tobin and Malkin models as calculated from curve fitting using SPSS software.

T_c (°C)	Avrami	Tobin	Malkin
245	0.919	0.956	0.924
246	0.901	0.948	0.908
247	0.985	0.998	0.987
248	0.987	0.999	0.990
249	0.987	1.000	0.990

As observed in Figure 5.8, the Tobin model provides the best overall fit to the experimental data across the entire crystallisation process. The curve fitting of the Avrami and Malkin models is similar throughout the transformation process and despite both models providing a good representation of the primary process, neither equation is adequate at modelling secondary crystallisation. These observations are further emphasised in Table 5.5 where it is shown that the Tobin model generates the highest R^2 values when the models are applied to the full crystallisation process. This is expected, as unlike the Avrami and Malkin models, the Tobin model is designed to account for spherulite impingement and thus, better describes the secondary crystallisation process. Though the Avrami model provides a good fit to the experimental data over the initial regions of the trace, where the rate of crystallisation is relatively consistent, when applied to the full fractional crystallinity range, the model no longer provides a good fit to the data, as reflected in the R^2 values recorded.

The applicability of the models to describe the isothermal crystallisation of PA66/GF was further analysed using the standard error of the regression, *S*.

$$S = \sqrt{\frac{\sum(X_t - X'_t)^2}{d-2}}$$

Equation 5-15

Where X_t is the experimental fractional crystallinity, X'_t is the modelled fractional crystallinity and d is the number of data points. Unlike the curve fitting, which was applied to the experimental data across the entire crystallisation process, the standard error of the regression is applied separately to four distinct stages of the transformation. These four regions are shown

schematically in Figure 5.9 and represent the initial nucleation and growth phase, primary crystallisation at a constant rate, the transition period between the primary and secondary processes, and secondary crystallisation. Each follows a sequential stage of the isothermal crystallisation process, whereby the rate of phase transformation varies from stage to stage. The boundaries of each region between which the standard error of the regression was measured were predetermined from the experimental traces at each individual crystallisation temperature. The smaller the value of *S*, the better the fit of the model to the experimental data.

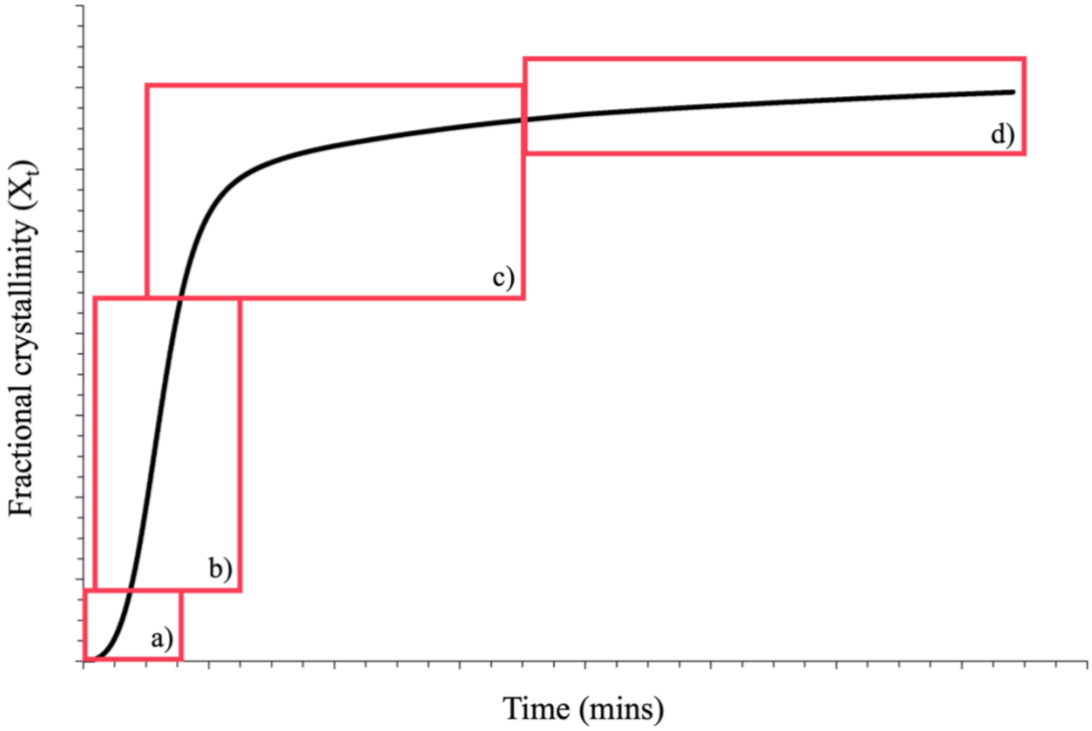

Figure 5.9: Schematic representation of the four stages of the crystallisation process namely, a) initial nucleation, b) primary crystallisation, c) transition period and d) secondary crystallisation, for which the standard error of the regression of each region was calculated.

Table 5.6: Calculated standard error of the regression of the Avrami, Tobin and Malkin equations over the four stages of crystallisation; a) initial, b) primary, c) transition and d) secondary.

a)

Tc (°C)	Initial		
	Avrami	Tobin	Malkin
245	0.0004	0.0022	0.0057
246	0.0009	0.0021	0.0042
247	0.0004	0.0024	0.0040
248	0.0005	0.0027	0.0042
249	0.0003	0.0019	0.0034

b)

Tc (°C)	Primary		
	Avrami	Tobin	Malkin
245	0.0009	0.0001	0.0007
246	0.0010	0.0003	0.0009
247	0.0009	0.0008	0.0010
248	0.0003	0.0005	0.0004
249	0.0003	0.0003	0.0004

c)

Tc (°C)	Transition		
	Avrami	Tobin	Malkin
245	0.0443	0.0273	0.0421
246	0.0500	0.0305	0.0472
247	0.0153	0.0028	0.0134
248	0.0182	0.0029	0.0154
249	0.0145	0.0028	0.0124

d)

Tc (°C)	Secondary		
	Avrami	Tobin	Malkin
245	0.0072	0.0071	0.0072
246	0.0088	0.0085	0.0088
247	0.0034	0.0027	0.0034
248	0.0037	0.0014	0.0037
249	0.0045	0.0007	0.0043

The standard error of the regression calculated across all four stages of the crystallisation process for each of the Avrami, Tobin and Malkin models is shown in Table 5.6. The initial increase in fractional crystallinity with time, representative of the onset of nucleation and subsequent crystal growth, is best described by the Avrami equation. The values of *S* over this initial stage are shown to be lower for the Avrami model than the Tobin model despite the non-linear regression analysis indicating that the Tobin equation provides the best overall fit to the transformation process. Both the Avrami and Tobin models provide a better fit to the experimental data than the Malkin model over this region.

As shown by the comparably small values of *S*, all three kinetic models provide an excellent fit to the experimental data over the primary crystallisation process where the rate of transformation is consistent. This is expected as all three models have been developed to describe the crystallisation kinetics throughout the primary process.

On impingement of the growing spherulites throughout the transition period between the primary and secondary crystallisation processes, the Tobin model is shown to outperform both the Avrami and Malkin models across all crystallisation temperatures. This is in good agreement with the observations made from Figure 5.8 and confirms that, by consideration of the impingement process, the Tobin model can provide a better fit to the experimental data over the transition period than both the Avrami and Malkin models.

Over the final stage of the transformation process, characteristic of secondary crystallisation, the standard error of the regression is comparable between both the Avrami and Malkin models. In addition, the error associated with the Tobin model is similar to the other two models over the crystallisation temperature range, $T_c \leq 246$ °C, where values of $S < 0.01$ were recorded. As crystallisation temperature is increased the similarity between the three models ceases and the

standard error of the regression of the Tobin model continues to fall. Above $T_c \geq 247$ °C, the Tobin model provides the best fit to the experimental data over the secondary crystallisation region.

5.3.2.4.1 Conclusions

In summary, combining the analysis of the coefficients of determination and the standard error of the regression to compare the fit of the models to the experimental data using SPSS software and fitting parameters predetermined by traditional methods, the Tobin equation is shown to provide a better fit than both the Avrami and Malkin equations. This inference contradicts multiple studies within the literature, whereby when qualitatively evaluating the Avrami, Tobin and Malkin models, most authors conclude that the Tobin model is less suitable at describing the isothermal crystallisation kinetics of polymers than both the Avrami and Malkin models [102,113,126,128–130].

5.3.2.5 Non-linear multi-variable regression analysis of the isothermal crystallisation of PA66/GF

In addition to curve fitting with predetermined kinetic parameters, the SPSS software can be used to model the experimental data directly using non-linear multi-variable regression analysis. Modelling the data with no fixed parameters, SPSS software predicts the best fit of the respective kinetic models to the experimental data, whilst simultaneously deriving the kinetic parameters. Though considerably quicker than determining the kinetic parameters using traditional methods, it is important to note that modelling using non-linear multi-variable regression analysis does not necessarily result in an improved fit across all regions of the trace due to the software attempting to reduce the value of error across the entire data set.

Modelling of the Avrami, Tobin and Malkin equations using non-linear multi-variable regression analysis at a crystallisation temperature of 248 °C is shown in Figure 5.10 – Figure 5.12, along with the predicted kinetic parameters and coefficients of determination across all crystallisation temperatures in Table 5.7 – Table 5.9.

As calculated by the greater coefficients of determination (R^2), modelling of the Avrami equation using non-linear multi-variable regression analysis is predicted to provide a better fit to the experimental data than direct curve fitting of the equation using predetermined parameters. This is true across all isothermal crystallisation temperatures, where the closer the value of R^2 to 1.0 the better the predicted fit of the model to the experimental data. However, despite implying an improved fit across the whole transformation process, it is apparent from Figure 5.10 that open parameter modelling of the Avrami equation does not give an accurate representation of the data throughout all stages of the crystallisation process. In addition, the modelled Avrami exponent, n_a^* was consistently lower than n_a, with values ranging from 1.33

to 2.23. According to the physical meaning of n, the predicted values of n_a^* suggest an alternate mechanism of nucleation compared to that of the Avrami exponent derived using traditional methods. An n value of approximately 2.0 infers that the geometry of crystal growth is likely one- or two-dimensional depending on the mechanism of nucleation (instantaneous or sporadic). This is unlikely considering the volume and geometry of the samples used in this study, with n values ≤ 2.0 usually only obtained when the volume of the sample is constrained. The modelled crystallisation rate constant, k_a^* is consistently greater than k_a over the crystallisation temperature range and is observed to decrease with increasing T_c.

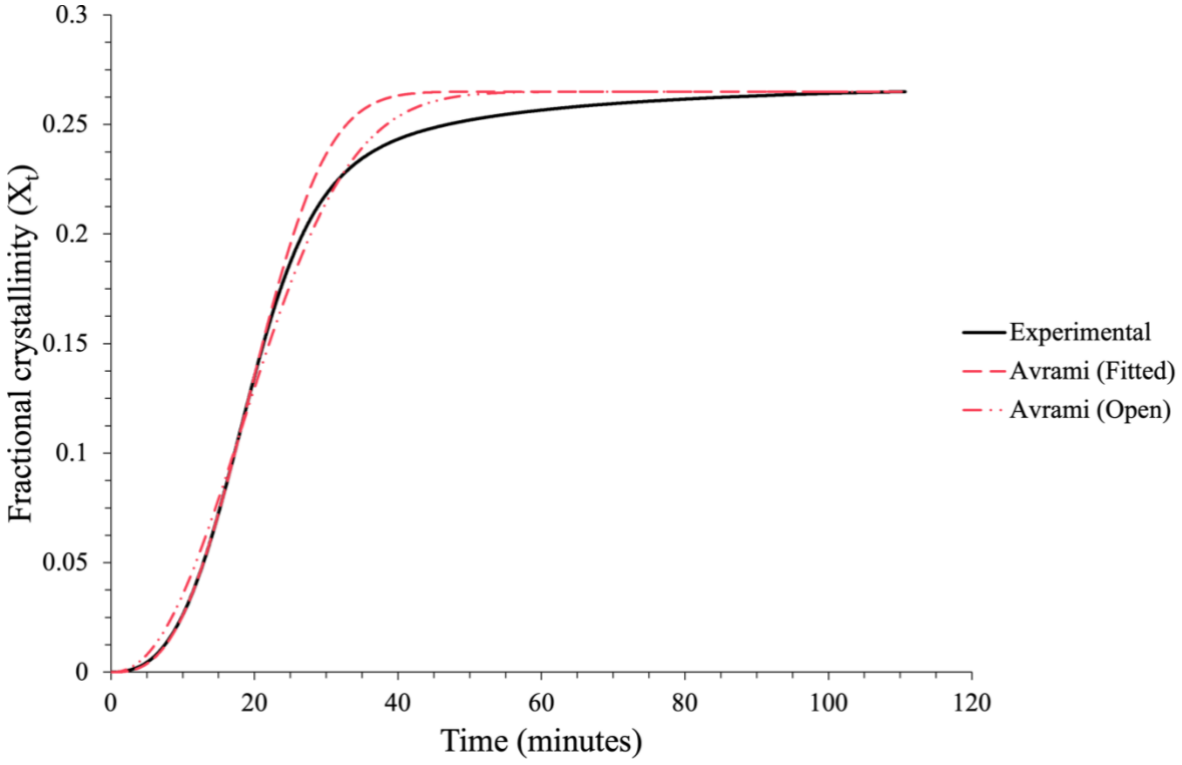

Figure 5.10: Comparison between curve fitting using predetermined kinetic parameters and non-linear multi-variable regression analysis modelling of the Avrami equation to the isothermal crystallisation data recorded at a T_c of 248 °C.

Table 5.7: Avrami parameters and coefficients of determination calculated by the modelling of fitting parameters, where X_t was limited to the linear region, and non-linear multi-variable regression analysis (*) over the crystallisation temperature range 245 to 249 °C.

T_c (°C)	Fitted Parameters			Open parameters		
	n_a	k_a (min^{-n})	R^2	n_a^*	k_a^* (min^{-n})	R^2
245	2.94	0.00272	0.919	1.45	0.04038	0.951
246	3.14	0.00027	0.901	1.33	0.02200	0.958
247	2.65	0.00110	0.985	2.11	0.00391	0.991
248	2.80	0.00016	0.987	2.23	0.00085	0.994
249	2.72	0.00011	0.987	2.15	0.00063	0.995

At isothermal crystallisation temperatures ≥ 247 °C the Tobin equation is shown to provide a very good fit to the experimental data independent of the modelling procedure used (fitted or open parameter). This is emphasised in Figure 5.11, where both traces are observed to predict an accurate representation of the experimental data over the whole crystallisation process at T_c = 248 °C, with calculated R^2 values greater than 0.998. Over this temperature range ($T_c \geq$ 247 °C), the Tobin exponents, rate constants and coefficients of determination are equivalent irrespective of the modelling method used to derive them. However, as T_c is reduced to temperatures below 247 °C, the equivalence of the Tobin parameters derived from fitted parameter and open parameter modelling ceases. Comparisons between the two sets of parameters and resulting R^2 values show a similar trend to that observed with Avrami, that is, n_t^* decreases with crystallisation temperature and is predicted to be lower than n_t, with the crystallisation rate constants following the inverse relationship. The fit of the traces to the experimental data over this temperature range ($T_c \leq$ 246 °C) is observed to improve when using

non-linear multi-variable regression analysis, as emphasised by the greater R^2 values (Table 5.8).

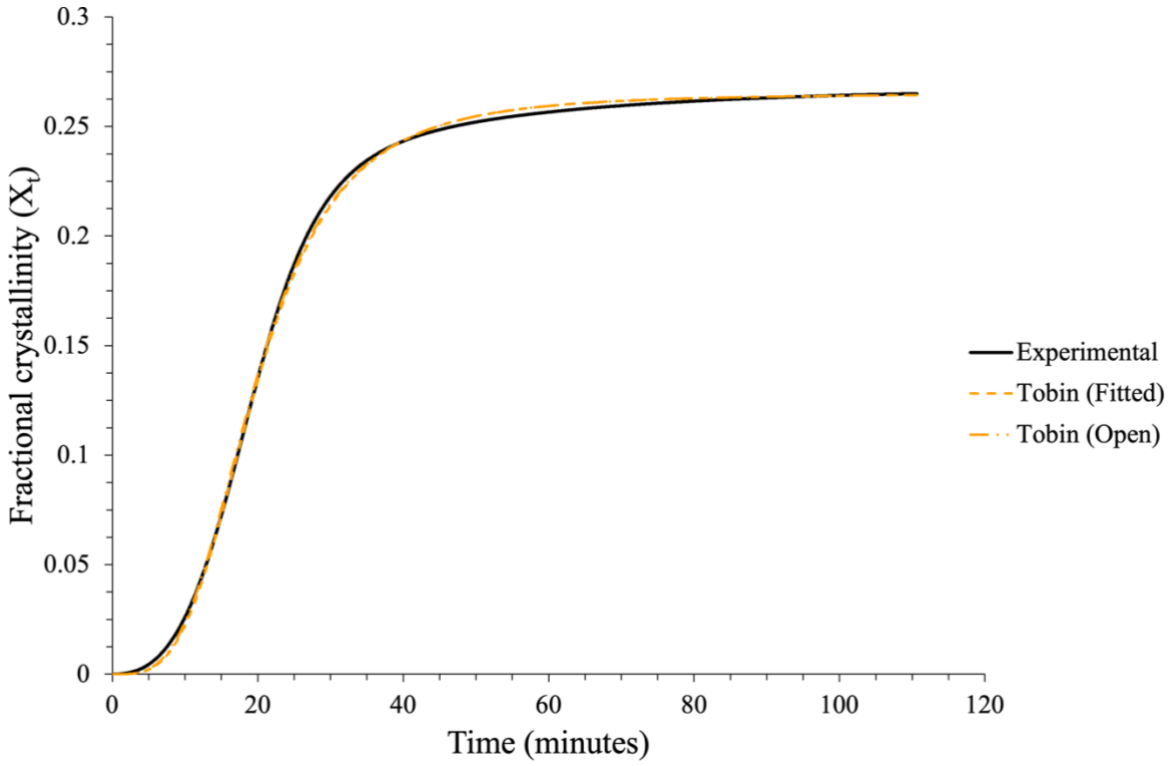

Figure 5.11: Comparison between curve fitting using predetermined kinetic parameters and non-linear multi-variable regression analysis modelling of the Tobin equation to the isothermal crystallisation data recorded at a T_c of 248 °C.

Table 5.8: Tobin parameters and coefficients of determination calculated by the modelling of fitting parameters, where X_t was limited to the linear region, and non-linear multi-variable regression analysis (*) over the crystallisation temperature range 245 to 249 °C.

T_c (°C)	Fitted Parameters			Open parameters		
	n_t	k_t (min^{-n})	R^2	n_t^*	k_t^* (min^{-n})	R^2
245	3.51	0.00129	0.956	2.16	0.01606	0.980
246	3.70	0.00009	0.948	2.20	0.00355	0.985
247	3.27	0.00034	0.998	3.17	0.00046	0.998
248	3.47	0.00003	0.999	3.42	0.00004	0.999
249	3.33	0.00002	1.000	3.35	0.00002	1.000

The disparities between the Malkin kinetic parameters calculated from non-linear multi-variable regression analysis and those predicted from modelling of the fitting parameters follow a similar trend to that observed in the Avrami analysis. The modelled Malkin exponent C_0^* generally decreases with crystallisation temperature (Table 5.9) and is comprehensively smaller than C_0 throughout the T_c range with average values of 13.07 and 49.69, respectively. Compared to the exponent values, the crystallisation rate constants were far more comparable. The coefficients of determination generated from open parameter modelling of the Malkin equation to the experimental data show R^2 to increase with crystallisation temperature and predict a marginally better fit to the data than the predetermined Malkin parameters.

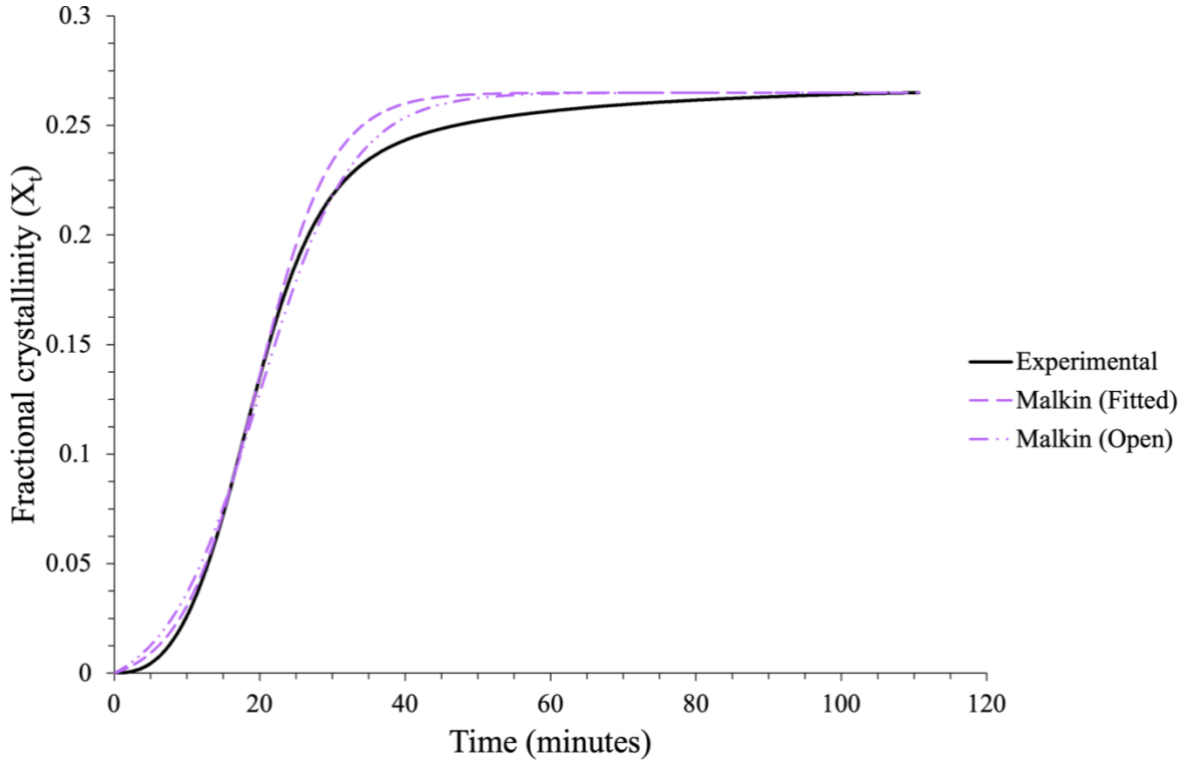

Figure 5.12: Comparison between curve fitting using predetermined kinetic parameters and non-linear multi-variable regression analysis modelling of the Malkin equation to the isothermal crystallisation data recorded at a T_c of 248 °C.

Table 5.9: Malkin parameters and coefficients of determination calculated by the modelling of fitting parameters and non-linear multi-variable regression analysis (*) over the crystallisation temperature range 245 to 249 °C.

T_c (°C)	Fitted Parameters			Open parameters		
	C_0	C_1	R^2	C_0^*	C_1^*	R^2
245	54.96	0.614	0.924	3.80	0.246	0.949
246	74.19	0.356	0.908	1.91	0.101	0.955
247	35.29	0.318	0.987	17.67	0.252	0.991
248	44.62	0.194	0.990	22.59	0.157	0.994
249	39.39	0.148	0.990	19.39	0.117	0.995

5.3.2.5.1 Modelling of the experimental data using the Urbanovici-Segal equation

Fitted directly using non-linear multi-variable regression analysis, the Urbanovici-Segal equation is essentially a generalisation of the Avrami equation where the Urbanovici-Segal exponent, n_{us} and crystallisation rate constant, k_{us} share the same physical meaning as the Avrami kinetic parameters n_a and k_a [108]. The principal difference between the two models is the addition of a third fitting parameter, r to the Urbanovici-Segal model. When r tends to 1 the two equations are equivalent, leading to the postulation that r is merely a fitting factor used to determine the similarity in modelling of Urbanovici-Segal and Avrami equations [113].

Modelling of the Urbanovici-Segal equation to the experimental data over all isothermal crystallisation temperatures is shown in Figure 5.13. The traces display a good fit of the equation to the data, emphasised by R^2 values greater than 0.992 across all crystallisation temperatures (Table 5.10). Comparable to the Avrami rate constant, k_{us} generally increases as T_c is reduced. It follows that, on cooling from the melt, isothermal crystallisation rates increase as T_c decreases and approaches the optimal crystallisation rate temperature.

The Urbanovici-Segal exponent was consistently higher than n_a across all crystallisation temperatures, with recorded values ranging from 3.37 to 4.0. Based on the understanding that n_{us} and n_a have an identical physical meaning, it is assumed that the Urbanovici-Segal model expects an alternative mechanism of nucleation than that predicted from the Avrami analysis. The denotations of the value of n reported in Table 5.1, follows that as n_{us} is consistently greater than 3.0, the geometry of crystal growth must be three-dimensional. When n_{us} has an integer value equal to 4.0 (T_c = 246 °C), the mechanism of nucleation is assumed to be completely sporadic. However, non-integer values recorded across the remaining four crystallisation temperatures could suggest a combination of both instantaneous and sporadic nucleation. Simultaneous nucleation via the two mechanisms has previously been proposed when

attempting to explain the non-integer *n* values commonly derived when using the Avrami equation [102]. It seems plausible that both nucleation mechanisms are present in the crystallisation of polymer matrix composites, where sporadic nucleation occurs in the bulk matrix and instantaneous nucleation off the surface of the reinforcement fibres.

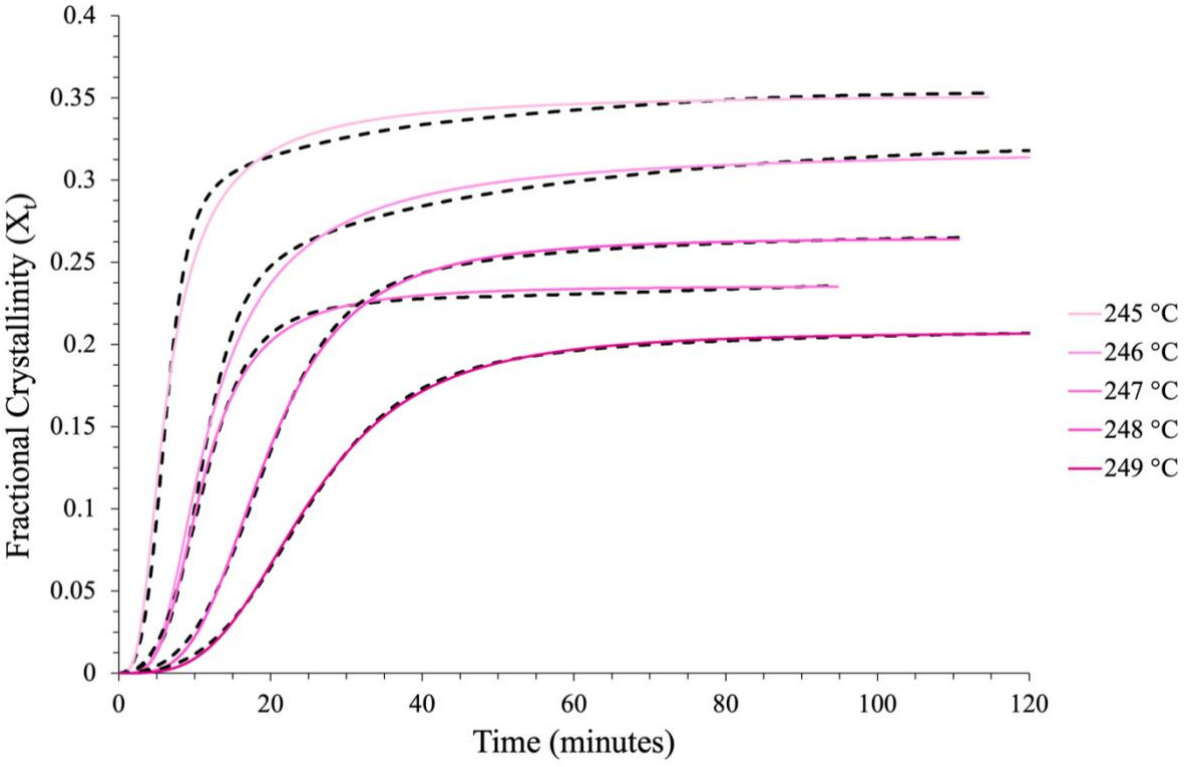

Figure 5.13: Predicted fits of the Urbanovici-Segal equation (*pink*) to the isothermal data (*dashed*) using non-linear multi-variable regression analysis over a crystallisation temperature range 245 to 249 °C.

Table 5.10: Predicted Urbanovici-Segal kinetic parameters derived using SPSS software and non-linear multi-variable regression analysis over a crystallisation temperature range 245 to 249 °C.

T_c (°C)	n_{us}	k_{us} (min^{-n})	r	R^2
245	3.52	0.00223	3.30	0.992
246	4.00	0.00008	3.62	0.995
247	3.80	0.00013	2.47	0.998
248	3.64	0.00002	2.15	1.000
249	3.37	0.00002	2.02	1.000

In a study on poly(L-lactic acid) Urbanovici et al. concluded that whilst the Avrami equation was satisfactory at describing the kinetics of isothermal crystallisation, it was not as accurate as the Urbanovici-Segal equation at modelling the experimental data [109]. It was postulated that the differences between the two models was attributed to the effect of the third fitting parameter, *r* [109]. Similar observations were reported by Supaphol in studies on polypropylene [113], where it was shown that when *r* satisfies the condition $r > 1$, the larger the value of *r*, the greater the discrepancy between the two kinetic models. The results of this study are in agreement with the aforementioned literature. The value of *r* is repeatedly greater than 1.0 ranging from 2.02 at 249 °C to 3.62 at 246 °C. This infers that there is little comparability between the predicted fit of the Urbanovici-Segal and Avrami models.

5.3.2.5.2 Modelling of the experimental data using the Velisaris-Seferis equations

Following the detection of two competing crystallisation processes whilst using the conventional Avrami analysis, Velisaris and Seferis devised a new analytical model to quantify the crystallisation kinetics of PEEK [110]. The two processes were attributed to the primary and secondary stages of crystallisation. The newly proposed model comprises two separate equations; the first, in parallel, where the primary and secondary processes are considered to occur simultaneously and the second, in series, where it is believed that secondary crystallisation only commences upon completion of the primary process (section 5.1.2.1). It is worth noting that in the case of the parallel model, secondary crystallisation can only occur following the onset of primary crystallisation.

When modelled using non-linear multi-variable regression analysis, both the parallel and series equations provide a good fit to the isothermal data throughout the crystallisation process and across all temperatures (Figure 5.14 and Figure 5.15). This is emphasised in Table 5.11 and Table 5.12, where excluding an anomaly at 245 °C (Table 5.12), both the parallel and series equations generate R^2 values greater than 0.997. The predicted kinetic parameters of each equation are also listed in Table 5.11 and Table 5.12.

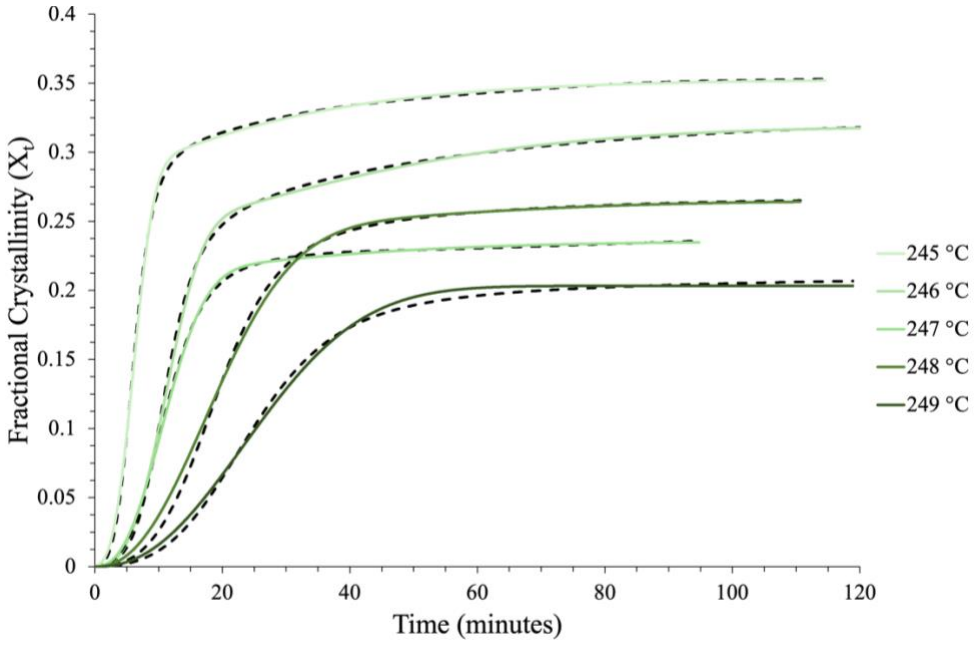

Figure 5.14: Predicted fits of the Velisaris-Seferis parallel equation (*green*) to the isothermal data (*dashed*) using non-linear multi-variable regression analysis over a crystallisation temperature range 245 to 249 °C.

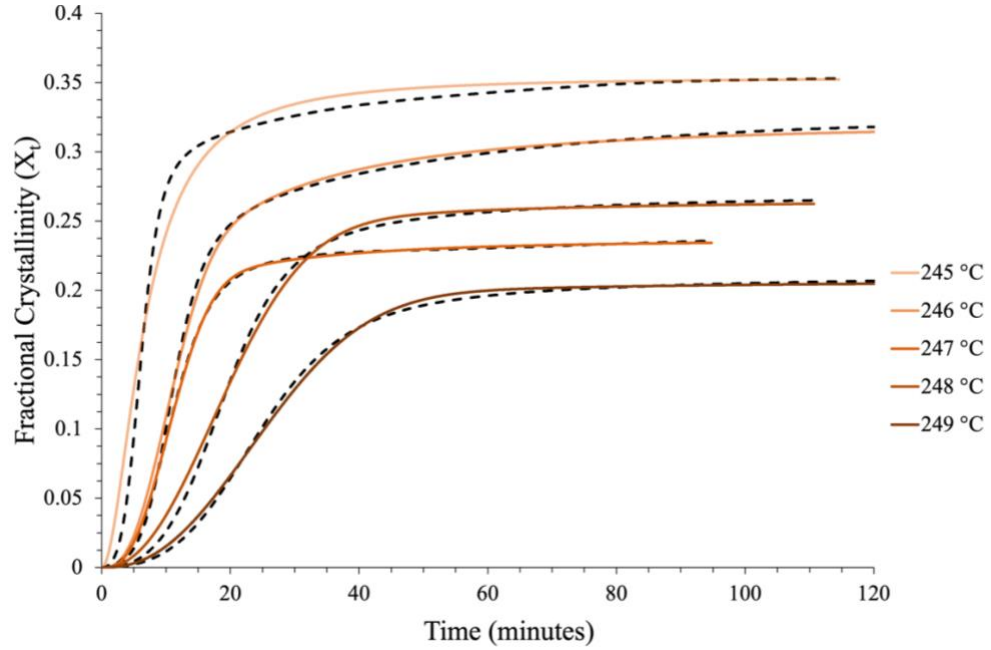

Figure 5.15: Predicted fits of the Velisaris-Seferis series equation (*brown*) to the isothermal data (*dashed*) using non-linear multi-variable regression analysis over a crystallisation temperature range 245 to 249 °C.

Table 5.11: Predicted Velisaris-Seferis kinetic parameters derived using the parallel Velisaris-Seferis equation and non-linear multi-variable regression analysis over a crystallisation temperature range 245 to 249 °C.

T_c (°C)	w_p	w_s	z_p (min^{-n})	z_s (min^{-n})	n_{vs}	m_{vs}	R^2
245	0.77	0.23	0.0034	0.0266	2.92	1.08	0.999
246	0.74	0.26	0.0005	0.0035	2.98	1.47	0.999
247	0.87	0.13	0.0014	0.0102	2.58	1.28	1.000
248	0.91	0.09	0.0008	0.0005	2.29	1.86	0.998
249	0.98	0.02	0.0004	0.0000	2.28	0.06	0.997

Table 5.12: Predicted Velisaris-Seferis kinetic parameters derived using the series Velisaris-Seferis equation and non-linear multi-variable regression analysis over a crystallisation temperature range 245 to 249 °C.

T_c (°C)	w_p	w_s	z_p (min^{-n})	z_s (min^{-n})	n_{vs}	m_{vs}	R^2
245	0.01	0.99	0.0002	1.6984	1.89	4.25	0.976
246	0.93	0.07	0.0008	0.0079	2.81	1.13	0.997
247	0.87	0.13	0.0008	0.0595	2.78	0.87	1.000
248	0.98	0.02	0.0008	0.0032	2.28	1.23	0.997
249	0.98	0.02	0.0003	0.0073	2.37	0.98	0.998

In general, when applying the parallel model to the experimental data, the weight fraction of the primary process is shown to increase with T_c. As w_p and w_s must summate to 1.0, it follows that the weight fraction of the secondary process shares the inverse relationship with T_c and is observed to decrease by 21% over the crystallisation temperature range 245 to 249 °C. The ratio of w_p to w_s with increasing T_c could be explained by the varying rates of crystallisation. At lower crystallisation temperatures ($T_c \leq 247$ °C) the secondary rate constant (z_s) is consistently higher than the primary rate constant (z_p) and due to the assumption of the parallel equation that primary and secondary crystallisation occur simultaneously, may explain why w_s comprises approximately 25% of the final fractional crystallinity. Nevertheless, the secondary process cannot proceed without prior primary nucleation and crystal growth, therefore, despite the predicted value of z_s being approximately seven times greater than z_p, it is unlikely that the weight fraction of the secondary process will ultimately be larger than that of the primary. Conversely, at crystallisation temperatures above 247 °C, z_p is greater than z_s. This explains why w_s is significantly reduced at elevated crystallisation temperatures and why w_p generally comprises over 90% of the overall fractional crystallinity.

The Velisaris-Seferis primary exponent holds the same physical meaning as the Avrami exponent and should therefore, be an integer value between 0 and 4. The primary exponent, n_{vs} calculated from the parallel equation ranges from 2.28 to 2.98 and is comparable to the values obtained in the conventional Avrami analysis. Excluding the anomaly at T_c = 249 °C, the secondary exponent, m_{vs} averages 1.42 over the crystallisation temperature range 245 to 248 °C. This implies that crystal growth throughout the secondary process is one dimensional and a combination of instantaneous and sporadic nucleation. This fits with the general assumption

that secondary crystallisation occurs via the thickening of existing lamella and/or the formation of new thin lamella from within the amorphous regions of existing spherulites [73,74].

In contrast to the parallel model, where the weight fractions of the primary and secondary processes vary considerably, and excluding the anomaly at 245 °C, weight fractions derived using the series equation were far more consistent over the T_c range. The average weight fraction of the primary process was 94% using the series equation, an 8% increase on that of the parallel model. The increased proportion of w_p to w_s observed using the series model is likely due to the assumption that secondary crystallisation does not commence until the completion of the primary process and as such, any increase in crystallinity prior to spherulite impingement and completion of the primary process is attributed to w_p.

The observed anomalies at 245 °C are suspected to result from minor differences within the raw data at the lowest crystallisation temperature potentially caused by baseline drift, impurities in the sample or local fibre distribution. Further, as mentioned in section 5.3.1, the behaviour of the baseline prior to and after the crystallisation exotherm can drastically affect the subsequent kinetic analysis and thus, modelling of the data[1].

Similar to that of the parallel equation, z_s of the series model was consistently greater than z_p.

The primary and secondary exponents, n_{vs} and m_{vs} predicted using the series equation were remarkably consistent across all crystallisation temperatures with both exponents in approximate agreement with the values derived from the parallel equation. Additionally, like the parallel equation, the predicted values of n_{vs} using the series equation were comparable to the Avrami exponent, suggesting it too gives an accurate indication of the primary crystallisation process.

[1] It was intended for the isothermal study at T_c = 245 °C to be repeated. This would have been completed were it not for time constraints and lab closures due to the covid-19 pandemic.

5.3.2.5.3 Comparison of the standard error of the regression of the models fitted using non-linear regression multi-variable regression analysis

Despite improvements in the coefficients of determination (R^2) when modelling the crystallisation process compared to using predetermined parameters, an accurate representation of the data over all four stages of the crystallisation process is not guaranteed. To assess the accuracy in the modelling of the kinetic equations to the experimental data over the four stages of the crystallisation process (initial, primary, transition and secondary), the standard error of the regression was applied. For visual comparison, the fit of each of the models to the experimental data at an isothermal crystallisation temperature of 248 °C is shown in Figure 5.16. All six models appear to provide a good fit to the data over the initial and primary stages of the crystallisation process, with the Tobin, Urbanovici-Segal and Velisaris-Seferis equations seemingly providing a better fit than the Avrami and Malkin models over the transition and secondary regions. The standard error of the regression *S,* recorded for each of the models throughout the four stages of crystallisation and over the T_c range 245 to 249 °C are listed in Table 5.13.

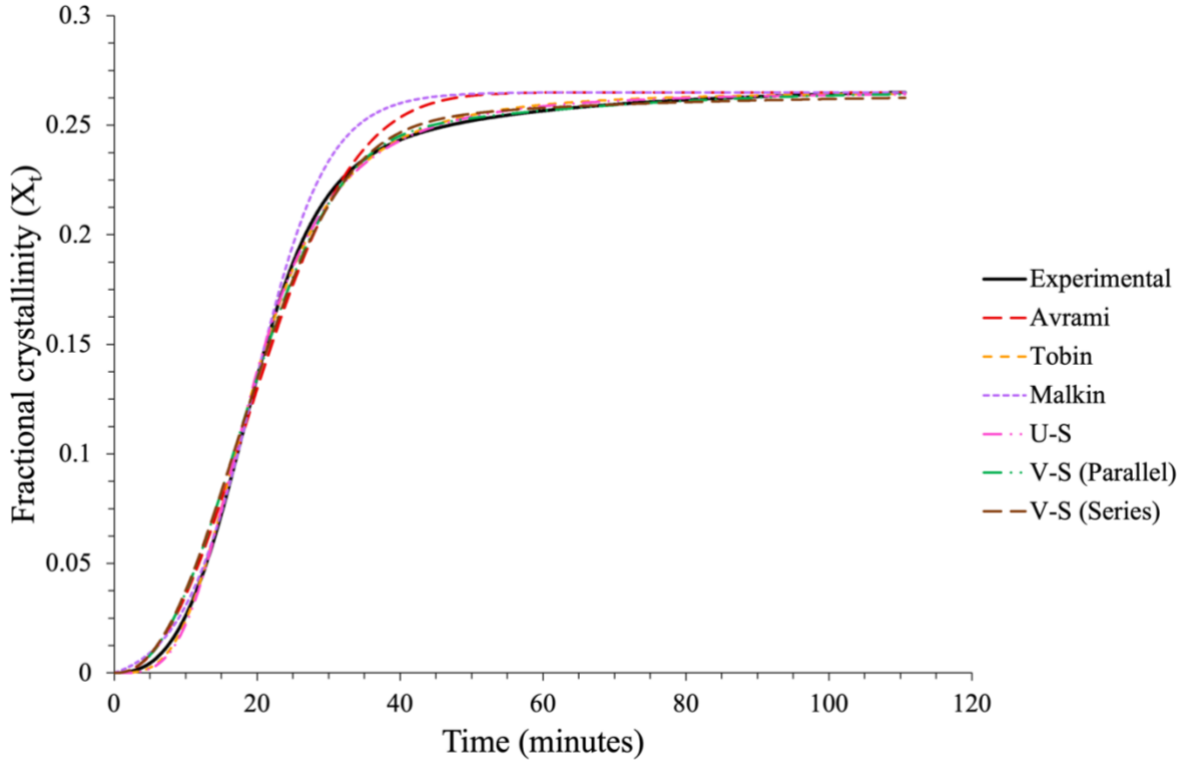

Figure 5.16: Predicted fits of the Avrami, Tobin, Malkin, Urbanovici-Segal and Velisaris-Seferis models to the isothermal data (Experimental) using non-linear multi-variable regression analysis at a crystallisation temperature of 248 °C.

When compared to the fitting of the predetermined parameters (Figure 5.10 – Figure 5.12), the standard error of the regression of the Avrami, Tobin and Malkin equations was observed to be higher over the initial and primary crystallisation regions using non-linear multi-variable regression analysis. The opposite observation was made over the transition and secondary crystallisation regions where, without the constraints of fitting parameters designed for primary crystallisation, the SPSS software was able to generate a better fit to the experimental data. The discrepancy between open and fitted parameter modelling over the two halves of the crystallisation process (initial-primary and transition-secondary) is typical when modelling kinetic equations that do not account well for secondary crystallisation [131]. Non-linear multi-variable regression analysis predicts the best possible fit of a kinetic model to the entire

experimental data set leading to improvements in the fit of the transition and secondary regions of models which do not consider secondary crystallisation. Consequently, this reduces the accuracy in the fit of the model to the initial and primary regions, ultimately increasing the standard error of the regression over these two stages.

The accuracy in the modelling of the kinetic equations to the experimental data using non-linear multi-variable regression analysis is observed to be temperature dependent. A comparison of the kinetic models at crystallisation temperatures ≤ 246 °C shows the Velisaris-Seferis model to provide the best fit over all stages of the crystallisation process, with the parallel equation consistently providing a slightly better representation of the experimental data than the series equation (Table 5.13). The Urbanovici-Segal model performs comparably well to the Velisaris-Seferis model over the initial and secondary regions of the trace; however, the standard error of the regression is observed to increase over the primary and transition stages. The standard error associated with the modelling of the Avrami, Tobin and Malkin equations was highest across all four stages. The Tobin model was shown to generate a marginally better fit to the experimental data than the Avrami and Malkin models over the initial, transition and secondary regions, with all three models performing adequately well throughout the primary crystallisation stage. The standard error of the regression of the Avrami and Malkin models was consistent throughout.

At crystallisation temperatures ≥ 247 °C the measured standard error of regression over the initial and primary stages of the crystallisation process was relatively consistent, independent of the kinetic model used. However, in the latter stages of the crystallisation process, namely the transition and secondary regions, the lowest values of S were recorded for the Tobin,

Urbanovici-Segal and Velisaris-Seferis models. This was expected as all three models were derived to account for secondary crystallisation and so somewhat inevitably provide a better fit over this stage than the Avrami and Malkin models.

Table 5.13: Calculated standard error of the regression of the Avrami, Tobin, Malkin, Urbanovici-Segal and Velisaris-Seferis models using non-linear multi-variable regression analysis over the 4 stages of the crystallisation process; a) initial, b) primary, c) transition and d) secondary.

a)

Tc (°C)	Avrami	Tobin	Malkin	Urbanovici -Segal	Velisaris-Seferis	
					Parallel	Series
245	0.0266	0.0165	0.0295	0.0042	0.0033	0.0244
246	0.0297	0.0152	0.0338	0.0026	0.0025	0.0068
247	0.0052	0.0014	0.0077	0.0037	0.0013	0.0005
248	0.0054	0.0020	0.0081	0.0029	0.0060	0.0065
249	0.0047	0.0017	0.0068	0.0018	0.0034	0.0030

b)

Tc (°C)	Avrami	Tobin	Malkin	Urbanovici -Segal	Velisaris-Seferis	
					Parallel	Series
245	0.0196	0.0199	0.0172	0.0171	0.0023	0.0276
246	0.0194	0.0147	0.0199	0.0110	0.0034	0.0084
247	0.0044	0.0030	0.0048	0.0039	0.0017	0.0010
248	0.0040	0.0029	0.0044	0.0032	0.0061	0.0061
249	0.0030	0.0017	0.0029	0.0017	0.0022	0.0021

c)

Tc (°C)	Avrami	Tobin	Malkin	Urbanovici -Segal	Velisaris-Seferis	
					Parallel	Series
245	0.0217	0.0140	0.0227	0.0107	0.0029	0.0170
246	0.0195	0.0130	0.0198	0.0078	0.0027	0.0036
247	0.0082	0.0028	0.0078	0.0029	0.0016	0.0011
248	0.0085	0.0023	0.0081	0.0020	0.0033	0.0043
249	0.0049	0.0013	0.0047	0.0013	0.0040	0.0035

d)

Tc (°C)	Avrami	Tobin	Malkin	Urbanovici -Segal	Velisaris-Seferis	
					Parallel	Series
245	0.0072	0.0048	0.0072	0.0028	0.0011	0.0041
246	0.0085	0.0041	0.0084	0.0030	0.0009	0.0025
247	0.0034	0.0026	0.0034	0.0020	0.0007	0.0008
248	0.0037	0.0014	0.0036	0.0010	0.0005	0.0016
249	0.0041	0.0008	0.0039	0.0008	0.0029	0.0017

5.3.2.5.4 Conclusions

In summary, accounting for both the coefficients of determination and the standard error of the regression, modelling using non-linear multi-variable regression analysis of the Velisaris-Seferis equations provides the best fit to the isothermal crystallisation of PA66/GF over the crystallisation temperature range studied. This is in good agreement with Kelly and Jenkins [131], who concluded that in comparison to the Avrami, Tobin, Malkin and Urbanovici-Segal equations, modelling of the Velisaris-Seferis equation generated the most satisfactory fit to the isothermal crystallisation of PHB-co-HV [131]. The Urbanovici-Segal equation also generates an accurate representation of the experimental data, as predicted in the literature [109,113], with the Tobin model providing a better fit to the isothermal crystallisation of PA66/GF than the Avrami and Malkin models. Despite improvements in the modelling of the secondary process using non-linear multi-variable regression analysis compared to that of curve fitting using predetermined parameters, the Avrami and Malkin models were inadequate at accurately describing the isothermal crystallisation process.

5.3.3 A new analytical approach to quantifying isothermal crystallisation kinetics using Differential Scanning Calorimetry (DSC)

5.3.3.1 Theory of the Hay approach

Dissimilar to the traditional methods of analysis which only assume completion of the crystallisation process, Hays approach models the data and calculates where secondary crystallisation tends to zero, thus, providing a more accurate estimation of the end of the crystallisation process. Using the same experimental data set as above (section 5.3.1), but excluding the corrections for t_i and t_{end}, the isothermal crystallisation of PA66/GF, as measured by DSC (section 5.2.2) and recorded as heat flow as a function of log time over a crystallisation temperature range of 245 to 249 °C is shown in Figure 5.17.

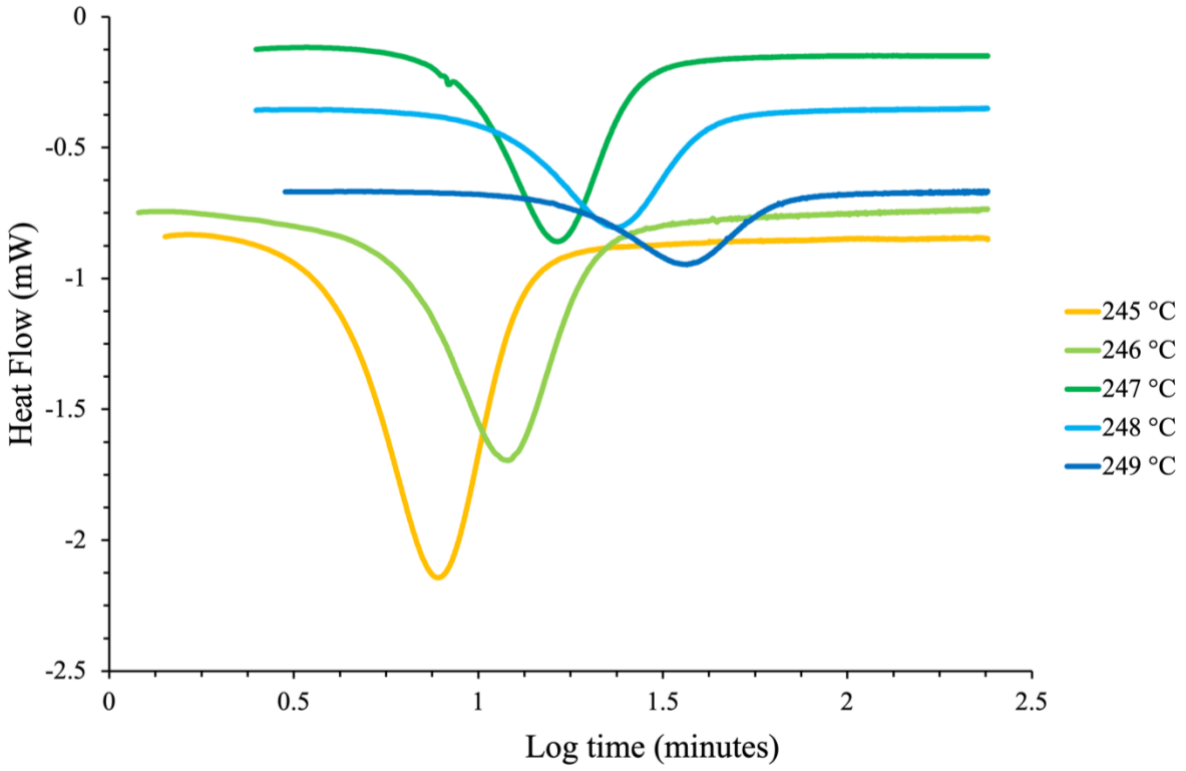

Figure 5.17: Recorded heat flow of the isothermal crystallisation of PA66/GF as a function of log time over the crystallisation temperature range 245 to 249 °C.

Following a recent study where the modelling showed the rate of primary crystallisation to fall to zero at three times the half-life of crystallisation when $n = 2$ and twice the half-life when $n = 3$ [111], an isothermal crystallisation time period greater than six times the half-life of the primary process was used throughout this study. Increasing the time period to over six times the half-life of crystallisation is thought to ensure full completion of the primary process and enable further development of secondary crystallisation over the extended time period. Prior to the onset of crystallisation, there is an observed induction period shown to increase with crystallisation temperature (Figure 5.17). Unlike traditional methods of analysis where induction time is frequently taken as the final time point before the onset of crystallisation, the Hay model uses the induction time as an adjustable parameter limited by a maximum value corresponding to the onset of crystallisation. Additionally, the Hay model predicts that upon completion of the primary process, heat flow continues to rise relative to the rate of secondary crystallisation and so to account for this, a baseline correction is applied by modelling the end of the secondary process using experimental data between 3 and 6 times the half-life of crystallisation. Equation 5-16 gives an expression for heat flow at time *t*.

$$J_t = -\left(\frac{\Delta H_f w X_{p,\infty} k_s}{2(t - t_i)^{1/2}}\right) + J_{s,\infty}$$

Equation 5-16

Where J_t is heat flow, $J_{s,\infty}$ is equivalent to heat flow at the end of the secondary process, w represents sample mass and ΔH_f is the enthalpy of crystallisation, taken as 191 Jg^{-1} [11,134,135]. Figure 5.18 shows a linear plot of heat flow (J_t) against $(1/(t\text{-}t_i)^{1/2})$ with an intercept value equivalent to heat flow at infinite time ($J_{s,\infty}$) upon completion of the secondary crystallisation process. This value was determined at each crystallisation temperature and used to perform a baseline shift to the experimental data prior to the kinetic analysis.

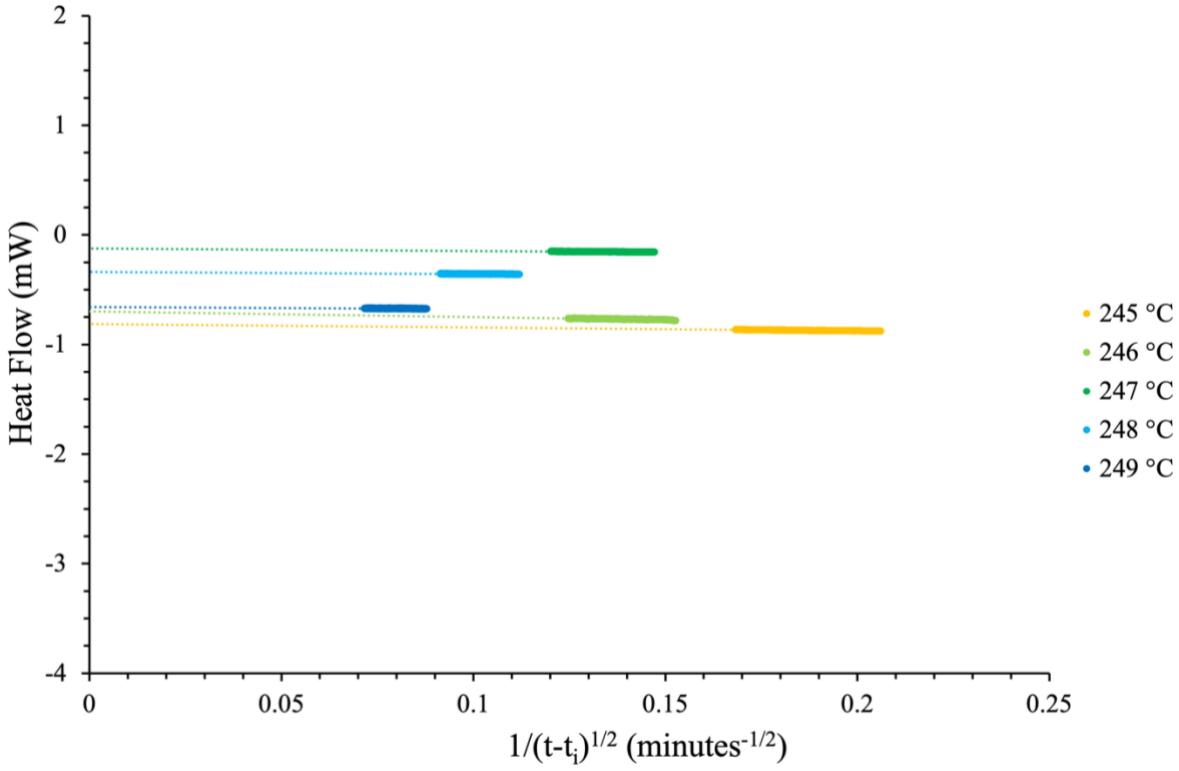

Figure 5.18: Measured heat flow at the theoretical completion of the secondary crystallisation process as determined from Equation 5-16.

5.3.3.1.1 Quantifying the secondary crystallisation contribution

Following the baseline corrections and removal of the induction periods, the isothermal traces were integrated and fractional crystallinity (X_t) as a function of time determined (Figure 5.19). X_t was recorded as the *real* crystalline volume fraction, as opposed to being made *relative* to 1. Though the rate of phase transformation is observed to increase with decreasing crystallisation temperature, the contribution of the secondary process generally increases with T_c over a time period of six times the half-life of crystallisation.

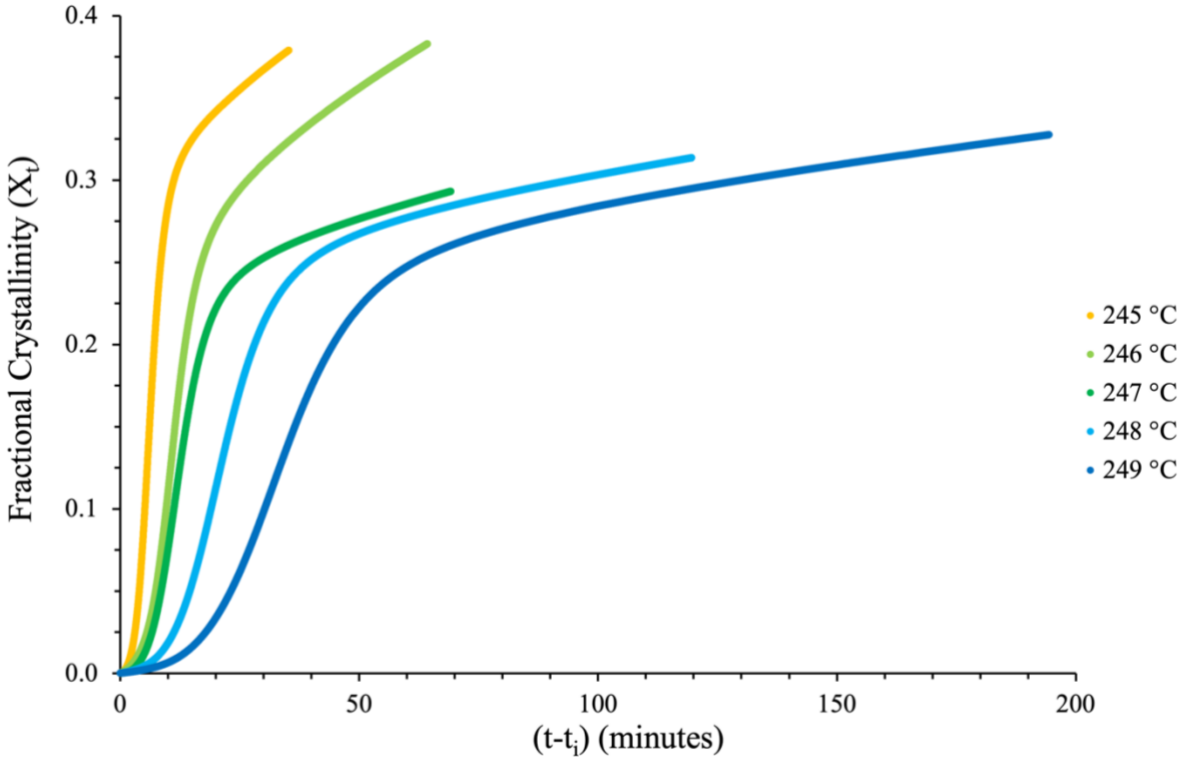

Figure 5.19: Fractional crystallinity as a function of time, calculated via integration of the isothermal DSC traces over the data range (t_i - t_{end}) derived using the Hay approach.

The limits of the primary crystallisation process $X_{p,\infty}$ and the secondary rate constants k_s can be determined from a plot of fractional crystallinity vs. $t^{1/2}$ (Figure 5.20). As described in section 5.1.2.2 and emphasised by the linearity of the trace following the transition period, secondary crystallisation appears to follow a square root time dependence. To confirm this, experimental data was limited to values of $X_t > X_{p,\infty}$ (Figure 5.21), where a linear dependence was observed across all crystallisation temperatures, with $X_{p,\infty}$ and k_s calculated from the intercept and gradient of the lines, respectively (Table 5.14).

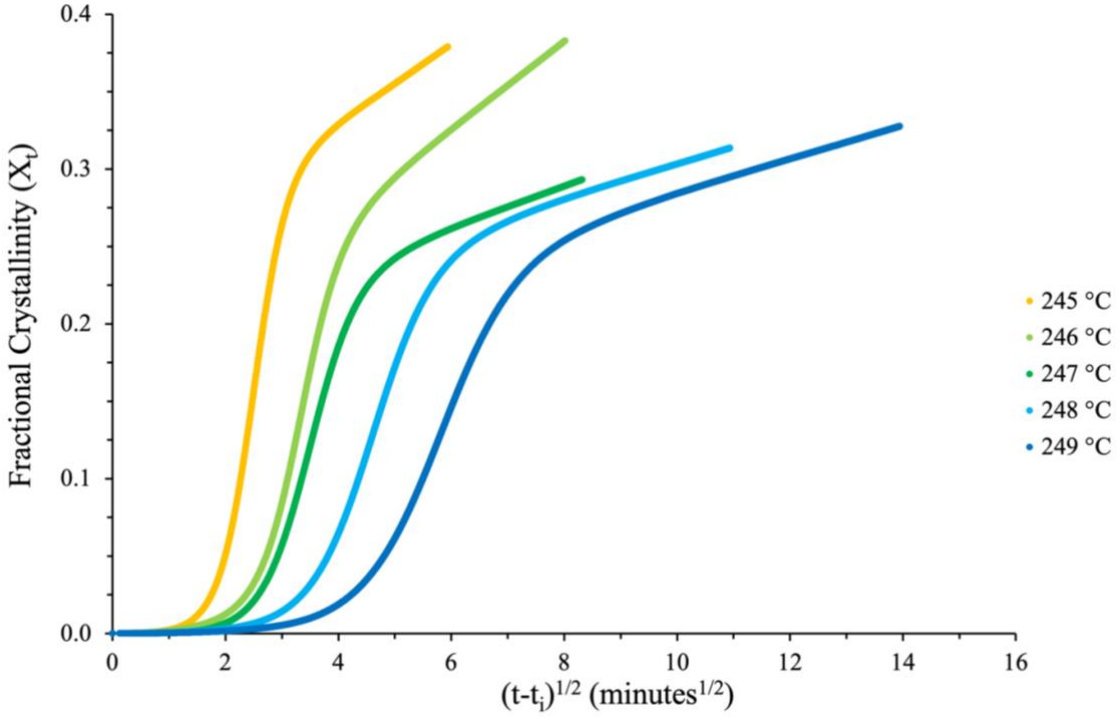

Figure 5.20: Fractional crystallinity as a function of the square root of crystallisation time.

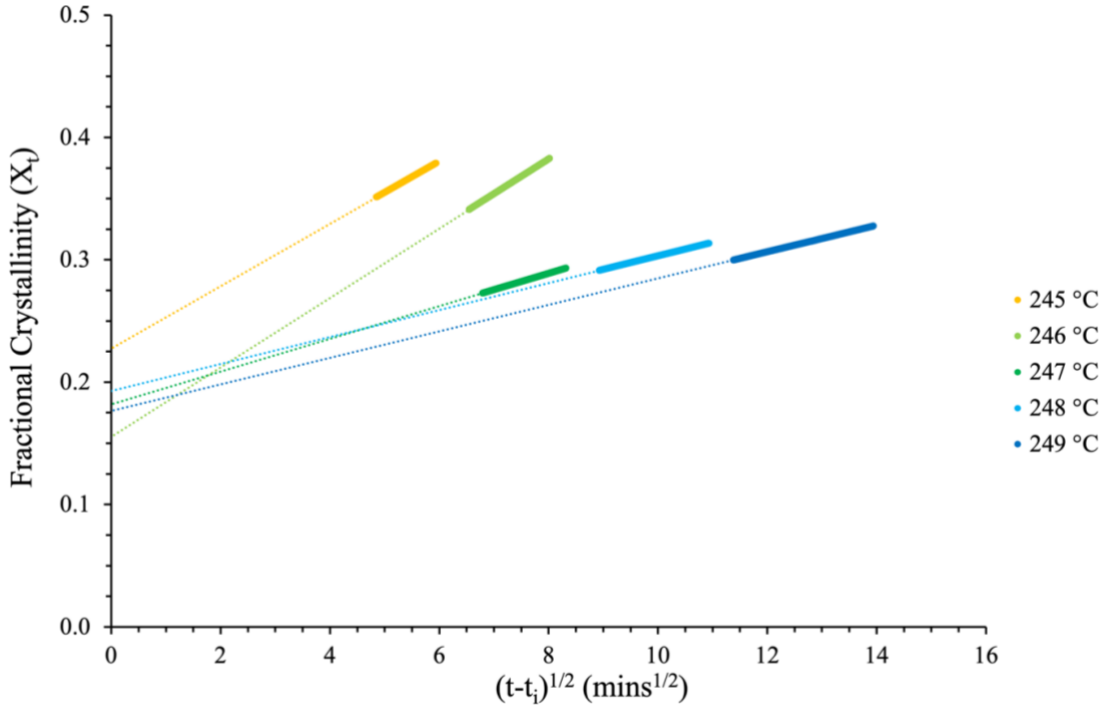

Figure 5.21: Determination of the limits of the primary crystallisation process $X_{p,\infty}$ and secondary rate constants through the plotting of Equation 5-11.

The limits of the primary crystallisation process listed in Table 5.14 remained relatively consistent and independent of crystallisation temperature. On average, the primary process was observed to reach completion at $X_t \approx 0.19$, past which secondary crystallisation is assumed to occur in isolation. In contrast to $X_{p,\infty}$, the secondary rate constant was shown to be temperature dependent. At $T_c \geq 247$ °C k_s averaged 0.064 $s^{-1/2}$, whereas at $Tc \leq 246$ °C the average increased to 0.147 $s^{-1/2}$. Though the values remained consistent across both temperature ranges, there is an obvious increase in the rate of secondary crystallisation with decreasing T_c.

Table 5.14: Master table of the Hay kinetic parameters derived from Figure 5.18 and Figure 5.19 using Equation 5-8 and Equation 5-11. Coefficients of determination were generated from the modified Avrami plot (R^2) and curve fitting of the Hay parameters using SPSS software ($*R^2$), respectively.

T_c (°C)	n	k_p (min^{-n})	k_s (min^{-n})	$X_{p\infty}$	R^2	$*R^2$
245	3.00	0.00312	0.11209	0.228	1.000	0.999
246	3.00	0.00060	0.18211	0.155	0.999	0.999
247	3.00	0.00041	0.07363	0.182	0.999	0.998
248	3.00	0.00008	0.05702	0.193	0.999	0.998
249	3.00	0.00002	0.06116	0.177	0.999	0.999

5.3.3.1.2 Quantifying kinetic parameters from the primary contribution

Determining the primary crystallisation parameters using the Hay equation requires the prior removal of the secondary component from the experimental data and is achieved via the rearrangement of Equation 5-10 resulting in the following equation:

$$\frac{X_t}{X_{p,\infty}(1+kt^{1/2})} = 1 - e^{-k_p t^n}$$

Equation 5-17

By isolating the primary component, Equation 5-17 now follows a standard Avrami equation. The kinetic parameters n and k_p are calculated from the gradient and intercept of the plot $\log\left[-\ln\left[1-\left(\frac{X_t}{X_{p,\infty}(1+k(t-t_i)^{1/2})}\right)\right]\right]$ vs. log time, respectively. The fit of the modified Avrami equation to the experimental data over a fractional crystallinity range $0.15 \leq X_t \leq 0.65$ is shown in Figure 5.22. Contrary to conventional Avrami analysis, in the case where non-integer n values were recorded, t_i was used as an adjustable parameter to correct for the induction time, resulting in n values of 3.0 being obtained at each crystallisation temperature (Table 5.14). k_p was observed to decrease with increasing T_c, indicative of a nucleation-controlled process.

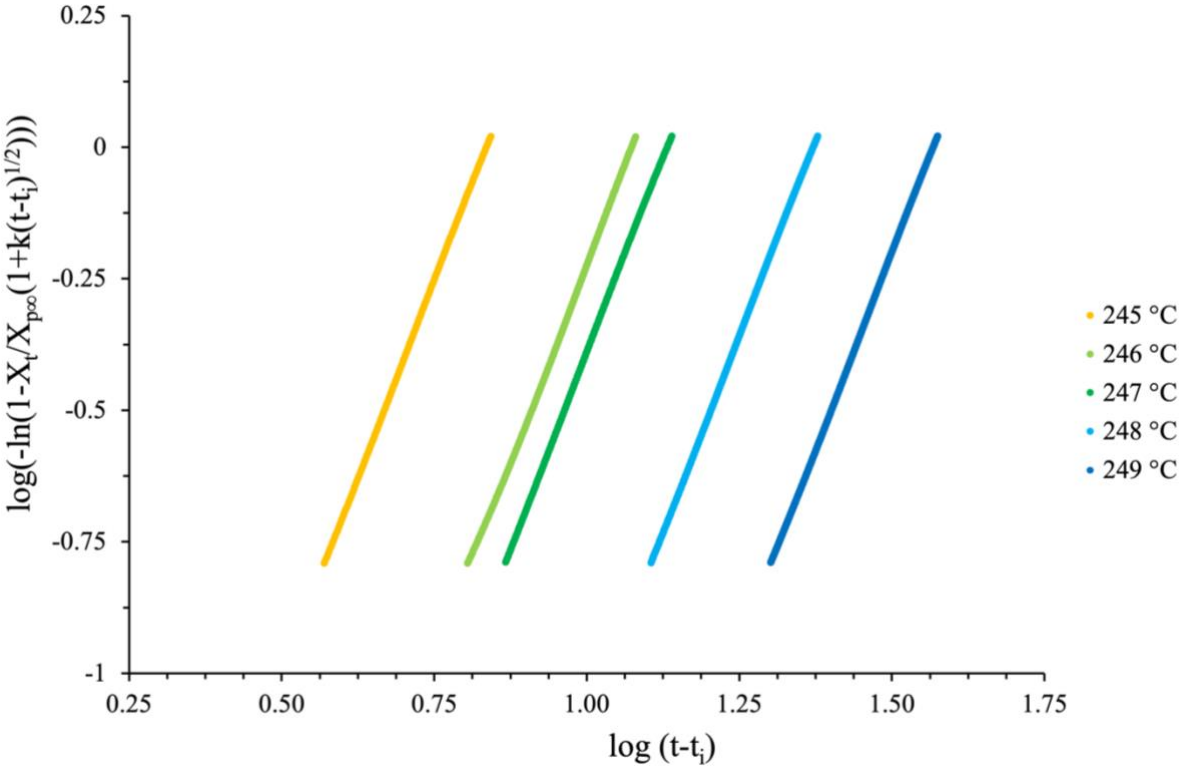

Figure 5.22: Fit of the modified Avrami equation (Equation 5-17) to the isothermal data ($0.15 \leq X_t \leq 0.65$) over a crystallisation temperature range of 245 to 249 °C.

5.3.3.2 Comparison of Hay's theory to traditional methods of analysis

5.3.3.2.1 Deriving the kinetics of primary crystallisation

Contrary to traditional analysis (section 5.3.2), where t_i and t_{end} are predicted by eye from the initial deviation and return of the exotherm to a baseline value, Hay's model calculates the contribution of the primary process using Equation 5-17. In doing so, the contribution of secondary crystallisation is removed from the total fractional crystallinity (X_t) prior to analysis of the primary component. Furthermore, due to the poor sensitivity of the DSC in detecting minor changes in heat flow, such as those associated with the onset of nucleation (section 1.3.1), Hay employs t_i as an adjustable parameter.

After removing the contribution of the secondary process, Hay's method of deriving the kinetics of primary crystallisation follows a standard Avrami equation, whereby the crystallisation

kinetic parameters are determined from conventional double-log plots. This allows for direct comparison between the Hay, Avrami, Tobin and Malkin models.

In contrast to the Avrami and Malkin models, which produced non-integer exponent values (Table 5.2 and Table 5.4) with limited scientific meaning, the removal of secondary crystallisation from the overall crystallinity prior to analysis, results in the Hay model returning integer values of *n*, from which the nucleation and growth mechanisms can be more easily defined. Despite the observed differences in the exponent values, the primary crystallisation rate constants were observed to follow a similar trend over the isothermal crystallisation temperature range (Table 5.2 - Table 5.4 and Table 5.14).

5.3.3.2.2 Curve fitting of the predetermined kinetic parameters using SPSS software

SPSS software was used to fit the Hay equation to the experimental data using the kinetic parameters listed in Table 5.14 as fitting parameters (Figure 5.23). The equation was shown to provide a very good fit to the experimental data across all crystallisation temperatures, with coefficients of determination (R^2) greater than 0.998 recorded over the entire T_c range (Table 5.14).

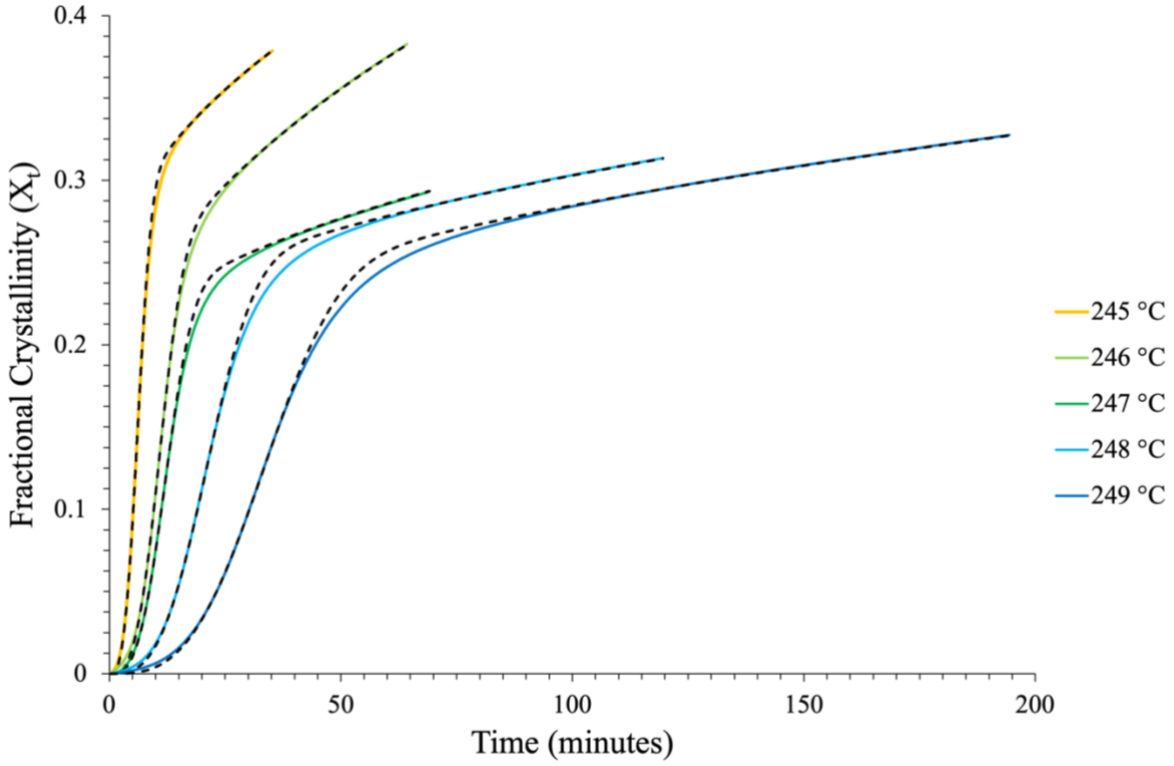

Figure 5.23: Curve fitting of the Hay model to the experimental data (*dashed*) using SPSS software and pre-determined fitting parameters over a crystallisation temperature range 245 to 249 °C.

As described in detail in section 5.3.2.4, curve fitting of the Avrami, Tobin and Malkin equations to the experimental data (defined by traditional methods of analysis), using the predetermined crystallisation kinetic parameters (Table 5.2 - Table 5.4) as fitting parameters is shown in Figure 5.8 for an isothermal crystallisation temperature of 248 °C.

Table 5.15: Calculated standard error of the regression of the Hay equation over the four stages of crystallisation; a) initial, b) primary, c) transition and d) secondary.

Tc (°C)	Hay			
	Initial	Primary	Transition	Secondary
245	0.0016	0.0003	0.0084	0.0001
246	0.0033	0.0006	0.0047	0.0004
247	0.0007	0.0004	0.0350	0.0004
248	0.0016	0.0003	0.0080	0.0002
249	0.0016	0.0003	0.0084	0.0023

Despite all four models providing an excellent fit to the data over the initial and primary crystallisation process, emphasised by the low standard error of regression values listed in Table 5.6 and Table 5.15, the fit of the Avrami and Malkin equations to the transition and secondary periods is poor. Contrary, the Hay equation, which successfully accounts for the secondary process, provides a very good fit to the experimental data over the later stages of crystallisation (Figure 5.23 and Table 5.15). The results of the Tobin model are much more complex. It is expected that the Tobin equation should provide a more accurate fit to the experimental data over the transition and secondary regions than both the Avrami and Malkin models, this is due to accounting for spherulite impingement. However, as highlighted in Table 5.6, at lower crystallisation temperatures ($T_c \leq 246$ °C), the Tobin equation performs comparably poorly to that of the Avrami and Malkin models over the later stages of crystallisation. Despite this, at higher isothermal temperatures ($T_c \geq 247$ °C), the Tobin model generates a similar fit to the experimental data (Figure 5.8) and comparable *S* values (Table 5.6) to that of the Hay equation (Table 5.15). This is further emphasised by the coefficients of determination (R^2) of the Tobin model (Table 5.5), where values of 0.956 and 0.948 were recorded at $T_c \leq 246$ °C and R^2 values approaching unity at $T_c \geq 247$ °C.

5.3.3.2.3 Non-linear multi-variable regression analysis using SPSS software

In addition to deriving the crystallisation kinetic parameters using the standard Avrami approach, modelling of the Hay equation via non-linear multi-variable regression analysis was also performed. The fit of the model to the experimental data over the isothermal crystallisation temperature range can be seen in Figure 5.24, along with the predicted kinetic parameters listed in Table 5.16.

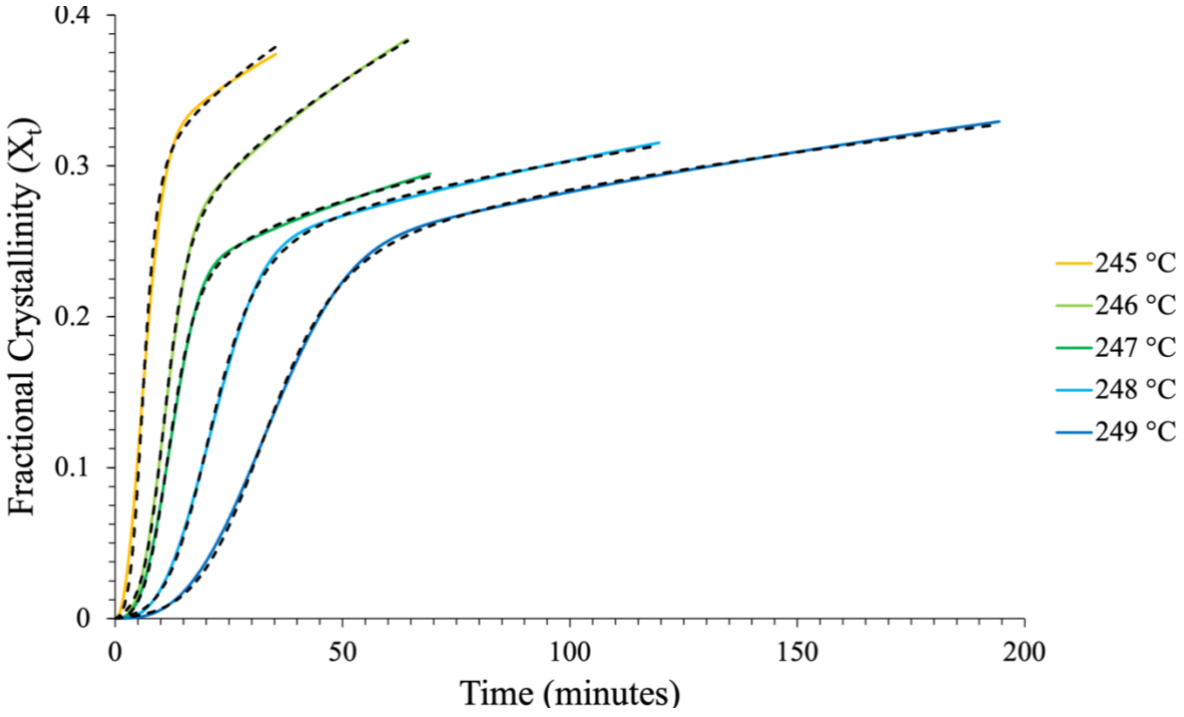

Figure 5.24: Predicted fits of the Hay equation to the isothermal experimental data (*dashed*) using non-linear multi-variable regression analysis over a crystallisation temperature range 245 to 249 °C.

Table 5.16: Predicted Hay kinetic parameters derived using SPSS software and non-linear multi-variable regression analysis over a crystallisation temperature range 245 to 249 °C.

T_c (°C)	n	k_p (min^{-n})	k_s (min^{-n})	$X_{p\infty}$	R^2
245	2.12	0.01482	0.08035	0.253	0.996
246	2.84	0.00090	0.20500	0.145	1.000
247	2.80	0.00069	0.08952	0.169	1.000
248	2.79	0.00015	0.07027	0.178	1.000
249	2.72	0.00006	0.07188	0.164	1.000

Contrary to the standard analysis, which was shown to generate integer *n* values of 3.0 across each of the five isothermal crystallisation temperatures (Table 5.14), modelling of the Hay equation using non-linear multi-variable regression analysis, produces non-integer *n* values ranging between 2.12 and 2.80. As previously highlighted in section 5.1.1.1.1, non-integer *n* values have limited scientific meaning and thus, make predicting the mechanisms of nucleation complex.

Despite consistently being slightly larger than the values derived from standard analysis, the modelled primary crystallisation rate constant, k_p follows a comparable trend to that of the standard analysis (Table 5.14) with increasing isothermal crystallisation temperature. Conversely, dissimilar to the standard analysis, which showed fluctuations in the value of k_s with increasing T_c, k_s derived from modelling of the Hay equation largely remained consistent over the isothermal crystallisation temperature range except for at 246 °C (Table 5.16).

Finally, despite the predicted value of $X_{p\infty}$ generally being lower in the modelled results, signifying that less of the overall crystallinity was attributed to the primary process, both the standard analysis and modelling of the Hay equation return excellent R^2 values of greater than 0.996.

5.3.3.2.3.1 Modelling of the Hay equation versus traditional equations

As discussed previously in section 5.3.3.2.2, modelling of the Hay equation using non-linear multi-variable regression analysis, provides an excellent fit to the experimental data over the isothermal crystallisation temperature range 245 to 249 °C. This is shown in Figure 5.24, where it can be seen that the predicted fit of the Hay model closes matches that of the experimental data, and further emphasised in Table 5.16 by the high R^2 values.

A comprehensive comparison between the fit of the Hay model to the experimental data, and that obtained using the traditional kinetic models, namely: Avrami, Tobin, Malkin, Urbanovici-Segal and Velisaris-Seferis, can be made using the coefficients of determination (R^2) recorded over each of the isothermal crystallisation temperatures. For ease of comparison, the R^2 values of each of the equations, modelled using non-linear multi-variable regression analysis to the experimental data over the T_c range 245 to 249 °C, are listed in Table 5.17.

Table 5.17: Comparison of the predicted coefficients of determination (R^2) generated from the modelling of the kinetic equations to the experimental data using non-linear multi-variable regression analysis.

T_c (°C)	Hay	Avrami	Tobin	Malkin	U-S	V-S Series	V-S Parallel
245	0.996	0.951	0.980	0.949	0.992	0.999	0.976
246	1.000	0.958	0.985	0.955	0.995	0.999	0.997
247	1.000	0.991	0.998	0.991	0.998	1.000	1.000
248	1.000	0.994	0.999	0.994	1.000	0.998	0.997
249	1.000	0.995	1.000	0.995	1.000	0.997	0.998

The goodness in the predicted fit of the equations, modelled to the experimental data, is observed to differ between low ($T_c \leq 246$ °C) and high ($T_c \geq 247$ °C) isothermal crystallisation temperatures. Over the low temperature range, the parallel Velisaris-Seferis equation is shown to provide the best, most consistent fit to the experimental data, closely followed by the Hay and Urbanovici-Segal equations. However, at high isothermal crystallisation temperatures, the Hay, Tobin, Urbanovici-Segal and both Velisaris-Seferis equations were observed to provide comparably excellent fits to the experimental data, with R^2 values greater than 0.997 recorded for each of the models. The goodness in the predicted fit of the models between the upper and lower isothermal crystallisation temperatures is likely due to subtle differences in the DSC raw data resulting from the ratio of primary to secondary crystallisation at either end of the T_c range. Hay postulates that secondary crystallisation is a diffusion-controlled process facilitated by increasing temperature [91]. Thus, as secondary crystallisation is observed to increase at higher temperatures (Figure 5.24) and the Hay, Tobin, Urbanovici-Segal and Velisaris-Seferis models designed to account for the secondary process, it follows that a better fit and superior R^2 value be achieved at higher T_c. Nevertheless, the goodness in the fit of the Hay model was shown to outperform each of the traditional models at $T_c \geq 246$ °C, with R^2 values equal to 1.0 recorded. Over the entirety of the T_c range, the fit of the equations to the experimental data could be described best by Hay, followed by Velisaris-Seferis (parallel), Urbanovici-Segal, Velisaris-Seferis (Series), Tobin, Avrami and Malkin.

Despite the possibility of demonstrating an excellent overall fit to the experimental data throughout the crystallisation process, this does not necessarily equate to the models providing an excellent fit across all four stages of the process. Therefore, to further clarify which of the

modelled equations best predicts the isothermal crystallisation of PA66/GF, the standard error of the regression, *S* of curves fit using the Hay and traditional equations were analysed using Equation 5-15, with the calculated values of *S* listed in Table 5.13 and Table 5.18, respectively.

Table 5.18: Calculated standard error of the regression of the modelled Hay equation over the four stages of crystallisation; a) initial, b) primary, c) transition and d) secondary.

Tc (°C)	Hay			
	Initial	Primary	Transition	Secondary
245	0.0099	0.0119	0.0085	0.0027
246	0.0024	0.0016	0.0018	0.0007
247	0.0010	0.0017	0.0101	0.0012
248	0.0012	0.0018	0.0022	0.0011
249	0.0016	0.0019	0.0022	0.0018

Excluding the isothermal crystallisation temperature, $T_c = 245$ °C, the value of error associated with the predicted fit of the Hay equation over the initial nucleation and primary stage of the crystallisation process is generally observed to be lower than that of the traditional kinetic equations. This suggests that at $T_c \geq 246$ °C the Hay equation provides a more representative fit to the experimental data than each of the Avrami, Tobin, Malkin, Urbanovici-Segal and Velisaris-Seferis equations.

Additionally, excluding the anomaly at $T_c = 247$ °C, the value of *S* calculated when using the Hay equation is shown to be comparable to that of the Tobin, Urbanovici-Segal and parallel Velisaris-Seferis equation over the transition stage of the crystallisation process, where

spherulite impingement occurs. Furthermore, the Hay equation is shown to provide a better fit than the Avrami, Malkin and series Velisaris-Seferis equations over this region.

Finally, similar to the transition region, the Hay equation is shown to provide a comparably good fit to the experimental data as the Tobin, Urbanovici-Segal and series Velisaris-Seferis models, outperforming the Avrami and Malkin models. However, the parallel Velisaris-Seferis equation is observed to provide a marginally better fit to the experimental data over most of the isothermal crystallisation temperatures within the secondary crystallisation region. Despite this, as a result of the parallel Velisaris-Seferis and Hay equations generally providing the best fit and lowest values of S over the secondary crystallisation region, one could deduce that the theory of both models – secondary crystallisation occurs simultaneously alongside primary crystallisation – is plausible.

5.3.3.2.4 Summary of comparison

In summary, compared to traditional analysis, Hay's model was shown to provide a more accurate representation of both the primary and secondary crystallisation kinetics.

When deriving the primary crystallisation kinetics, dissimilar to the Avrami and Malkin models, Hay's model generates integer exponent values giving them scientific meaning. Additionally, curve fitting of the predetermined kinetic parameters, generally showed that Hay's model provides the best overall fit to the experimental data and the least error over the four stages of the crystallisation process.

Finally, when modelled using non-linear multi-variable regression analysis, the Hay equation was generally shown to outperform each of the Avrami, Tobin, Malkin, Urbanovici-Segal and Velisaris-Seferis equations, as highlighted by the fit of the equation to the experimental data

and R^2 recorded. Furthermore, the standard error of regression applied over the four stages of the crystallisation process showed the Hay equation to perform comparably well or better than each of the traditional models over three of the four stages, only being surpassed by the parallel Velisaris-Seferis equation over the secondary crystallisation stage.

5.3.3.3 The applicability of Hay's theory to the Avrami, Tobin and Malkin kinetic models

Hay's method of establishing the end of the crystallisation process by calculating the time at which the rate of secondary crystallisation tends to zero appears far more reliable and accurate than that of traditional analysis, which remains open to interpretation. After a baseline correction, and when restricted to time periods between t_i and t_{end}, the experimental data modified using Hay's approach can be applied to the previously discussed models.

After correcting the experimental data, the conventional Avrami analysis was applied over the fractional crystallinity range ($0.1 \leq X_t \leq 0.5$), with the Avrami parameters n_a and k_a, derived using standard Avrami double log plots, listed in Table 5.19. Despite similarity between the primary rate constants k_a and k_p, non-integer n_a values were generated using the conventional Avrami analysis, which as highlighted in section 5.1.1.1.1 to have little meaning when describing the mechanisms of nucleation. When compared to the traditional Avrami analysis (section 5.3.2.1), which yields an average n_a value of 2.85 with a standard deviation of 0.19, Avrami analysis using Hays approach generates a more consistent value of n_a across the isothermal temperature range (average = 2.90, standard deviation = 0.03). The coefficients of determination using both theories are comparable ($R^2 > 0.999$), however, using Hays approach to quantify n_a generally returns values closer to an integer value of 3 than via the traditional methods of analysis.

Table 5.19: Avrami kinetic parameters derived from double log plots and the predicted coefficient of determination (*R^2) generated from curves fit using the predetermined fitting parameters over the isothermal crystallisation temperature range of 245 to 249 °C.

T_c (°C)	n_a	k_a (min^{-n})	R^2	*R^2
245	2.91	0.00254	0.9997	0.927
246	2.85	0.00047	0.9991	0.844
247	2.92	0.00035	0.9996	0.929
248	2.92	0.00007	0.9997	0.928
249	2.89	0.00002	0.9995	0.900

The Tobin and Malkin parameters were derived from the standard double log plots ($0.2 \leq X_t \leq 0.55$) and pre-determined Avrami parameters, respectively (Table 5.20 and Table 5.21). The Tobin exponent, n_t need not be integer and averaged 3.79 across the T_c range. Both the values of n_t and R^2 remained comparable to the values quantified in section 5.3.2.2 using the traditional methods of analysis.

As the Malkin exponent, C_0 is attained directly from that of n_a and possesses the same physical meaning, it follows that C_0 should also be an integer value corresponding to the value of n obtained from the prior Avrami analysis ($n_a \approx 2.89$). As observed in Table 5.21, C_0 is generally a non-integer value, with an average index of approximately 51.6. This is in good agreement with the Avrami exponent, where for an n value of 3.0, C_0 is expected to be 60.

Table 5.20: Tobin kinetic parameters derived from double log plots and the predicted coefficient of determination (*R^2) generated from curves fit using the predetermined fitting parameters over the isothermal crystallisation temperature range of 245 to 249 °C.

T_c (°C)	n_t	k_t (min^{-n})	R^2	*R^2
245	3.69	0.000890	0.9999	0.965
246	3.90	0.000060	1.0000	0.876
247	3.54	0.000101	1.0000	0.975
248	3.95	0.000005	0.9998	0.950
249	3.89	0.000001	0.9999	0.918

Table 5.21: Malkin kinetic parameters derived from the Avrami parameters and coefficient of determination (R^2) generated from curves fit using the predetermined fitting parameters over the isothermal crystallisation temperature range of 245 to 249 °C.

T_c (°C)	C_0	C_1	R^2
245	52.82	0.58	0.934
246	48.00	0.30	0.855
247	53.56	0.30	0.936
248	53.13	0.17	0.935
249	50.65	0.10	0.908

Curve fitting of the kinetic equations to the experimental data at 248 °C, using SPSS software and the predetermined kinetic parameters listed in Table 5.19 – Table 5.21 as fitting constraints, is presented in Figure 5.25. Though each of the Avrami, Tobin and Malkin models perform comparably well to the Hay equation over the primary process, none of the three models provide an adequate fit to the data over the stages of spherulite impingement and secondary crystallisation. This is observed across all five of the isothermal crystallisation temperatures, reflected in the average R^2 values of the Avrami (0.906), Tobin (0.937) and Malkin (0.914) equations, recorded across the T_c range. Conversely, as the Hay model successfully accounts for the secondary process, the Hay equation provides a very good fit to the entirety of the experimental trace. This is emphasised by the recorded coefficients of determination being greater than 0.998. This is consistent with the findings of Kelly et al. who concluded that compared to the Avrami equation, the Hay model provided a more accurate representation of the data when considering the isothermal crystallisation kinetics of PHB-co-HV [111].

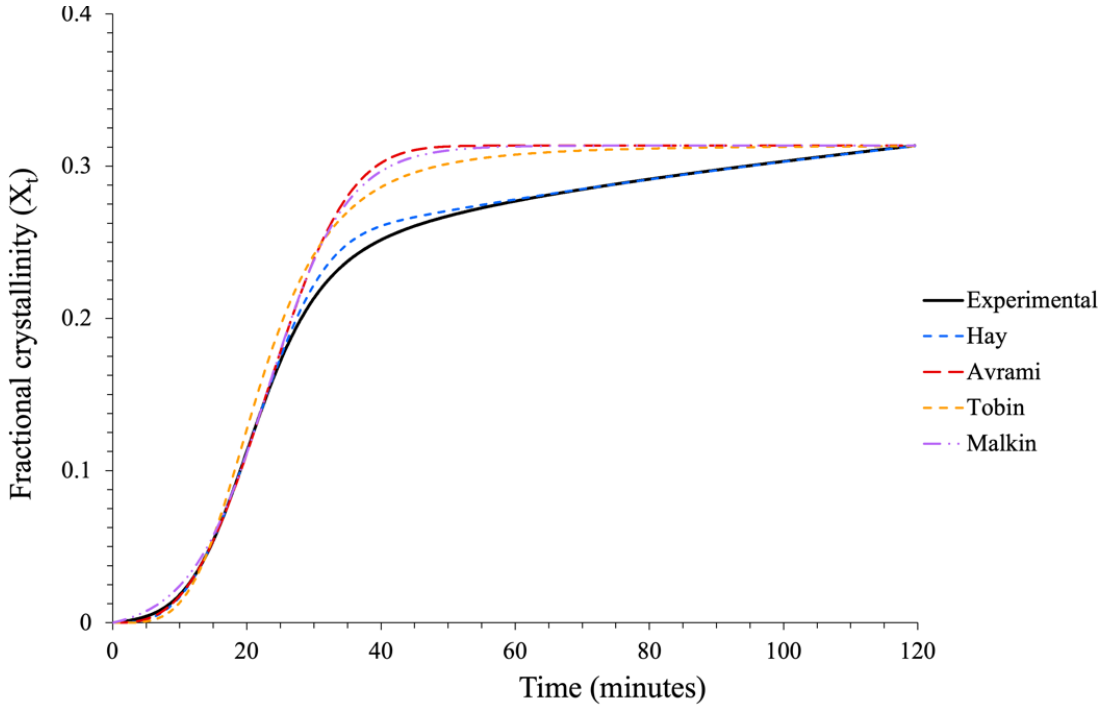

Figure 5.25: Predicted fit of the Hay, Avrami, Tobin and Malkin models to the experimental data using non-linear regression analysis and predetermined fitting parameters at an isothermal crystallisation temperature of 248 °C.

5.3.3.3.1 Standard error of the regression analysis

The standard error of the regression, *S,* was also considered to more accurately determine which of the four models provides the best representation of the data over the initial, primary, transition and secondary stages. The calculated values of *S* at each of the four stages of the crystallisation process and over the crystallisation temperature range are reported in Table 5.22 - Table 5.25. The tables show the Hay and Avrami models to generate the best fit over the initial crystallisation stage, with the Hay, Avrami and Malkin models also providing a good fit to the primary process. The standard error of the regression analysis showed the Tobin model to be less accurate over these two regions. *S* is observed to increase over the latter stages of the transformation process in the Avrami, Tobin and Malkin models, confirming the inadequacy of

the models to describe the secondary process. Despite a slight increase in *S* throughout the transition period, the Hay model performs consistently well across all four stages of the crystallisation process, comfortably providing the best fit to the experimental data. This verifies that the modified Avrami equation developed by Hay successfully accounts for the secondary crystallisation process and confirms Hay's assumption that secondary crystallisation follows a square root of time dependence.

Table 5.22: Standard error of the regression of curves fit using the Hay, Avrami, Tobin and Malkin equations, with predetermined fitting parameters, over the initial stage of the crystallisation process at isothermal crystallisation temperatures of 245 to 249 °C.

T_c (°C)	Hay	Avrami	Tobin	Malkin
245	0.0016	0.0011	0.0036	0.0054
246	0.0033	0.0024	0.0054	0.0044
247	0.0007	0.0005	0.0020	0.0046
248	0.0016	0.0013	0.0037	0.0043
249	0.0016	0.0012	0.0030	0.0015

Table 5.23: Standard error of the regression of curves fit using the Hay, Avrami, Tobin and Malkin equations, with predetermined fitting parameters, over the primary stage of the crystallisation process at isothermal crystallisation temperatures of 245 to 249 °C.

T_c (°C)	Hay	Avrami	Tobin	Malkin
245	0.0003	0.0009	0.0064	0.0010
246	0.0006	0.0018	0.0177	0.0014
247	0.0004	0.0009	0.0018	0.0008
248	0.0003	0.0010	0.0152	0.0007
249	0.0003	0.0016	0.0220	0.0022

Table 5.24: Standard error of the regression of curves fit using the Hay, Avrami, Tobin and Malkin equations, with predetermined fitting parameters, over the transition stage of the crystallisation process at isothermal crystallisation temperatures of 245 to 249 °C.

T_c (°C)	Hay	Avrami	Tobin	Malkin
245	0.0084	0.0536	0.0296	0.0486
246	0.0047	0.0700	0.0606	0.0666
247	0.0350	0.2046	0.1085	0.1946
248	0.0080	0.0425	0.0327	0.0390
249	0.0084	0.0372	0.0403	0.0037

Table 5.25: Standard error of the regression of curves fit using the Hay, Avrami, Tobin and Malkin equations, with predetermined fitting parameters, over the secondary stage of the crystallisation process at isothermal crystallisation temperatures of 245 to 249 °C.

T_c (°C)	Hay	Avrami	Tobin	Malkin
245	0.0001	0.0163	0.0142	0.0163
246	0.0004	0.0186	0.0175	0.0186
247	0.0004	0.0046	0.0036	0.0046
248	0.0002	0.0168	0.0152	0.0167
249	0.0023	0.0581	0.0497	0.0071

5.3.3.4 Non-linear multi-variable regression analysis of the kinetic models using isothermal data modified by the Hay approach

Direct modelling of the isothermal crystallisation data modified using the Hay approach and fitted by non-linear multi-variable regression analysis was also performed. The predicted fit of each of the Hay, Avrami, Tobin, Malkin, Urbanovici-Segal and Velisaris-Seferis models at a crystallisation temperature of 248 °C is shown graphically in Figure 5.26 and Figure 5.27, with the predicted kinetic parameters and coefficients of determination of each model listed in Table 5.26 - Table 5.32. The results indicate that the crystallisation kinetics of PA66/GF can be best described by the Hay and Velisaris-Seferis equations, with each of the models returning R^2 values greater than 0.993 across the chosen crystallisation temperature range (Table 5.33). The effectiveness of the two models in describing the isothermal crystallisation of PA66/GF is unsurprising as both models account for the primary and secondary contributions. Despite improvements in the coefficients of determination (R^2) when using non-linear multi-variable regression analysis to model the Avrami, Tobin and Malkin equations (compared to curves fit using predetermined parameters), the accuracy in the fitting of the primary process appears greatly reduced. This is attributed to the SPSS software estimating the best fit over the entire transformation, resulting in improved modelling of the secondary process at the expense of the fit to primary process.

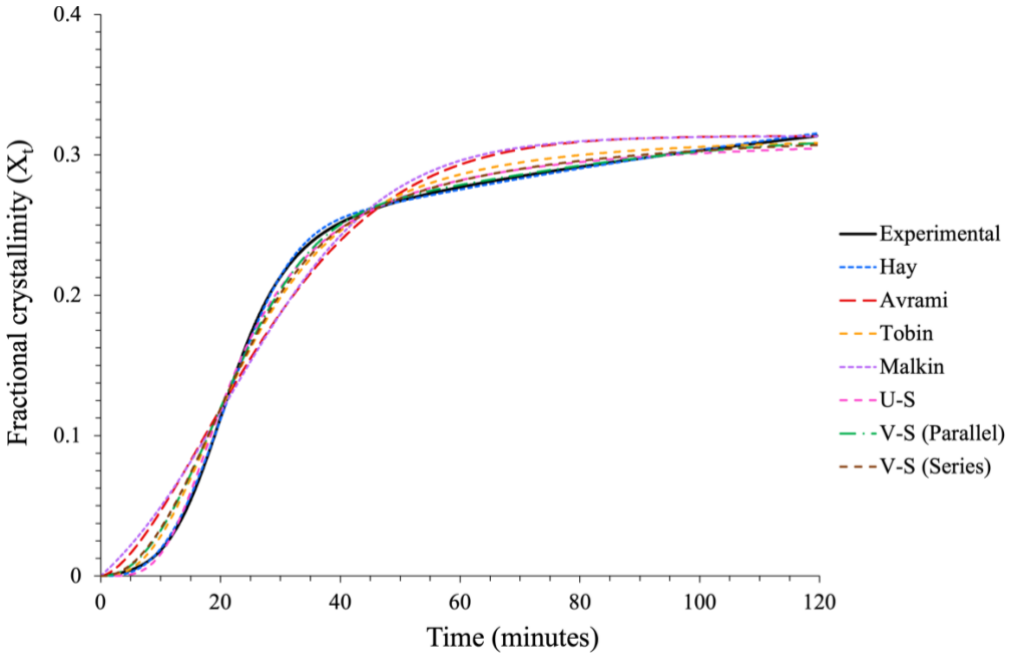

Figure 5.26: Predicted fits of the Hay, Avrami, Tobin, Malkin, Urbanovici-Segal and Velisaris-Seferis models to the isothermal data (*Experimental*) using non-linear multi-variable regression analysis at a crystallisation temperature of 248 °C.

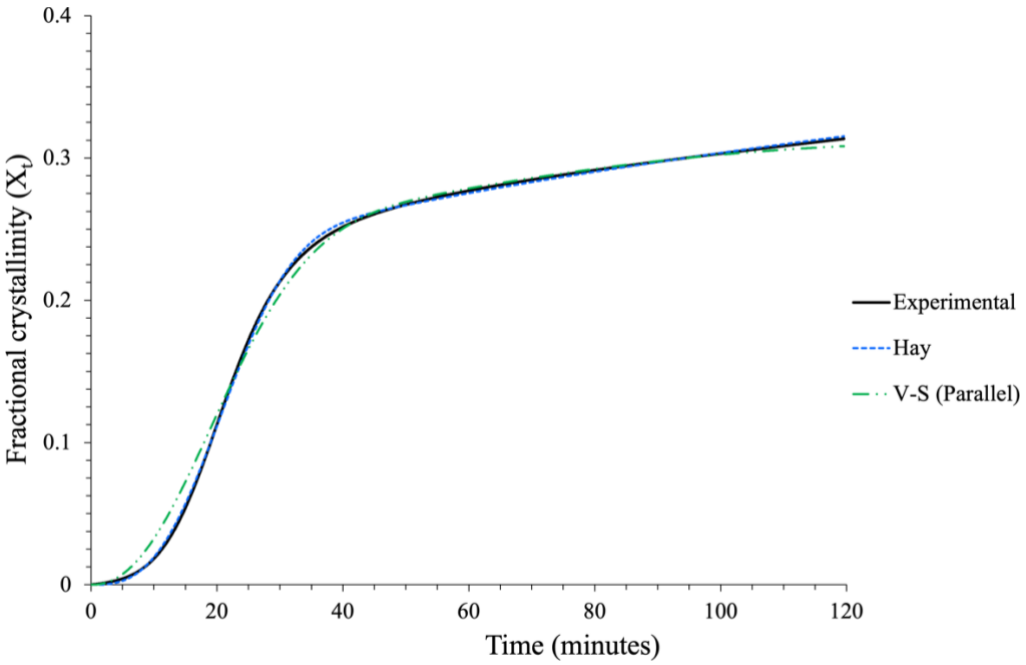

Figure 5.27: Demonstrating how the Hay and parallel Velisaris-Seferis equations provide the best fit to the isothermal data (*Experimental*) using non-linear multi-variable regression analysis at a crystallisation temperature of 248 °C.

Table 5.26: Predicted Hay kinetic parameters derived from the experimental data range defined by Hays theory; using the Hay equation and non-linear multi-variable regression analysis over an isothermal crystallisation temperature range of 245 to 249 °C.

T_c (°C)	n	k_p (min^{-n})	k_s (min^{-n})	$X_{p\infty}$	R^2
245	2.12	0.01482	0.08035	0.253	0.996
246	2.84	0.00090	0.20500	0.145	1.000
247	2.795	0.00069	0.08952	0.169	1.000
248	2.792	0.00015	0.07027	0.178	1.000
249	2.716	0.00006	0.07188	0.164	1.000

Table 5.27: Predicted Avrami kinetic parameters derived from the experimental data range defined by Hays theory; using the Avrami equation and non-linear multi-variable regression analysis over an isothermal crystallisation temperature range of 245 to 249 °C.

T_c (°C)	n_a	k_a (min^{-n})	R^2
245	1.58	0.02957	0.973
246	1.30	0.02093	0.972
247	1.60	0.00960	0.974
248	1.59	0.00415	0.974
249	1.43	0.00333	0.971

Table 5.28: Predicted Tobin kinetic parameters derived from the experimental data range defined by Hays theory; using the Tobin equation and non-linear multi-variable regression analysis over an isothermal crystallisation temperature range of 245 to 249 °C.

T_c (°C)	n_t	k_t (min^{-n})	R^2
245	2.58	0.00628	0.993
246	2.18	0.00309	0.99
247	0.26	0.00102	0.994
248	2.60	0.00025	0.994
249	2.40	0.00014	0.992

Table 5.29: Predicted Malkin kinetic parameters derived from the experimental data range defined by Hays theory; using the Malkin equation and non-linear multi-variable regression analysis over an isothermal crystallisation temperature range of 245 to 249 °C.

T_c (°C)	C_0	C_1	R^2
245	5.25	0.26	0.970
246	1.52	0.08	0.967
247	5.62	0.14	0.971
248	5.35	0.08	0.971
249	2.94	0.04	0.967

Table 5.30: Predicted Urbanovici-Segal kinetic parameters derived from the experimental data range defined by Hays theory; using the Urbanovici-Segal equation and non-linear multi-variable regression analysis over an isothermal crystallisation temperature range of 245 to 249 °C.

T_c (°C)	n_{us}	k_{us} (min^{-n})	r	R^2
245	4.00	7.09E-04	3.18	0.998
246	4.00	6.20E-05	3.74	0.995
247	4.00	3.00E-06	0.99	0.677
248	3.93	6.00E-06	0.97	0.998
249	4.00	7.88E-07	3.40	0.997

Table 5.31: Predicted Velisaris-Seferis kinetic parameters derived from the experimental data range defined by Hays theory; using the parallel Velisaris-Seferis equation and non-linear multi-variable regression analysis over an isothermal crystallisation temperature range of 245 to 249 °C.

T_c (°C)	w_p	w_s	z_p (min^{-n})	z_s (min^{-n})	n	m	R^2
245	0.71	0.29	0.00348	0.00713	2.91	1.68	1.000
246	0.37	0.63	0.00070	0.00049	1.99	3.04	1.000
247	0.76	0.24	0.00083	0.00055	2.70	2.02	0.999
248	0.80	0.20	0.00084	0.00014	2.21	2.04	0.997
249	0.64	0.36	0.00002	0.00371	3.02	1.23	0.998

Table 5.32: Predicted Velisaris-Seferis kinetic parameters derived from the experimental data range defined by Hays theory; using the series Velisaris-Seferis equation and non-linear multi-variable regression analysis over an isothermal crystallisation temperature range of 245 to 249 °C.

T_c (°C)	w_p	w_s	z_p (min^{-n})	z_s (min^{-n})	n	m	R^2
245	0.99	0.01	0.06275	0.00009	1.93	2.39	0.993
246	0.90	0.10	0.00084	0.00236	2.89	1.49	0.996
247	0.94	0.06	0.00084	0.00187	2.74	1.51	0.998
248	0.96	0.04	0.00084	0.00023	2.32	1.78	0.995
249	0.11	0.89	0.00084	0.00001	1.42	3.37	0.999

Table 5.33: Predicted coefficients of determination (R^2) generated from the modelling of the kinetic equations to the experimental data using non-linear multi-variable regression analysis.

T_c (°C)	Hay	Avrami	Tobin	Malkin	U-S	V-S Parallel	V-S Series
245	0.996	0.973	0.993	0.970	0.998	1.000	0.993
246	1.000	0.972	0.990	0.967	0.995	1.000	0.996
247	1.000	0.974	0.994	0.971	0.677	0.999	0.998
248	1.000	0.974	0.994	0.971	0.998	0.997	0.995
249	1.000	0.971	0.992	0.967	0.997	0.998	0.999

As demonstrated by the badly predicted modelling of the Avrami and Malkin equations over all stages of the crystallisation process, high R^2 values do not necessarily result in accurate representations of the experimental data. Non-linear multi-variable regression analysis generates the best fit over the whole crystallisation process with no consideration of the individual stages. This is best reflected in models which only account for the primary process, such as those derived by Avrami and Malkin. The SPSS software will regularly improve the fit of these models over the secondary process, however, this reduces the accuracy of the modelling over the primary regions. To gain a better understanding as to which of the models provides the best fit to the experimental data throughout the entire crystallisation process, the standard error of the regression over the individual regions needs to be considered.

As indicated by the lowest recorded values of *S*, the primary crystallisation process consisting of the initial and primary regions of the trace is best described by the Hay, Urbanovici-Segal and Velisaris-Seferis models (Table 5.34 and Table 5.35). It is also worth noting that over the initial and primary regions, modelling of the fitting parameters generally provides a more accurate fit to the experimental data than non-linear multi-variable regression analysis of the Hay, Avrami, Tobin and Malkin equations.

Though obvious improvements in the modelling of the Avrami, Tobin and Malkin equations over the transition and secondary regions, the Hay, Urbanovici-Segal and Velisaris-Seferis models still provide the best fits (Table 5.36 and Table 5.37).

Table 5.34: Standard error of the regression calculated from the modelling of the kinetic equations using non-linear multi-variable regression analysis over the initial stage of the crystallisation process and across the crystallisation temperature range 245 to 249 °C.

Tc (°C)	Hay	Avrami	Tobin	Malkin	Urbanovici -Segal	Velisaris-Seferis	
						Parallel	Series
245	0.0099	0.0221	0.0071	0.0264	0.0032	0.0017	0.0085
246	0.0024	0.0280	0.0105	0.0339	0.0045	0.0022	0.0048
247	0.0010	0.0182	0.0064	0.0212	0.0112	0.0030	0.0052
248	0.0012	0.0187	0.0062	0.0220	0.0027	0.0089	0.0102
249	0.0016	0.0232	0.0085	0.0275	0.0028	0.0045	0.0015

Table 5.35: Standard error of the regression calculated from the modelling of the kinetic equations using non-linear multi-variable regression analysis over the primary stage of the crystallisation process and across the crystallisation temperature range 245 to 249 °C.

Tc (°C)	Hay	Avrami	Tobin	Malkin	Urbanovici -Segal	Velisaris-Seferis	
						Parallel	Series
245	0.0119	0.0192	0.0124	0.0169	0.0086	0.0020	0.0127
246	0.0016	0.0162	0.0096	0.0179	0.0048	0.0015	0.0067
247	0.0017	0.0103	0.0067	0.0093	0.0912	0.0025	0.0050
248	0.0018	0.0102	0.0067	0.0092	0.0060	0.0082	0.0089
249	0.0019	0.0135	0.0083	0.0132	0.0058	0.0027	0.0022

Table 5.36: Standard error of the regression calculated from the modelling of the kinetic equations using non-linear multi-variable regression analysis over the transition stage of the crystallisation process and across the crystallisation temperature range 245 to 249 °C.

Tc (°C)	Hay	Avrami	Tobin	Malkin	Urbanovici -Segal	Velisaris-Seferis	
						Parallel	Series
245	0.0085	0.0217	0.0121	0.0201	0.0070	0.0011	0.0117
246	0.0018	0.0207	0.0131	0.0213	0.0077	0.0019	0.0065
247	0.0101	0.0762	0.0421	0.0791	0.3602	0.0058	0.0160
248	0.0022	0.0167	0.0093	0.0165	0.0051	0.0052	0.0078
249	0.0022	0.0259	0.0150	0.0266	0.0068	0.0045	0.0037

Table 5.37: Standard error of the regression calculated from the modelling of the kinetic equations using non-linear multi-variable regression analysis over the secondary stage of the crystallisation process and across the crystallisation temperature range 245 to 249 °C.

Tc (°C)	Hay	Avrami	Tobin	Malkin	Urbanovici -Segal	Velisaris-Seferis	
						Parallel	Series
245	0.0027	0.0142	0.0063	0.0143	0.0052	0.0026	0.0057
246	0.0007	0.0091	0.0067	0.0088	0.0117	0.0035	0.0083
247	0.0012	0.0044	0.0022	0.0043	0.0046	0.0022	0.0054
248	0.0011	0.0132	0.0061	0.0135	0.0043	0.0019	0.0037
249	0.0018	0.0217	0.0124	0.0229	0.0100	0.0082	0.0071

5.3.3.5 Conclusions

Considering both the standard error of the regression values and coefficients of determination calculated over the entire crystallisation process, the Hay and parallel Velisaris-Seferis equations generally provide the best fit over each of the individual stages and crystallisation temperatures. Both models are observed to accurately describe the primary crystallisation process and have been developed to consider the latter stages of crystallisation resulting in the best representations of the secondary process. Finally, as the parallel Velisaris-Seferis equation is shown to provide a more accurate fit to the experimental data than the series equation, Hay's assumption that both primary and secondary crystallisation occur simultaneously and that total crystallinity at time *t*, is the sum of the two contributions, can be confirmed.

CHAPTER 6 - NON-ISOTHERMAL CRYSTALLISATION KINETICS OF PA66/GF

6.1 Introduction

As emphasised in Chapter 1, both the rate and degree of undercooling from the melt have an extensive impact on polymer matrix composite formability (PMC) formability. During stamp forming, upon contact with the colder tooling, the temperature of the PMC falls rapidly, initiating the onset of crystallisation. If a critical crystallinity is reached prior to the completion of the forming process, defects relating to sample geometry and consolidation of the part may arise. It is therefore imperative that the non-isothermal crystallisation kinetics associated with the forming process are understood.

The non-isothermal crystallisation kinetics of polyamides [119,136–139] and polyamide composites [9,49,139,140] have been extensively studied using differential scanning calorimetry (DSC). Despite traditionally being used to analyse the isothermal crystallisation of polymers, the Avrami equation (Equation 5-1, Chapter 5.1.1.1) has also been applied when attempting to quantify the non-isothermal crystallisation behaviour of PMC [141,142]. Comparable to isothermal studies (Chapter 5), the Avrami exponent, n_a and non-isothermal crystallisation rate constant, Z_t are determined from plots of $\ln[-\ln(1 - X_t)]$ vs $\ln t$, where the kinetic parameters are defined by the gradient and intercept of the lines, respectively. However, Avrami assumes that crystallisation develops at a constant temperature and thus, without adequate correction, the Avrami model is unsuitable in defining the non-isothermal crystallisation kinetics of PMC. This was widely recognised and on consideration of the non-

isothermal character of many forming processes, numerous authors attempted to modify the Avrami equation, the most notable being Jeziorny [143], Ozawa [144] and Liu et al. [145].

6.1.1 Jeziorny model

Jeziorny assumes that non-isothermal crystallisation occurs at a constant rate of cooling and proposes a two-step model in quantifying the kinetics of crystallisation [143]. Initially consisting of the application of the Avrami model [95,96], whereby the exponent value (n_a) and crystallisation rate constant (Z_t) are determined from traditional Avrami plots (Chapter 5.3.2.1), Jeziorny applies a correctional procedure in which, cooling rate is accounted for. Jeziorny modifies the crystallisation rate coefficient Z, relative to the cooling rate using Equation 6-1, hypothesising that the Avrami model is now applicable to non-isothermal crystallisation.

$$\ln Z_c = \frac{\ln Z_t}{\varphi}$$

Equation 6-1

Where Z_c is the Jeziorny modified crystallisation rate constant and φ is cooling rate.

6.1.2 Ozawa model

Maintaining the assumption that crystallisation occurs at a constant cooling rate, Ozawa [144] adopted an alternative approach by extending the Avrami equation:

$$1 - X_T = \exp\left[\frac{-K(T)}{\varphi^m}\right]$$

Equation 6-2

$$\ln[-\ln(1-X_T)] = \ln K(T) - m\ln\varphi$$

Equation 6-3

Where *K(T)* is the crystallisation rate constant as a function of temperature and *m* is the Ozawa exponent. The validity of the Ozawa model to the non-isothermal data is dependent on the linearity of the plot $\ln[-\ln(1-X_T)]$ vs. $\ln\varphi$ at a given temperature. If a linear relationship is observed, the model is assumed to accurately describe the crystallisation process and the kinetic parameters *K(T)* and *m* can be derived from the intercept and slope of the line, respectively.

6.1.3 Mo's model

Aiming to formulate an equation which more accurately describes the non-isothermal crystallisation procedure, Liu et al. [145] devised a new kinetic model. The so-called 'Mo theory' essentially combines the aforementioned Avrami and Ozawa models. By merging Equation 5-1, which relates X_t to time *t*, with Equation 6-3, relating X_T to cooling rate φ; Liu et al. derived the following equations:

$$\log Z_t + n\log t = \log K(T) - m\log\varphi$$

Equation 6-4

$$\log\varphi = \log F(T) - b\log t$$

Equation 6-5

Where $F(T) = [K(T)/Z_t]^{1/m}$, and $b = n/m$

F(T) refers to the necessary cooling rate required to achieve a defined degree of crystallinity at unit crystallisation time, giving it both a physical and practical meaning [145,146]. *b* is the ratio of the Avrami exponent *n*, to the Ozawa exponent *m*. Liu et al. [145] found that the plot of $\log\varphi$

vs $\log t$ gave a series of straight lines at a given relative degree of crystallinity, from which the values of *b* and *F(T)* could be determined from the slopes of these lines and the intercept, respectively.

6.1.4 A review of the literature

The non-isothermal crystallisation kinetics of polyamides are widely reported throughout the literature, including multiple studies on pure PA66 [119,136,139] and fibre reinforced PA66 samples [9,49,139,140].

6.1.4.1 Influence of fillers on the crystallisation rate of polymer matrix composites (PMC)

The inclusion of additives, such as glass fibre reinforcement, to polymer matrix composites is proven to have a profound effect on the rate of crystallisation. It is generally accepted that additives have a synergistic effect on the nucleation of PMC, thus, promoting the formation of crystal nuclei at elevated temperatures [9,146]. This is emphasised in crystallisation exotherms, whereby $T_{c\ (onset)}$ of PMC occurs earlier and at higher temperatures than that of pure polyamide samples [49]. This indicates that the inclusion of additives promotes the crystallisation process, which in turn results in an increase in the recorded crystallisation rate constants [146].

That said, additives can also hinder crystallisation, whereby the diffusion of molecular chains to the surface of growing nuclei is obstructed by the reinforcement material [9,146]. Fillers can become an obstacle and result in the premature impingement of spherulites due to constraining crystal growth. In this case, additives are shown to impede the crystallisation process causing a decrease in the value of the crystallisation rate constant [146].

Several studies have reported the effects of GF on the rate of crystallisation in polyamide matrix composites [9,49,139]. All of which conclude that at low glass fibre quantities (<30 wt.%), the

crystallisation rate of PMC increases with glass fibre content. Proven to be independent of cooling rate, this observed increase in the rate of crystallisation with increasing content of glass fibres infers that the nucleating effect of the fibres outweighs the aforementioned hindrance to crystal growth. Conversely, at high fibre contents (>30 wt.% GF), it was found that both the rate of crystallisation and onset temperature decrease [9]. This implies that an optimum glass fibre quantity exists, beyond which fibre reinforcement impedes the crystallisation process.

6.1.4.2 Suitability of non-isothermal crystallisation kinetic models

Contrary to isothermal crystallisation kinetic studies, where there is often little consistency in the selection of the models applied to the experimental data set, studies on non-isothermal crystallisation kinetics typically report a comprehensive comparison of the Jeziorny, Ozawa and Mo kinetic models [138–142,146,147].

Determined through traditional double-log plots, the Avrami exponent, n obtained using the Jeziorny model is shown to vary considerably throughout the literature [49,136,139–142,146]. Several studies on PA66 and PA66/GF report n values of approximately 2.0 across the chosen cooling rates [49,139], whereas others report values fluctuating between 3.5 and 6.0 [136,140]. Additionally, contrary to the crystallisation rate parameter, Z_c, which is generally observed to increase with cooling rate, the value of n does not follow a dependable trend [49,139,140]. Furthermore, due to originating from a modification of the Avrami equation, the Jeziorny model does not adequately account for secondary crystallisation and thus, is largely assumed to be undesirable in describing the non-isothermal crystallisation kinetics of polyamides [49,136,139,140].

Derived from the assumption that non-isothermal crystallisation is fundamentally composed of an infinite number of isothermal steps, it follows that the Ozawa exponent, m shares a similar

physical meaning to the Avrami exponent, *n* [140]. Furthermore, comparable to the values of *n* derived using the Jeziorny model, *m* does not follow a dependable trend with varying cooling rate and instead, is observed to differ considerably between the sequential isothermal steps of the Ozawa analysis [138–140]. This makes defining the nucleation mechanism of polyamides complicated [140] and most likely arises due to the rate of crystallisation no longer being constant, but rather a function of both time and cooling rate [138,142].

Comparable to the model proposed by Jeziorny, Ozawa's theory does not account for secondary crystallisation [138,140,146]. Assuming secondary crystallisation only commences on completion of the primary process and thus, occurs in the later stages, where temperature has decreased significantly due to constant cooling associated with the non-isothermal process, Ozawa neglects the influence of the secondary process [138,140,146]. Consequently, linearity in the fit of the Ozawa model to the experimental data is rarely observed and hence, the model is frequently considered unsuitable in describing the non-isothermal crystallisation kinetics of polyamides [138–140,142,146,148].

Originating from a combination of the Avrami and Ozawa models, Mo's theory of quantifying the degree of fractional crystallinity, X_t relative to both cooling rate and time, is generally considered to describe the non-isothermal crystallisation kinetics of polyamides most successfully [49,138–140,142,147,148] [Zhang et al. 2006]. The kinetic parameter *b* relates the ratio of the Avrami exponent, *n* to the Ozawa exponent, *m* and is typically found to be a value between 1 and 2 for both pure and fibre reinforced PA66 samples [49,136,139,140]. Furthermore, dissimilar to the values of *n* and *m* which are reported to show various trends with cooling rate and temperature, respectively, the value of *b* remains remarkably consistent throughout the fractional crystallinity range studied and across multiple reports [49,136,139,140,149].

The rate parameter *F(T)* referring to the necessary cooling rate required to achieve a defined degree of crystallinity at unit crystallisation time, is observed to continually increase with X_t. This signifies that at any given crystallisation time, a higher cooling rate is required to achieve a greater degree of crystallinity [49,136,138–140,142,148].

6.1.5 Aims and objectives

The Jeziorny-modified Avrami and Ozawa models have generally proven unsuitable in describing the non-isothermal crystallisation kinetics of polyamides, with only the combined approach derived by Liu et al. [145] (Mo theory) successfully modelling the crystallisation process. Nevertheless, much of the non-isothermal crystallisation studies published on pure and fibre reinforced PA66 are limited to cooling rates between 2 and 40 °C/min.

As discussed previously in Chapter 3, stamp forming is a distinctly non-isothermal process with cooling rates are frequently observed to be in excess of 100 °C/min and as such a reliable model is required in order to accurately quantify the non-isothermal kinetics of crystallisation. The following chapter aims to qualitatively clarify which of the aforementioned models most adequately describes the non-isothermal crystallisation kinetics of PA66/GF over an extended cooling rate range of 10 to 60 °C/min (limit of DSC capability).

6.2 Methodology

6.2.1 Materials and sample preparation

Samples were obtained from the pre-impregnated glass fibre reinforced polyamide 66 (PA66/GF) tape and consisted of three hole-punched discs (diameter 4.8 mm); ensuring that the combined mass of the polyamide matrix was comfortably above the level of sensitivity of the instrument (sample mass = 28.5 ± 0.7 mg).

6.2.2 Non-isothermal crystallisation kinetics

All non-isothermal crystallisation kinetics studies were performed on a Mettler Toledo DSC 1 (Greifensee, Switzerland) with Huber TC100 intracooler attachment and nitrogen purge (30 ml/min). Samples were initially heated to above T_m^0 (300 °C) and held for 3 minutes to erase the thermal history of the polyamide and remove any residual stresses from the tape forming process. Furthermore, this enabled the three discs to consolidate into a single sample. The samples were then cooled to 10 °C at one of six cooling rates: 10, 20, 30, 40, 50 or 60 °C/min and change in heat flow as a function of time recorded. After performing a baseline correction procedure (section 6.3.1.1), the non-isothermal crystallisation kinetics of PA66/GF were quantified using each of the kinetic models outlined in section 6.1.

6.3 Results and discussion

6.3.1.1 Quantitative analysis of non-isothermal crystallisation kinetics using Differential Scanning Calorimetry (DSC)

Prior to the application of any kinetic models, a baseline correction was applied to the experimental data, resulting in all traces sitting along the abscissas, allowing for the area of the exotherm to be more easily determined. The correction procedure involved the plotting a straight line along the baseline of the DSC trace either side of the exothermic crystallisation peak (Figure 6.1). To improve repeatability in the drawing of the baseline, the initial inflection in heat flow upon cooling ($T \geq 280$ °C) and continual change in heat capacity post-crystallisation ($T \leq 150$ °C) were ignored. The equation of this straight line was then used to correct the raw data.

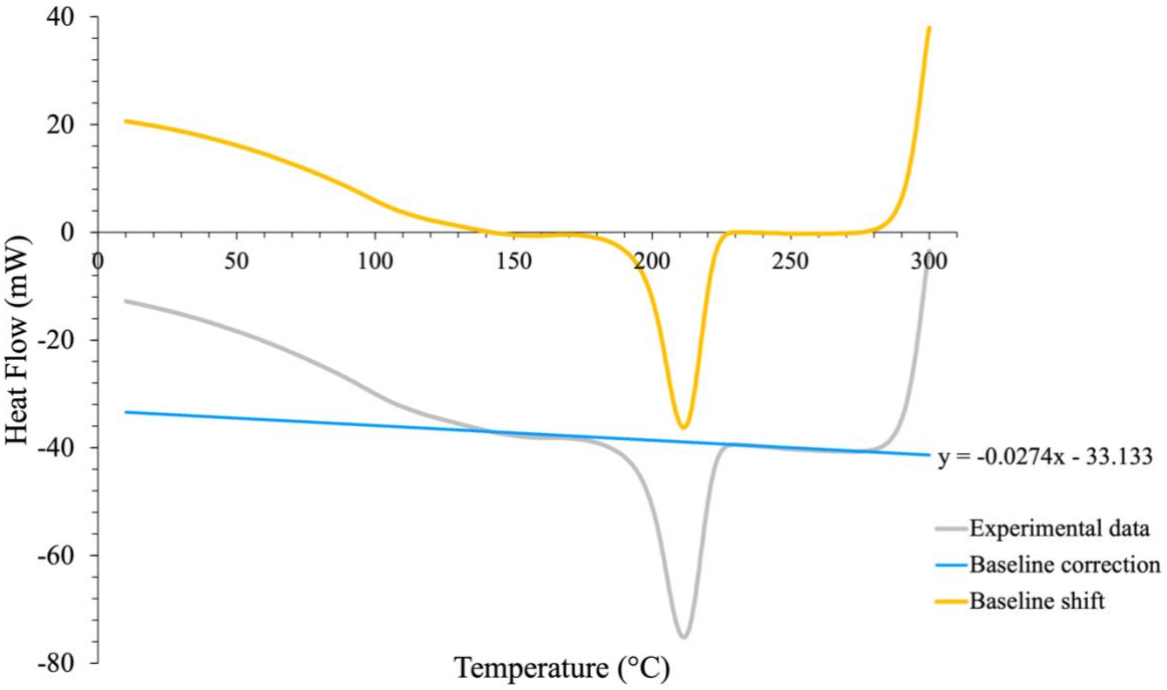

Figure 6.1: Demonstrating the baseline correction procedure, where a straight line (*blue*) was applied to the raw data (*grey*) along the baseline either side of the exothermic peak. The equation of this line was then used as a correction factor, yielding a trace (*yellow*) that sits level with the x-axis.

Following the baseline correction procedure, the experimental data was limited to the temperature range 150 to 250 °C, within which, the completion of all six crystallisation exotherms could be observed.

The recorded heat flow as a function of temperature at various cooling rates is shown in Figure 6.2. As observed from the crystallisation exotherms, the onset ($T_{c\,(onset)}$), peak ($T_{c\,(peak)}$) and endset ($T_{c\,(endset)}$) crystallisation temperatures are profoundly cooling rate (φ) dependent, with all values shifting to lower temperatures with increasing cooling rate. $T_{c\,(endset)}$ was observed to decrease the most (32.9 °C) over the φ range, with $T_{c\,(onset)}$ and $T_{c\,(peak)}$ falling by approximately 13 °C and 19.5 °C, respectively (Table 6.1). This observation is common throughout the literature [9,49,136,138,140–142,146,147,149] and attributed to molecular chain motion, whereby at higher cooling rates, the time available for the molecular chains to diffuse into the crystal lattice before a decline in chain mobility is reduced [49,138,146]. This generally results in a broadening of the exothermic peak and reduction in the degree of crystallinity, as the rate of crystallisation is insufficient in keeping up with the rapidly reducing temperature.

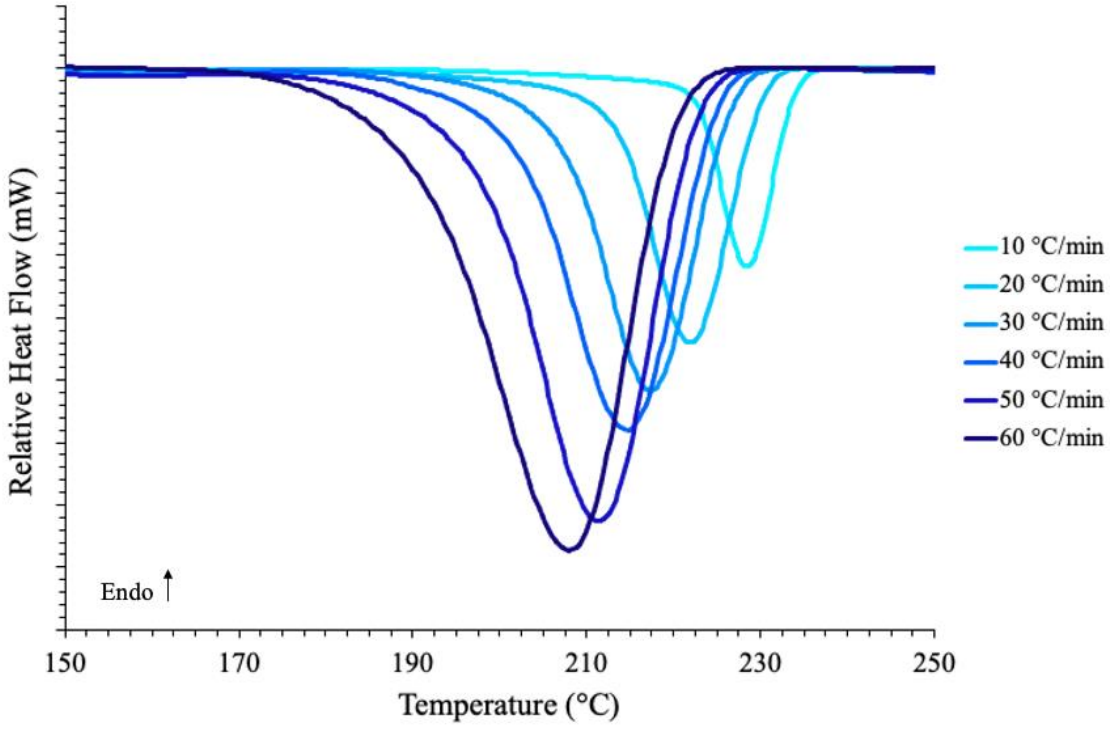

Figure 6.2: Showing the variations in heat flow (mW) of the non-isothermal crystallisation exotherms with temperature (°C) over a variety of cooling rates (10 to 60 °C/min).

Table 6.1: Displaying the crystallisation half-life (mins) values, along with the onset, peak and endset temperatures (°C) of the crystallisation exotherms over a cooling rate range 10 to 60 °C/min.

(°C/min)	$t^{1/2}$ (min)	$T_{c(onset)}$ (°C)	$T_{c(peak)}$ (°C)	$T_{c(endset)}$ (°C)
10	1.18	234.3	229.5	223.1
20	0.72	230.9	224.5	215.8
30	0.55	228.8	221.3	209.9
40	0.44	227.5	218.2	203.7
50	0.39	224.1	214.3	197.4
60	0.37	221.3	210.0	190.2

Fractional crystallinity (X_T) as a function of temperature at each cooling rate was quantified by dividing the cumulative area at sequential temperatures by the total area of the exotherm at $T_{c\ (endset)}$. The resulting traces, indicative of the rate of non-isothermal crystallisation at various cooling rates, follow a characteristic sigmoidal shaped curve, typical of phase transformation in polymers (Figure 6.3).

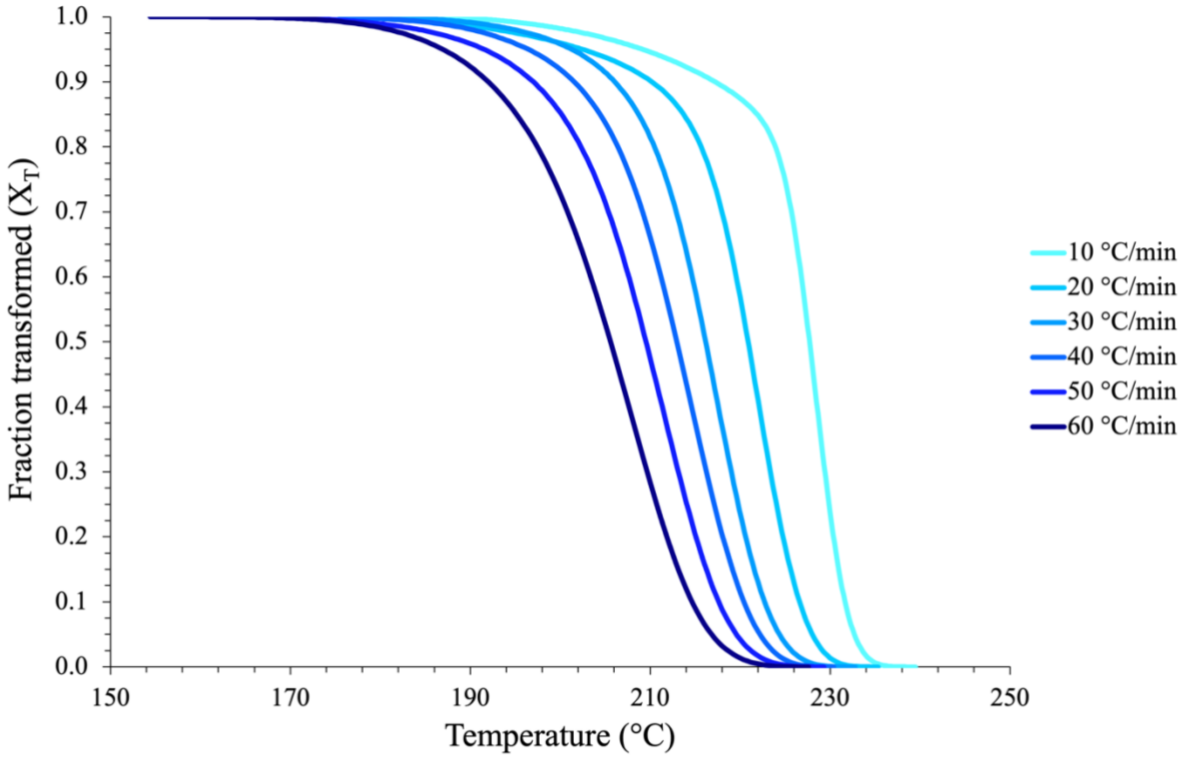

Figure 6.3: Illustrating the development of fractional crystallinity (X_T) with temperature (°C) throughout the non-isothermal crystallisation process at various cooling rates (10 to 60 °C/min).

The aforementioned shift of the crystallisation process, whereby the onset and subsequent crystallisation is shown to shift to lower crystallisation temperatures with incremental increases in cooling rate, is further emphasised in Figure 6.3. It is also worth noting from Figure 6.3, that at given temperature, the degree of fractional crystallinity increases with decreasing cooling rate. At slower cooling rates (e.g. 10 °C/min) the polymer system has more time to form crystal

nuclei at higher temperatures, resulting in the growth of polymer crystals with a higher degree of perfection. Conversely, at higher cooling rates (e.g. 60 °C/min) and where the crystallisation process shifts to lower temperatures, the kinetic energy of the molecular chains reduces, resulting in crystal imperfections and an observed broadening of the exothermic peak [140]. Similar observations were made on PA6/GF [141] and PA66/GF [49] composites, with the latter concluding that the addition of glass fibres to the polyamide matrix reduces the time required to form crystal nuclei and thus, increases $T_{c\,(onset)}$ and $T_{c\,(peak)}$ by 3 and 7 °C, respectively [49].

Fractional crystallinity as a function of time can also be determined by the following equation:

$$t = \frac{|T_s - T|}{\varphi}$$

Equation 6-6

Where T is the temperature at a given crystallisation time t, T_s is the temperature at which crystallisation starts and φ is cooling rate. As shown in Figure 6.4, the time taken to achieve completion of the crystallisation process is reduced with increasing cooling rate.

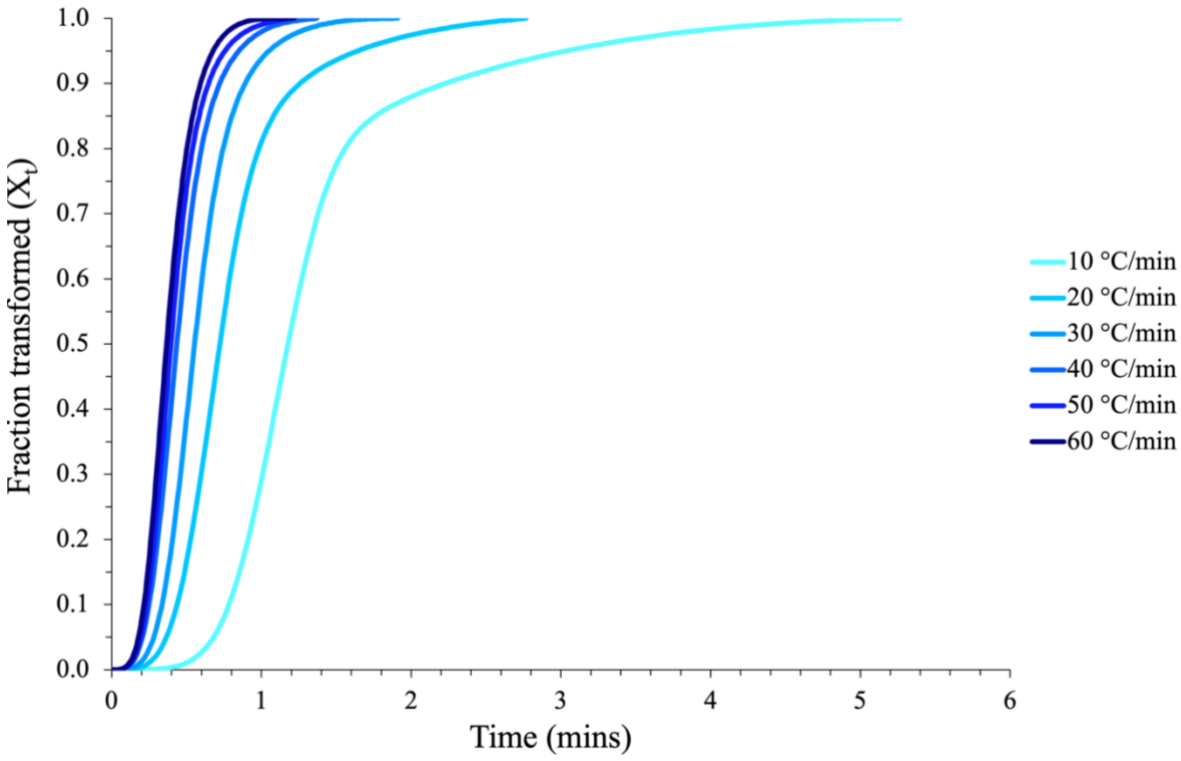

Figure 6.4: Development in Fractional crystallinity (X_t) as a function of crystallisation time (mins) at a variety of cooling rates (10 to 60 °C/min).

This is reflected in the values of $t_{1/2}$ (Table 6.1). On cooling from the melt at 60 °C/min, a fractional crystallinity of 50% is achieved three times faster than cooling at 10 °C/min. Additionally, as cooling rate is increased, the time difference between sequential curves for any given value of X_t decreases. The progressively faster crystallisation rate observed with increased φ is in large due to the quicker rate of crystallisation at lower temperatures compared to those seen at higher temperatures, as highlighted previously with isothermal crystallisation (Chapter 5).

6.3.2 Non-isothermal crystallisation kinetic analysis using the Jeziorny model

Jeziorny adopts a two-stage analytical procedure, in which the traditional Avrami analysis is initially applied, before being adapted using Equation 6-1 to modify the crystallisation rate constant Z, relative to the cooling rate. The traditional Avrami plots of $\ln(-\ln(1-X_t))$ vs. $\mathrm{Ln}\, t$ are shown in Figure 6.5, where similar to the isothermal Avrami analysis discussed in Chapter 5.3.2.1, experimental data was restricted to fractional crystallinities between 3 and 50%. This accounts for both the incipient crystallisation (below 3%) where spontaneous nuclei growing from the melt have not overcome the energy (ΔG) required for the formation of a stable nuclei (section 1.3.1) and the limitations of the Avrami model in neglecting the secondary process (above 50%). Thus, data was restricted to the primary crystallisation region.

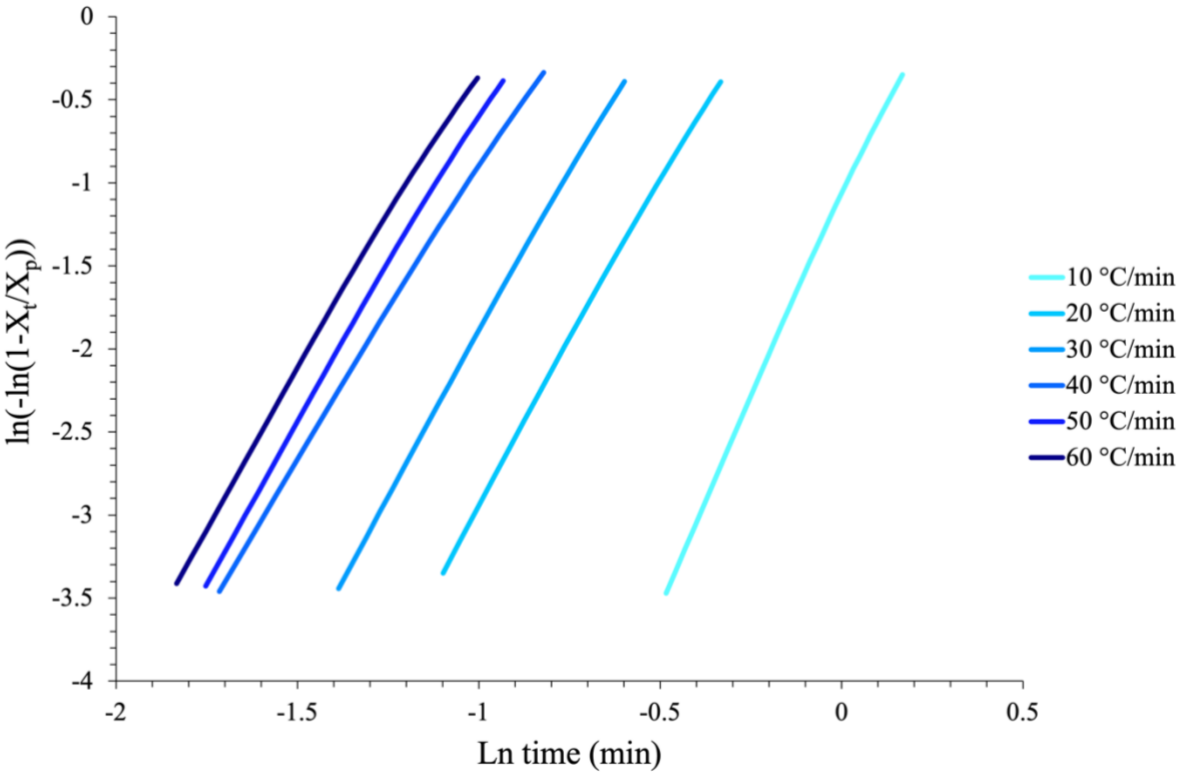

Figure 6.5: Avrami plot of fractional crystallinity ($0.03 < X_t < 0.5$) over the cooling rate range 10 to 60 °C/min.

The linearity of the plots shows the Avrami equation to provide a good fit to the experimental data over the primary region, with coefficients of determination (R^2) greater than 0.9988 generally recorded. The crystallisation kinetic parameters n_a and Z_t were determined from the gradient and intercept of the plots, respectively, with Z_t modified using the Jeziorny equation (Equation 6-1) and the results displayed in Table 6.2.

Table 6.2: Jeziorny crystallisation kinetic parameters derived from the standard Avrami double log plots over the cooling rate range 10 to 60 °C/min and corrected using Equation 6-1.

(°C/min)	n	Ln Z_t	Ln Z_c	Z_c	R^2
10	4.83	-1.088	-0.109	0.897	0.9989
20	3.87	0.945	0.047	1.048	0.9993
30	3.89	1.980	0.066	1.068	0.9995
40	3.51	2.599	0.065	1.067	0.9992
50	3.73	3.160	0.063	1.065	0.9991
60	3.70	3.410	0.057	1.058	0.9988

Excluding the Avrami exponent recorded at 10 °C/min, the value of *n* remains reasonably consistent across all cooling rates, with a recorded average of 3.74. This is comparable to a previous study on PA66 [136] and indicates that the nucleation and growth mechanisms are complex but implies that the geometry of crystal growth is three-dimensional, which is in general agreement with previous studies of pure PA66 [119,136] and PA12 [138]. The difference in the value of *n* recorded at a cooling rate of 10 °C/min is likely a result of a change in the crystal growth mechanism between slow and fast cooling rates. Furthermore, as this was the slowest cooling rate used within this study, thus providing the polymer chains with the longest time to crystalise, it seems plausible that secondary crystallisation could be greater at

this rate (10 °C/min) compared to that achievable at high cooling rates. It would be fascinating to widen the cooling rate range by reducing the minimum rate to see if similar observations are made.

Z_c is shown to be independent of cooling rate, with an average value of 1.03 min^{-n} recorded across the cooling rate range. This finding contradicts several previous studies on polyamides, where it was reported that Z_c gradually increases with cooling rate [49,136,139–141]. That said, in two recent studies on PA66 [136,149], Z_c was observed to increase with cooling rate between 2 and 10 °C/min, before leveling off at cooling rates >10 °C/min, comparable to the findings of this study. Furthermore, as discussed in section 6.1.4.1 the rate of crystallisation of PMC is greatly dependent on the quantity of fibre reinforcement. As the PA66/GF samples used throughout this study contain approximately 10 wt.% more glass fibre reinforcement than the reported optimum value, it could be assumed that the quantity of glass fibre impedes the crystallisation of the polyamide matrix. This could also explain why the values of Z_c listed in Table 6.2, which remain unchanged irrespective of cooling rate, differ to the values of Z_c reported in the literature, where PMC with glass fibre quantities <30 wt.% have been used [9,49,139].

6.3.3 Non-isothermal crystallisation kinetic analysis using the Ozawa model

Formed on the assumption that crystallisation occurs at a constant cooling rate and that the non-isothermal process is fundamentally composed of an infinite number of isothermal steps, Ozawa endeavoured to modify the Avrami equation (Equation 6-2). Ozawa's model essentially quantifies fractional crystallinity as a function of crystallisation temperature at various cooling rates.

Fractional crystallinity as a function of temperature was determined by integrating the area of the exothermic peaks and dividing the cumulative area at sequential crystallisation temperatures by the cumulative area at T_{end} (assumed to be the temperature at which the exotherm first returns to the baseline value). A suitable temperature range (202 to 220 °C), which incorporates a portion of each of the crystallisation exotherms was then selected and fractional crystallinity as a function of temperature and cooling rate determined for each isothermal step. In order for the equation to be valid, linearity in the plot of $\ln(-\ln(1-X_T))$ vs $\ln\varphi$ should be observed. Figure 6.6 shows that over a crystallisation temperature range of 202 to 220 °C, the Ozawa plot does not produce a linear fit and thus, the Ozawa model was deemed unsuitable in describing the non-isothermal crystallisation kinetics of PA66/GF over the cooling rate range 10 to 60 °C/min. This is in agreement with findings in the literature, where the Ozawa equation was shown to be inadequate in modelling the non-isothermal crystallisation kinetics of numerous polyamides [138,146,148]. The most frequent explanation for this being Ozawa's failure to consider the effects of secondary crystallisation [138,146,148].

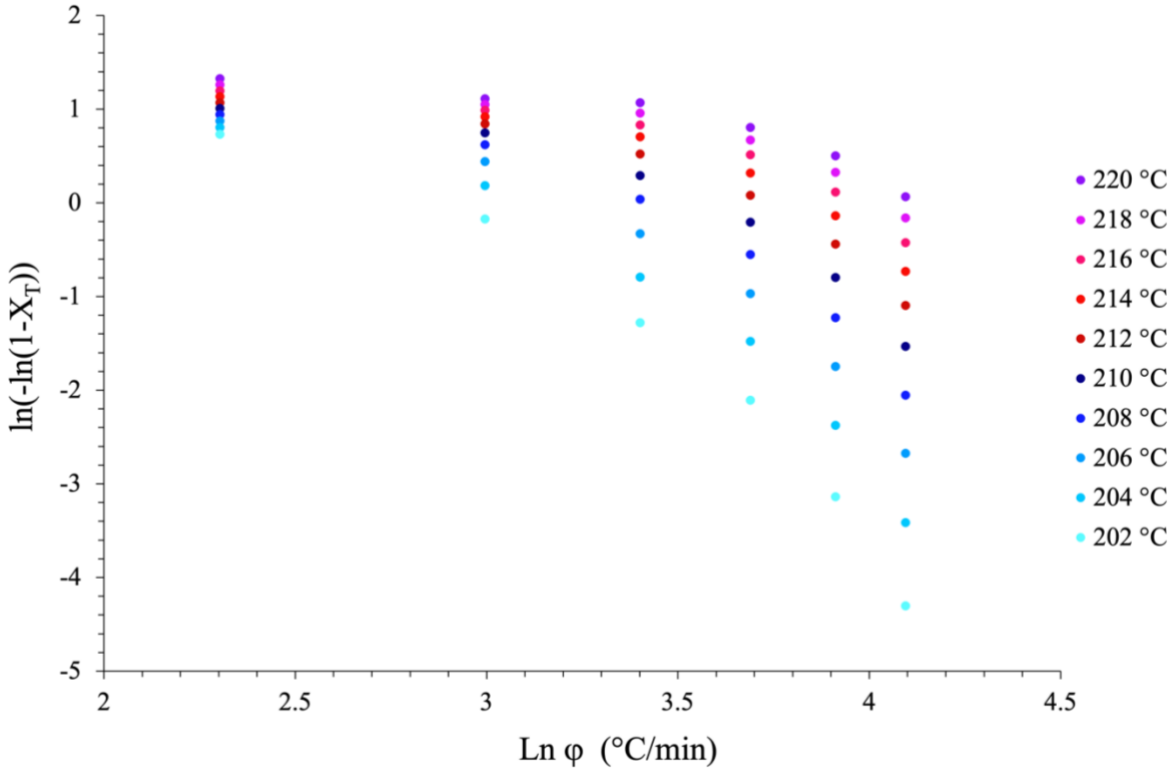

Figure 6.6: Ozawa plot of $\ln(-\ln(1-X_t))$ vs $\ln\varphi$ for PA66/GF over the crystallisation temperature range 202 to 220 °C.

Ozawa assumes that as temperature continuously decreases throughout the non-isothermal crystallisation process and that secondary crystallisation only occurs in the latter stages, its effect on the resulting crystallisation kinetics is negligible [138,144,146]. However, as proven recently by Hay et al. [91,92] in studies on the kinetics of isothermal crystallisation, the secondary process was shown to proceed in parallel to primary crystallisation [91,92]. This in agreement with the results of the earlier isothermal study (Chapter 5), where the Hay and parallel Velisaris-Seferis models were shown to describe the isothermal crystallisation kinetics of PA66/GF most effectively. This implies that secondary crystallisation occurs throughout the crystallisation process, profoundly influencing the resulting fractional crystallinity and thus, must be accounted for [91,92,138,140,146].

Despite the Ozawa model failing to accurately describe the non-isothermal crystallisation process over the entire cooling rate range, some linearity was observed at higher cooling rates (30 to 60 °C/min). Figure 6.7 shows the fit of the Ozawa model to the experimental data restricted to the cooling rates between 30 and 60 °C/min. A similar observation was made by McFerran et al. [138] in the study of PA12, where a two-stage crystallisation process was observed [138]. Using Figure 6.7, the Ozawa exponent *m* and temperature dependent crystallisation rate constant *K(T)*, were determined from the gradient and intercept of the lines, respectively. These values are listed in Table 6.3 along with the resulting coefficients of determination (R^2) recorded over the reduced cooling rate range.

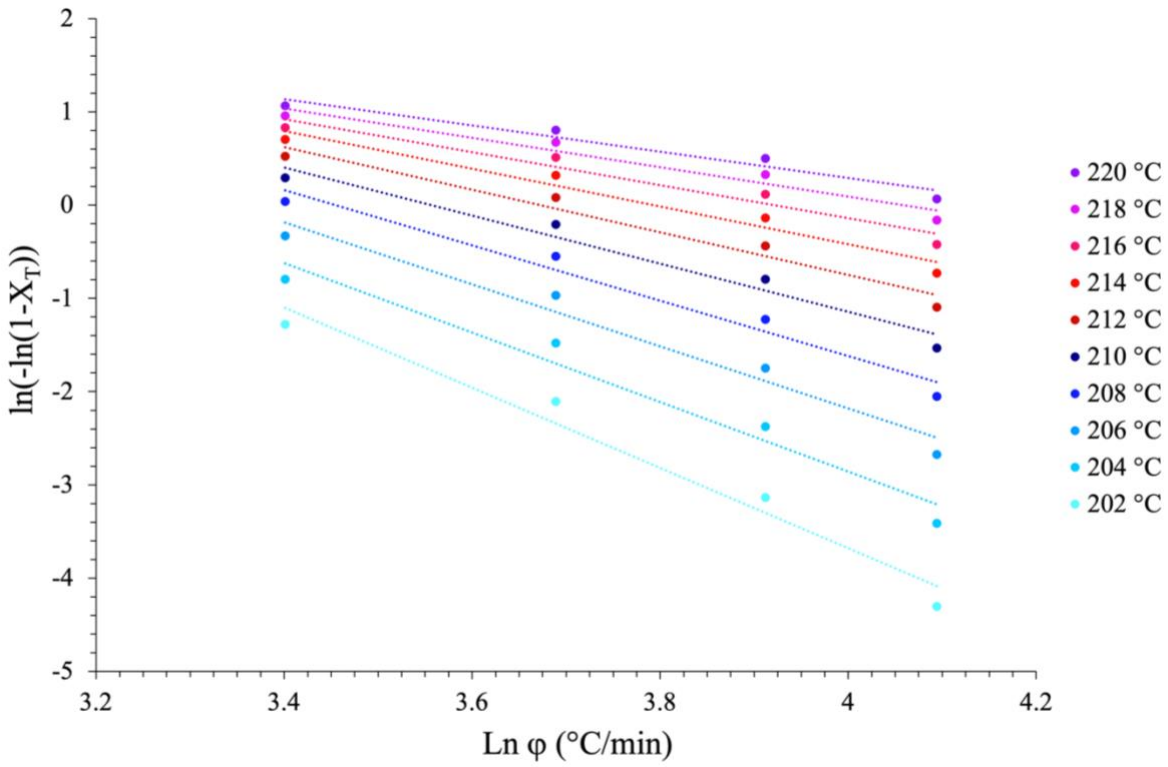

Figure 6.7: Ozawa plot of $\ln(-\ln(1-X_t))$ vs $\ln\varphi$ for PA66/GF over the crystallisation temperature range 202 to 220 °C, where φ was restricted to rates between 30 and 60 °C/min.

Table 6.3: Ozawa crystallisation kinetic parameters derived from a plot of $\ln(-\ln(1-X_t))$ vs $\ln\varphi$ over the crystallisation temperature range 202 to 220 °C.

Temperature (°C)	*m*	Ln K_c	K_c (x10^{-3})	R^2
202	4.31	13.55	765.28	0.969
204	3.73	12.05	170.76	0.963
206	3.33	11.13	67.91	0.966
208	2.96	10.24	28.00	0.969
210	2.58	9.18	9.69	0.965
212	2.29	8.41	4.48	0.964
214	2.03	7.69	2.18	0.961
216	1.77	6.93	1.02	0.953
218	1.57	6.38	0.59	0.952
220	1.41	5.92	0.37	0.952

Derived from a modification of the Avrami equation, *m* and *K(T)* share a similar physical meaning to that of the non-isothermal Avrami kinetic parameters, *n* and Z_t. The recorded values of *m* and *K(T)* are listed in Table 6.3 and are observed to decrease with increasing temperature. As described in Chapter 5, when considering the kinetics of isothermal crystallisation, an optimal crystallisation temperature is found to exist between the upper and lower bounds of the T_c range (T_g and T_m). At this temperature, the rate of crystallisation is at its fastest due to an optimum compromise between the two competing stages of the crystallisation process: nucleation and crystal growth. This would explain why, that with decreasing temperature the value of *K(T)* and thus, the rate of crystallisation is observed to increase, as T_c approaches an optimal crystallisation rate temperature.

The values of *m* were found to be consistent with a previous study on PA66/GF [139], however, *m* was observed to vary significantly across the temperature range studied. This implies that the mechanism of nucleation and geometry of crystal growth are somewhat complicated. Previous

work [138,140] on polyamides has also shown this, with the variation in *m* believed to be caused by the dynamic crystallisation process, whereby the rate of crystallisation is no longer constant, but a function of time and cooling rate [138,142].

6.3.4 Non-isothermal crystallisation kinetic analysis using Mo's theory

After acknowledging the theories proposed by Avrami and Ozawa, and recognising their limitations, Liu et al. [145] derived a new kinetic model (Mo's theory) comprising both the Avrami and Ozawa equations [145]. For Mo's theory to be valid, a plot of $\log \varphi$ vs $\log t$ as a function of the relative degree of crystallinity, should produce a series of straight lines, from which the kinetic parameters, *b* and *F(T)* can be determined.

Figure 6.8 shows that Mo's theory accurately describes the non-isothermal crystallisation process of PA66/GF. This is emphasised by the goodness in fit over the relative crystallinity range 10 to 90 %, as reflected in the coefficients of determination ($R^2 > 0.989$) listed in Table 6.4.

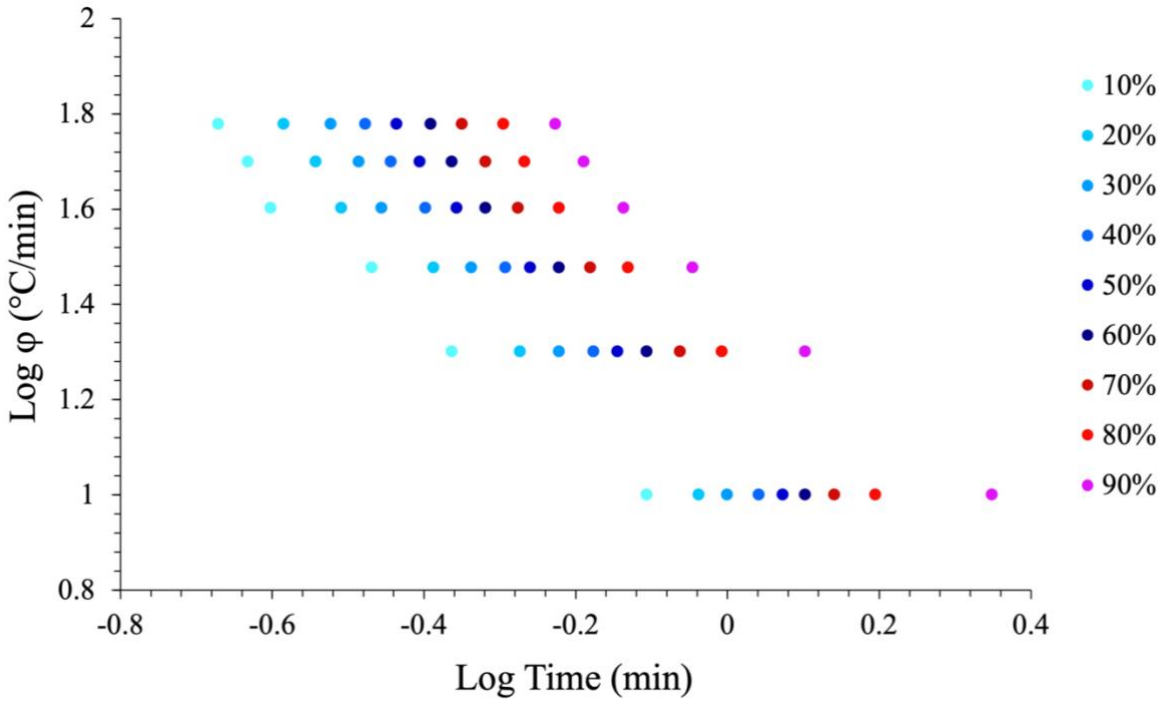

Figure 6.8: Combined Avrami/Ozawa plots for PA66/GF over the fractional crystallinity range 10 to 90% X_t.

Table 6.4: Values of the kinetic parameters F(T) and b as a function of X_t as derived from a combined Avrami/Ozawa approach.

X_t (%)	Log *F(T)*	*F(T)*	*b*	R^2
10	0.841	2.32	1.34	0.989
20	0.936	2.55	1.39	0.993
30	0.990	2.69	1.44	0.992
40	1.051	2.86	1.46	0.995
50	1.096	2.99	1.49	0.995
60	1.146	3.14	1.53	0.994
70	1.208	3.35	1.54	0.995
80	1.290	3.63	1.53	0.994
90	1.444	4.24	1.32	0.993

After validating the model, the kinetic parameters, *b* and *F(T)* were derived from the gradient and intercept of the lines, respectively (Table 6.4). *F(T)* refers to the necessary cooling rate required to achieve a defined degree of crystallinity at unit crystallisation time and was observed to increase systematically with relative crystallinity. This is in good agreement with findings in the literature and signifies that at a given unit crystallisation time, a greater cooling rate is required to obtain a higher degree of relative crystallinity [49,138–142]. Additionally, the smaller the value of *F(T)*, the quicker the rate of crystallisation [139,140]. Therefore, excluding nucleation where the rate of crystal growth is typically slow, this denotes that crystallisation rate is fastest at low degrees of relative crystallinity, gradually decreasing as X_t increases and approaches 1.0.

In contrast to *K(T)*, the value of *b* remained somewhat unchanged with increasing crystallinity, remaining comparatively consistent throughout the crystallisation process with an average value of 1.45. This is in approximate keeping with studies on PA66 and PA66/GF, where *b* was also found to be consistent throughout the crystallisation process with recorded values of 1.33 to 2.14 [49,136,139,140].

6.4 Conclusions

In keeping with the findings of the literature, Mo's theory is shown to provide the best fit to the experimental data when describing the non-isothermal crystallisation of polyamides [49,136,138–140,142,146–148]. Contrary to both the Jeziorny and Ozawa models, where neither model provides a linear fit to the experimental data, nor accurately accounts for secondary crystallisation, Mo's combined Avrami/Ozawa approach is proven to successfully describes the non-isothermal crystallisation of PA66/GF.

CHAPTER 7 - THE EFFECT OF LOW TEMPERATURE ANNEALING ON MORPHOLOGICAL EVOLUTION AND CREEP RESISTANCE IN PA66/GF COMPOSITES

7.1 Introduction

7.1.1 Thermoplastics and creep behaviour

The use of thermoplastics for engineering applications, specifically within the automotive industry, requires that the mechanical properties of the thermoplastic part are adequate and sufficient to replace that of the existing structural metallic components. The mechanical performance, thermal properties and shape stabilisation of thermoplastics can be improved by the addition of glass or carbon fibre reinforcement (Table 1.1). PA66 fibre reinforced composites exhibit excellent thermo-mechanical properties, including fatigue strength (64.1 MPa) and flexural strength (270 MPa), further compared to unfilled PA66, glass filled PA66 have improved Young's moduli (10 GPa) and fracture toughness (10.3 MPa.m$^{0.5}$) ideal for engineering applications [9,11]. In addition to possessing desirable mechanical properties, PA66 is cheaper than alternative engineering thermoplastics such as PEEK [10], making it highly appealing for automotive applications such as, dashboards, air intake manifolds and engine covers. The mechanical properties of polyamide 66 glass fibre reinforced composites including fatigue behaviour [150] and tensile performance [10] are widely reported throughout the literature, however, despite many admirable properties, a significant shortcoming of polyamides is their inherent susceptibility to creep.

Creep is a time-dependent permanent deformation process resulting from prolonged exposure to a constant stress below the elastic limit (yield stress) of a material. Owing to their viscoelastic

nature, that is, demonstrating solid- or liquid-like behaviour as a function of time, thermoplastics are inherently susceptible to creep [13,15]. The creep behaviour of a polymeric material can typically be divided into four regions (Figure 7.1); instantaneous, primary, secondary and tertiary, each determined by a variation in the velocity of creep deformation (creep rate) [13]. After the initial rise in creep rate caused by the application of a constant stress and the elastic, instantaneous strain placed upon the material, rate deteriorates throughout the primary process [13,151]. Here chain slippage and orientation are deemed to occur under the persistent stress inducing a strain hardening effect and thus, a decrease in creep rate [13,151]. Subsequently, a steady-state creep rate is observed whereby a time-dependent viscoelastic flow of the thermoplastic occurs [13,15,151]. Deemed the secondary region, this steady-state creep rate generally persists for extended periods of time conditional to the applied stress and environmental conditions [13,152]. Eventually, creep rate increases, and failure occurs, characteristic of the tertiary stage.

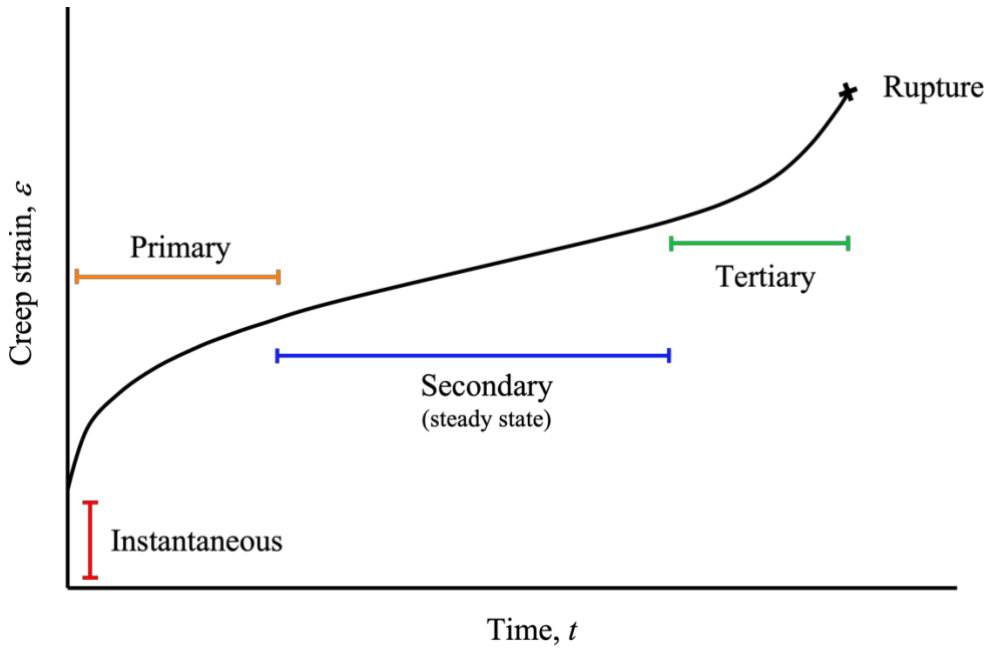

Figure 7.1: Schematic illustration of creep strain as a function of time, showing the four stages of the creep cycle; instantaneous strain, primary, secondary and tertiary regions.

Creep behaviour is incredibly important in engineering applications, especially for structural components where dimensional stability is a necessity. Thermoplastics demonstrating significant time sensitive properties under the necessary working conditions will be of limited use [13,15]. That said, resulting from their viscoelastic nature, thermoplastic mechanical properties including modulus and impact strength are inherently time sensitive [13]. Typically, the instantaneous response to an applied load is elastic, with load-bearing capability determined by the crystalline fraction of the material. However, with increasing time, viscoelastic strains develop within the amorphous fraction and orientational strain hardening occurs [14,153]. Despite this, if the time sensitivity of the properties is well understood, creep behaviour of thermoplastics can be accounted for by shrewd part design, modification of crystal morphology or the addition of fillers [13,154].

The creep performance of polyamide composites [152–160], including time-sensitive, flexural properties such as bending stiffness [157] and strength [158] have been studied previously, with the effect of crystallinity and influence of fibre-reinforcement widely reported [154,157–160]. In addition to improving mechanical properties such as Young's modulus and strength, the incorporation of fibre-reinforcement has been proven to enhance the creep resistance properties of polyamide matrix composites [154,157,159,160]. Creep compliance is observed to decrease with increasing fibre volume fraction and length [158,160], with long glass fibre reinforcement shown to outperform short fibres through improved load transfer, ultimately reducing the stress endured by the matrix material [158]. Moreover, Lafranche et al. [158] and Chevali et al. [160] report that fibre orientation is critical in maximising the effect on creep performance [158,160]. Longitudinally orientated fibres improve creep resistance by reducing both the instantaneous deformation of the material and creep rate during the secondary creep stage compared to that of transversely sequenced fibres [158,160].

Furthermore, the mechanical properties and creep behaviour of polyamide composites can be controlled by the crystal microstructure. Sakai et al. [154,157] demonstrated that both the load-bearing ability of carbon fibre reinforced PA6 [157] and creep behaviour of glass fibre reinforced PA66 [154] are heavily influenced by crystallinity. They report that performance depends on the geometry of crystalline domains, with improvements in creep behaviour post-high temperature annealing (T_a = 220 or 250 °C), attributed to increased crystallinity [154]. Consequently, improvements in the mechanical properties and creep resistance of polyamide composites can be enhanced by fibre reinforcement and/or modifications of the crystal microstructure such as those resulting from post-processing annealing. Despite this, studies on the effects of heat treatment processes, such as low temperature annealing and its associated microstructural adaptations on the creep performance of polyamide fibre reinforced composites are limited.

7.1.2 Annealing of thermoplastics

As discussed in detail in Chapters 1.1.3 – 3.3, thermoforming (and the associated processing parameters) of thermoplastics and PMC can profoundly influence the microstructure and morphology of polymeric materials. Throughout the forming process, the degree of crystallinity, crystal form (polymorphism) and subsequent morphology (lamella thickness/ crystal perfection) of the thermoplastic is controlled by the rate of cooling. In thicker samples of PMC, this can lead to disparities in through-thickness crystallisation kinetics, often resulting in microstructural gradient effects between the skin and core regions [57–59]. Typically, the high cooling rates associated with thermoforming provide insufficient time for completion of the crystallisation process, which can consequentially cause a deterioration in mechanical properties.

Annealing is a time-temperature dependent; heat treatment process used to enhance the thermal and mechanical properties of thermoplastics post-processing. Both parameters (temperature and time) of the heat treatment procedure must be sufficient to enable the microstructural adaptations required for improvements in the aforementioned properties of the material. Annealing of thermoplastics occurs between T_g and T_m, where the mobility of the polymer chains is adequate for such modifications. The extent of the annealing process on microstructural changes [36,161–166] and the resulting mechanical properties [161,167] of thermoplastics are widely reported throughout the literature.

Frequently characterised using differential scanning calorimetry (DSC) [162–166], the annealing of thermoplastics routinely results in the appearance of multiple endothermic melting peaks within a DSC thermogram [162–166]. This typically consists of the main melting peak and a new post-annealing low temperature peak. The area of the peaks and temperature at which they occur is evidenced to be dependent on annealing temperature (T_a) and time (t_a) [162–166]. The low-temperature melting peak characteristically appears slightly above T_a, with Kaya and Mathias [162] reporting a 12 °C difference in temperature (ΔT) between T_a and the resulting low temperature melting peak in PA18 18 [162]. Conversely, Castagnet and Thilly [163] report that for PA11 the value of ΔT is not constant and was observed to decrease as T_a increased towards T_m [163]. Several explanations have been provided as to the nature of the subsequent low-temperature melting peak, these include polymorphic transitions, lamella thickening, melt-recrystallisation, crystal perfecting and secondary crystallisation [162–165,168]. Furthermore, owing to the temperature dependence of the annealing process, the microstructural changes contributing to the existence of the peak have been shown to differ under high and low annealing temperatures, with a critical cross-over temperature often reported [162–165].

At high annealing temperatures ($T_a \geq 190$ °C), energy is sufficient to enable perfecting of the existing polymer crystals and the thickening of crystalline lamella [161,163,168]. Consequently, the low temperature melting peak generally occurs close to T_m, often appearing as a low temperature shoulder off the main melting peak [162,163,165]. However, despite the effects of high temperature annealing on the crystal structure, the overall crystallinity has been shown to remain somewhat unchanged unless the thermal energy is adequate to allow excessive chain motion and the re-ordering of pre-formed hydrogen bonds established during primary crystallisation [162,165]. This was verified by Shan et al. [165], who in a study on PA6 reported that as T_a approaches T_m ($T_a \geq 190$ °C), partial melting of the pre-existing crystals occurs throughout the annealing process, with a so-called melt-recrystallisation process resulting in the merging of the low and high temperature melting peaks within the respective DSC thermogram [165]. The re-ordering of hydrogen bonds was further confirmed by FTIR spectroscopy [36]. Lu et al. [36] revealed that their observed changes in intensity and breadth of the amide 1 peak of PA66 were characteristic of a reduced distribution in the perfection of hydrogen bonding, whereby annealing close to T_m ($T_a = 210$ °C) allowed for improvements in the ordering of previously disordered bonds [36]. Despite this, resulting from known strength of hydrogen bonds and knowledge of their retention above T_m, Lu et al. [36] conclude that only disordered bonds can become more perfected, with enhancements in the perfection of pre-existing ordered bonds not feasible throughout the annealing process and thus, only small enhancements in the overall crystal framework are made [36]. This is in good agreement with the aforementioned findings of Kaya and Mathias [162].

Conversely, on lowering T_a, the size, area and temperature at which the low temperature melting peak occurs are reduced. Additionally, in contrast to annealing at higher temperatures, annealing close to T_g is not observed to influence the main melting peak, with T_m and the

enthalpy of fusion remaining relatively unchanged [162]. This discrepancy is attributed to the disparity in thermal energy available to the molecular chains throughout the high and low temperature annealing processes [162,163]. Dissimilar to the perfecting of crystals at high T_a, the energy existing at low annealing temperatures is considered insufficient for the extensive molecular motion required for the re-organisation of thermally stable, thick lamella structures [36,162,163]. Instead, a secondary process is believed to ensue in the mobile interlamella amorphous regions [163,164,168]. Here small crystalline arrangements and thin lamella are thought to form, with Marand et al. [166] defining this secondary process as any improvement in crystallinity not attributed to the chain folding lamella growth associated with that of primary crystallisation [166]. The process was further characterised by Castagnet and Thilly [163] and Shan et al. [165] who describe the secondary process and low temperature endothermic peak of polyamides as the melting of thin lamella structures formed on annealing at temperatures slightly above T_g. They demonstrate that at annealing temperatures between 60 and 175 °C the temperature and area of the low temperature peak grows with T_a, deducing that at higher T_a, crystals of greater perfection and lamella thickness are formed [163,165]. Thus, it follows that the melting of these crystals will occur at higher temperatures as defined by Lauritzen and Hoffman [169]. Despite this observed temperature dependence, Castagnet and Thilly [163] report that at annealing temperatures <160 °C the enthalpy of fusion of the low temperature peak is typically only 1-3% of that of the main melting peak [163]. Furthermore, they speculate that as annealing often occurs within the Brill transition of polyamides, polymorphic transitions may also result in the appearance of a post-annealing low temperature peak, such as those observed by Dencheva et al. [170] in cold-drawn PA6. Nevertheless, when characterising the effects of annealing on the microstructural changes of PA6, Shan et al. [165] conclude that no crystal transformations were observed in the WAXS patterns of PA6 post-annealing and as

such, deduce that the low temperature melting peak observed in the DSC thermograms was not a result of a polymorphic crystal transformation [165].

Besides the temperature dependence of the annealing process, annealing time (t_a) has an influential effect on the extent of microstructural changes observed throughout the annealing process [163–166]. Multiple studies on various polyamides have shown the low temperature melting peak, characteristic of microstructural adaptations post-annealing, to increase in amplitude and area with increasing t_a [165,166]. This increase in area and thus, enthalpy of fusion with increasing t_a is attributed to the excess time available for the formation of thin lamella structures and small secondary crystals [163–166] at a given annealing temperature.

7.1.2.1 Influence of moisture on annealing of polyamides

Resulting from the polarity of the amide (N-H) and carbonyl (C=O) groups, polyamides are inherently hygroscopic materials. The strong attraction between the polar groups of the water molecules and that of the amide functional groups typically results in the weakening of intermolecular hydrogen bonds (H-bonds) and the formation of new H-bonds between the polymer chains and absorbed water molecules [171,172]. This generally causes a reduction in T_g, with an observed deterioration in dimensional stability [173]. The impact of this, known as plasticisation, strongly influences the mechanical performance of the polymer by enhancing molecular mobility and thus, causing a reduction in mechanical properties such as yield stress and fracture strain [174,175]. Furthermore, diffusion of the water molecules into the matrix polymer is enhanced upon heating above T_g. This thermally activated diffusion process often results in the hydrothermal decomposition of the polyamide chains [173,176].

7.1.3 Aims and objectives

As discussed in the retrospective chapters, stamp forming of thermoplastic composites is a distinctly non-isothermal process in which, the time available for crystallisation of the polymer matrix on cooling from the melt is limited. This can have a profound effect on the resulting degree of crystallinity of the PMC and when combined with thermoplastics inherent susceptibility to creep behaviour, can be influential in the mechanical performance of the composite part.

It has been shown previously that post-processing low temperature annealing can alter the crystal microstructure of thermoplastics, however no study is yet to relate these changes to improvements in creep performance of thermoplastic parts. This chapter aims to further the work of previous authors by both qualitatively analysing and quantitatively measuring the effects of low temperature annealing on the crystal morphology and creep performance of PA66/GF composites. Contrary to previous studies in the literature, differential scanning calorimetry and creep testing will be employed simultaneously to both quantify differences in lamellar thickness using the Thomson-Gibbs equation and determine the subsequent changes in creep performance (creep strain and creep modulus) as a result of post-processing low temperature annealing, respectively.

7.2 Methodology

7.2.1 Morphological effects of low temperature annealing as measured by DSC analysis

7.2.1.1 Materials and sample preparation

Pre-impregnated glass fibre reinforced polyamide 66 (PA66/GF) tape was used to study the morphological effects of low temperature annealing. Prior to the annealing process, samples suitable for DSC analysis were extracted from the tape using a circular hole-punch (4.8 mm diameter) and dried in a desiccator for a minimum of 24 hours.

7.2.1.1.1 Annealing process

After drying, three of the disc-shaped samples were stacked, weighed, and hermetically sealed within 40 µl aluminium crucibles. Annealing of the samples was performed using a Mettler Toledo DSC1 (Greifensee, Switzerland), calibrated with indium and zinc standards. Prior to annealing samples were heated to 295 °C and held for 30 s to enable consolidation of the stacked discs and erase the effects of thermal history. Samples were then cooled to -10 °C at 50 °C/min before being re-heated at 40 °C/min to one of six annealing temperatures (60 – 110 °C) and isothermally held for various lengths of time (1 – 12 hrs).

7.2.1.2 Differential scanning calorimetry measurements

Post-annealing samples were quickly cooled (50 °C/min) to -10 °C before being re-heated to 295 °C at 40 °C/min with change in heat flow as a function of temperature recorded. Peak melting temperatures were determined, and the heat of fusion calculated from integrating the area of the melting peak and interpolated baseline between the onset of melting and last trace of crystallinity (Chapter 2.2.1.1). The weight fraction degree of crystallinity was determined

using Equation 2-1 (Chapter 2.2.1.1), where a literature value of 191 J/g [43] was taken as the heat of fusion of a perfectly crystalline PA66 sample ($\Delta H_{f\infty}$).

Given that the measurement of the heat of fusion requires an accurate value for the polyamide mass fraction, each of the DSC samples was removed from the aluminium crucible post-analysis and subjected to a matrix burnout procedure outlined in Chapter 2.2.3.

7.2.2 Creep testing

7.2.2.1 Materials and sample preparation

Creep tests were performed on fully consolidated PA66/GF composite laminates. Square (300 x 300 mm) pre-impregnated sheets of PA66/GF tape were stacked into 4-ply laminates of unidirectional (0°) and cross-ply (0/90/90/0) sequence. The laminates were then heated to 270 °C and rapidly stamp formed in a heated press. Tool temperature and applied clamping force were approximately 120 °C and 800 kN, respectively. Laminates were then cut into beams suitable for testing (~130 x 20 x 1.2 mm).

7.2.2.1.1 Annealing process

Prior to annealing, samples were dried in a desiccator for a minimum of 24 hours. To determine the effect of water present within the samples, annealing was also performed on an undried sample and the results compared. After drying, the test specimens were annealed in a preheated oven at one of two annealing temperatures (80 or 110 °C) for various lengths of time (1 to 164 hrs).

7.2.2.2 Creep measurements

Creep measurements were performed under flexural bending using a three-point bend testing fixture. Test specimens were carefully positioned atop two support fixtures (100 mm apart) and a constant load of 0.5 kg (hooked weight) applied to the centre of the test beams. Measurements of displacement (mm) as a function of time under constant load were recorded for all samples. For the undried samples (section 7.3.4.1) a displacement dial gauge was used to record changes in deflection. However thereafter, a linear variable displacement transducer (LVDT) was attached to the testing fixture directly above the centre of the test specimen with changes in resistance (ohms) measured before being converted to displacement (mm). Samples were tested over an 8-hour period with a data point frequency of 180 seconds[2]. Data was recorded using LabView software and analysed using Microsoft Excel.

[2] Creep tests were limited to an 8-hour period resulting from covid-19 laboratory restrictions. Ideally samples would have been run over several weeks/months, however providing the measurement time exceeds the initial non-linear creep strain response the results should not be compromised.

7.3 Results and discussion

7.3.1 Morphological refinements of PA66/GF with low temperature annealing

Low temperature annealing of polyamide 66 glass fibre reinforced (PA66/GF) laminates was performed above the glass-to-liquid transition temperature (T_g) of the matrix polymer at multiple annealing temperatures (T_a); 60, 70, 80, 90, 100 and 110 °C, and for various lengths of time (1 to 12 hours). As illustrated in Figure 7.2 for an annealing temperature of 90 °C, DSC thermograms obtained post-annealing were all observed to show a small endothermic peak within the DSC trace irrespective of T_a or annealing time (t_a). Located at temperatures slightly above that of T_a, the newly formed low temperature peak is separate to that of the high temperature endothermic peak associated with melting of the bulk polymer crystals and furthermore, was not present within the DSC thermograms during the second heating run. These findings are consistent with those previously reported within the literature [163,165].

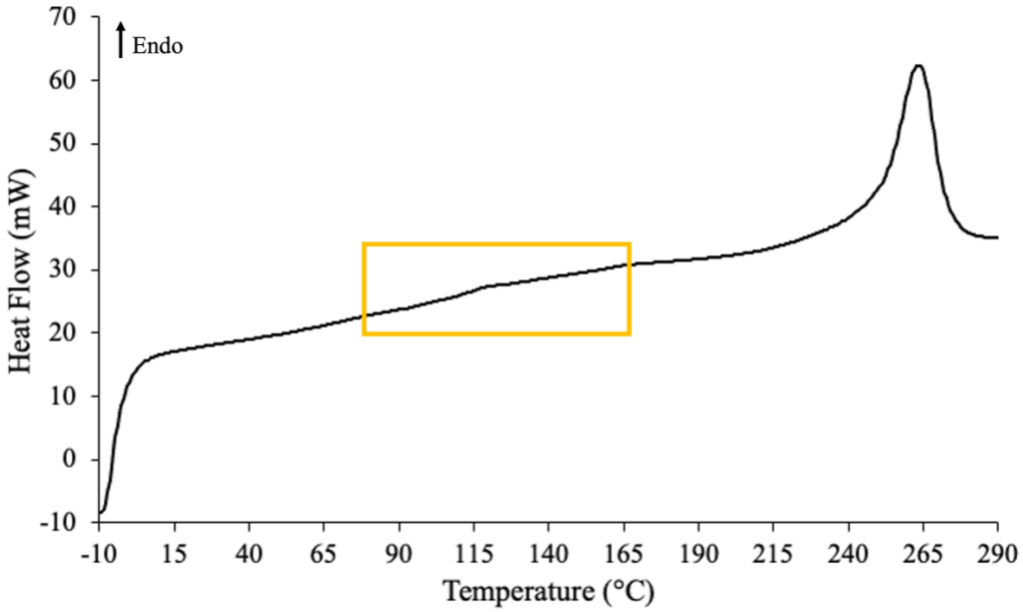

Figure 7.2: DSC thermogram of a PA66/GF sample showing a low temperature endothermic peak at ~120 °C in addition to the characteristic high temperature melting peak (~260 °C) after annealing at a temperature of 90 °C for 4 hours.

7.3.1.1 Characterising the low temperature endothermic peak – T_g or T_m?

One explanation for the existence of a post-annealing low temperature endothermic peak could be that associated with enthalpy relaxation. Enthalpy relaxation is an ageing process in which a polymer with excess thermodynamic quantities undergoes structural relaxation to achieve thermodynamic equilibrium [177]. However, despite appearing as an endothermic peak (superimposed on the glass-to-liquid transition step) within a DSC thermogram, enthalpy relaxation occurs at temperatures below T_g and thus, cannot be responsible for the low temperature peak observed within this study (Figure 7.2).

An alternative explanation could be an increased shift in temperature of the glass-to-liquid transition. By annealing at temperatures above T_g, the amorphous regions, located between the crystalline lamella structures formed on cooling from the melt, are in the liquid state. Providing thermal energy is sufficient, the characteristically disordered polymer chains within these interlamella regions are mobile and if time permits, can rearrange to form ordered crystalline structures. Crystallisation typically drives up T_g, whereby a higher volume fraction of crystalline material generally constrains that of the amorphous phase and thus, superior heat energy is required to overcome the barriers to chain motion. Despite this, the T_g of polyamide 66 is approximately 50 °C [11] and one would not expect the value to shift to temperatures greater than 100 °C even if crystallinity does increase throughout the annealing process. Furthermore, T_g would not typically appear as a peak within a DSC trace, but rather as a stepped increase in heat flow characteristic of a change in specific heat capacity and is rarely observed in the DSC thermograms of polyamides. Consequently, it can be deduced that the small endothermic peak is not representative of the glass-to-liquid transition, but rather the melting of crystalline structures formed during the low temperature annealing process. This conclusion is in accordance with previous studies of polyamides where multiple melting peaks

varying in temperature and amplitude have often been reported after annealing at temperatures between T_g and T_m [162,163,165].

7.3.2 Effect of annealing temperature and time on the low temperature melting peak

DSC thermograms obtained after annealing close to T_g show the low temperature melting peak to be highly dependent on the annealing conditions. However, despite this, the high temperature melting peak was shown to be unaffected by the low temperature annealing process (section 7.3.3).

As shown in Figure 7.3, peak melting temperature of the low temperature peak (T_m') incrementally shifts to higher temperatures with increasing T_a. The temperature at which T_m' appears is greater than that of the associated annealing temperature, with the difference ($\Delta T = T_m' - T_a$) calculated to be approximately 28 °C and seemingly independent of annealing temperature and time. This finding is consistent with that of Kaya and Mathias [162] who also reported that ΔT was independent of T_a and t_a in their study of PA18 18, however, contradicts that of Castagnet and Thilly [163] who showed a systematic increase in ΔT with increasing annealing time, yet conversely, observed an inverse relationship between ΔT and T_a in their study of PA11 [163].

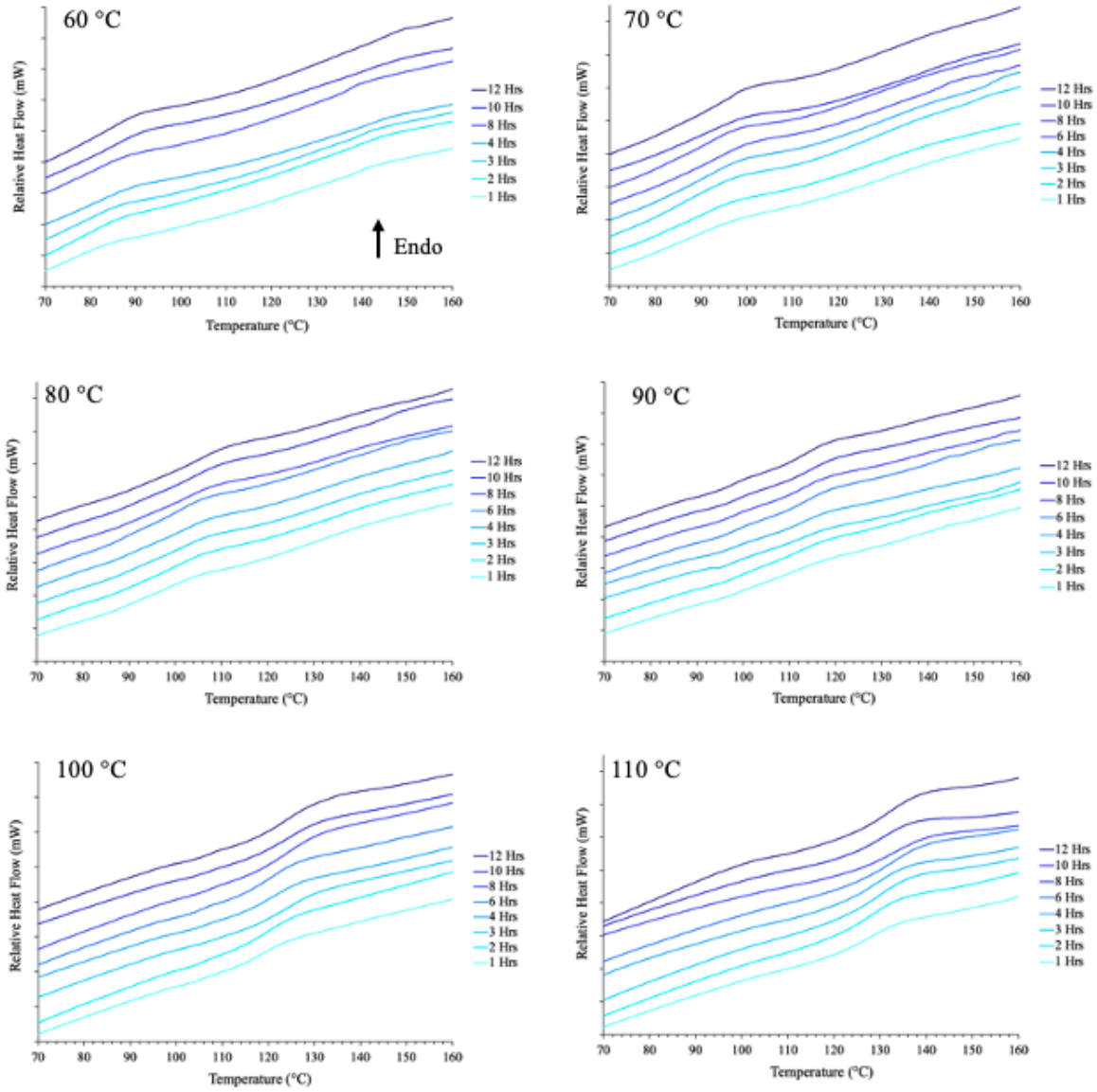

Figure 7.3: DSC thermograms of the low temperature endotherm as a function of annealing temperature (T_a) and time (t_a), showing the incremental shift in peak melting temperature (T_m') with increasing T_a.

Furthermore, T_m' is observed to increase linearly with T_a (Figure 7.4 a)), whereby a 50 °C increase in T_m' can be seen between the two limits of the annealing temperature range (60 and 110 °C). This is thought to result from the formation and melting of thicker, more thermally stable lamella that are generated with greater annealing temperatures (section 7.3.2.1). However, despite the obvious effect of T_a on the resulting low temperature melting peak,

annealing time (t_a) is shown to have a nominal effect on T_m', with no systematic trend between t_a and T_m' being observed over the 12-hour annealing period (Figure 7.4 b) and Table 7.1).

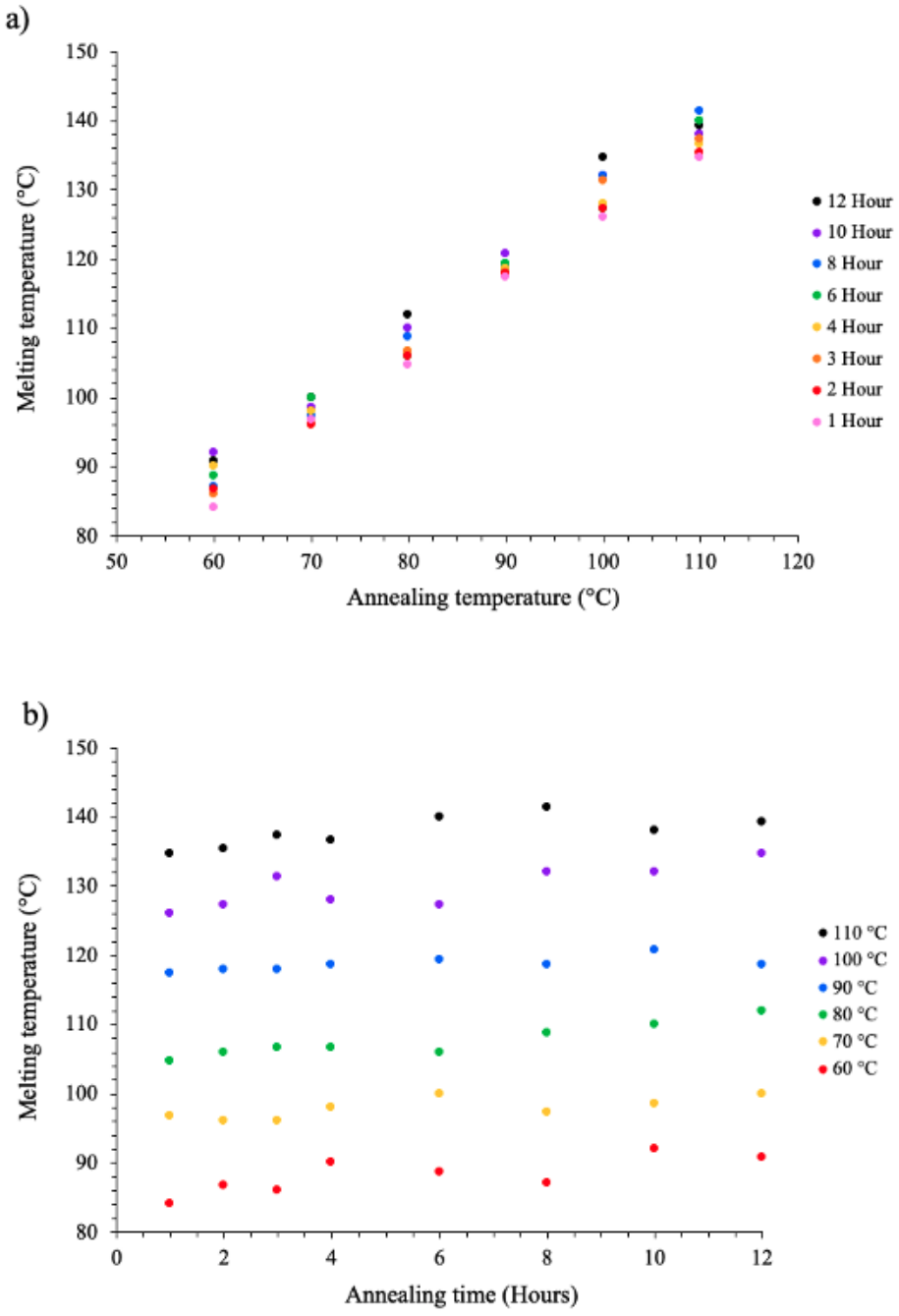

Figure 7.4: Showing the increase in peak melting temperature (T_m') of the low temperature melting endotherms as a function of a) annealing temperature and b) time. T_m' is shown to increase linearly with T_a resulting from the formation of more thermally stable lamella with greater annealing temperatures.

Table 7.1: Master table listing the variation in polyamide mass fraction as determined from a matrix burnout procedure, peak melting temperature (T_m') and degree of crystallinity (X_c') of the low temperature melting endotherm, and lamella thickness (*l*) of the interlamella crystals.

Time (Hrs)	Temperature (°C)	PA (mg)	PA (%)	T_m' (°C)	X_c' (%)	*l* (nm)
1	60	11.4	40.5	84.0	0.97	0.115
	70	11.8	41.8	96.7	0.71	0.122
	80	11.0	39.9	104.7	0.49	0.127
	90	11.0	42.4	117.3	0.77	0.136
	100	11.6	40.2	126.0	0.87	0.142
	110	10.8	39.7	134.7	0.88	0.150
2	60	11.7	41.5	86.7	1.20	0.116
	70	10.7	40.2	96.0	0.86	0.122
	80	11.1	40.9	106.0	0.76	0.128
	90	10.2	39.3	118.0	1.18	0.136
	100	11.6	40.4	127.3	0.97	0.143
	110	11.5	38.9	135.3	1.54	0.150
3	60	11.3	39.4	86.0	1.25	0.116
	70	11.5	40.7	96.0	0.95	0.122
	80	11.0	40.2	106.7	0.92	0.128
	90	10.8	40.8	118.0	1.07	0.136
	100	11.5	40.0	131.3	0.94	0.147
	110	11.8	42.3	137.3	1.66	0.152
4	60	11.2	40.0	90.0	1.10	0.118
	70	11.9	41.8	98.0	0.97	0.123
	80	10.7	39.3	106.7	0.99	0.128
	90	11.1	40.6	118.7	1.07	0.137
	100	10.6	39.2	128.0	1.05	0.144
	110	11.3	39.6	136.7	1.57	0.151
6	60	9.7	36.0	88.7	1.28	0.118
	70	11.7	41.3	100.0	0.97	0.124
	80	10.8	38.9	106.0	1.30	0.128
	90	11.6	40.4	119.3	1.25	0.137
	100	11.6	40.8	127.3	1.20	0.143
	110	11.0	41.4	140.0	1.39	0.155
8	60	10.5	40.0	87.1	1.20	0.117
	70	11.3	39.3	97.3	1.07	0.122
	80	11.8	43.2	108.7	0.97	0.130
	90	11.1	40.6	118.7	1.23	0.137
	100	11.9	41.5	132.0	1.12	0.147
	110	10.8	40.4	141.3	1.21	0.156
10	60	11.4	42.1	92.0	1.29	0.119
	70	11.0	40.0	98.6	1.02	0.123
	80	11.6	40.7	110.0	0.77	0.130
	90	11.7	42.3	120.7	1.06	0.138
	100	10.1	37.6	132.0	1.20	0.147
	110	11.2	39.5	138.0	1.53	0.153
12	60	11.6	40.7	90.7	1.41	0.119
	70	11.2	42.7	100.0	1.18	0.124
	80	10.1	36.1	112.0	1.26	0.132
	90	11.1	41.8	118.7	1.37	0.137
	100	10.9	38.2	134.7	1.27	0.150
	110	11.2	38.9	139.3	1.35	0.154

Contrary to the clear and obvious trend in T_m' with T_a, the area of the low temperature peak and thus, measured enthalpy of fusion and resulting degree of crystallinity (X_c') was not observed to show a methodical trend with annealing temperature or time (Figure 7.5).

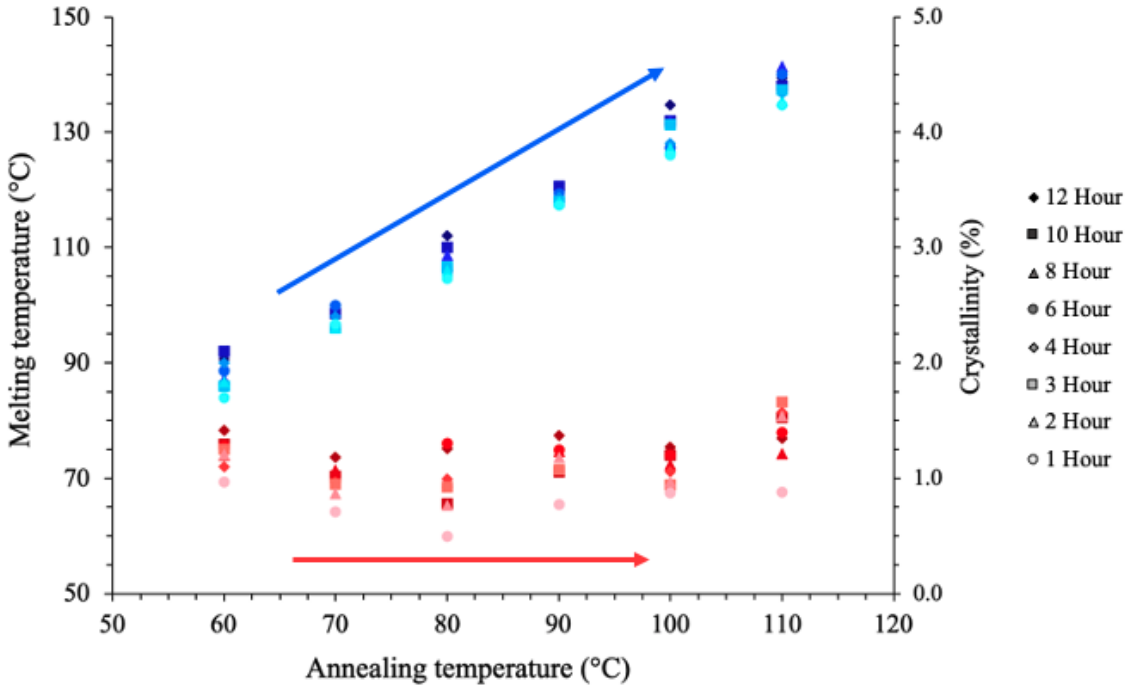

Figure 7.5: Showing the differing trends in peak melting temperature (*blue*) and degree of crystallinity (*red*) of the low temperature melting endotherm as a function of annealing temperature and time.

The calculated values of the weight fraction crystallinity for all annealing conditions are listed in Table 7.1 along with T_m' and sample-to-sample variations in polyamide mass fraction. The area of the low temperature melting peak was relatively small and did not noticeably increase with annealing temperature or time as reported previously [163,165], thus, the crystalline fraction did not markedly differ and remained small (<1.7%) over all annealing conditions. If one considers the sensitivity of the instrument and error associated with measurement of the

heat of fusion, along with the substantial overlapping of the results, it is deemed that few meaningful conclusions can be drawn with regards to the effect of both T_a and t_a on X_c'. That said, despite no systematic and conclusive trend, it was generally observed that at any given T_a the smallest and largest values of X_c' coincided with the shortest and longest annealing times, respectively. X_c' was found to equivalate to approximately 1.2 to 4.7% of the total matrix crystallinity (determined from the melting endotherm of the high temperature melting peak). Therefore, regardless of the seemingly modest values of X_c', it is irrefutable that crystalline structures are formed on annealing and could have a considerable impact on mechanical performance, specifically creep behaviour.

As alluded to in section 7.3.1.1, the low temperature endotherm that appears within the DSC thermograms of annealed samples is characteristic of the melting of small, ordered volumes located within the constrained interlamella amorphous regions. These so-called secondary crystals form on annealing at temperatures above T_g, but below that of the critical annealing temperature (T_c'). The thermal energy supplied to the molecular chains within this low temperature annealing range ($T_g < T_a < T_c'$) is insufficient for the morphological changes and crystal perfecting of the highly ordered primary crystalline volumes observed at annealing temperatures above T_c, close to T_m. Despite this, molecular motion of the polymer chains within the interlamella amorphous regions is adequate for the formation of small metastable crystalline volumes. Several theories have been proposed with regards to the formation of the secondary crystals and their effect on the resulting post-annealing low temperature melting peaks, however, given the annealing temperatures used in this study, the most plausible explanations for their existence are secondary crystallisation and melt-recrystallisation of very thin primary lamella.

Secondary crystallisation refers to the formation and growth of small crystalline volumes, termed infill lamella, that materialise within the constrained amorphous phase between highly ordered crystalline lamella. The process of secondary crystallisation is shown schematically in Figure 7.6 a). Dissimilar to the thick lamella structures formed during the primary crystallisation process, secondary crystals formed at low T_a are thought to be bundle-like structures [164,168] lacking the regular re-entry and chain folding associated with highly ordered primary crystals and therefore, show inferior thermal stability. Moreover, established within constrained interlamella regions, secondary crystals typically incorporate tie molecules and loose loops within the vicinity of the primary structures [164]. Given that both T_a and t_a are sufficient, newly formed secondary crystals will thicken throughout the annealing process via the addition of previously disordered molecular chains to the crystal growth face (Figure 7.6 a)).

Alternatively, it has been suggested that the multiple melting peaks observed in post-annealing DSC thermograms are associated with a distribution in lamella thickness [165]. Shan et al. [165] have previously reported that on crystallisation from the liquid melt, a distribution in thickness of primary lamella exists within the semi-crystalline microstructure. Upon annealing at temperatures close to T_g, melt-recrystallisation of these thin primary lamella occurs. Here the thin, imperfect lamella with low thermal stability melt, re-organise into thicker and more stable lamella structures (Figure 7.6 b)). It is thought that prior to annealing an insufficient population of the very thin crystalline lamella exist, resulting in the appearance of only a single endothermic peak within the DSC thermogram, characteristic of the melting of thick lamella. However, owing to the re-organisation and thickening of the thin lamella throughout the low temperature annealing process, the melting of these thicker structures is now sensitive to the

subsequent DSC heating run and thus, multiple melting peaks are observed within the DSC thermogram of an annealed sample [165].

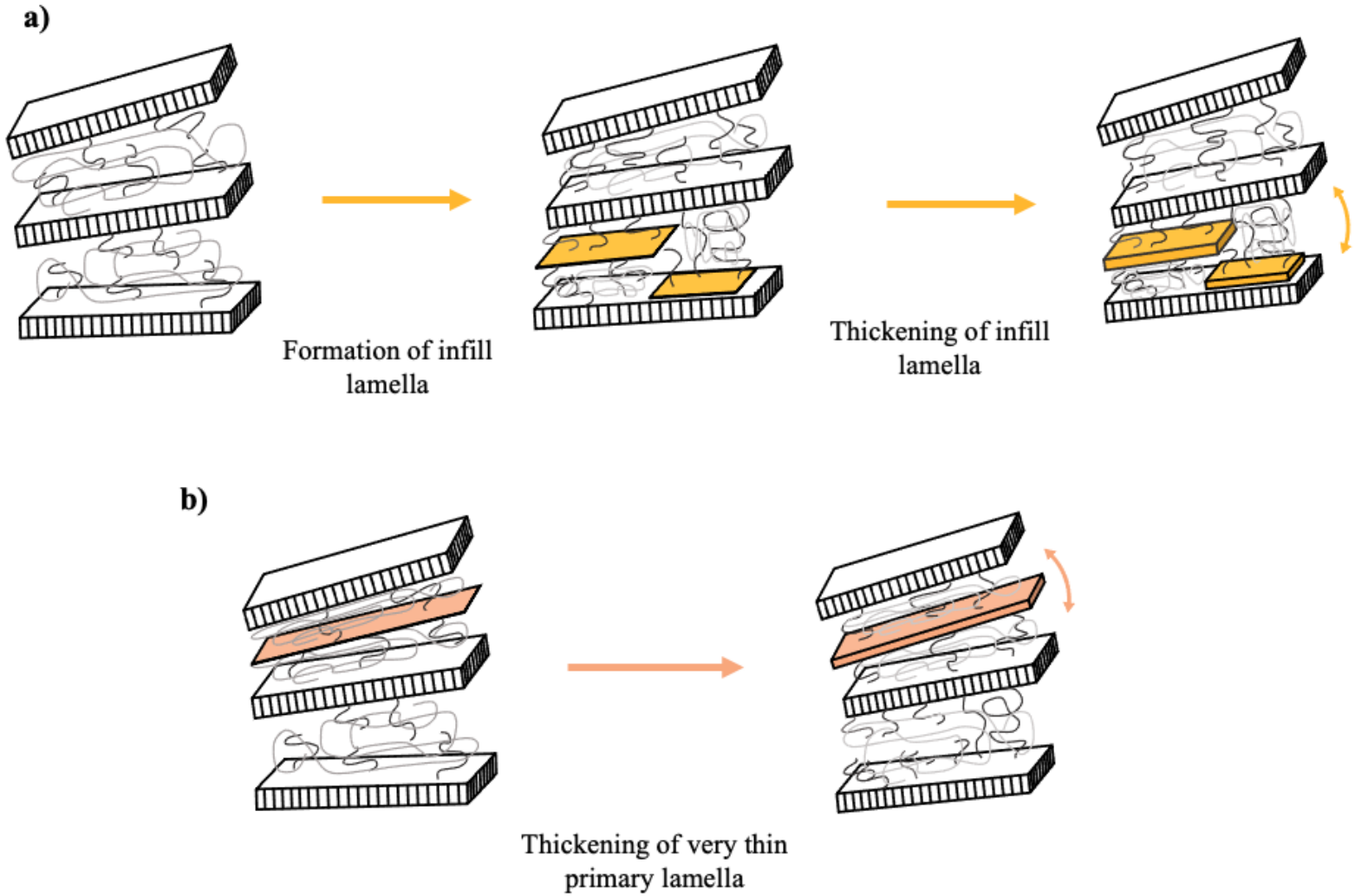

Figure 7.6: Schematic depicting a) the formation and thickening of infill lamella characteristic of secondary crystallisation and b) melt-recrystallisation of very thin lamella formed during primary crystallisation, resulting in the thickening of said lamella throughout annealing.

7.3.2.1 Temperature dependence of lamella thickness

In accordance with the Gibbs-Thomson equation (Equation 7-1), the melting temperature of a crystalline material is related to its stability and lamella thickness, with crystals of greater perfection and thickness melting at higher temperatures. The annealing temperature dependence on the thickness of the resulting interlamella crystalline structures was determined using Equation 7-1 and the results listed in Table 7.1.

$$l = \frac{2\sigma_e \cdot {T_m}^0}{\Delta H_{f\infty} \left({T_m}^0 - {T_m}'\right)}$$

Equation 7-1

Where l is lamella thickness, σ_e surface free energy of the fold surface taken as 6.4×10^{-3} J/m^2 [178], ${T_m}^0$ the equilibrium melting temperature (303 °C) [179] and $\Delta H_{f\infty}$ the theoretical enthalpy of fusion of a perfectly crystalline polyamide 66 crystal. As shown in Table 7.1, lamella thickness was observed to be highly T_a dependent, incrementally increasing in thickness with annealing temperature. This is in accordance with the T_m' results presented in section 7.3.2 and Figure 7.4, whereby an increase in T_a results in the elevation of T_m' due to the formation of thicker and more thermally stable lamella.

7.3.3 Effect of low temperature annealing on the high temperature melting peak

Annealing of polymer materials typically ensues at temperatures above the glass-to-liquid transition and below the onset of melting. At low annealing temperatures, providing sufficient thermal energy and time are available, the formation of secondary crystals or melt-recrystallisation of thermally unstable lamella is possible [162,165]. However, the perfecting of thermally stable primary crystals including crystal growth and the re-ordering of hydrogen bonded chains within highly ordered crystalline lamella requires greater annealing temperatures far in excess of T_g, much closer to T_m. The morphological changes associated with high temperature annealing (close to T_m) typically results in the low temperature melting peak shifting to greater temperatures, often appearing as a shoulder off the main melting peak before eventually merging with that of the high temperature peak at longer annealing times [162,163,165]. This generally results in a broadening of the high temperature melting peak due to a greater distribution of crystal perfection, with T_m often observed to shift to lower temperatures as the two peaks merge [165]. The annealing temperatures adopted in this study ($60\ °C < T_a < 110\ °C$) are lower than those used in previous works and adequately below the temperatures required for such morphological changes. This is reflected by both the absence of a shoulder peak on the high temperature melting endotherms and in the similarity of the peaks recorded for both unannealed and annealed samples (Figure 7.7). Furthermore, as shown in Figure 7.8 a) and b) no systematic deviation (outside that considered to be due to sample-to-sample variation) in peak melting temperature (T_m) or degree of crystallinity (X_c) was observed with increasing annealing temperature or time. Thus, it can be concluded that the annealing conditions used within this study had no known effect on the thermally stable primary crystals, nor on the resulting high temperature melting endotherm recorded in the DSC thermogram. This finding is consistent with that of both Lu et al. [36], who show that the perfecting of

ordered hydrogen bonds can only occur at T_a in the vicinity of T_m and Castagnet and Thilly [163] who propose a critical annealing temperature (T_c'), below which crystal growth and organisation of thermally stable primary crystals is not possible [36,163].

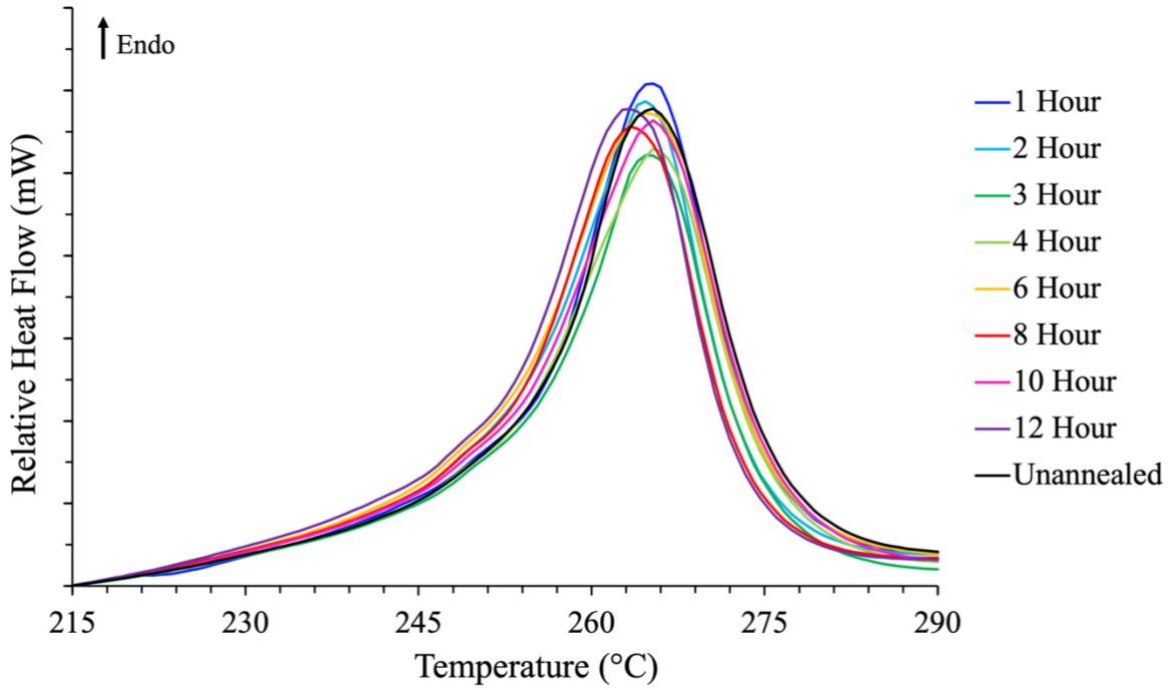

Figure 7.7: Showing the similarity in profile and peak melting temperature of the high temperature melting endotherm of an unannealed PA66/GF sample and samples annealed at 90 °C for various lengths of time (1-12 hours).

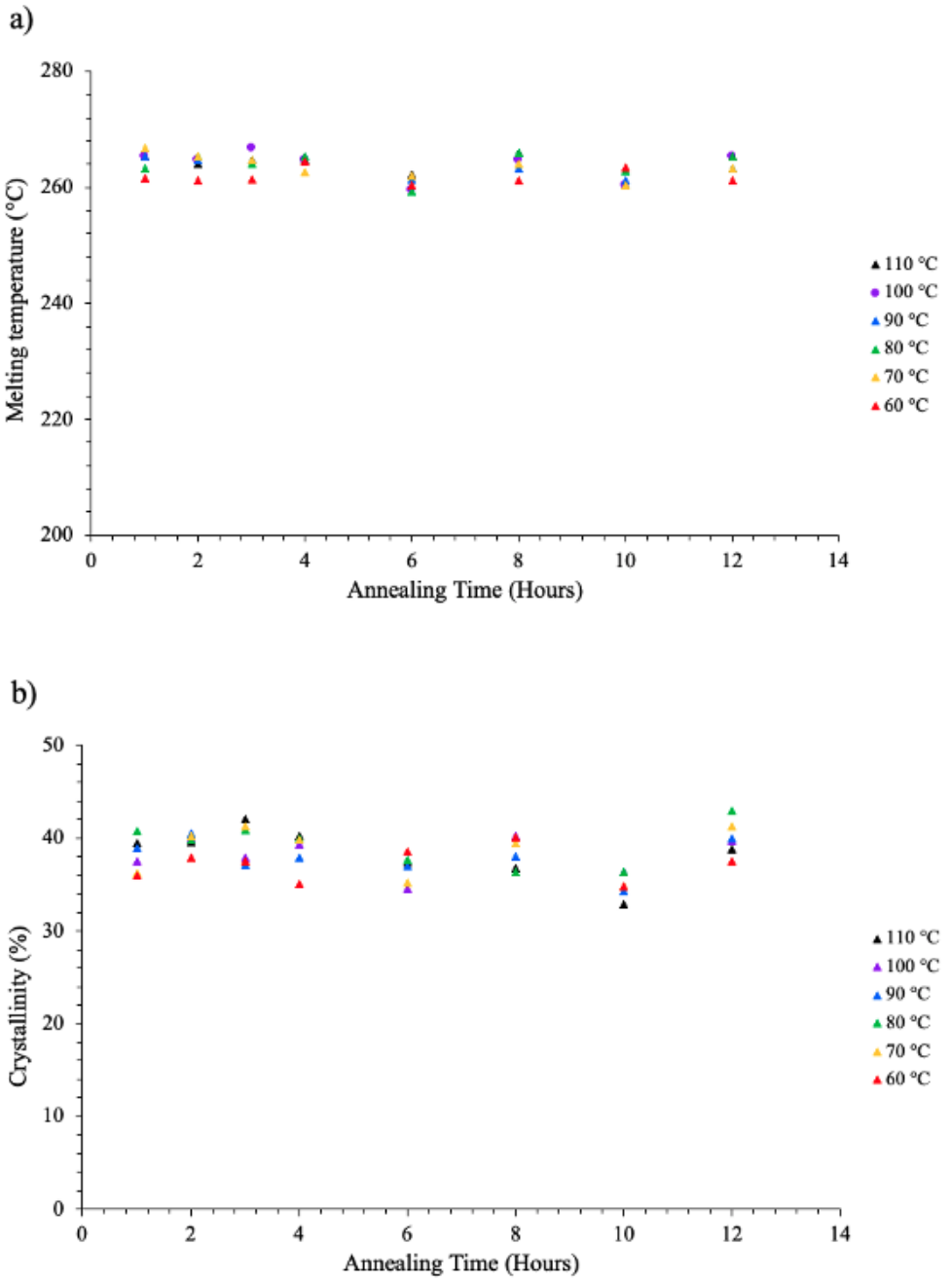

Figure 7.8: Showing a) peak melting temperature and b) degree of crystallinity of the high temperature melting endotherm as a function of annealing temperature and time.

7.3.4 Creep behaviour of a PA66/GF laminate

Creep is a time-dependent permanent deformation process resulting from prolonged exposure to a constant stress below the elastic limit (yield stress) of a material. As specified in section 7.2.2.1, creep tests were performed on 4-ply unidirectional and cross-ply laminates under three-point flexural bending with deflection of the test specimen at the mid-point of the two supports determined as a function of time. Figure 7.9 shows a deflection-time plot of a cross-ply (0/90/90/0) PA66/GF laminate under constant load and then throughout the recovery of the sample once the load is removed.

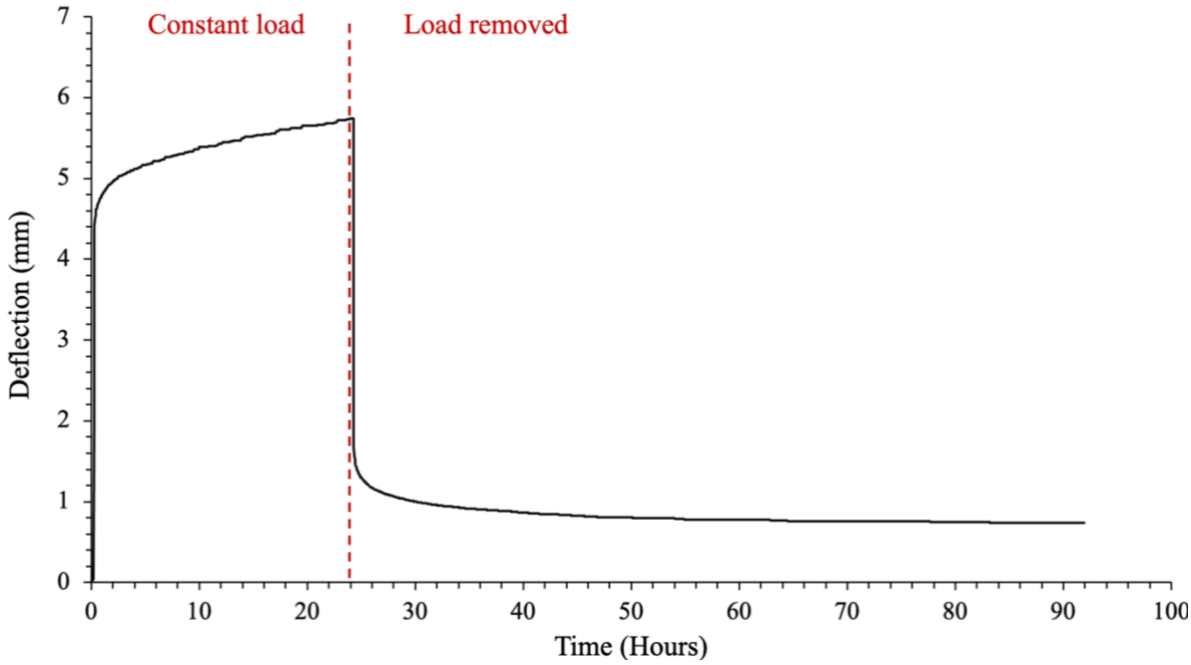

Figure 7.9: Deflection vs time plot of a cross-ply (0/90/90/0°) PA66/GF laminate under constant load (0.5 kg) and on recovery upon on load removal.

Upon initial application of the load, deflection at the centre of the composite is observed to immediately increase, characteristic of the instantaneous, elastic strain placed on the material (Figure 7.9). This instantaneous response to the applied load is believed to be endured

predominantly by the reinforcement fibres and crystalline phase of the polyamide matrix. That said, after this initial rise, and with elapsing time, the rate of increasing deflection reduces representative of the primary process. Here viscoelastic strains develop within the amorphous phase of the polymer matrix, with the disordered amorphous chains, situated within the interlamella regions of crystalline structures, playing a pivotal role in the time-sensitive creep behaviour of semi-crystalline thermoplastics [151]. Under the persistent stress of the applied load, amorphous chains become 'load-bearing', with chain slippage and orientation inducing a strain hardening effect, ultimately reducing creep rate as observed in Figure 7.9. Subsequently, orientational strain hardening of the amorphous phase results in a constant steady-state creep rate characteristic of the secondary stage of the creep cycle (Figure 7.9), whereby a time-dependent viscoelastic flow of the thermoplastic materialises [13,15,151]. Due to the length of time that this penultimate stage of the creep cycle can persist, the final tertiary stage in which, creep rate is once again observed to increase as the test specimen fails under the applied stress is not observed. On removal of the load, deflection resulting from the persistent stress under which the sample was placed, instantaneously falls (Figure 7.9). This immediate reduction in displacement is representative of the elastic recovery of the material. Beyond this initial recovery, the sample continues to slowly recover over an extended period of time before a plateau in the rate of recovery can be observed. The fact that the test specimen never returns to the pre-stressed value is characteristic of creep and the permanent deformation of the polymer matrix composite.

In order to more reliably compare the creep performance of various test specimens, creep modulus, flexural stress and creep strain of each sample were determined using BS EN ISO 899-2 and Equation 7-2 – Equation 7-4.

Creep modulus:

$$E_t = \frac{L^3 \cdot F}{4b \cdot h^3 \cdot s_t}$$

Equation 7-2

Where, E_t is creep modulus, L the distance between the two support fixtures, F the force applied, s_t the displacement at the centre of the test specimen at time, *t*, with b and h the width and thickness of the test specimen, respectively.

Flexural stress:

$$\sigma = \frac{3F \cdot L}{2b \cdot h^2}$$

Equation 7-3

Where, σ is the flexural stress placed on the sample from the applied load.

Creep strain:

$$\varepsilon_t = \frac{6s_t \cdot h}{L^2}$$

Equation 7-4

Where, ε_t is the creep strain of the test specimen as a function of time, *t*.

7.3.4.1 Effect of moisture on the creep performance of an annealed PA66/GF composite

As illustrated in Figure 7.10, after annealing an undried cross-ply laminate at 80 °C for 4 hours, the effect of the thermally activated water molecules on the PA66/GF laminate resulted in the deterioration of creep performance compared to that of an unannealed sample (flexural stress ~25 MPa).

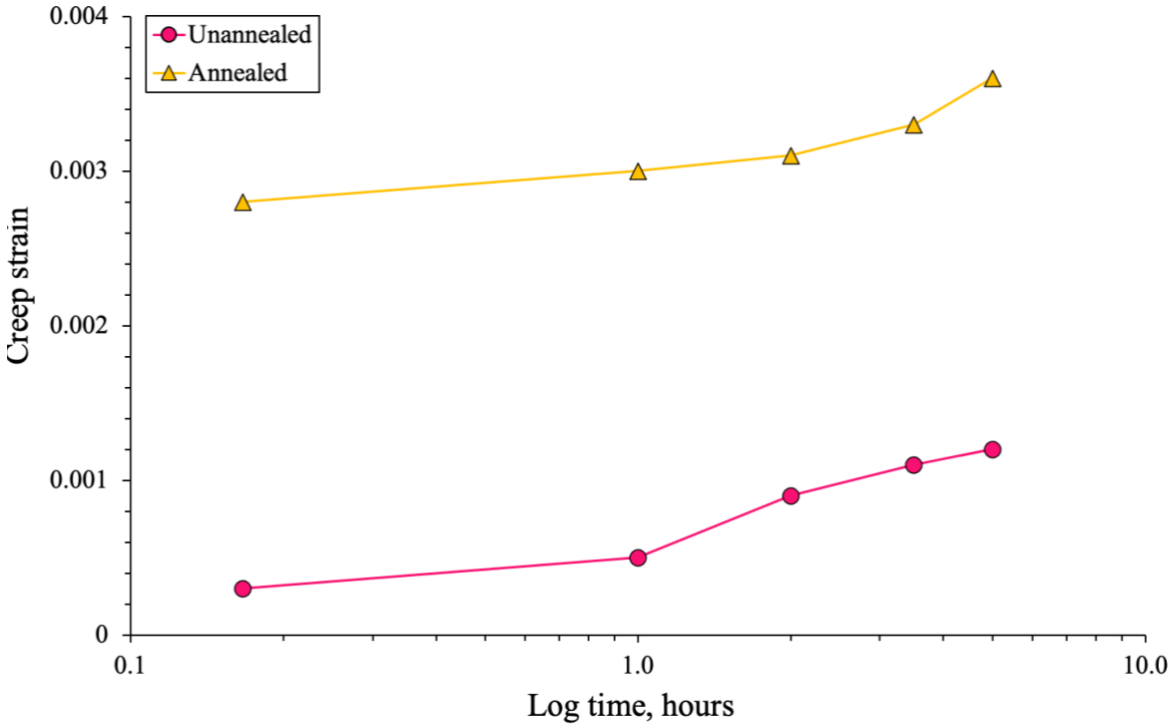

Figure 7.10: Creep strain vs log time of annealed (T_a = 80 °C) and unannealed cross-ply (0/90/90/0°) PA66/GF laminates with no prior drying before the annealing process.

The increased creep strain and thus, reduction in creep performance of the undried, annealed test sample compared to that of the unannealed sample was attributed to the effects of hydrolysis and a deterioration in the interfacial properties between the matrix and glass-fibre reinforcement. Hydrolysis is a thermally activated process typically occurring within the less dense, highly entangled amorphous regions of a semi-crystalline polymer. On annealing,

hydrolysis can result in chain scission, leading to both a reduction in molecular weight (M_n) and increase in chain mobility due the reduced number of entanglements within the amorphous phase of the polyamide matrix, ultimately resulting in a deterioration in mechanical performance. Similarly, the thermally activated water molecules may weaken the interfacial bonds between the matrix and fibre-reinforcement. Consequently, this leads to a reduction in load transfer between the matrix and fibres, resulting in poorer creep properties of the composite materials (Figure 7.10).

Resulting from the undesirable effects of water molecules on the matrix microstructure and subsequent creep performance, all samples were dried in a desiccator for a minimum of 24 hours prior to annealing.

7.3.4.2 Effect of low temperature annealing on creep performance of PA66/GF laminates

Contrary to the undried test samples, which on annealing were observed to worsen the creep resistance of post-processed PA66/GF laminates, drying of the test specimens prior to the annealing process was shown to improve the creep behaviour of the material. As can be seen in Figure 7.11 a) and b) annealing of the dried, 4-ply laminates at 80 °C for 4 hours noticeably reduced creep strain and enhanced the creep modulus of the material compared to that of an unannealed sample.

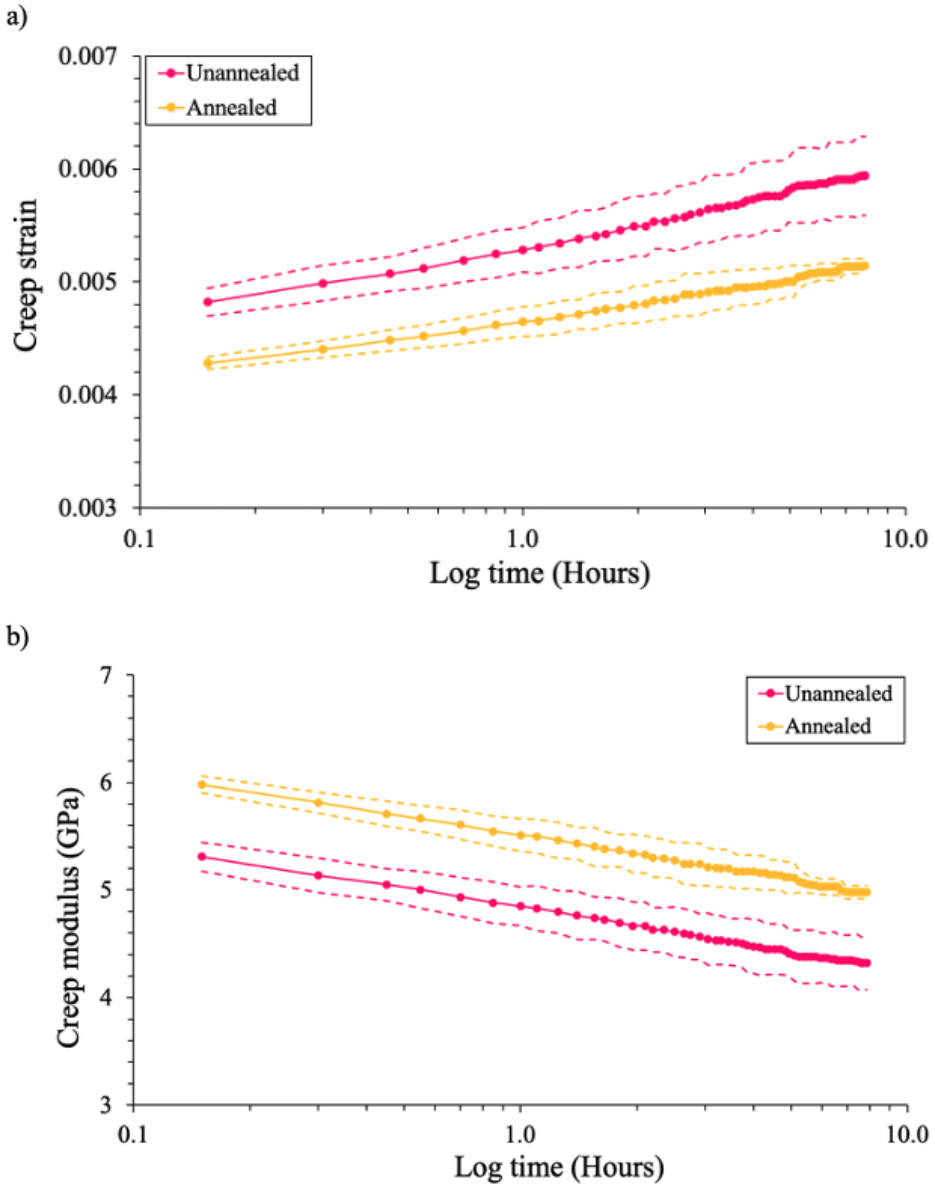

Figure 7.11: Plots of the average and standard deviation (---) in a) creep strain and b) creep modulus as a function of log time in annealed (T_a = 80 °C, t_a = 4 hours) and unannealed cross-ply (0/90/90/0°) PA66/GF laminates. [Averages were determined from 4 samples per condition].

Compared to unannealed samples, the creep strain of annealed PA66/GF laminates was observed to fall by approximately 14% when exposed to persistent flexural stress of ~25 MPa. Furthermore, despite gradually decreasing over time, the creep modulus of annealed samples

(as determined from Equation 7-2) was shown to remain approximately 700 MPa greater than that of unannealed samples throughout testing.

As alluded to in sections 7.1.1, in semi-crystalline polymer matrix composites (PMC) the instantaneous increase in strain upon the initial application of a load is determined by the elastic modulus of the reinforcement fibres and crystalline lamella of the matrix polymer. That said, the linear elastic limit of the viscoelastic matrix and the time-dependent creep response under a constant stress is profoundly reliant on the interlamella amorphous regions of the matrix polymer. The highly disordered molecular chains within the amorphous phase are responsible for transmitting the load between crystalline lamella [180]. However, due to the lack of structural order within the amorphous phase, an abundance of molecular chain slippage can ensue under the applied load. Owing to this, it follows that a reduction in crystallinity and thus, increased amorphous fraction results in poorer creep resistant properties of the PMC [156].

As discussed in section 7.3.1, low temperature annealing of PA66/GF at $T_a > T_g$ results in the formation of small, ordered crystalline volumes within the confined interlamella amorphous regions of the primary crystal structures. Therefore, compared to the unannealed samples which, after cooling from the melt, were dried for 24 hours without any subsequent annealing process, samples annealed at 80 °C are believed to contain a greater volume of interlamella crystal structures. These small crystals which, typically incorporate tie molecules within the vicinity of the highly ordered crystalline material, constrain the amorphous phase restricting the mobility of the molecular chains and thus, reduce the time-dependent viscoelastic flow. Moreover, the restrained mobility of the polymer chain segments extends the linear elastic limit of the viscoelastic matrix polyamide and restricts chain slippage and orientation under the applied load. Both of which, are advantageous to creep performance. Ensuing from the formation of thin, interlamella crystals and thus, improved transfer of the applied stress

throughout the semi-crystalline microstructure, annealing of the samples above T_g reduces the instantaneous strain on loading (Figure 7.11 a)) and improves creep modulus by ~14% compared to that of an unannealed sample (Figure 7.11 b)). Furthermore, the newly ordered volumes formed on annealing effectively constrain the movement of chains within the amorphous phase, reducing the abundance of chain slippage (characteristic of poor creep resistance), thus, reducing creep strain over the secondary creep stage (constant creep rate) and ultimately improving the creep performance of the PA66/GF laminates.

A similar trend was observed between annealed and unannealed in unidirectional composites (Figure 7.12 a) and b)), however, compared to that of cross-ply (0/90/90/0°) sequencing, unidirectional (0°) laminates were shown to provide substantial improvements in the resistance to creep behaviour of PA66/GF composites (Figure 7.12 a) and b)). This is in keeping with the findings of Lafranche et al. [158] and Chevali et al. [160] who showed the transverse mechanical properties of glass fibre reinforced polyamides to be far inferior to that of the longitudinal properties.

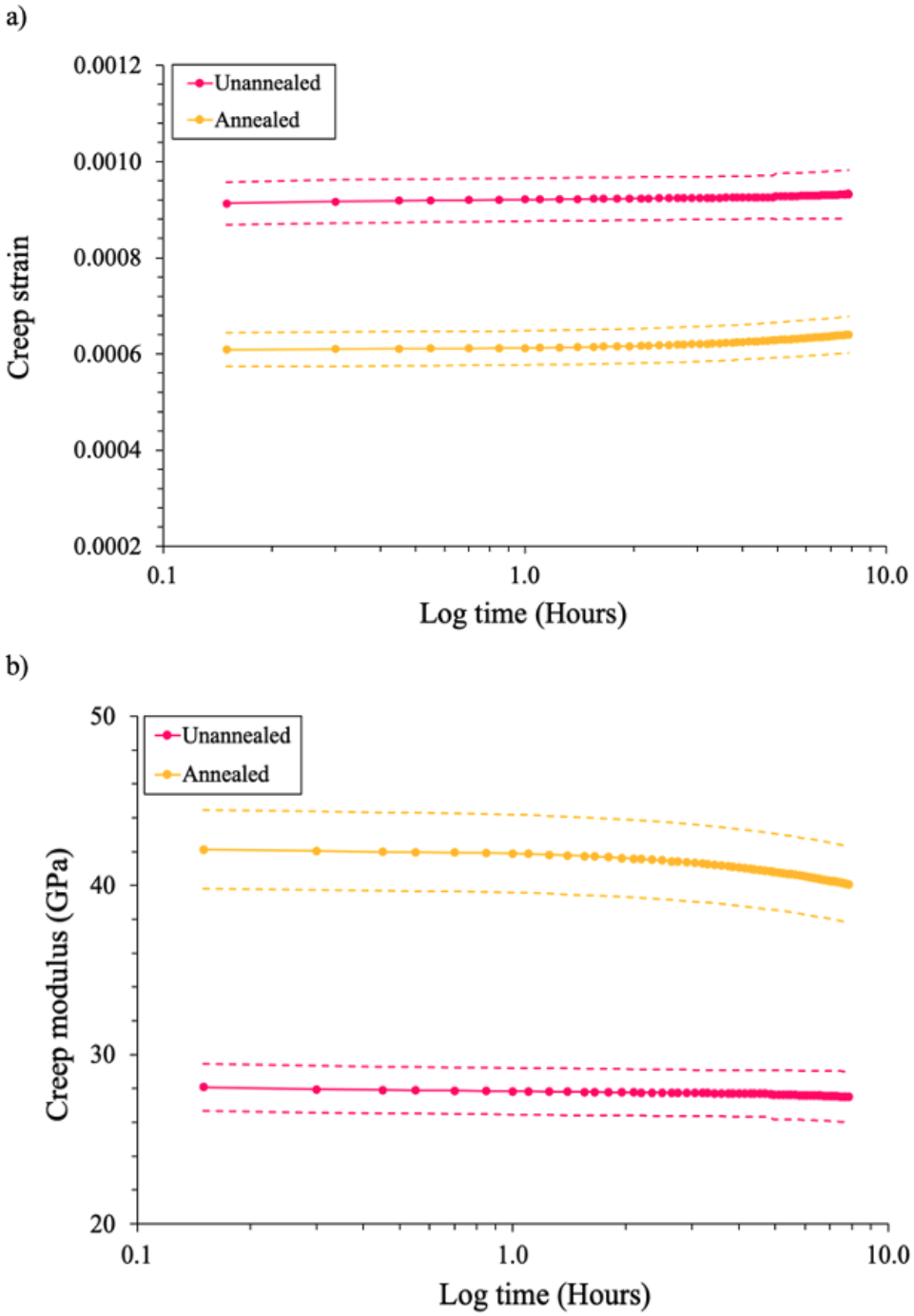

Figure 7.12: Plots of the average and standard deviation (---) in a) creep strain and b) creep modulus as a function of log time in annealed (T_a = 80 °C, t_a = 4 hours) and unannealed unidirectional (0°) PA66/GF laminates. [Averages were determined from 4 samples per condition].

Moreover, creep strain and modulus values of both annealed and unannealed samples were found to vastly improve compared to that of cross-ply laminates independent of whether the specimens were annealed prior to testing. Under constant flexural stress (~25 MPa) creep strain and modulus were shown to improve by approximately 85 and 500% in comparison to cross-ply laminates, respectively (Figure 7.11 and Figure 7.12). These clear improvements in creep resistance with unidirectional fibre orientation are believed to result from improved load bearing capabilities of the fibres and ultimately enhanced load transfer from the matrix to fibres, thus, leading to a reduction in both instantaneous deformation on application of the load and creep deformation with prolonged time [159,160].

Despite the differences resulting from fibre orientation, the effect of annealing on the percentage improvement in creep strain and modulus between annealed and unannealed samples remained consistent independent of laminate sequencing. That is, comparable to the cross-ply laminate results, unidirectional laminates annealed for 4 hours at 80 °C were observed to both reduce creep strain and increase creep modulus by 14 and 48%, respectively, compared to that of an unannealed sample. Thus, it was assumed that despite variations in the absolute values of strain and modulus resulting from fibre orientation effects, the influence of annealing and the subsequent formation of interlamella crystals on creep performance was equivalent across all samples.

7.3.4.3 Influence of annealing temperature and time on creep behaviour

Based on the results presented in section 7.3.2, samples were annealed at one of two annealing temperatures (80 or 110 °C) for various lengths of time (0.5 to 168 hours). Annealing at both temperatures improved the creep resistance of the PA66/GF laminates compared to that of an unannealed sample (Figure 7.13 a) and b)), however, the extent of the improvement in creep

strain and modulus was found to be T_a dependent. Both Figure 7.13 a) and b) show comparable profiles to that of the unannealed samples, yet, as observed in Figure 7.13 a) the instantaneous creep strain was lower in the annealed samples.

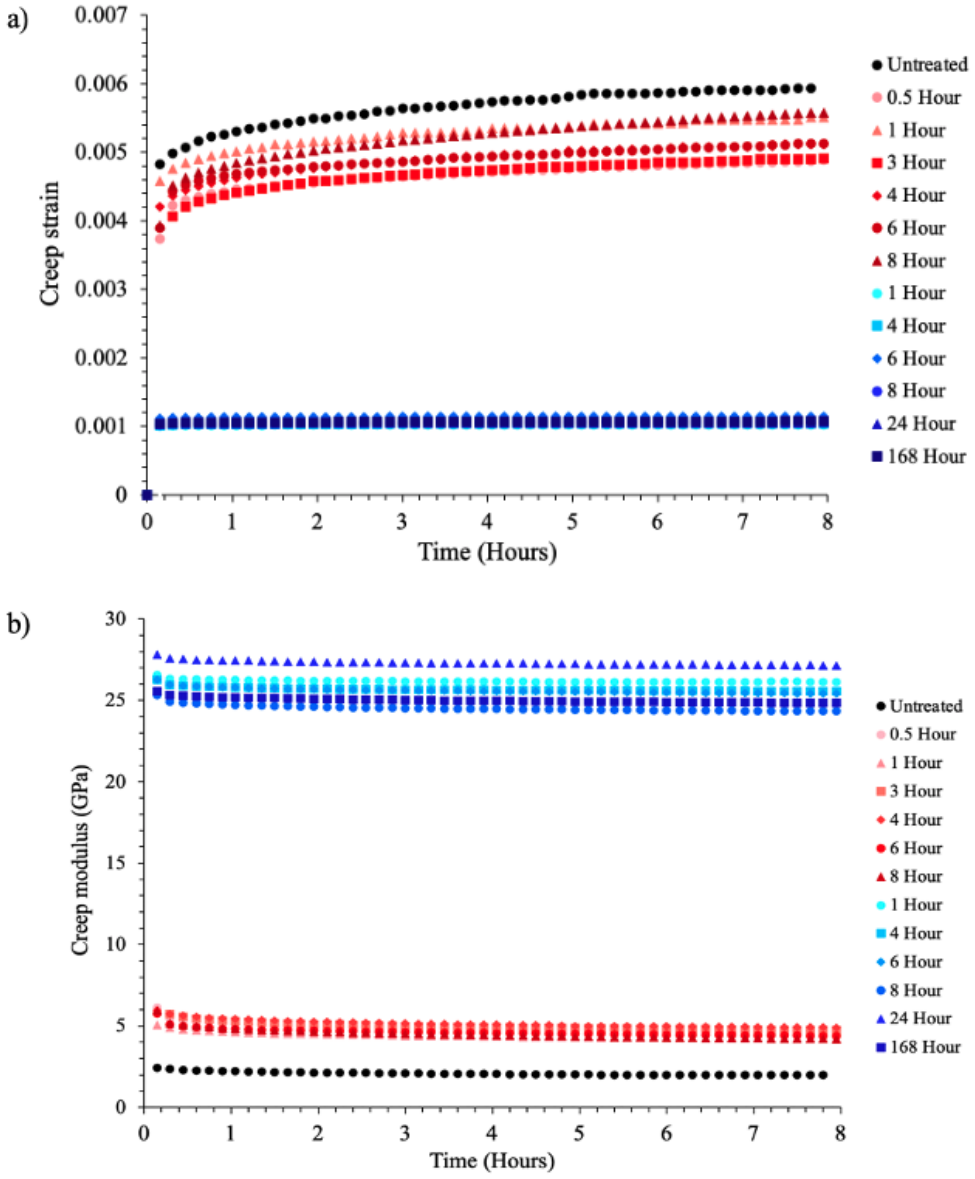

Figure 7.13: Variation in a) creep strain and b) creep modulus as a function of annealing temperature in annealed and unannealed cross-ply (0/90/90/0°) PA66/GF laminates (T_a - *Red* = 80 °C, *Blue* = 110 °C).

After annealing at 80 °C, instantaneous creep strain reduced by approximately 7 to 21% under an applied stress of ~25 MPa, whereas at a T_a of 110 °C, the value decreased by ~313 to 453% compared to that of the unannealed sample. Despite the gradual increase in creep strain with time, due to the similarities in curve profiles, the difference in strain between the annealed samples and that of the unannealed sample remained relatively consistent over the 8-hour testing period. In contrast to the decreasing creep strain, creep modulus was observed to increase with annealing temperature. By comparison to the unannealed sample, test specimens annealed at 80 °C showed a modest 2.3 to 3.1 GPa (112 to 148%) improvement in creep modulus compared to the 15.4 to 25.2 GPa (742 to 1218%) enhancements observed when annealing at 110 °C. Despite an annealing temperature dependence on both creep strain and modulus, a systematic trend between creep resistance and annealing time (t_a) was not found (Figure 7.14). This complements the earlier findings where no trends were observed between t_a and its effect on the post-annealing low temperature melting peak.

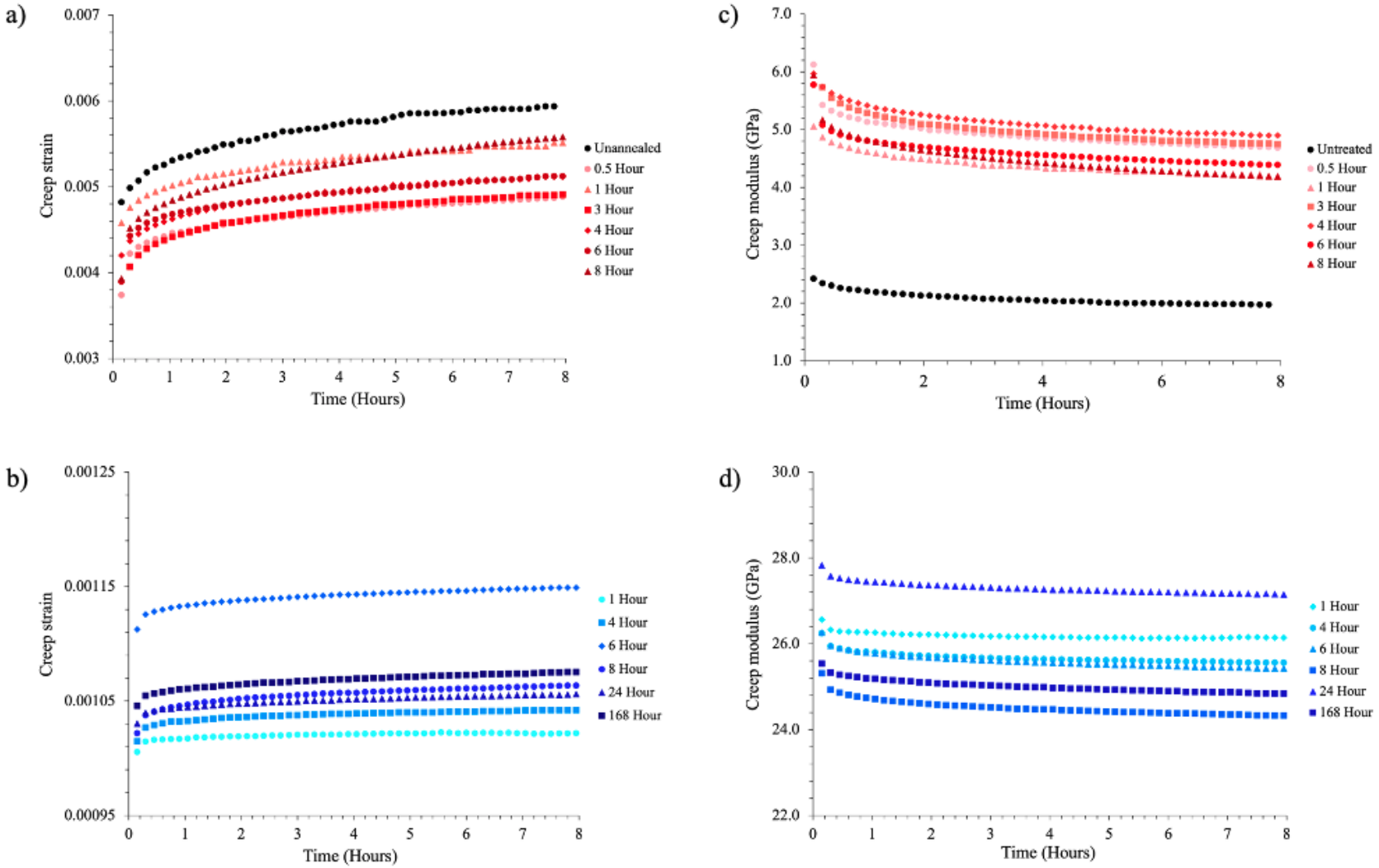

Figure 7.14: Variation in (a-b) creep strain and (c-d) creep modulus as a function of annealing time in annealed and unannealed cross-ply (0/90/90/0°) PA66/GF laminates (T_a - *Red* = 80 °C, *Blue* = 110 °C).

By analysing the data presented in Figure 7.13 a) and b) it is immediately obvious that annealing of the PA66/GF laminates at 110 °C has a greater effect on creep resistance than samples annealed at the lower T_a of 80 °C. This variation between the two datasets was attributed to the thickness of the interlamella crystalline structures formed upon low temperature annealing. As discussed in section 7.3.2 and presented in Table 7.1, it was shown that compared to samples annealed at 80 °C the lamella thickness and resulting T_m' is consistently greater in samples annealed at 110 °C. Therefore, it was deduced that the thicker lamella formed at an annealing temperature of 110 °C more effectively constrain the polymer chains within the amorphous phase, restricting their mobility and thus, enhancing creep performance by extending the linear elastic limit of the of the viscoelastic matrix and simultaneously reducing creep rate via the deterioration in chain slippage under the applied load.

7.4 Conclusions

In summary, the creep performance of unidirectional and cross-ply PA66/GF laminates was improved by low temperature annealing of the laminate post-forming. In keeping with the findings of the literature, the multiple melting behaviour observed within DSC thermograms post-annealing was attributed to the distribution in lamella thickness and thermal stability of crystals formed during annealing at $T_a > T_g$ [162,163,165]. The thickening of these interlamella crystals was found to be highly T_a dependent, with structures of greater thickness and crystal perfection developing at higher annealing temperatures. Further, having not previously been reported in PA66 or PA66/GF composites, low temperature annealing (60 °C < T_a < 110 °C) was shown to improve the creep performance of PMC via the formation/thickening of thin

crystalline structures within the interlamella amorphous regions. By constraining the amorphous chains, the secondary crystals were shown to improve load transfer between the matrix polyamide and glass fibres, reducing the instantaneous strain and extending the linear elastic limit of the material. Moreover, owing to greater thickness of the thin lamella structures, creep performance was shown to vastly improve with increasing T_a. Additional restrictions on the mobility of the amorphous chains after annealing at higher T_a, ultimately resulted in a deterioration in chain slippage under the applied flexural stress and thus, improved creep performance compared to that of unannealed samples or samples annealed at lower temperatures.

CHAPTER 8 - CONCLUSIONS AND FUTURE WORK

8.1 Conclusions

Through-thickness characterisation of crystal morphology and microstructure in stamp formed glass fibre reinforced polyamide 66 has been achieved using a variety of characterisation techniques, including thermal analysis and x-ray diffraction.

As determined by calorimetry, the degree of crystallinity of an 11-ply PA66/GF laminate was observed to vary throughout the thickness of the part and shown to be highly dependent on the rate of heat loss experienced during the stamp forming process. Using the process simulated laminate approach with strategically placed thermocouples and a tool temperature of 120 °C, it was shown that thermal gradients were evident throughout the thickness of the laminate, with a 1400 °C/min disparity in maximum cooling rate observed between the base and central plies during application of the applied load (800 kN). This parabolic trend in through-thickness cooling rate resulted in a 3.0% increase in the degree of crystallinity on moving from the rapidly crystallising surface regions to the comparably quasi-isothermal crystallisation conditions experienced at the centre of the laminate.

Despite the assessment of bulk crystallinity being readily accomplished by traditional characterisation techniques such as DSC analysis, issues such as the meta-stability of the crystalline phase and re-organisation that occurs on heating from T_g to T_m must be carefully considered. Therefore, mapping of crystal morphology through the thickness of the laminate was performed using x-ray diffraction. Analysis of 1D WAXS patterns demonstrated that despite the distinctly non-isothermal crystallisation conditions of the stamp forming process,

the matrix polymer rapidly crystallises into the more stable triclinic unit cell characteristic of the α-phase of PA66. Intensities of the α_1 and α_2 peaks were found to differ through the thickness of the laminate, indicative of a change in crystal structure resulting from the disparity in cooling rates shown throughout the forming process. However, owing to poor S/N resulting from several factors including: the resolution of the optical camera, the fly scanning approach (necessitating the averaging of data over rows rather than obtaining discrete mapping measurements), and beam diameter, quantitative analysis including calculation of crystallinity through the thickness of the laminate was limited.

The isothermal crystallisation of PA66/GF was used to critically evaluate the applicability of several kinetic models, namely Avrami, Tobin, Malkin, Urbanovici-Segal, Velisaris-Seferis and Hay. Statistical modelling and regression analysis using SPSS software show that the Velisaris-Seferis and Hay models provide the best fit to the experimental data over the isothermal crystallisation temperature range studied (T_c = 245 to 249 °C). Both models were found to accurately account for primary crystallisation and were shown to provide the best representation of the secondary crystallisation process. This was confirmed using standard error of the regression to compare the models with the experimental data, where R^2 values in excess of 0.995 were generated. Furthermore, as the parallel Velisaris-Seferis equation was shown to provide a more accurate fit to the experimental data than that of the series equation, Hay's assumption that both primary and secondary crystallisation occur simultaneously and that total crystallinity at time *t*, is the sum of the two contributions, can be confirmed. Ultimately, having not previously been applied to polyamides or thermoplastic reinforced composites, the findings of this study support the use of the Hay model in determining the isothermal crystallisation kinetics of polymeric materials and extend the current knowledge of the literature.

Owing to the distinctly non-isothermal crystallisation conditions of the stamp forming process, where cooling rates can often exceed 100 °C/min, the non-isothermal crystallisation of PA66/GF was also evaluated. In keeping with the findings of the literature, Mo's theory was shown to provide the best fit to the experimental data over an extended cooling rate range of 10 to 60 °C/min. Contrary to both the Jeziorny and Ozawa models, where neither was shown to provide a linear fit to the experimental data, nor accurately and reliably account for the secondary crystallisation process, Mo's combined Avrami/Ozawa approach was proven to successfully describe the non-isothermal crystallisation of PA66/GF.

It is well documented that the crystal microstructure of thermoplastics can be altered by post-processing low temperature annealing. However, the effect of these morphological changes on the susceptibility of thermoplastics to creep behaviour has yet to determined. Chapter 7 showed that post-stamp forming, low temperature annealing of unidirectional and cross-ply PA66/GF laminates improved the creep performance of the thermoplastic composites by increasing creep modulus and reducing the instantaneous creep strain of the material. DSC thermograms obtained post-annealing showed the appearance of a low temperature melting peak (T_m') characteristic of the melting of thin crystalline structures. The value of T_m' was shown to be dependent on annealing temperature (T_a) with a 46.7 °C difference in T_m' observed between annealing temperatures of 60 and 110 °C (t = 4 hrs). With rising T_a the thickness of the thin lamella structures forming within the interlamella amorphous regions was found to increase which, in accordance with the Thomson-Gibbs equation resulted in T_m' shifting to higher temperatures. Further, by constraining the amorphous chains, these secondary crystals were shown to improve load transfer between the matrix polyamide and glass fibres, reducing the instantaneous strain and extending the linear elastic limit of the material. The greater thickness

of the thin interlamella crystals formed at higher T_a further reduces the mobility of the amorphous chains, ultimately resulting in a deterioration in chain slippage and thus, improved creep performance compared to that of unannealed laminates or laminates annealed at lower temperatures.

Overall, this work has shown that the distinctly non-isothermal cooling conditions associated with the stamp forming process, result in through-thickness variations in both the degree of crystallinity and crystal morphology. Novel work at Diamond Light Source synchrotron radiation facility showed that despite the polyamide matrix rapidly crystallising into the more stable triclinic α-phase, the intensities of the α_1 and α_2 peaks, characteristic of crystal packing and the degree of intermolecular hydrogen bonding, were found to differ through the thickness of the laminate - indicative of a change in crystal structure. Furthermore, the study showed that the isothermal crystallisation kinetics of PA66/GF were best described by the recent Hay model, which having not previously been applied to polyamides or thermoplastic reinforced composites, extends the current findings of the literature. Finally, though previous studies have disclosed the effects of low temperature annealing on crystal microstructure, this work relates the morphological effects of the low temperature annealing process to improvements in mechanical performance, specifically the creep behaviour of thermoplastic composites.

8.2 Future work

X-ray diffraction has proven to beneficial in interpreting local crystalline morphology developed throughout the stamp forming process, however, resulting from limitations in the resolution of the optical camera, beam size (30 μm) and an adapted fly scanning approach, the S/N was inadequate for quantitative analysis. It would be desirable to repeat the experimental work using a reduced beam diameter (~10 μm) to eliminate the adverse effect of the fibres on the S/N and increase the optical resolution in the imaging stage to precisely locate polymer-rich regions prior to the XRD analysis. Further, through the use of an increased integration time at each selected location it should be possible to record WAXS patterns of much higher quality such that the crystal forms can be identified robustly. A beam diameter of 10 μm will enable the larger resin rich pockets to be characterised in more detail, potentially enabling the presence of a transcrystalline phase on the fibre surface to be detected. Ultimately an improvement in S/N should enable diffraction peaks within 1D WAXS patterns to be more accurately resolved and quantitative analysis of the crystalline domains performed. Thus, by changing the experimental parameters, it is expected that mapping of the crystal phase, crystallinity and structural orientation of the polyamide matrix can be determined. Moreover, the effect of glass fibres on the resulting crystallinity and morphology of the matrix polymer can be determined. These findings would be fundamental in understanding the mechanical and physical properties of the part and further, the knowledge gained with regards to the effect of stamp forming parameters on the resulting crystalline morphology, could be used to manufacture parts with specific microstructural or physical requirements.

Mechanical testing provided new and important information on the effects of post-processing low temperature annealing on the creep behaviour of PA66/GF laminates. To further this work,

a wider range of annealing temperatures could be used, and the creep performance of the laminates tested over extended periods of time (days/weeks) to more closely examine the influence of annealing on the time-dependent viscoelastic properties and creep rate of the matrix material. Furthermore, to extend existing knowledge within the literature, XRD could be performed on unannealed and annealed samples to explore the crystal structures formed throughout the low temperature annealing process. Small angle x-ray scattering (SAXS) could be used to identify whether the secondary structures formed on annealing are the result of lamella infill or merely the thickening of very thin, pre-existing primary lamella.

Finally, owing to the exceptionally high cooling rates observed upon closing of the tool and application of the clamping force within the stamp forming process, it is not possible to replicate these cooling conditions using conventional DSC analysis. Therefore, to more accurately model the distinctly non-isothermal conditions experienced throughout the forming process, it could be beneficial to use a fast-scanning calorimetry technique such as the Flash DSC where cooling conditions can be replicated, and the range of cooling rates used within non-isothermal crystallisation kinetic studies extended.

REFERENCES

[1] Emissions in the automotive sector [Internet]. *European commission.* 2018 [cited 2021 Dec 19]. Available from: https://ec.europa.eu/growth/sectors/automotive-industry/environmental-protection/emissions-automotive-sector_en

[2] Colucci, G., Ostrovskaya, O., Frache, A., Martorana, B. & Badini, C. The effect of mechanical recycling on the microstructure and properties of PA66 composites reinforced with carbon fibers. *J Appl Polym Sci.* 2015, 132(29): pp. 42275.

[3] Donderwinkel, T.G., Rietman, B., Haanappel, S.P. & Akkerman, R. Stamp forming optimization for formability and crystallinity. *In: AIP Conference Proceedings.* AIP Publishing LLC; 2016. p. 170029.

[4] Bigg, D.M., Hiscock, D.F., Preston, J.R. & Bradbury, E.J. High Performance Thermoplastic Matrix Composites. *Journal of Thermoplastic Composite Materials.* 1988, 1(2): pp. 146–60.

[5] Hou, M. Stamp forming of continuous glass fibre reinforced polypropylene. *Compos Part A Appl Sci Manuf.* 1997, 28(8): pp. 695–702.

[6] Granta EduPack Software. Granta Design Limited, Cambridge, UK; 2022.

[7] Lee, Y. & Porter, R.S. Crystallization of poly(etheretherketone) (PEEK) in carbon fiber composites. *Polym Eng Sci.* 1986, 26(9): pp. 633–9.

[8] Gohn, A.M., Rhoades, A.M., Wonderling, N., Tighe, T. & Androsch, R. The effect of supercooling of the melt on the semicrystalline morphology of PA 66. *Thermochim Acta.* 2017, 655pp. 313–8.

[9] Frihi, D., Layachi, A., Gherib, S., Stoclet, G., Masenelli-Varlot, K., Satha, H., et al. Crystallization of glass-fiber-reinforced polyamide 66 composites: Influence of glass-fiber content and cooling rate. *Compos Sci Technol.* 2016, 130pp. 70–7.

[10] Nikforooz, M., Golzar, M., Shokrieh, M.M. & Montesano, J. Processability and tensile performance of continuous glass fiber/polyamide laminates for structural load-bearing applications. *Compos Part A Appl Sci Manuf.* 2018, 105pp. 156–64.

[11] Meng, Q., Gu, Y., Luo, L., Wang, S., Li, M. & Zhang, Z. Annealing effect on crystalline structure and mechanical properties in long glass fiber reinforced polyamide 66. *J Appl Polym Sci.* 2017, 134(23): .

[12] Botelho, E.C., Nogueira, C.L. & Rezende, M.C. Monitoring of nylon 6,6/carbon fiber composites processing by x-ray diffraction and thermal analysis. *J Appl Polym Sci.* 2002, 86(12): pp. 3114–9.

[13] McKeen, L.W. Polyamides (Nylons). *In: The Effect of Creep and Other Time Related Factors on Plastics and Elastomers.* 2009. p. 197–262.

[14] Yang, J.L., Zhang, Z., Schlarb, A.K. & Friedrich, K. On the characterization of tensile creep resistance of polyamide 66 nanocomposites. Part I. Experimental results and general discussions. *Polymer (Guildf).* 2006, 47(8): pp. 2791–801.

[15] Fairhurst, A., Thommen, M. & Rytka, C. Comparison of short and long term creep testing in high performance polymers. 2019, .

[16] Hou, M., Friedrich, K. & Scherer, R. Optimization of stamp forming of thermoplastic composite bends. *Compos Struct.* 1994, 27(1–2): pp. 157–67.

[17] Cabrera, N.O., Reynolds, C.T., Alcock, B. & Peijs, T. Non-isothermal stamp forming of continuous tape reinforced all-polypropylene composite sheet. *Compos Part A Appl Sci Manuf.* 2008, 39(9): pp. 1455–66.

[18] Cowie, J.M.G. Polymers: chemistry and physics of modern materials. 3rd ed. *3rd ed.* Boca Raton, Fla; 2008.

[19] Sperling, L.H. Introduction to physical polymer science, 3rd edition. *Vol. 78, Journal of Chemical Education.* Wiley; 2001. p. 1469.

[20] Wunderlich, B. Macromolecular Physics Volume 2: Crystal Nucleation, Growth, Annealing. 1976. p. 462.

[21] Adam, G. & Gibbs, J.H. On the temperature dependence of cooperative relaxation properties in glass-forming liquids. *J Chem Phys.* 1965, 43(1): pp. 139–46.

[22] Mandelkern, Leo. Crystallization of Polymers: Kinetics and Mechanisms. *Vol. 2, Time.* Cambridge University Press; 2004. 467 p.

[23] Lauritzen, J.I. & Hoffman, J.D. Extension of theory of growth of chain-folded polymer crystals to large undercoolings. *J Appl Phys.* 1973, 44(10): pp. 4340–52.

[24] Young, R.J. (Robert J. & Lovell, P.A. (Peter A.). Introduction to polymers. 1991, pp. 443.

[25] Mark, J., Ngai, K., Graessley, W., Mandelkern, L., Samulski, E., Koenig, J., et al. The crystalline state. *Physical Properties of Polymers.* 2004, pp. 209–315.

[26] Perkins, W.G. Polymer toughness and impact resistance. *Polym Eng Sci.* 1999, 39(12): pp. 2445–60.

[27] Menges, G., Schmidt, L., Beyer, C. & Cordes, H. INFLUENCE ON PROPERTIES OF THERMOPLASTICS BY CHANGE OF THE PROCESS PARAMETERS AND BY THE USE OF ADDITIVES-Web of Science Core Collection. *Gummi Asbest Kunststoffe.* 1980, 33(7): pp. 469.

[28] Way, J.L., Atkinson, J.R. & Nutting, J. The effect of spherulite size on the fracture morphology of polypropylene. *J Mater Sci.* 1974, 9(2): pp. 293–9.

[29] Kolb, R., Wutz, C., Stribeck, N., Von Krosigk, G. & Riekel, C. Investigation of secondary crystallization of polymers by means of microbeam X-ray scattering. *Polymer (Guildf)*. 2001, 42(12): pp. 5257–66.

[30] Kohan, M.I. (Melvin I. Nylon plastics handbook. Hanser Publishers; 1995. 631 p.

[31] Garcia, D. & Starkweather, H.W. HYDROGEN BONDING IN NYLON 66 AND MODEL COMPOUNDS. *Journal of polymer science Part A-2, Polymer physics*. 1985, 23(3): pp. 537–55.

[32] Péron, M., Jacquemin, F., Casari, P., Orange, G., Bikard, J., Bailleul, J.-L., et al. Measurement and prediction of residual strains and stresses during the cooling of a glass fibre reinforced PA66 matrix composite. 2020, .

[33] Rhoades, A.M., Williams, J.L. & Androsch, R. Crystallization kinetics of polyamide 66 at processing-relevant cooling conditions and high supercooling. *Thermochim Acta*. 2015, 603pp. 103–9.

[34] Billon, N., Giraudeau, J., Bouvard, J.L. & Robert, G. Mechanical behavior-microstructure relationships in injection-molded polyamide 66. *Polymers (Basel)*. 2018, 10(10): pp. 1047.

[35] Brosse, A.C., Tencé-Girault, S., Piccione, P.M. & Leibler, L. Effect of multi-walled carbon nanotubes on the lamellae morphology of polyamide-6. *Polymer (Guildf)*. 2008, 49(21): pp. 4680–6.

[36] Lu, Y., Zhang, Y., Zhang, G., Yang, M., Yan, S. & Shen, D. Influence of thermal processing on the perfection of crystals in polyamide 66 and polyamide 66/clay nanocomposites. *Polymer (Guildf)*. 2004, 45(26): pp. 8999–9009.

[37] Quintanilla, L. & Pastor, J.M. Structural analysis of polyamide-6,6 reinforced with glass fibre by the use of Fourier transform infra-red spectroscopy with photoacoustic detection and differential scanning calorimetry. *Polymer (Guildf).* 1994, 35(24): pp. 5241–6.

[38] Murthy, N.S., Curran, S.A., Aharoni, S.M. & Minor, H. Premelting Crystalline Relaxations and Phase Transitions in Nylon 6 and 6,6. *Macromolecules.* 1991, 24(11): pp. 3215–20.

[39] Wolanov, Y., Feldman, A.Y., Harel, H. & Marom, G. Amorphous and crystalline phase interaction during the Brill transition in nylon 66. *Express Polym Lett.* 2009, 3(7): pp. 452–7.

[40] Kang, X., He, S., Zhu, C., Lü, L.W.L. & Guo, J. Studies on crystallization behaviors and crystal morphology of polyamide 66/clay nanocomposites. *J Appl Polym Sci.* 2005, 95(3): pp. 756–63.

[41] Bertoldo Menezes, D., Reyer, A., Marletta, A. & Musso, M. Determination of the temperatures of the γ, β and α relaxation processes in nylon 6,6 by Raman spectroscopy. *Polymer (Guildf).* 2016, 106pp. 85–90.

[42] Klein, N., Selivansky, D. & Marom, G. The effects of a nucleating agent and of fibers on the crystallization of nylon 66 matrices. *Polym Compos.* 1995, 16(3): pp. 189–97.

[43] Haberkorn, H., Illers, K.H. & Simak, P. Molekülordnung und Kristallinität in Polyhexamethylenadipamid. *Colloid Polym Sci.* 1979, 257(8): pp. 820–40.

[44] Stewart, R. Thermoplastic composites - Recyclable and fast to process. *Reinforced Plastics.* 2011, 55(3): pp. 22–8.

[45] Friedrich, K. Carbon fiber reinforced thermoplastic composites for future automotive applications. *In: AIP Conference Proceedings.* 2016. p. 20032.

[46] Spoerer, Y., Androsch, R., Jehnichen, D. & Kuehnert, I. Process induced skin-core morphology in injection molded polyamide 66. *Polymers (Basel)*. 2020, 12(4): .

[47] Hoffman, J.D. & Miller, R.L. Kinetics of crystallization from the melt and chain folding in polyethylene fractions revisited: Theory and experiment. *Vol. 38, Polymer*. 1997. p. 3151–212.

[48] Chen, Z., Jenkins, M.J. & Hay, J.N. Annealing of poly (ethylene terephthalate). *Eur Polym J*. 2014, 50(1): pp. 235–42.

[49] Makhlouf, A., Layachi, A., Kouadri, I., Belaadi, A. & Satha, H. Structural study and thermal behavior of composites: Polyamide 66/glass fibers: The reinforcement ratio effect on the kinetics of crystallization. *J Compos Mater*. 2020, 54(11): pp. 1467–81.

[50] Behrens, B.A., Raatz, A., Hübner, S., Bonk, C., Bohne, F., Bruns, C., et al. Automated Stamp Forming of Continuous Fiber Reinforced Thermoplastics for Complex Shell Geometries. *Procedia CIRP*. 2017, 66pp. 113–8.

[51] Breuer, U., Ostgathe, M. & Neitzel, M. Manufacturing of all-thermoplastic sandwich systems by a one-step forming technique. *Polym Compos*. 1998, 19(3): pp. 275–9.

[52] Jamin, T., Dubé, M. & Lebel, L.L. Effect of stamp-forming parameters and bend radius on the mechanical performance of curved beam carbon fiber/polyphenylene sulfide specimens. *J Compos Mater*. 2016, 50(9): pp. 1213–25.

[53] Wakeman, M.D., Zingraff, L., Bourban, P.E., Månson, J.A.E. & Blanchard, P. Stamp forming of carbon fibre/PA12 composites - A comparison of a reactive impregnation process and a commingled yarn system. *Compos Sci Technol*. 2006, 66(1): pp. 19–35.

[54] Hou, M. & Friedrich, K. 3-D stamp forming of thermoplastic matrix composites. *Applied Composite Materials*. 1994, 1(2): pp. 135–53.

[55] Lessard, H., Lebrun, G., Benkaddour, A. & Pham, X.T. Influence of process parameters on the thermostamping of a [0/90]12 carbon/polyether ether ketone laminate. *Compos Part A Appl Sci Manuf.* 2015, 70pp. 59–68.

[56] McCool, R., Murphy, A., Wilson, R., Jiang, Z., Price, M., Butterfield, J., et al. Thermoforming carbon fibre-reinforced thermoplastic composites. *Proceedings of the Institution of Mechanical Engineers, Part L: Journal of Materials: Design and Applications*. 2012, 226(2): pp. 91–102.

[57] Lawrence, W.E., Manson, J.-A.A.E. & Seferis, J.C. Thermal and morphological skin-core effects in processing of thermoplastic composites. *Composites.* 1990, 21(6): pp. 475–80.

[58] Parlevliet, P.P., van der Werf, W.A.W., Bersee, H.E.N. & Beukers, A. Thermal effects on microstructural matrix variations in thick-walled composites. *Compos Sci Technol.* 2008, 68(3–4): pp. 896–907.

[59] Ijaz, M., Robinson, M. & Gibson, A.G. Cooling and crystallisation behaviour during vacuum-consolidation of commingled thermoplastic composites. *Compos Part A Appl Sci Manuf.* 2007, 38(3): pp. 828–42.

[60] McCallum, S., Tsukada, T. & Takeda, N. The influence of skin-core residual stress and cooling rate on the impact response of carbon fibre/polyphenylenesulphide. *Journal of Thermoplastic Composite Materials*. 2018, 31(9): pp. 1232–51.

[61] Tsukada, T., Minakuchi, S. & Takeda, N. Identification of process-induced residual stress/strain distribution in thick thermoplastic composites based on in situ strain monitoring using optical fiber sensors. *J Compos Mater.* 2019, 53(24): pp. 3445–58.

[62] Mulle, M., Wafai, H., Yudhanto, A., Lubineau, G., Yaldiz, R., Schijve, W., et al. Process monitoring of glass reinforced polypropylene laminates using fiber Bragg gratings. *Compos Sci Technol.* 2016, 123pp. 143–50.

[63] Baran, I., Cinar, K., Ersoy, N., Akkerman, R. & Hattel, J.H. A Review on the Mechanical Modeling of Composite Manufacturing Processes. *Archives of Computational Methods in Engineering.* 2017, 24(2): pp. 365–95.

[64] Parlevliet, P.P., Bersee, H.E.N. & Beukers, A. Residual stresses in thermoplastic composites-A study of the literature-Part I: Formation of residual stresses. *Vol. 37, Composites Part A: Applied Science and Manufacturing.* 2006. p. 1847–57.

[65] Quintanilla, L., Rodríguez-Cabello, J.C., Jawhari, T. & Pastor, J.M. Structural analysis of injection-moulded semicrystalline polymers by Fourier transform infra-red spectroscopy with photoacoustic detection and differential scanning calorimetry: 1. Poly(ethylene terephthalate). *Polymer (Guildf).* 1993, 34(18): pp. 3787–95.

[66] Vasanthan, N. & Salem, D.R. Structure characterization of heat set and drawn polyamide 66 fibers by FTIR spectroscopy. *Materials Research Innovations.* 2001, 4(2–3): pp. 155–60.

[67] Vasanthan, N. & Salem, D.R. Infrared spectroscopic characterization of oriented polyamide 66: band assignment and crystallinity measurement. *J Polym Sci B Polym Phys.* 2000, 38(4): pp. 516–24.

[68] Murty, E.M. & Yehl, T.W. Adaptation of photoacoustic fourier transform infrared spectroscopy for studying the thermal oxidation of nylon 66 at 150°c correlated to mechanical properties. *Polym Eng Sci.* 1990, 30(24): pp. 1595–8.

[69] Galimberti, D., Quarti, C., Milani, A., Brambilla, L., Civalleri, B. & Castiglioni, C. IR spectroscopy of crystalline polymers from ab initio calculations: Nylon 6,6. *Vib Spectrosc.* 2013, 66pp. 83–92.

[70] Skrovanek, D.J., Painter, P.C. & Coleman, M.M. Hydrogen Bonding in Polymers. 2. Infrared Temperature Studies of Nylon 11. *Macromolecules.* 1986, 19(3): pp. 699–705.

[71] Quintanilla, L. & Pastor, J.M. Structural analysis of polyamide-6,6 reinforced with glass fibre by the use of Fourier transform infra-red spectroscopy with photoacoustic detection and differential scanning calorimetry. *Polymer (Guildf).* 1994, 35(24): pp. 5241–6.

[72] Mandelkern, L. The relation between structure and properties of crystalline polymers. *Polym J.* 1985, 17(1): pp. 337–50.

[73] Chen, Z., Hay, J.N. & Jenkins, M.J. The kinetics of crystallization of poly(ethylene terephthalate) measured by FTIR spectroscopy. *Eur Polym J.* 2013, 49(6): pp. 1722–30.

[74] Phillipson, K., Jenkins, M.J. & Hay, J.N. The kinetics of crystallization of poly(ε-caprolactone) measured by FTIR spectroscopy. *J Therm Anal Calorim.* 2016, 123(2): pp. 1491–500.

[75] Price, D.M. & Jarratt, M. Thermal conductivity of PTFE and PTFE composites. *Thermochim Acta.* 2002, 392–393pp. 231–6.

[76] Sengupta, R., Tikku, V.K., Somani, A.K., Chaki, T.K. & Bhowmick, A.K. Electron beam irradiated polyamide-6,6 films - I: Characterization by wide angle X-ray scattering and infrared spectroscopy. *Radiation Physics and Chemistry.* 2005, 72(5): pp. 625–33.

[77] Liu, X., Wu, Q., Zhang, Q. & Mo, Z. Phase transition in polyamide-66/montmorillonite nanocomposites on annealing. *J Polym Sci B Polym Phys.* 2002, 41(1): pp. 63–7.

[78] Liu, X., Wu, Q. & Berglund, L.A. Polymorphism in polyamide 66/clay nanocomposites. *Polymer (Guildf).* 2002, 43(18): pp. 4967–72.

[79] Militký, J., Venkataraman, M. & Mishra, R. The chemistry, manufacture, and tensile behavior of polyamide fibers. *In: Handbook of Properties of Textile and Technical Fibres*. Elsevier; 2018. p. 367–419.

[80] Brill, R. Über das Verhalten von Polyamiden beim Erhitzen. *Journal für Praktische Chemie*. 1942, 161(1–3): pp. 49–64.

[81] Feldman, A.Y., Wachtel, E., Vaughan, G.B.M., Weinberg, A. & Marom, G. The Brill transition in transcrystalline nylon-66. *Macromolecules*. 2006, 39(13): pp. 4455–9.

[82] Drummer, D. & Meister, S. Correlation of processing, inner structure, and part properties of injection moulded thin-wall parts on example of polyamide 66. *Int J Polym Sci.* 2014, 2014.

[83] Spoerer, Y., Androsch, R., Jehnichen, D. & Kuehnert, I. Process Induced Skin-Core Morphology in Injection Molded Polyamide 66. *Polymers 2020, Vol 12, Page 894*. 2020, 12(4): pp. 894.

[84] Marie Rhoades, A., Louis Williams, J., Wonderling, N., Androsch, R. & Guo, J. Skin/core crystallinity of injection-molded poly (butylene terephthalate) as revealed by microfocus X-ray diffraction and fast scanning chip calorimetry. *J Therm Anal Calorim*. 127.

[85] Bunn, C.W. & Garner, E. V. The crystal structures of two polyamides (‘nylons’). *Proc R Soc Lond A Math Phys Sci.* 1947, 189(1016): pp. 39–68.

[86] Kobayashi, D., Hsieh, Y.-T. & Takahara, A. Interphase structure of carbon fiber reinforced polyamide 6 revealed by microbeam X-ray diffraction with synchrotron radiation. 2016, .

[87] Feldman, A.Y., Wachtel, E., Zafeiropoulos, N.E., Schneider, K., Stamm, M., Davies, R.J., et al. In situ synchrotron microbeam analysis of the stiffness of transcrystallinity in aramid fiber reinforced nylon 66 composites. 2006, .

[88] Feldman, A.Y., Fernanda Gonzalez, M., Wachtel, E., Moret, M.P. & Marom, G. Transcrystallinity in aramid and carbon fiber reinforced nylon 66: Determining the lamellar orientation by synchrotron X-ray micro diffraction. *Polymer (Guildf)*. 2004, 45(21): pp. 7239–45.

[89] Klein, N., Marom, G. & Wachtel, E. Microstructure of nylon 66 transcrystalline layers in carbon and aramid fibre reinforced composites. *Polymer (Guildf)*. 1996, 37(24): pp. 5493–8.

[90] Schindelin, J., Arganda-Carreras, I., Frise, E., Kaynig, V., Longair, M., Pietzsch, T., et al. Fiji: an open-source platform for biological-image analysis. *Nature Methods 2012 9:7*. 2012, 9(7): pp. 676–82.

[91] Chen, Z., Hay, J.N. & Jenkins, M.J. The effect of secondary crystallization on crystallization kinetics - Polyethylene terephthalate revisited. *Eur Polym J.* 2016, 81pp. 216–23.

[92] Phillipson, K., Jenkins, M.J. & Hay, J.N. The effect of a secondary process on crystallization kinetics – Poly (ϵ-caprolactone) revisited. *Eur Polym J.* 2016, 84pp. 708–14.

[93] Marsh, J.J., Turner, R.P., Carter, J. & Jenkins, M.J. Thermal diffusivity and secondary crystallisation kinetics in poly(lactic acid). *Polymer (Guildf)*. 2019, 179.

[94] Torre, F.J., Cortázar, M.M., Gómez, M.Á., Ellis, G. & Marco, C. Isothermal crystallisation of iPP/Vectra blends by DSC and simultaneous SAXS and WAXS

measurements employing synchrotron radiation. *Polymer (Guildf).* 2003, 44(18): pp. 5209–17.

[95] Avrami, M. Kinetics of phase change. I: General theory. *J Chem Phys.* 1939, 7(12): pp. 1103–12.

[96] Avrami, M. Kinetics of phase change. II Transformation-time relations for random distribution of nuclei. *J Chem Phys.* 1940, 8(2): pp. 212–24.

[97] Avrami, M. Granulation, phase change, and microstructure kinetics of phase change. III. *J Chem Phys.* 1941, 9(2): pp. 177–84.

[98] Lorenzo, A.T., Arnal, M.L., Albuerne, J. & Müller, A.J. DSC isothermal polymer crystallization kinetics measurements and the use of the Avrami equation to fit the data: Guidelines to avoid common problems. *Polym Test.* 2007, 26(2): pp. 222–31.

[99] Verhoyen, O., Dupret, F. & Legras, R. Isothermal and non-isothermal crystallization kinetics of polyethylene terephthalate: Mathematical modeling and experimental measurement. *Polym Eng Sci.* 1998, 38(9): pp. 1594–610.

[100] Piorkowska, E., Galeski, A. & Haudin, J.M. Critical assessment of overall crystallization kinetics theories and predictions. *Vol. 31, Progress in Polymer Science (Oxford).* 2006. p. 549–75.

[101] Hay, J.N. Secondary crystallization kinetics. *Vol. 1, Polymer Crystallization.* 2018.

[102] Supaphol, P. & Spruiell, J.E. Application of the Avrami, Tobin, Malkin, and simultaneous Avrami macrokinetic models to isothermal crystallization of syndiotactic polypropylenes. *J Macromol Sci Phys.* 2000, 39(2): pp. 257–77.

[103] Hay, J.N. & Przekop, Z.J. ON A NONEXPONENTIAL TRANSFORMATION EQUATION FOR SPHERULITIC CRYSTALLIZATION. *J Polym Sci Polym Phys Ed.* 1978, 16(1): pp. 81–9.

[104] Tobin, M.C. Theory of phase transition kinetics with growth site impingement. I. Homogeneous nucleation. *Journal of Polymer Science: Polymer Physics Edition.* 1974, 12(2): pp. 399–406.

[105] Tobin, M.C. The theory of phase transition kinetics with growth site impingement. II. Heterogeneous nucleation. *Journal of Polymer Science: Polymer Physics Edition.* 1976, 14(12): pp. 2253–7.

[106] Tobin, M.C. Theory of phase transition kinetics with growth site impingement. III. Mixed heterogeneous–homogeneous nucleation and nonintegral exponents of the time. *Journal of Polymer Science: Polymer Physics Edition.* 1977, 15(12): pp. 2269–70.

[107] Malkin, A.Y., Beghishev, V.P., Keapin, I.A. & Bolgov, S.A. General treatment of polymer crystallization kinetics—Part 1. A new macrokinetic equation and its experimental verification. *Polym Eng Sci.* 1984, 24(18): pp. 1396–401.

[108] Urbanovici, E. & Segal, E. New formal relationships to describe the kinetics of crystallization. *Thermochim Acta.* 1990, 171(C): pp. 87–94.

[109] Urbanovici, E., Schneider, H.A., Brizzolara, D. & Cantow, H.J. Isothermal melt crystallization kinetics of poly(L-lactic acid). *Journal of Thermal Analysis.* 1996, 47(4): pp. 931–9.

[110] Velisaris, C.N. & Seferis, J.C. Crystallization kinetics of polyetheretherketone (peek) matrices. *Polym Eng Sci.* 1986, 26(22): pp. 1574–81.

[111] Kelly, C.A., Hay, J.N., Turner, R.P. & Jenkins, M.J. The effect of a secondary process on the analysis of isothermal crystallisation kinetics by differential scanning calorimetry. *Polymers (Basel).* 2020, 12(1): .

[112] Thanomkiat, P., Phillips, R.A. & Supaphol, P. Influence of molecular characteristics on overall isothermal melt-crystallization behavior and equilibrium melting temperature of syndiotactic polypropylene. *Eur Polym J.* 2004, 40(8): pp. 1671–82.

[113] Supaphol, P. Application of the Avrami, Tobin, Malkin, and Urbanovici - Segal macrokinetic models to isothermal crystallization of syndiotactic polypropylene. *Thermochim Acta.* 2001, 370(1–2): pp. 37–48.

[114] Chen, Z., Hay, J.N. & Jenkins, M.J. The effect of secondary crystallization on melting. *Eur Polym J.* 2013, 49(9): pp. 2697–703.

[115] Phillipson, K., J Jenkins, M. & Hay, J.N. The ageing of poly(ε-caprolactone). *Polym Int.* 2015, 64(12): pp. 1695–705.

[116] Zhang, F., Zhou, L., Xiong, Y., Liu, G. & Xu, W. Isothermal Crystallisation Kinetics of High-Flow Nylon 6 by Differential Scanning Calorimetry. *J Appl Polym Sci.* 2008, 111pp. 2930–7.

[117] Zhang, F., Wang, B., Man, R. & Peng, Z. Isothermal Crystallisation Kinetics of In Situ Nylon 6/Graphene Composites by Differential Scanning Calorimetry. *Polym Eng Sci.* 2014, pp. 2610–6.

[118] Seo, J., Takahashi, H., Nazari, B., Rhoades, A.M., Schaake, R.P. & Colby, R.H. Isothermal Flow-Induced Crystallization of Polyamide 66 Melts. *Macromolecules.* 2018, 51(11): pp. 4269–79.

[119] Won, J.C., Fulchiron, R., Douillard, A., Chabert, B., Varlet, J. & Chomier, D. Crystallization kinetics of polyamide 66 in non-isothermal and isothermal conditions: Effect of nucleating agent and pressure. *Polym Eng Sci.* 2000, 40(9): pp. 2058–71.

[120] Cui, X., Qing, S. & Yan, D. Isothermal and nonisothermal crystallization kinetics of novel odd-odd polyamide 9 11. *Eur Polym J.* 2005, 41(12): pp. 3060–8.

[121] Li, Y., Zhu, X. & Yan, D. Isothermal and nonisothermal crystallization kinetics of Nylon 10 12. *Polym Eng Sci.* 2000, 40(9): pp. 1989–95.

[122] Neugebauer, F., Ploshikhin, V., Ambrosy, J. & Witt, G. Isothermal and non-isothermal crystallization kinetics of polyamide 12 used in laser sintering. *J Therm Anal Calorim.* 2016, 124(2): pp. 925–33.

[123] Neugebauer, F., Ploshikhin, V., Ambrosy, J. & Witt, G. Isothermal and non-isothermal crystallization kinetics of polyamide 12 used in laser sintering. *J Therm Anal Calorim.* 2016, 124(2): pp. 925–33.

[124] Shi, X., Wang, J., Jiang, B. & Yang, Y. Influence of nanofiller dimensionality on the crystallization behavior of HDPE/carbon nanocomposites. *J Appl Polym Sci.* 2013, 128(6): pp. 3609–18.

[125] Khoshkava, V., Ghasemi, H. & Kamal, M.R. Effect of cellulose nanocrystals (CNC) on isothermal crystallization kinetics of polypropylene. *Thermochim Acta.* 2015, 608pp. 30–9.

[126] Dangseeyun, N., Srimoaon, P., Supaphol, P. & Nithitanakul, M. Isothermal melt-crystallization and melting behavior for three linear aromatic polyesters. *Thermochim Acta.* 2004, 409(1): pp. 63–77.

[127] Somsunan, R. & Mainoiy, N. Isothermal and non-isothermal crystallization kinetics of PLA/PBS blends with talc as nucleating agent. *J Therm Anal Calorim.* 2020, 139(3): pp. 1941–8.

[128] Al-Mulla, A., Al-Omairi, L., Mathew, J. & Bhattacharya, S. Isothermal crystallization kinetics of tricomponent blends of polycarbonate, poly(trimethylene terephthalate) and polybutylene terephthalate. *Polymers and Polymer Composites.* 2010, 18(6): pp. 307–13.

[129] Huang, J.W., Kang, C.C. & Chen, T.H. Isothermal crystallization of poly(ethylene-co-glycidyl methacrylate)/clay nanocomposites. *J Appl Polym Sci.* 2005, 97(3): pp. 1051–64.

[130] Nikam, P.N. & Deshpande, V.D. Isothermal crystallization kinetics of PET/alumina nanocomposites using distinct macrokinetic models. *J Therm Anal Calorim.* 2019, 138(2): pp. 1049–67.

[131] Kelly, C.A. & Jenkins, M.J. Modeling the crystallization kinetics of polymers displaying high levels of secondary crystallization. *Polym J.* 2022, 54(3): pp. 249–57.

[132] Albano, C., Papa, J., Ichazo, M., González, J. & Ustariz, C. Application of different macrokinetic models to the isothermal crystallization of PP/talc blends. *Compos Struct.* 2003, 62(3–4): pp. 291–302.

[133] Li, X., He, Y., Dong, X., Ren, X., Gao, H. & Hu, W. Effects of hydrogen-bonding density on polyamide crystallization kinetics. *Polymer (Guildf).* 2020, 189.

[134] Simal, A.L. & Martin, A.R. Structure of heat-treated nylon 6 and 6.6 fibers. I. The shrinkage mechanism. *J Appl Polym Sci.* 1998, 68(3): pp. 441–52.

[135] Starkweather, H.W., Zoller, P. & Jones, G.A. HEAT OF FUSION OF 66 NYLON. *Journal of polymer science Part A-2, Polymer physics.* 1984, 22(9): pp. 1615–21.

[136] Wang, Y., Kang, H.L., Wang, R., Liu, R.G. & Hao, X.M. Crystallization of polyamide 56/polyamide 66 blends: Non-isothermal crystallization kinetics. *J Appl Polym Sci.* 2018, 135(26): .

[137] Faraj, J., Boyard, N., Pignon, B., Bailleul, J.L., Delaunay, D. & Orange, G. Crystallization kinetics of new low viscosity polyamides 66 for thermoplastic composites processing. *Thermochim Acta.* 2016, 624pp. 27–34.

[138] McFerran, N.L.A., Armstrong, C.G. & McNally, T. Nonisothermal and isothermal crystallization kinetics of nylon-12. *J Appl Polym Sci.* 2008, 110(2): pp. 1043–58.

[139] Layachi, A., Frihi, D., Satha, H., Seguela, R. & Gherib, S. Non-isothermal crystallization kinetics of polyamide 66/glass fibers/carbon black composites. *J Therm Anal Calorim.* 2016, 124(3): pp. 1319–29.

[140] Lou, S., Zhang, H., Liu, F., Yin, W., Ren, G., Chen, Z., et al. Effects of post-treatment on crystallization behavior of glass fiber-reinforced polyamide 66 composite with red phosphorus flame retardant. *J Therm Anal Calorim.* 2021, .

[141] Şanli, S., Durmus, A. & Ercan, N. Effect of nucleating agent on the nonisothermal crystallization kinetics of glass fiber- and mineral-filled polyamide-6 composites. *J Appl Polym Sci.* 2012, 125(SUPPL. 1): .

[142] Li, J., Fang, Z., Tong, L., Gu, A. & Liu, F. Effect of multi-walled carbon nanotubes on non-isothermal crystallization kinetics of polyamide 6. *Eur Polym J.* 2006, 42(12): pp. 3230–5.

[143] Jeziorny, A. Parameters characterizing the kinetics of the non-isothermal crystallization of poly(ethylene terephthalate) determined by d.s.c. *Polymer (Guildf).* 1978, 19(10): pp. 1142–4.

[144] Ozawa, T. A New Method of Analyzing Thermogravimetric Data. *Bull Chem Soc Jpn.* 1965, 38(11): pp. 1881–6.

[145] Liu, T., Mo, Z., Wang, S. & Zhang, H. Isothermal melt and cold crystallization kinetics of poly(aryl ether ether ketone ketone) (PEEKK). *Eur Polym J.* 1997, 33(9): pp. 1405–14.

[146] Liu, Y. & Yang, G. Non-isothermal crystallization kinetics of polyamide-6/graphite oxide nanocomposites. *Thermochim Acta.* 2010, 500(1–2): pp. 13–20.

[147] Layachi, A., Makhlouf, A., Frihi, D., Satha, H., Belaadi, A. & Seguela, R. Non-isothermal crystallization kinetics and nucleation behavior of isotactic polypropylene composites with micro-talc. *J Therm Anal Calorim.* 2019, 138(2): pp. 1081–95.

[148] Tjong, S.C. & Bao, S.P. Preparation and nonisothermal crystallization behavior of polyamide 6/montmorillonite nanocomposites. *J Polym Sci B Polym Phys.* 2004, 42(15): pp. 2878–91.

[149] Jape, S.P. & Deshpande, V.D. Nonisothermal crystallization kinetics of nylon 66/LCP blends. *Thermochim Acta.* 2017, 655pp. 1–12.

[150] Handa, K., Kato, A. & Narisawa, I. Fatigue characteristics of a glass-fiber-reinforced polyamide. *J Appl Polym Sci.* 1999, 72(13): pp. 1783–93.

[151] Pan, Y., Gao, X., Lei, J., Li, Z. & Shen, K. Effect of different morphologies on the creep behavior of high-density polyethylene. 2016, .

[152] Yang, J.L., Zhang, Z., Schlarb, A.K. & Friedrich, K. On the characterization of tensile creep resistance of polyamide 66 nanocomposites. Part II: Modeling and prediction of long-term performance. *Polymer (Guildf).* 2006, 47(19): pp. 6745–58.

[153] Starkova, O., Yang, J. & Zhang, Z. Application of time-stress superposition to nonlinear creep of polyamide 66 filled with nanoparticles of various sizes. 2007, .

[154] Sakai, T., Hirai, Y. & Somiya, S. Estimating the creep behavior of glass-fiber-reinforced polyamide considering the effects of crystallinity and fiber volume fraction. *Mech Adv Mater Mod Process.* 2018, 4(1): .

[155] Seltzer, R., Mai, Y.-W. & Frontini, P.M. Creep behaviour of injection moulded polyamide 6/organoclay nanocomposites by nanoindentation and cantilever-bending. 2011, .

[156] Shen, L., Phang, I.Y., Chen, L., Liu, T. & Zeng, K. Nanoindentation and morphological studies on nylon 66 nanocomposites. I. Effect of clay loading. *Polymer (Guildf).* 2004, 45(10): pp. 3341–9.

[157] Sakai, T., Shamsudim, N.S.B., Fukushima, R. & Kageyama, K. Effect of matrix crystallinity of carbon fiber reinforced polyamide 6 on static bending properties. *Advanced Composite Materials.* 2021, 30(S2): pp. 71–84.

[158] Lafranche, E., Coulon, A., Krawczak, P., Ciolczyk, J.P. & Gamache, E. A microstructural approach for modelling flexural properties of long glass fibre reinforced polyamide6.6. *J Compos Mater.* 2017, 51(1): pp. 3–16.

[159] Coulon, A., Lafranche, E., Douchain, C., Krawczak, P., Ciolczyk, J.P. & Gamache, E. Flexural creep behaviour of long glass fibre reinforced polyamide 6.6 under thermal-oxidative environment. *J Compos Mater.* 2017, 51(17): pp. 2477–90.

[160] Chevali, V.S. & Janowski, G.M. Flexural creep of long fiber-reinforced thermoplastic composites: Effect of processing-dependent fiber variables on creep response. *In: Composites Part A: Applied Science and Manufacturing.* 2010. p. 1253–62.

[161] Parodi, E., Peters, G.W.M. & Govaert, L.E. Structure-properties relations for Polyamide 6, Part 1: Influence of the thermal history during compression moulding on deformation and failure kinetics. *Polymers (Basel).* 2018, 10(7): pp. 1–19.

[162] Kaya, E. & Mathias, L.J. Investigation of melting behaviors and crystallinity of linear polyamide with high-aliphatic content. *J Appl Polym Sci.* 2012, 123(1): pp. 92–8.

[163] Castagnet, S. & Thilly, L. High-pressure dependence of structural evolution in polyamide 11 during annealing. *J Polym Sci B Polym Phys.* 2009, 47(20): pp. 2015–25.

[164] Neidhöfer, M., Beaume, F., Ibos, L., Bernès, A. & Lacabanne, C. Structural evolution of PVDF during storage or annealing. *Polymer (Guildf).* 2004, 45(5): pp. 1679–88.

[165] Shan, G.F., Yang, W., Tang, X.G., Yang, M.B., Xie, B.H., Fu, Q., et al. Multiple melting behaviour of annealed crystalline polymers. *Polym Test.* 2010, 29(2): pp. 273–80.

[166] Marand, H., Alizadeh, A., Farmer, R., Desai, R. & Velikov, V. Influence of Structural and Topological Constraints on the Crystallization and Melting Behavior of Polymers. 2. Poly(arylene ether ether ketone). *Macromolecules.* 2000, 33(9): pp. 3392–403.

[167] Dencheva, N., Denchev, Z., Oliveira, M.J. & Funari, S.S. Relationship between crystalline structure and mechanical behavior in isotropic and oriented polyamide 6. *J Appl Polym Sci.* 2007, 103(4): pp. 2242–52.

[168] Alizadeh, A., Sohn, S., Quinn, J., Marand, H., Shank, L.C. & Darrell Iler, H. Influence of structural and topological constraints on the crystallization and melting behavior of polymers: 3. Bisphenol a polycarbonate. *Macromolecules.* 2001, 34(12): pp. 4066–78.

[169] Lauritzen, J.I. & Hoffman, J.D. Formation of polymer crystals with folded chains from dilute solution. *Vol. 31, The Journal of Chemical Physics.* 1959. p. 1680–1.

[170] Dencheva, N., Denchev, Z., Oliveira, M.J. & Funari, S.S. Relationship between crystalline structure and mechanical behavior in isotropic and oriented polyamide 6. *J Appl Polym Sci.* 2007, 103(4): pp. 2242–52.

[171] Parodi, E., Govaert, L.E. & Peters, G.W.M. Glass transition temperature versus structure of polyamide 6: A flash-DSC study. *Thermochim Acta.* 2017, 657(July): pp. 110–22.

[172] Chaichanawong, J., Thongchuea, C. & Areerat, S. Effect of moisture on the mechanical properties of glass fiber reinforced polyamide composites. *Advanced Powder Technology.* 2016, 27(3): pp. 898–902.

[173] Ksouri, I. & Haddar, N. Long term ageing of polyamide 6 and polyamide 6 reinforced with 30% of glass fibers: temperature effect. *Journal of Polymer Research.* 2018, 25(7): .

[174] Le Gac, P.Y. & Fayolle, B. Impact of fillers (short glass fibers and rubber) on the hydrolysis-induced embrittlement of polyamide 6.6. *Compos B Eng.* 2018, 153pp. 256–63.

[175] Deshoulles, Q., Le Gall, M., Dreanno, C., Arhant, M., Priour, D. & Le Gac, P.Y. Modelling pure polyamide 6 hydrolysis: Influence of water content in the amorphous phase. *Polym Degrad Stab.* 2021, 183pp. 109435.

[176] Zhang, S., Huang, Z., Zhang, Y. & Zhou, H. Experimental investigation of moisture diffusion in short-glass-fiber-reinforced polyamide 6,6. *J Appl Polym Sci.* 2015, 132(37): pp. 42369.

[177] Hutchinson, J.M. Physical aging of polymers. *Vol. 20, Progress in Polymer Science.* Pergamon; 1995. p. 703–60.

[178] Guo, B., Zou, Q., Lei, Y., Du, M., Liu, M. & Jia, D. Crystallization behavior of polyamide 6/halloysite nanotubes nanocomposites. *Thermochim Acta.* 2009, 484(1–2): pp. 48–56.

[179] Lee, S.S. & Phillips, P.J. Melt crystallized polyamide 6.6 and its copolymers, Part I. Melting point - Lamellar thickness relations in the homopolymer. *Eur Polym J.* 2007, 43(5): pp. 1933–51.

[180] Di Lorenzo, M.L. & Righetti, M.C. Crystallization-induced formation of rigid amorphous fraction. *Polymer Crystallization.* 2018, 1(2): .

APPENDIX A

Material Datasheet – PA66/GF

CELSTRAN® CFR-TP PA66 GF60-02 - PA66

Description

Celstran® CFR-TP PA66 GF60-02 is a 60% E-glass by weight polyamide 66 (nylon 66) continuous fiber (uni-directional) reinforced thermoplastic composite tape. This material exhibits a high strength-to-weight ratio, excellent toughness and impact resistance. It is well suited for industrial, automotive and sporting goods applications where weight, strength and toughness are critical, as well as higher thermal resistance of PA66 versus other nylon materials. This material is available in natural and black colors. Alternate tape widths and thicknesses may be available.

Physical properties	Value	Unit	Test Standard
Density	**1730**	kg/m³	ISO 1183
Fiber Content	**60**	% by wt.	-
Fiber Volume	**40.2**	% by vol.	-
Tape Thickness	**0.3**	mm	-
Tape Width	**305**	mm	-
Tape Areal Weight	**485**	g/m²	-
Fiber Areal Weight	**291**	g/m²	-

Mechanical properties (Tape)	Value	Unit	Test Standard
Tensile Strength, 0°	**759**	MPa	ASTM D 3039M
Tensile Modulus, 0°	**33.4**	GPa	ASTM D 3039M
Tensile Strain at Failure, 0°	**2.48**	%	ASTM D 3039M
Flexural Strength, 0°	**791**	MPa	ASTM D 790/Tape
Flexural Modulus, 0°	**32**	GPa	ASTM D 790/Tape
Flexural Strain at Failure, 0°	**3.32**	%	ASTM D 790/Tape

Thermal properties	Value	Unit	Test Standard
Melting temperature, 10°C/min	**260**	°C	ISO 11357-1/-3
Glass transition temperature, 10°C/min	**50**	°C	ISO 11357-1,-2,-3

Other text information

Compression molding

Celstran® CFR-TP Tape Laminate Processing Guidelines

Celstran® CFR-TP can be molded using a heated platen compression molding press. A hardened steel, aluminum or flexible tooling can be used depending on the application. The tool should be treated with a mold release prior to molding.

The molding cycle consists of the following steps:
1. The platens should be heated above the polymer matrix melt temperature.
2. The individual lamina should be constructed and placed in the tool to achieve the desired laminate reinforcement orientation.
3. The tool is placed between the platens and the platens are closed to achieve a contact pressure on the tool less than 30 psi (2 bar).
4. The tool is allowed to rise in temperature until stabilizing at the initial temperature the platens were set to.
5. The pressure is increased to the desired amount and held for a recommended time.
6. Air and/or water cooling is initiated until the material reaches a temperature sufficiently below the melt and peak crystallization temperatures wherein the pressure is reduced to a contact pressure less than 15 psi (1 bar).
7. The tool is continually cooled until reaching a temperature, typically at or below the glass transition point, at which the pressure is completely removed and the part de-molded from the tool. It should be noted that the choice of tooling, geometry and heating/cooling mechanisms will greatly dictate processing conditions, and thus, optimization specific to the individual molders' capabilities is necessary. Additionally, the resin is what dictates the molding temperatures, whereas the sample thickness is what determines the time. As the thickness increases, the time at melt should also increase to account for the time for heat to conduct to the center of the laminate.

It should be noted that the choice of tooling, geometry and heating/cooling mechanisms will greatly dictate processing conditions, and thus, optimization specific to the individual molders' capabilities is necessary.
Additionally, the resin is what dictates the molding temperatures, whereas the sample thickness is what determines the time. As the thickness increases, the time at melt should also increase to account for the time for heat to conduct to the center of the laminate.

Resin: PA66
Drying Time: 2 hours

CELSTRAN® CFR-TP PA66 GF60-02 - PA66

Drying Temperature: 180°F, 82°C
Platen Temperature: 585°F, 307°C
Press Pressure: 84 psi, 5.8 bar
Time at Melt: 5 min
Cooling Rate: 15-30°F/min, 8-17°C/min
Material Removal Temperature: 125°F, 52°C

Contact Information

Americas
8040 Dixie Highway
Florence, KY 41042 USA
Product Information Service
t: +1-800-833-4882
t: +1-859-372-3244
Customer Service
t: +1-800-526-4960
t: +1-859-372-3214
e: info-engineeredmaterials-am@celanese.com

Asia
4560 Jinke Road
Zhang Jiang Hi Tech Park
Shanghai 201203 PRC
Customer Service
t: +86 21 3861 9266
f: +86 21 3861 9599
e: info-engineeredmaterials-asia@celanese.com

Europe
Am Unisys-Park 1
65843 Sulzbach, Germany
Product Information Service
t: +49-800-86427-531
t: +49-(0)-69-45009-1011
e: info-engineeredmaterials-eu@celanese.com

General Disclaimer

Trademark